PhD-FSTC-2019-77
The Faculty of Sciences, Technology and Communication

DISSERTATION

Defense held on 11/12/2019 in Esch-sur-Alzette

to obtain the degree of

DOCTEUR DE L'UNIVERSITÉ DU LUXEMBOURG EN SCIENCES DE L'INGÉNIEUR

by

Gelen Gael CHEWE NGAPEYA

Born on 17th December 1991 in Yaoundé (Cameroun)

IMPROVEMENT OF THE LOAD-BEARING CAPACITY OF DRY-STACKED MASONRY

Dissertation defense committee

Dr.-Ing. Danièle Waldmann, dissertation supervisor
Assistant-Professor, Université du Luxembourg, Faculté des Sciences, de la Technologie et de la Médecine

Dr.-Ing. Frank Scholzen, Chairman
Assistant-Professor, Université du Luxembourg, Faculté des Sciences, de la Technologie et de la Médecine

Dr.-Ing. Andreas Zilian, Vice-chairman
Professor, Université du Luxembourg, Faculté des Sciences, de la Technologie et de la Médecine

Dr. Abdelouahab Khelil
Professor, Université de Lorraine, Institut Jean Lamour

Dr. Foudil Mohri
Professor, Université de Lorraine, Laboratoire d'Etude des Microstructures et de Mécanique des Matériaux

Contents

Acknowledgement

The current thesis was realised during my time as doctoral researcher, from January 2016 to December 2019, in the Laboratory of Solid Structures, part of the Research Unit in Engineering Science of the Faculty of Science, Technology and Communication of the University of Luxembourg. Throughout this thesis, I received significant supports and assistances.

First, I express my profound gratitude to my supervisor, Professor Danièle Waldmann, for offering me the opportunity to undertake my research in a pleasant environment. Then, I would like to express my recognition for her continuous mentoring, her constructive suggestions and the attentive ear paid to my personal matters. Many thanks dear Professor!

I would like to thank so much Professor Frank Scholzen and Professor Andreas Zilian for the valuable advises and suggestions provided for improving my research work. I express my profound acknowledgement to Pr. Abdel KHELIL for accepting to be a member of the jury of my dissertation defence, after having supervised me in Master Degree in the University of Lorraine and encouraged me to continue in PhD. I also express a great thank to Professor Foudil Mohri, my former lecturer in finite element calculation, for accepting to participate as member of the jury to my dissertation defence.

My depth acknowledgment to the management board of “Lëtzebuerger Contern” for the confidence in this research project and the significant financial support allocated for its achievement. To Mr. Carlo Spina, head of Construction and Innovation at “Lëtzebuerger Contern”, I express my sincere gratitude for the constructive exchanges.

I would like to express my depth recognition to Mr. Gilbert Klein and Mr. Marc Seil for the significant support and the valuable time spent for helping me to design and realise all the experimental tests. I wish also to thank the technical support staff members, Claude Collé, Logan Filipe Freitas Moreira, and Vincente Reis Adonis, for their daily help in the laboratory.

I express my gratefulness to my colleagues and friends, Dr. Michael Weiler, Dolgion Erdenebat, Patrick Pereira, Vishojit Bahadur Thapa and Lorenç Bogoviku, for the

constructive discussions and the warm and friendly atmosphere inside and outside from the work environment.

I express my gratitude to Mme. Madeleine Aka and Mr. Franck Agoussi for having welcomed and sponsored me since my arrival in Luxembourg. I also address great thanks to my friends, Dr. Thierry Titcheu, Dr. Patrick Kobou, Videline Tsokezo and Nora Tchassem, for the warm environment all along this time.

I express a particular acknowledgement to my family, my father Mr. Ngapeya Siewe, my sweet mother Mme Rosalie Chiede, my lovely wife Aude Inès Kameni and our lovely toddlers Yoan and Yonel Chewe, for their endless love and their moral support all along this "trip". Dear Aude, for sure this could have not been possible without you, thank you for all honey. Dear Yoan and Yonel, in practice, using my keyboard to write this dissertation was not easy because I had to wear each of you in my arms without conditions. However, I thank you so much because it was an inexhaustible source of inspiration.

Finally, I praise the Lord for the strength and health he gave me throughout this wonderful scientific adventure.

Luxembourg, December 2019

Gelen Gael CHEWE NGAPEYA

Keywords

Dry stacked masonry

Mortarless masonry

Block unit

Axial compressive strength

Load-bearing capacity

Actual contact area

Bed-joint imperfections

Bed-joint roughness

Contact surface unevenness

Block height variation

Contact layer

Prescale Fujifilm strips

Mitigation strategy

Finite element modelling

Abstract

Mortar bonded masonry is one of the oldest construction technics traditionally used around the world. However, dry-stacked masonry (DSM) is a competitive system that confers significant assets to masonry in the sense that, concisely, it saves construction time, requires less skill labourers and ease the construction as well as the de-construction. Despite all this major benefits, the current use of DSM is hindered by the geometric imperfections of the block units and the lack of adapted design codes. Indeed, the block geometric imperfections, i.e. the bed-joint roughness and the height difference, cause a significant uneven load-distribution in DSM, which generally leads to a premature cracking and a drop of the wall compressive strength. On the other hand, the lack of adapted design codes entail significant safety hazards in the construction of such masonry walls. In view of the foregoing, through systematic numerical, experimental and analytical investigations, the present thesis aims to analyse the impacts of the block bed-joint imperfections on the mechanical response of DSM axially loaded. Furthermore, the current thesis aims to develop a strategy to overcome the block geometric imperfections and alleviate its impacts on the load-bearing capacity of DSM. Finally, the present thesis intends to develop a design model for predicting the load-bearing capacity of DSM, while taking into account the effects of the block geometric imperfections for a safe design.

First of all, at the beginning of the research project, a new dry-stacked masonry block is designed and labelled ‘M-Block’. The impact of the bed-joint roughness and the block height variation on the stress distribution in a DSM is analysed through numerical modelling. It is shown that the block height difference yields five potential load cases that block units may suffer upon the axial compression of a DSM wall. Accordingly, it is also shown that a nominal DSM wall can exhibit different load percolation paths and different damages. Further, a strategy is presented to overcome the bed-joint imperfections, increase the actual contact area in the bed-joints and ultimately improve the load-bearing capacity of DSM, by adding a material layer (the ‘contact layer’) on the raw DSM_b. The capacity of the contact layer to increase the actual contact and level the stress distribution was first investigated through numerical models then evidenced through experimental tests on masonry triplets. The

contact layer was also investigated for improving the load-bearing capacity of dry-stacked masonry, with satisfactory results obtained on wallets tested in the lab.

As the finite element modelling is cumbersome and the experimental investigations onerous and laborious, an analytical model has then been developed for predicting the load-bearing capacity of DSM. A statistical modelling has been developed for determining a factor δ_h, which stands for the reduction of the nominal section of a DSM generated by the block height variation. Experimental tests were also performed on masonry triplets for measuring the ultimate actual contact in the bed-joints and defining a factor δ_r, which stands for the reduction of the nominal contact area generated by the block bed-joint roughness. The two defined parameters were then exploited to establish the design model that takes into account the block imperfections in the prediction of the load-bearing capacity of DSM. The design model was shown quite well capable of predicting the load-bearing capacity of DSM with a mean accuracy of 93% - 106% and a standard deviation of 12% - 10%.

Résumé

La maçonnerie liée au mortier est l'une des plus anciennes techniques de construction traditionnellement utilisée dans le monde. Cependant, le concept de maçonnerie posée à sec est une approche très compétitive qui confère d'importants avantages à la maçonnerie, soit entre autre le gain de temps de construction, le moindre besoin de main d'œuvre qualifiée, la facilité de construction et de déconstruction. Néanmoins, malgré tous ces atouts majeurs, l'usage courant de la maçonnerie posée à sec est entravée par l'influence des imperfections géométriques des blocs individuels et le manque de codes de conception adaptés. En effet, les imperfections géométriques des blocs que sont la rugosité des faces d'appuis et la différence de hauteur entre les blocs causent une importante inégale distribution des charges dans les murs, ce qui conduit généralement à la fissuration prématurée et à la chute de la capacité portante du mur en compression. D'autre part, le manque de code de conception accroit les risques de sécurité pour les murs de ce type. Au regard de ce qui précède, moyennant des investigations numériques, expérimentales et analytiques, la présente thèse vise à analyser l'impact des imperfections des blocs sur la résistance mécanique des murs posés à sec et sollicités en compression axiale. De plus, la présente thèse vise à développer une solution pour surmonter l'influence des imperfections des blocs et atténuer leurs impacts sur la capacité portante des murs posés à sec. Enfin, la présente thèse se destine à proposer un modèle de conception prédisant la capacité portante des murs posés à sec, en tenant compte de l'influence des imperfections des blocs individuels.

De prime abord, un nouveau modèle de maçonnerie emboîtable et posée à sec a été conçu et labélisé « M-Block ». L'impact de la rugosité des faces d'appuis et de la différence de hauteur des blocs sur la distribution des contraintes dans un mur a été analysée via la modélisation par élément finis. Il a été montré que la différence de hauteur entre les blocs génère cinq potentiels cas de charge que peuvent subir les blocs de maçonnerie lors de la compression axiale d'un mur. En conséquence, il a été montré qu'un mur posé à sec peut présenter différent chemin de descente de charge et d'endommagement. En outre, une stratégie consistant à ajouter une couche de matériaux sur les faces d'appuis des blocs bruts a été investiguée pour améliorer à la fois le contact réel dans les joints et la capacité portante des murs. À travers des tests expérimentaux et la modélisation par éléments finis des prismes de maçonneries, l’usage d’une couche additionnelle a montré des résultats prometteurs à la fois dans l’amélioration du contact réel et dans la distribution des contraintes dans les blocs. La performance de la couche additionnelle dans l’amélioration de la capacité portante des murs posés à sec a également été investiguée avec des résultats satisfaisants obtenus sur des murets testés au laboratoire. Il a été montré que l’usage d’une couche additionnelle à faible module de Young et/ou à coefficient de Poisson négatif permet d’améliorer significativement la résistance des murs posés à secs.

Enfin, l’approche expérimentale et par élément finis étant onéreuses et laborieuses, un modèle de conception a été développé pour prédire la capacité portante des murs posés à sec. Le facteur d’influence de la variation de hauteur des blocs sur la réduction de la section utile d’un mur (δ_h) a été déterminée par une modélisation statistique des éventuels chemins de descente de charge possible dans un mur. Les tests expérimentaux menés sur les prismes de maçonneries ont également permis de mesurer les surfaces maximales de contact réel entre les blocs, ce qui à terme a permis de définir le facteur de réduction de contact (δ_r) généré par la rugosité des faces d’appuis des blocs. Les deux facteurs définis ont été exploités pour établir un modèle de calcul de la capacité portante des murs posés à sec. Le modèle de conception proposé s’est montré assez bien capable de prédire la capacité portante des murs posés à sec avec une précision moyenne de 93% à 106% et un écart-type d’environ 12% à 10%.

List of publications

Peer reviewed journal papers (Elsevier)

1. Gelen Gael Chewe Ngapeya, Danièle Waldmann, Franck Scholzen, Impact of the height imperfections of masonry blocks on the load-bearing capacity of dry-stack masonry walls, *Construction and Building Materials 165 (2018), 898-913*. (SJR Index Q1, Scopus Top 10%: 96% in the field of Civil and Structural Engineering)

   doi.org/10.1016/j.conbuildmat.2017.12.183

2. Gelen Gael Chewe Ngapeya, Danièle Waldmann, Experimental and analytical analysis of the load-bearing capacity P_u of improved dry-stacked masonry, *Journal of Building Engineering 27 (2020), 100927*.(SJR Index Q1, Scopus Top 10%: 96% in the field of Civil and Structural Engineering)

   doi.org/10.1016/j.jobe.2019.100927

3. Gelen Gael Chewe Ngapeya, Danièle Waldmann, Overcome of bed-joint imperfections and improvement of actual contact in dry-stacked masonry, *Construction and Building Materials 233 (2020), 117173*. (SJR Index Q1, Scopus Top 10%: 96% in the field of Civil and Structural Engineering)

   doi.org/10.1016/j.conbuildmat.2019.117173

Conference paper

1. Gelen Gael Chewe Ngapeya, Danièle Waldmann, Frank Scholzen, Andreas Zilian, André Lecomte, Abdel Khelil, Prédiction de la résistance mécanique d’un bloc de maçonnerie sans joint par calcul numérique, *17^{e} édition des Journées Scientifiques du Regroupement Francophone pour la Recherche et la Formation sur le Béton (RF)^{2}B,* IFSTTAR, Marne-la-Vallée, juillet 2016.

1 Introduction

1.1 Motivations

Masonry is one of the oldest construction technics commonly used for centuries around the world. They are classified in different product families according to the nature of their materials, their internal structure [1] (full or hollow blocks, blocks with cells, etc.), their field of application, their mode of installation (with joints or dry-stacked) and their contribution to the stiffness of a structure. Over years, the construction regulations and constraints have become increasingly stringent, the demand in building products increasingly significant and the execution delays tighter. However, in the state of art, a great part of the literature investigates more on the traditional masonry system. In order to follow the evolution of needs, some researchers attempted to developed competitive masonry blocks. In this regard, a great number of interlocking dry-stacked masonry blocks have been developed and marketed along the recent 20 years.

In a dry-stacked system, the block units are laid without mortar, which provide practical advantages to such a system. Among others, one may note the time saving, the least need of skilled labourers, the erection ease, the environmental efficiency due to the least waste of materials and the ease of deconstruction. As well, one may cite e.g. the possibility to reuse the masonry blocks, the flexibility to modify a floor plan, the elimination of the mortar quality variation, the possibility to construct during cold time. However, the lack of mortar in the bed-joints of the dry-stacked masonry blocks (DSM_b) brings forward the influence of the geometric imperfections that constitute the key issues of this system. Indeed, the main geometric imperfections recognized to the masonry blocks are the roughness of the contact faces, and the height difference from one block to another. In the limited part of the literature tackling dry-stacking masonry, several authors cite the geometric imperfections without focusing on their impact on the mechanical response of both individual blocks and walls. In addition, regarding the designing of masonry structures, the current standards EN 1996-1-1 [1] only gives provisions for the designing of bonded mortar masonry. There is no existing specific guidelines safely applicable to dry-stacked masonry, which reduces its current use despite all its assets.

Based on the actual state of the art, it is of great interest for the construction industry to develop dry-stacked masonry blocks able for withstanding heavy loads without exhibiting cracks. In addition, for the structural Engineers, it is useful to have an appropriate design concept for safely design dry-stacked masonry walls. In this context, a research project has been set up between the laboratory of Solid Structures of the University of Luxembourg and the industrial partner Lëtzebuerger Contern for developing a new generation of dry-stacked masonry block; for investigating a solution to overcome the effects of the blocks imperfections; and for developing a design concept adapted to DSM.

1.2 Purposes

Through numerical and experimental investigations, the current research work aims at analysing the impact of the block imperfections on the behaviour of dry-stacked masonry under axial compression. Moreover, the present research work aims to investigate the use of an additional layer placed on the raw dry-stacked masonry as strategy for mitigating the impact of the block imperfections and ultimately improve the load-bearing capacity of dry-stacked masonry. Finally, the research work intends to develop a design model taking into account the impact of the block imperfections for safely predicting the load-bearing capacity of dry-stacked masonry.

1.3 Overview

The dissertation is laid out in fourth main parts. First of all, a literature review is presented in chapter 2. Then, the development of a new interlocking DSM is presented in chapter 3. In the third part, the analysis of the effectiveness of the additional layer for improving the load-bearing capacity P_u of DSM is addressed through experimental and numerical investigations respectively in chapter 4 and chapter 5. Finally, the development of a design model for predicting P_u is presented in chapter 6. The respective chapters deal with the following:

- **Chapter 2** focuses on the state-of-art and provides an insight on the behaviour of masonry in general, step required for identifying the issues of dry-stacked masonry. Firstly, the different scientific techniques used for studying masonry structures are presented. Then, a brief review of the influence of both mortar and block strength on the behaviour of masonry is presented. A non-exhaustive list of dry-stacked masonry blocks developed around the world is presented, as well as former numerical and experimental investigations addressing the behaviour of the dry-stacked masonry blocks. Next to the latter, the premise investigations carried out to mitigate the effect of the geometric imperfections on the masonry blocks are presented. Finally, a brief recall on the theories of contact mechanic is laid out.
- **Chapter 3** presents the new designed dry-stacked masonry block labelled M-block. Herein, a finite element modelling approach is exploited for (1) predicting the load-bearing capacity of the M-block and (2) for determining the strength correlation between the M-block and the constitutive materials. Thereafter, experimental tests are carried out on single block unit for validating the numerical model and determinate the actual compressive strength of the M-Block.
- **Chapter 4** presents the experimental tests carried out on both masonry prisms and wallets. The capacity of the contact layer with conventional and auxetic materials for (1) increasing the actual contact in the bed-joints, (2) promoting a better stress distribution and ultimately (3) improving the load-bearing capacity of DSM is experimentally evidenced.
- **Chapter 5** goes through the finite element analysis of the effect of the bed-joint roughness and of the height variation of the block units on the behaviour of DSM under axial compression. First in this FE approach, the failure criterion, the masonry block modelling and the contact interface modelling are presented. Then, the effect of the bed-joint roughness and of the height variation of the block units are addressed apart. A basic bed-joint roughness model is defined and its influence on the stress distribution and on the deformation of DSM-prisms is analysed. The results of the FE approach are compared to the experimental tests and a parametric study of the influence of the height of the surface asperities is carried out. Then, the effects of the

height variation of the masonry blocks is analysed on the scale of a singular block and on the scale of a wallet. The effectiveness of the additional layer for increasing the actual contact and for levelling the stress distribution in DSM-wallets is also discussed in function of the height difference purposely inserted between the block units. The results of the FE analysis provide a support for better understanding the failure mechanisms observed during the experimental tests.

- **Chapter 6** presents the design model proposed for predicting the load-bearing capacity of a dry-stacked masonry. Herein the new parameters designed for taking into account the effects of the block bed-joint roughness and of the block height difference on the load-bearing capacity of a dry-stacked masonry are presented. In addition, for engineering purposes, a simple MATLAB program with user' interface and a designer's diagram are presented for determining the value of the new introduced design parameters in function of the height and length of the wall to be design. Then, the design model is implemented for predicting the load-bearing capacity of DSM-walls experimentally tested by former researchers. Finally, the prediction of the proposed model is compared to the prediction made using the current provisions of Eurocode 6.

A summary of the core findings of the research work and the outlook are highlighted in the conclusion (**chapter 7**).

2 State of the art

2.1 Introduction

This chapter presents (1) a brief review of the scientific technics used to study masonry, (2) a short examination of the behaviour of mortared masonry and (3) a review of former investigations carried out in the field of dry-stack masonry. The overview of the state-of-art aims to identify the relevant issues not yet tackled or not enough analysed for drawing the research methodology of the current thesis.

2.2 Scientific technics to study masonry

2.2.1 Experimental approach

Several findings are based on experimental evidences. Most of the investigations are based on experimental tests carried out on masonry prisms, masonry wallets and full-scale masonry walls. The investigations carried out on prisms and wallets well approximate the response of full scale-walls and enable extensive analysis to affordable cost. However, the approximations influence the degree of accuracy. On the other hand, although more accurate, investigations on full-scale masonry walls are much less current because of the induced cost and accordingly the least possibility to carried out extensive tests. Nonetheless, it has been shown that compared to masonry prisms, masonry wallets reflect the actual behaviour of full-scale masonry walls with a good accuracy since they include both vertical and horizontal joints [1–4].

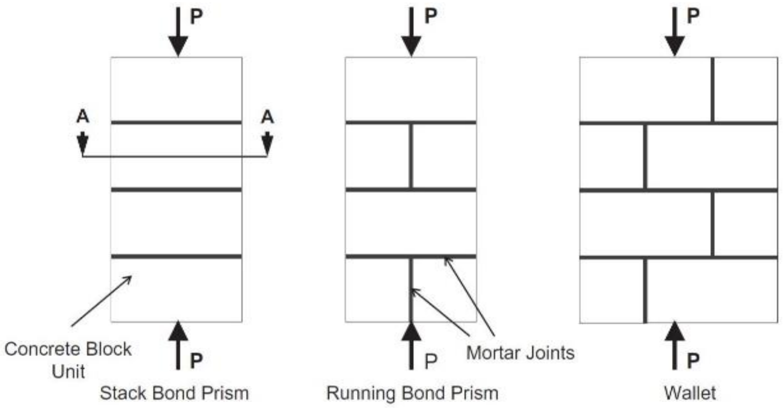

Figure 1. Configuration of concrete block masonry prism [5]

Dhanasekar et al. [6] reminded that in experimental tests on masonry prisms, the use of harder capping and stiffer patterns in the interface with the press plates imparts higher apparent compressive strength to the tested specimen. This is due to the non-uniform tri-axial state of stress in the bearing surfaces of the test specimens.

2.2.2 Numerical approach

Taking into account that full-scale experimental tests are expensive, finite element analysis has been used in many studies to predict the in-service and near-collapse behaviour of such complex structures with sufficient reliability. Former researchers have led investigations on numerical modelling of masonry blocks, especially for the investigation of the behaviour of mortared masonry walls. In the finite element modelling, two different approaches can be used: (1) the micro-model approach, which use individual properties of the constituent materials and their interfaces separately [7–10], and (2) the macro-model approach, which for its part uses homogenised properties for the blocks and the mortar [11–13]. The micro-model provides a good insight on the behaviour of each constituent (masonry block, mortar layer, contact areas) separately described by means of specific constitutive equations. This method leads to the most accurate prediction, whilst, the macro-model approach needs less computational effort and thus allows an analysis of high structure in short time.

Zucchini et al. [11] and Bati et al. [14] have proposed to apply the homogenisation techniques developed by Bakhvalov et al. [15] to analyse the behaviour of mortar masonry structures.

The developed homogenisation approach consists on describing the behaviour of the composite masonry walls in terms of macro-strains and stresses so that the composite structure can be assumed as homogeneous. The composite structure built up of basic cells (masonry blocks, vertical and horizontal joint layers) is transposed to a homogeneous structure whose stresses and strains in the loading plane are analytically expressed in function of the geometric dimensions, the stresses and strains of the basic cells. Indeed, the elastic response of the basic cells to a generic load is determined by the study of six basic loading conditions. Furthermore, the Poisson's ratio and the Young's modulus of the equivalent orthotropic homogeneous material are derived from the elastic strains of the basic cell loaded with a uniform normal stress on the two faces perpendicular to the loading plane. The outcomes of the homogenisation approach showed that up to a stiffness ratio of one thousand between masonry block and mortar layer, the maximum error in the calculation of the homogenised Young's modulus is lower than five percent compared to the Young's modulus obtained by finite element analysis of the heterogeneous structure. However, Anthoine [12,13] has shown that the standard homogenisation technique does not take into account the different bond patterns (tenon and mortise, solid seal, etc.).

Anastasios Drougkas et al. [10] focused on the numerical prediction of the compressive response of a masonry block, its failure mode, its hardening and softening behaviour under compression by means of finite element micro-modelling techniques. Based on a panel of fifty former experimental tests, they showed that a three-dimensional micro-model allows a more accurate and general simulation of the compressive behaviour of a masonry block. Nevertheless, Salah's [5] results on the prediction of the compressive strength of a masonry block have shown that most numerical codes underestimate the compressive strength of the ungrouted masonry block with high coefficients of variation. Based on statistical analysis of 248 experimental datasets, they fixed the underestimation at 82 % of the compressive strength of the hollow concrete masonry block. Abdulla et al. [16] exploited a simplified micro-model approach for simulating the progressive cracking and the non-linear post failure behaviour of mortared masonry.

2.3 Mortared masonry blocks

In the field of masonry, the term ‘masonry’ refers to an arrangement of block units (concrete blocks, stone, bricks) bonded together with a binder called mortar. The standard design codes EN 1996-1-1 [1] classifies the block units in terms of the constitutive material and the hollowness. Mortared masonry is widely used around the world and several scientific works have investigated its in-plane and out-of-plane behaviour including factors like e.g. the mortar strength and thickness, the block unit strength and the load eccentricity . A brief summary of the actual knowledge is given below.

2.3.1 Influence of mortar on the masonry behaviour

- Mortar strength - general behaviour and failure mechanism

Several researchers highlighted that the mortar layer is highly responsible for the nonlinear behaviour of a masonry wall. Gihad Mohamad et al. [17] carried out experimental research on the mechanics of hollow concrete masonry under compression. Out of their experiments, they concluded that in addition to govern the non-linear behaviour of masonry, the mortar layer is responsible for the large axial strain and the development of tensile stress in the block units, which lines up with the findings of Fahmy et al. [18], McNary et al. [19], Drougkas et al. [20] and Zucchini et al. [21]. These authors have shown that under axial compression, the decrease in mortar strength goes with a decrease of the elasticity modulus, which yields and increases the lateral tensile stresses in the block units. Indeed, for weak mortar strengths, while the mortar layer is in a tri-axial compression state because of the lateral confinement, the block units are under compression in the loading direction and under tension in the two other main directions [22]. This state of stress, especially the tensile stresses in the lateral direction, leads to an earlier development of cracks in the block units and a decrease of the compressive strength of the mortared masonry. Conversely, higher mortar strength leads to less induced lateral tensile stress in the block units of a masonry wall [5].

Gihad Mohamad et al. [17] found a non-linear relationship between the masonry elasticity modulus and its compressive strength, contradicting the linear relationship established in

EN 1996-1-1 [1]. Through a homogenisation approach, Zucchini et al. [21] have shown that under compressive load the nonlinear deformation of masonry starts very early for weak mortars. Likewise, Adrien Costigan et al. [23] and McNary et al. [19] noted that the stress-strain relationship of bounded masonry blocks becomes increasingly non-linear as the mortar strength lowers.

As shown in Figure 2, Gihad Mohamad et al. [17] found that the failure mechanism of masonry prisms is closely linked to the mortar strength: weak mortar strength induce face-shell spalling whereas strong mortar strength yield vertical cracks in the block units. More recently, Gihad Mohamad et al. [24] further investigated the influence of mortar of different strengths on the strength, the behaviour and the failure mode of hollow concrete masonry . They ascertained that in masonry stacked with weak mortars, failure starts earlier with a mortar crushing which leads to localized tensile stresses in the masonry blocks. In masonry stacked with a strong mortar, they observed that cracking starts much more later in the block units and grow until reaching the mortar layer. Fahmy et al. [18] noted that the compressive strength of masonry increases with increasing mortar strength, regardless the mortar thickness. For a three-course masonry prism, they showed that increasing the mortar strength by 40% leads increasing the masonry prism strength by 12%. However, Zeljka et al. [25] observed that the use of a mortar with a higher compressive strength than the block units decreases the load-bearing capacity of the masonry wall and makes the failure more brittle. Zucchini et al. [21] found that when the mortar is stiffer but still weaker in compression than the block units, the latter do not fail by an exceedance of the tensile stresses in the webs, but rather by a face-shell crushing. Finally, when the mortar is much stiffer than the block units, the failure occurs by crushing of the block face-shells and the block units govern the nonlinear response of the masonry. This latter finding meets the Drougkas et al. [20] ones who showed that the use of high strength cement mortars shifts the masonry failure mechanism towards compressive yielding of the block units.

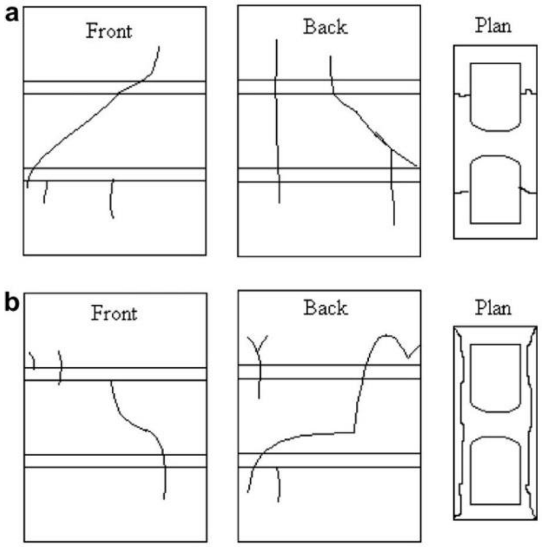

Figure 2. Failure modes for hollow concrete masonry prisms: (a) strong mortar; (b) weak mortar [17]

- Mortar thickness – general behaviour and failure mechanism

Regarding the influence of the mortar thickness, Gihad Mohamad et al. [24] noted that the increase in thickness of the mortar layer negatively affects the compressive strength of the hollow concrete masonry prisms by causing vertical cracks in the block units at lower applied load. As well, Feng et al. [26] investigated the effect of the mortar joint thickness on the compressive strength of autoclaved fly ash-lime brick masonry. They concluded that as the joint thickness decreases, masonry compressive strength improves. Thamboo et al. [27] and Zahra et al. [22] inferred that the masonry strength increases with the reduction in the mortar joint thickness since the incongruity between the block units and the mortar layers decreases.

2.3.2 Influence of block units on the masonry behaviour

Fahmy et al. [18] developed a 3D finite element model to study grouted and ungrouted concrete mortared masonry prisms under axial compression. They observed that the prism compressive strength increases with the block unit strength, therefore matching the findings reported in [17,28–41]. However, they noted that the rate of increase of the prisms' compressive strength decreases with increasing the block unit compressive strength.

Indeed, they showed that the block strength has two opposite effects on the prisms strength. (1) The compressive strength of a block unit makes increase its tensile strength, which plays in favour of a higher load-bearing capacity of the masonry prism. (2) At the same time, a block strength increase induces much more mortar confinement, which in turn induces higher lateral tensile stresses in the block units and accordingly detrimental effects on the prism strength. Nassif et al. [42] showed that in addition to the block unit strength and the mortar strength, the compressive strength of mortared masonry is also influenced by factors like the volume fraction of the block unit and the volume ratio of the mortar joint. They concluded that the block unit strength is directly proportional to the masonry strength. Zhou et al. [43] observed that the increase of a block compressive strength by 80% induces an increase of approximatively 60% in the masonry compressive strength with a height to thickness ratio (h/t) of 4,7. Thamboo et al. [27] showed that the type of block units (in terms of geometry, size and hollowness) significantly influences the compressive strength of masonry. They compared conventional two cell hollow blocks with H blocks and they found that the H blocks exhibit a loss of the compressive strength of about 16% to 25% with respect to the conventional two cell hollow blocks.

2.3.3 Design model for mortared masonry

Several researchers amongst which Nassif et al. [42] have proposed mathematical models (equation (1)) for predicting the characteristic compressive strength (f_k) of mortared masonry. In the proposal of Nassif et al. [42], f_b represents the compressive strength of the masonry unit, f_m the compressive strength of mortar, VF_b the volume fraction of masonry unit, VR_{mH} the volume ratio of bed-join to mortar and h/t the height to thickness ratio of the masonry.

$$f_k = \frac{0,54\, f_b^{1,06}\, f_m^{0.004}\, VF_b^{3,3}\, VF_{mH}^{0,6}}{h/t^{0,28}} \qquad (1)$$

Beyond the above, the standard design code EN 1996-1-1 [1] provides guidelines for the prediction of the characteristic compressive strength (f_k) of common and thin mortared masonry, based on the shape factor of the block unit (K), the compressive strength of the masonry unit (f_b), the compressive strength of mortar (f_m). The analytical models proposed by EN 1996-1-1 [1] are recalled in equation (2), (3) and (4).

$$f_k = K\, f_b^{0.7}\, f_m^{0.3} \tag{2}$$

$$f_k = K\, f_b^{0.85} \tag{3}$$

$$f_k = K\, f_b^{0.7} \tag{4}$$

2.4 Dry-stacked masonry (DSM)

2.4.1 Interlocking systems

Conventional mortared masonry is labour intensive and time-consuming. In the recent past, the trends to make masonry competitive and reusable while limiting the manufacturing costs have led to the development of a wide range of dry-stacked masonry blocks (DSM_b) around the world [44–51]. A non-exhaustive list of developed DSM blocks/bricks is presented in Figure 3. Waleed et al. [44], Agaajani [45] and Haener et al. [48] developed dry-stacked masonry blocks presenting an almost similar interlocking mechanism. Abang et al [47] designed an interlocking masonry block based on the LEGO’s concept. As well, Thallon [46] developed interlocking masonry blocks that were used to build a single-storey house. Sturm et al. [50] and Ben Ayed et al. [49] developed an Interlocking Stabilized Earth Block (ISEB). Cetholic et al. [51] designed a dry-stacked masonry block however without interlocking mechanisms in both vertical and horizontal direction.

Nor Azmi et al. [52] and Anand et al. [53] have deeply investigated on the effectiveness of DSM_b in terms of construction productivity. Nor Azmi et al. [52] investigated the environmental awareness and benefits of industrialized building systems (IBS) using interlocking dry-staked masonry blocks. Along their research project, they performed a comprehensive analysis comparing the conventional method of masonry wall constructions with an IBS using interlocking masonry blocks. As outcomes, they found that with respect to conventional masonry, constructions using interlocking DSM_b reduce the overall cost, time and labour requirements to produce better house quality. In addition, they showed that IBS using interlocking masonry blocks facilitate the waste minimization, thus further highlighting the positive environmental footprint of DSM$_b$. Anand et al. [53] carried out investigations to assess and compare the productivity of construction methods using conventional and interlocking DSM$_b$. Table 1 summaries the productivity measured for each type of masonry block, for the completion of 1,50 m^2 of wall. They came out with the conclusion that the use of DSM$_b$ leads to a productivity enhancement of 80-120 % compared to conventional masonry blocks.

In addition to the above, DSM is easily demountable and reusable following a deconstruction, which supports the idea of sustainable circular economy.

Table 1. Overall construction output of different masonry systems [53]

	Time for the completion of 1.5 m^2 panel (min)			Net output (m^2 per productive hour)
Type of masonry	Trial 1	Trial 2	Trial 3	
Brick masonry	107	116	110	0.96
Hollow-block masonry	90	89	84	1.27
Dry-stacked, solid interlocking block masonry	55	56	50	2.33
Mortar-bedded, solid interlocking block masonry	62	65	64	1.86
Thin-jointed, solid interlocking block masonry	59	64	61	1.89
Dry-stacked, hollow interlocking block masonry	56	55	55	2.21
Thin-jointed, hollow interlocking block masonry	68	69	66	1.71

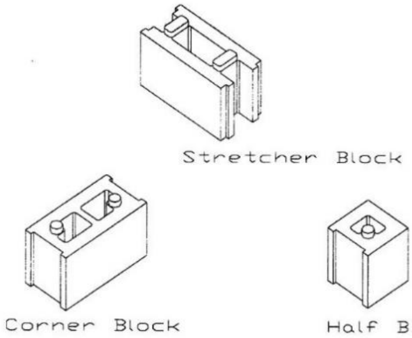

Putra block [44]

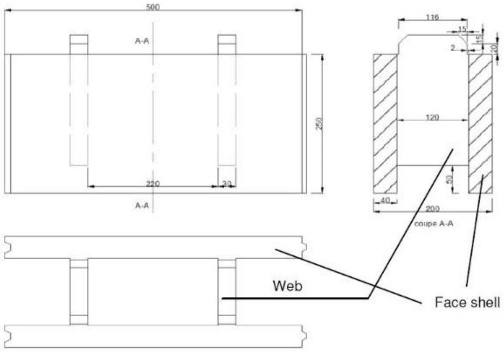

Agaajani' block [45]

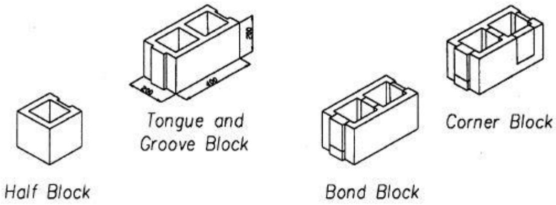

R. Thallon' block [46]

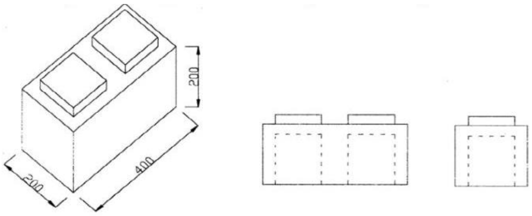

Abang' block [47]

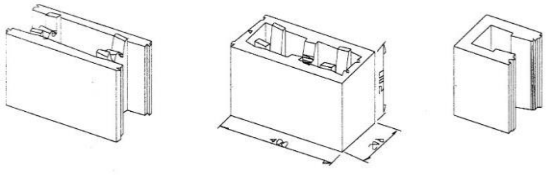

Haenar' block [48]

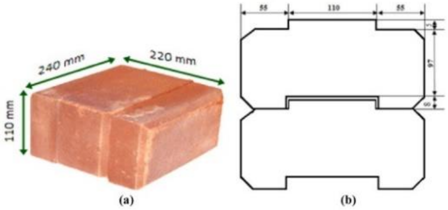

Interlocking stabilized earth brick [49]

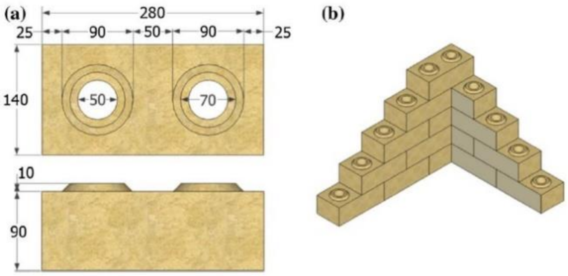

Sturm' block [50]

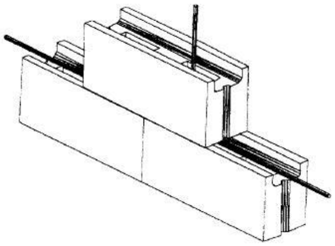

Cetholic' block [51]

Figure 3. A non-exhaustive list of developed interlocking dry-stacked masonry blocks/bricks

Anand et al. [54] carried out a performance evaluation of interlocking block masonry. They proposed a classification of mortarless masonry systems (Figure 4) in terms of geometry, interlocking mechanism, constitutive material and application.

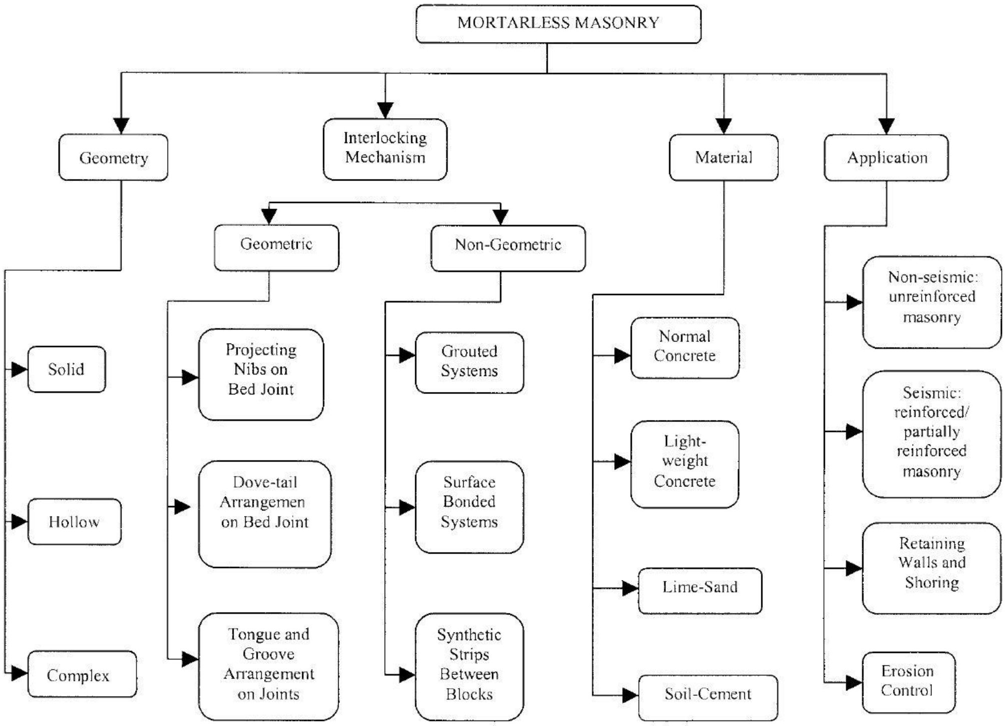

Figure 4. Classification of mortarless masonry systems [54]

2.4.2 Strategies for measuring the actual contact in dry-stacked masonry

In the field of dry-stacked masonry, as it will be shown later, the actual contact between the block units plays a significant role in the mechanical response of the overall masonry. Thus, monitoring the actual contact in dry-stacked masonry is useful for mastering its behaviour. Three main means have been identified in the literature for measuring the actual contact in a contact interface of two dry-stacked block units. They are the matrix based tactile surface sensors (MBTSS), the Prescale Fujifilm strips and the Carbon Footprint papers.

2.4.2.1 Matrix Based Tactile Surface Sensors (MBTSS)

The matrix based tactile surface sensors is a sensor manufactured by Tekscan Inc and commonly used in mechanical engineering to quantify the stress distribution in the contact interface between two solids. Indeed, the MBTSS is constituted of sensors, data acquisition electronics and a Tekscan's I-Scan software (Figure 5). The sensor itself is constituted of a conductive silver ink sealed in two thin polyester sheets sandwiched together. A stress sensitive semi-conductive material is placed in the interfaces between the polyester sheets.

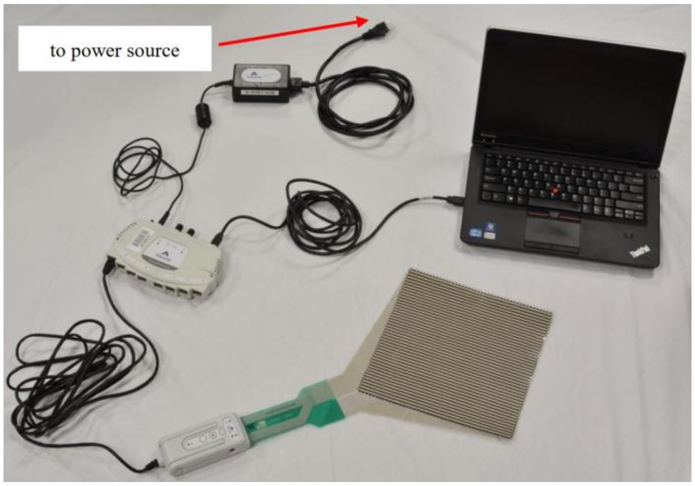

Figure 5. Tekscan data acquisition system of a MBTSS [55]

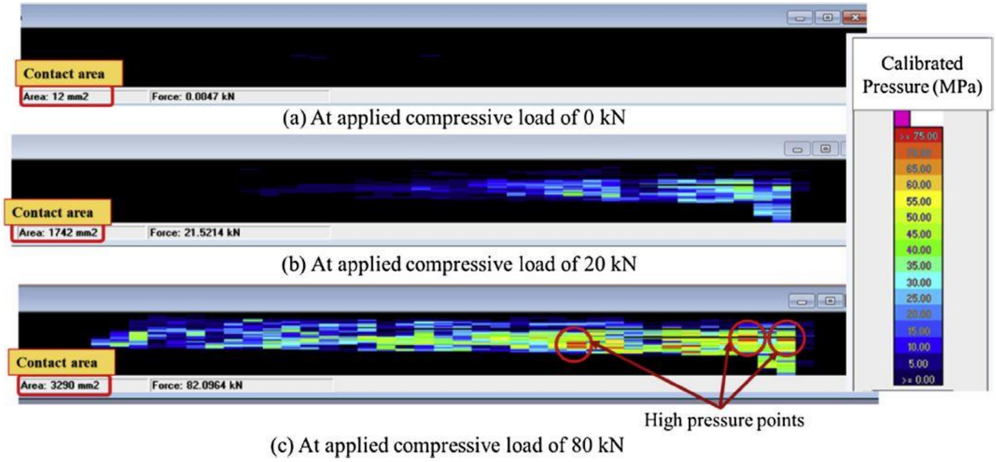

(a) At applied compressive load of 0 kN

(b) At applied compressive load of 20 kN

(c) At applied compressive load of 80 kN

Figure 6. Actual contact area and stress distribution instantly measured [55].

The MBTSS strip is inserted in the expected contact interface between solids and it instantly measures both the actual contact and the stress distribution under compression (Figure 6). Greve [56], Ghosh [57] and Tatheer [55] are among the first authors who used this type of sensors in the fields of civil engineering. Greve [56] experienced the use of the MBTSS in the interface analysis of ballast - rail road, whereas Tatheer exploited the MBTSS in the experimental investigation on the dry-joint surface of interlocking blocks under a compressive load. These authors concluded that the MBTSS are suitable and more accurate for measuring the actual contact area and the compressive stress in a contact interface in real time. In addition to the above, the MBTSS well depicts the stress peaks in a contact interface. However, this method is expensive and the MBTSS strips are very limited in size.

2.4.2.2 Prescale Fujifilm strips

Prescale Fujifilm strips are stress sensors enabling at once measuring the actual contact area and the contact stress intensity in a contact interface. However, the measure is indirect as the Prescale Fujifilm strips must undergo additional processes for collecting the data results. Prescale Fujifilm strips are constituted of two thin strips (Figure 7), one of which is composed of fine bubbles that burst under a specific compressive stress for releasing a red ink that impregnates the second sheet. The footprint left by the ink makes it possible to identify an actual contact area. Further, the density of the footprint increases with the contact stress intensity, which enables to point out the stress peaks sections (Figure 8).

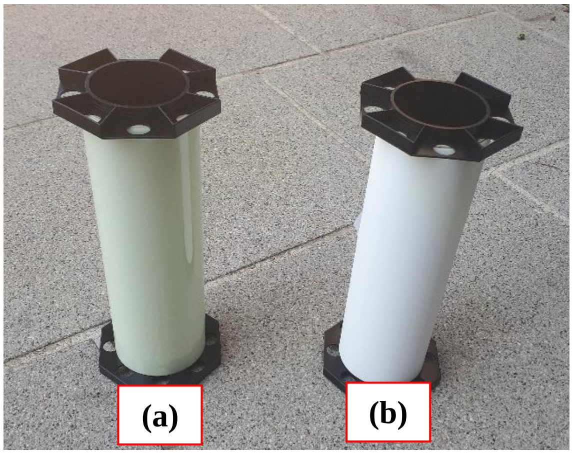

Figure 7. Prescale Fujifilm strips. (a) A-strip or sheet with the bubbles; (b) C-strip or sheet capturing the footprint of the actual contact.

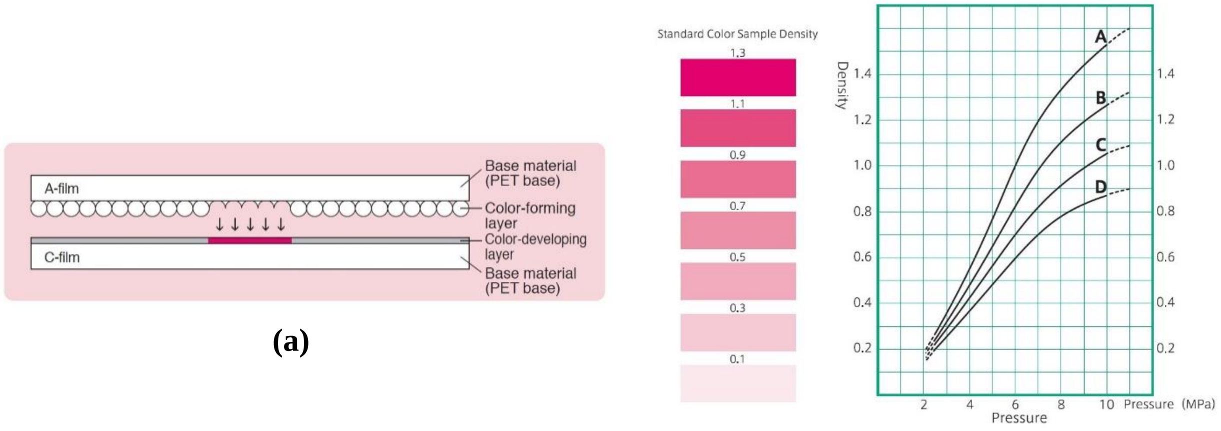

(a)

(b)

Figure 8. Operation and interpretation of a Prescale Fujifilm strip [58]

The Prescale Fujifilm strips are manufactured with a wide range of sensitivity in a way to capture the actual contact area and the stress intensity for low loads as for heavy loads. As shown in Figure 9, in any contact interface, a Prescale Fujifilm sensor is able to record a compressive stress ranged from 0,05 MPa to 300 MPa. As shown in Figure 9, this range is covered by eight sensors, from the extreme low pressure 0,05 MPa to the super high pressure 300 MPa.

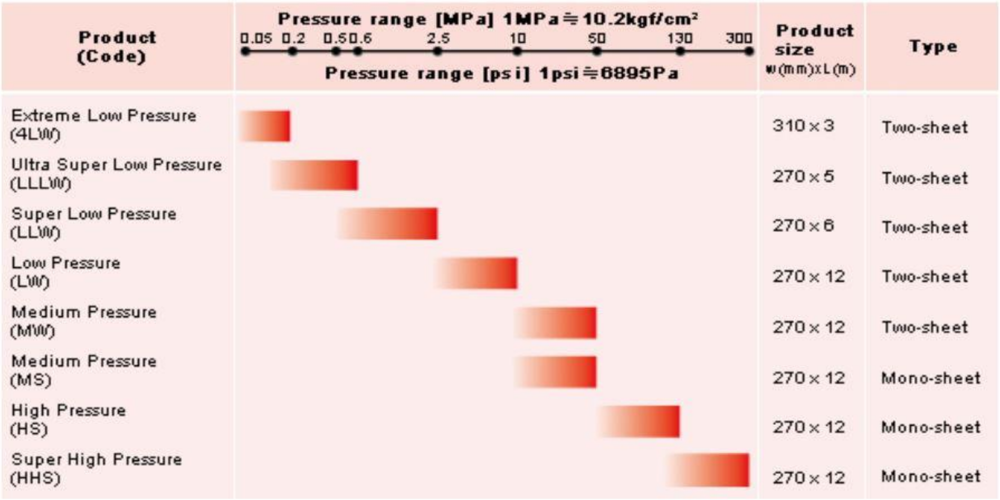

Product (Code)	Pressure range [MPa] 1MPa≒10.2kgf/cm² 0.05 0.2 0.5 0.6 2.5 10 50 130 300 Pressure range [psi] 1psi≒6895Pa	Product size w(mm)xL(m)	Type
Extreme Low Pressure (4LW)		310×3	Two-sheet
Ultra Super Low Pressure (LLLW)		270×5	Two-sheet
Super Low Pressure (LLW)		270×6	Two-sheet
Low Pressure (LW)		270×12	Two-sheet
Medium Pressure (MW)		270×12	Two-sheet
Medium Pressure (MS)		270×12	Mono-sheet
High Pressure (HS)		270×12	Mono-sheet
Super High Pressure (HHS)		270×12	Mono-sheet

Figure 9. Categories of marketed Prescale Fujifilm sensors [58]

Furthermore, the use of Prescale Fujifilm sensors requires a post-treatment to identify the applied pressures. The post-treatment can be done either by the FPD-8010E software of

Fujifilm or by an autonomous way. Following the way using the Fujifilm's FPD-8010E software, the C-strip having the imprints is scanned and the digital file is analysed with the FPD-8010E software. Indeed, the latter minimize the scanner read-errors and converts the Prescale density values into stress, in a way to show the stress distribution over the C-strip. However, the FPD-8010E software does not provide tools to automatically evaluate the percentage of actual contact areas. Following the autonomous way, once the footprints of the actual contact are captured on the C-strip, the latter is digitized and transformed in pixels. The percentage of actual contact area is obtained by reporting the number of red pixels to the whole number of pixels of the C-strip. As well, the stress intensity is assessed by comparing the R-G-B (Red-Green-Blue) features of each pixels of the C-film with the one of the density references (Figure 8) provided for each category of Prescale Fujifilm strips.

Agaajani [45] is one of the researchers who experienced the use of Prescale Fujifilm Strips for characterising the actual contact in dry-stacked masonry. This sensor has the advantage of being adaptable to all the block shapes as the films can be easily cut according to the shape and dimensions of the surfaces intended to come into contact. However, unlike the MBTSS, the Prescale Fujifilm strips do not enable a continuous measurement of the increase of the actual contact with increasing loads. Nonetheless, Prescale Fujifilm strips rather enable measuring the actual contact per load steps.

2.4.2.3 Carbon Footprint Paper

The carbon footprint paper is the cheap mean used for capturing the actual contact at an interface between solids. The method consists to insert a white paper between the contacting faces of block units, after having coated one of the faces with an ink. Upon compression, the areas that actually come into contact leave an imprint on the white paper inserted at the interface. By a scan, the imprints of the carbon paper is transformed in white and black pixels and the percentage of the actual contact is deduced by reporting the number of black pixels to the whole number of pixels of the imprint carbon paper.

Figure 10. Identification of the actual contact area using a carbon footprint paper [49]

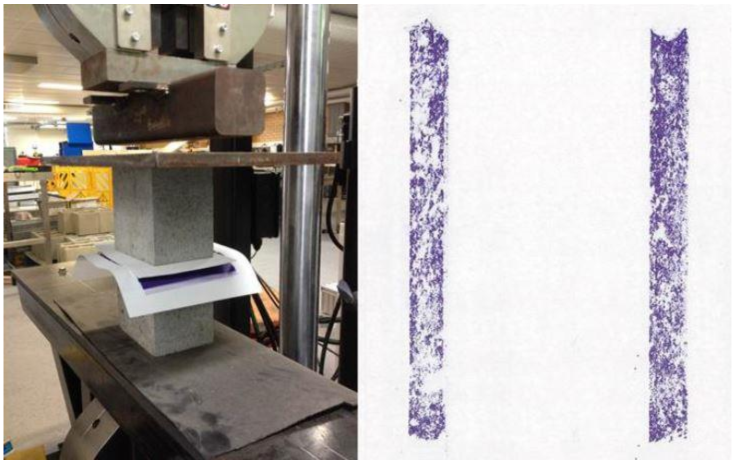

Figure 11. Carbon footprint paper [59]

Indeed, former authors like Ben Ayed et al. [49] and Zahra et al. [59] experienced the effectiveness of a carbon footprint paper for capturing the actual contact area between dry-stacked masonry blocks. Ayed et al. [49] carried out investigations on interlocking stabilised earth blocks (ISEB$_S$), whereas Zahra et al. [59] investigated on the dry joint surface and closure characteristic of interlocking blocks under compression. Based on their respective investigation (Figure 10 and Figure 11), it has been inferred that the carbon footprint papers significantly underestimate the actual contact area with respect to the MBTSS strips and the Prescale Fujifilm strips. In addition, the carbon footprint paper does not provide information about the contact stress intensity.

2.4.3 Behaviour of Dry-stacked masonry under axial compression

2.4.3.1 Factors influencing the behaviour of dry-stacked masonry

Factors influencing the behaviour (load-bearing capacity and stress-strain response) of dry-stacked masonry include among others: (*i*) the compressive strength of the block unit; (*ii*) the bed-joints imperfections (bed-joint unevenness and block height variation); (*iii*) the interlocking mechanisms and (*iv*) the load eccentricity.

(i) Compressive strength of the block units

The influence of the compressive strength of the block units have been extensively studied for mortared masonry (see section 2.3.2) and it has been demonstrated that the compressive strength of a wall increases with increasing block compressive strengths. Similar analysis has not been found in the literature regarding dry-stacked masonry, but a similar trend can be expected.

(ii) Bed-joint imperfections

In regards to the characterisation of the bed-joints roughness, some authors measured the height of the surface asperities on block units [60] whereas other measured the closure of the bed-joints under a compression stress [61–64]. According to Kang-Ho et al. [60], the height of the asperities in a bed-joint surface of a dry-stacked masonry block varies between 0,03 and 0,15 mm. In their numerical investigations, Zahra et al. [55] assumed a maximum bed-joint roughness of 0,10 mm whereas Andreev et al. [62] assumed 0,20 mm. However, using the digital image correlation technic, Andreev et al. [62] measured a bed-joint closure varying between 0,10 and 0,25 mm in the contact interface of two blocks dry-stacked (three samples tested). Exploiting the same technic, Gasser et al. [63] measured a bed-joint closure of 0,11 mm and Allaoui et al. [61] measured an average and a maximum bed-joint closure of respectively 0,13 and 0,25 mm in the horizontal joint of two dry-stacked blocks. Using common displacement gauges, Jaafar et al. [64] measured the bed-joint closure of two dry-stacked masonry blocks and found on average 0,12 mm over ten prisms tested.

In regards to the characterisation of the block height variation, the dry-stack masonry block developed by Cetholic [51] showed a height variation of +/- 0,50 mm. Thamboo [65] investigated the development of thin layer mortared masonry. He observed that the used masonry blocks exhibited a tighter height variance of +/- 2,00 mm. Agaajani et al. [66] measured the actual height of randomly selected blocks to the nearest of 0,01 mm. They found that the height variation follows a Gaussian law with a standard deviation of 1,20 mm. Jaafar et al. [64] found a height difference of +/- 0,25 mm.

Thamboo [65] also noted that for a mortar thickness of 10 mm as commonly practiced in conventional masonry, a height difference of roughly 2 mm between adjacent masonry blocks is quite reasonable. However, for thin mortar layer, a height difference of about 2 mm is not acceptable as the mortar thickness can be less than 2 mm. He concluded that the block units have to undergo additional processes of grinding/cutting before being used in thin layer mortared masonry. Nonetheless, when examining the European standards [67] fixing the tolerances for masonry blocks, it appears that although significant, these variations (height and bed-joint roughness) are allowed.

Fonseca et al. [68] studied the axial capacity of dry-stacked masonry walls constructed using ENDURA blocks. First, they reminded the fundamental issues of mortarless masonry that are the irregularities of individual blocks and the difficulty to manufacture blocks with little or no height variation. Over the wide variety of interlocking dry-stacked masonry blocks developed and marketed up to date, the authors [7,44–49,61,69,70] all agree to recognize the geometric imperfections as being the main shortcoming of such blocks. Indeed, the geometric imperfections pointed out are the bed-joint roughness and the height variation of the block units.

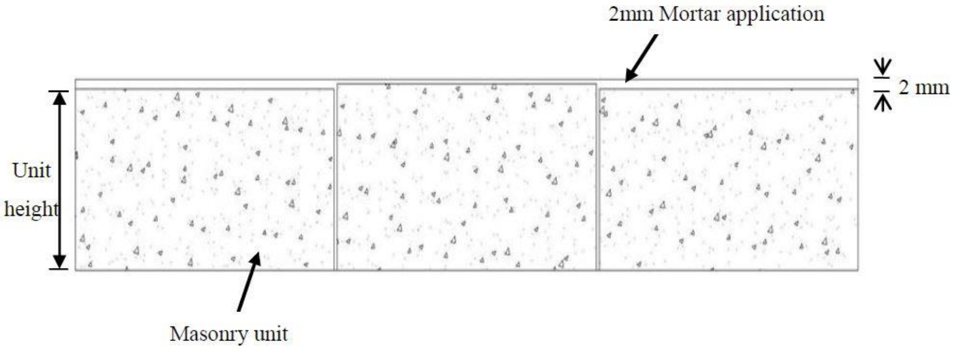

Figure 12. Block height difference [65]

Indeed, Nguyen et al. [71] observed that under compression the stiffness of the refractory lining masonry decreases with increasing amount of joints.

(iii) Interlocking mechanism

Anand et al. [54] performed experimental tests on wallets with an h/t ratio of 4 in order to assess the behaviour of dry-stacked masonry under eccentric compression and flexural loading. Without giving an improvement ratio, they found that a better interlocking mechanism leads to a relatively higher flexural strength.

Hongjun et al. [72] investigated the cyclic behaviour of mortarless brick joint, comparing non-interlocking mortarless bricks (N-IMB) to three interlocking mortarless bricks (IMB). They showed that circular interlocking mechanisms are preferable to rectangular and trapezoidal ones because they absorb more in-plane energy dissipation, they exhibit better out-of-plane behaviour under seismic actions, they show a maximum friction coefficient and a minimum degradation rate of the friction coefficient under cyclic loads.

(iv) Load eccentricity

Regarding the performance of dry-stacked masonry in compression, Anand et al. [54] found that the increase of the eccentricity makes decrease the wall compressive strength. They showed that for wallets with an h/t ratio of 4, an eccentricity of t/6 on the upper and the bottom part of the wallet makes decrease the compressive strength by 9% with respect to a same wallet axially loaded. As well, they found that an eccentricity of t/3 weakened the wall compressive strength by 60%.

Waleed et al. [73] investigated the structural behaviour of mortarless interlocking masonry under eccentric compressive loads. They tested full-scale walls with an h/t ratio of 20 and varied the eccentricity between 0, 20 mm (i.e. t/7,5), 40 mm (i.e. t/3,8) and 55 mm (i.e. t/2,7). They tested reinforced and unreinforced walls ranged in three groups, i.e. group A, B, C, then they compared their results with the compressive strength of similar bonded walls collected in the literature (bonded wall 1 and bonded wall 2). First, they defined the reinforced walls as being those for which the voids of the block units are filled with concrete grout and steel reinforcement. In group A, no reinforced concrete stiffeners and no mortar layer were used, the masonry blocks were dry-stacked. In group B, the masonry blocks were also dry-stacked, but reinforced concrete stiffeners were added at the perimeter of the wall. In group C, the masonry blocks were also dry-stacked and reinforced concrete stiffeners were added both at the perimeter and at the mid height of the wall. In this investigation, As reported in Figure 13, they showed that the load-bearing capacity of dry-stacked masonry decreases with increasing load eccentricity.

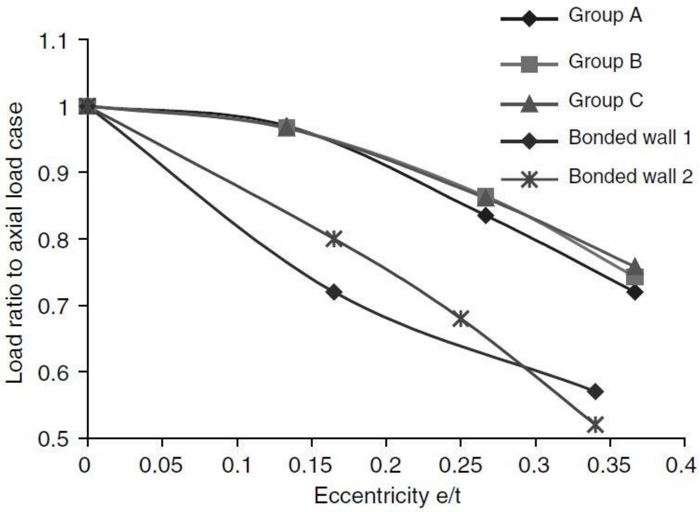

Figure 13. Load reduction factor due to the load eccentricity, by Waleed et al. [73]

2.4.3.2 Contact unevenness and load percolation system

- **Contact unevenness**

The bed-joint roughness mentioned in the previous section (section 2.4.2.1) affects the actual contact in the closed bed-joints of a dry-stacked masonry as it is shown in the forthcoming paragraphs.

Marzahn et al. [74] investigated the flattening process of a bed-joint of two dry-stacked masonry blocks using carbon paper sheets for monitoring the actual contact area in the bed-joint. They observed that from the initial load stage until the maximum load that they applied, the actual contact varied between 60% and 90% of the nominal contact area.

Andreev et al. [62,75] investigated the behaviour of the bed-joints in refractory ceramic masonry under compression, exploiting the carbon paper sheets and the digital image correlation to respectively capture the actual contact in the bed-joint and monitor the bed-joint closure. They found that for a compressive load of 3 MPa, the contact area in the bed-joint was respectively about 20% and 30% of the nominal contact area for magnesia carbon blocks and magnesia-chromite blocks. Regarding the actual contact between the blocks and the testing machine, they found a ratio of 80% at the same load level. Unfortunately, they did not provide information on the ultimate strength of the blocks to relate the rate of the actual contact area to the load level of the blocks. In addition, they showed that the bed-joint closure exhibits an exponential curve caused by the progressive closure of the initially non-parallel surfaces coming into contact. They also found that temperature influences the bed-joint closure since it influences the material stiffness by thermal expansion.

Ben Ayed et al. [49] analysed the behaviour of dry-stack interlocking stabilised earth blocks (ISEB). For measuring the actual contact area in the bed-joints, they painted the contact faces of the ISEB units and inserted a plain white paper in the bed-joint of the ISEB units during the prism construction. Out of fifty prisms of two dry-stacked ISEB units, they found that under the self-weight that the actual contact area was on average 23% of the nominal contact area, however with a high variance. The wide scatter of the data outlined by the variance reveals that the bed-joint roughness could significantly vary from one block to another. In addition, they subjected one of the prism to a compressive load to assess the contact surface increase. Out of this experiment, they concluded that the contact area linearly increased with the applied load but did not exceed 50% of the nominal contact area.

Uzoegbo et al. [76,77] investigated the load bearing capacity of dry-stack masonry walls under in-plane and out-of-plane loading. They stated in conclusion that the actual contact area for the load transmission between the masonry blocks was approximatively 50% of the nominal contact area. However, they did not provide an explanation on the origin of this figure.

More recently, Zahra et al. [55,59,78] exploited the matrix based tactile surface sensors (MBTSS) for measuring the increase of the actual contact area in the bed-joints of a prism of two dry-stacked masonry blocks subjected to an axial compression. They showed that the actual contact varied between 50% and 95% of the nominal contact area at 50% of the expected failure load.

- **Nonlinear response of dry-stacked masonry**

Waleed et al. [7] carried out a compressive test on a dry-stacked masonry prism to assess the impact of the bed-joint roughness on the behaviour of the mortarless bed-joint. They showed that dry-stacked masonry exhibits a nonlinear stress-deformation response (Figure 14). Based on their experimental results, they proposed a mathematical model (eq. (5)) describing the nonlinear compressive stress in function of the joint closure.

$$\sigma_n = a \cdot d_n^b + c \cdot d_n \qquad (5)$$

With

σ_n	Compressive stress (N/mm^2)
d_n	Close-up deformation (mm)
a, b, c	Constants determined from data analysis of the test results

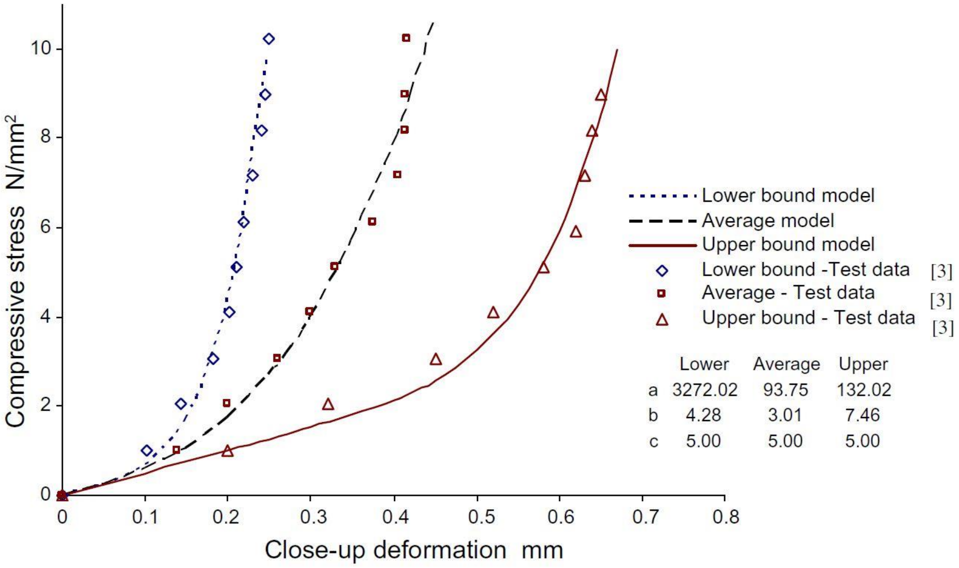

Figure 14. Close-up deformation versus the compressive stress of dry joint [7]

Using a FE approach, Alwathaf et al. [69] investigated the behaviour of an alternative interlocking mortarless block under concentric and eccentric compressive load. They compared stiffened and unstiffened dry-stacked masonry wall in terms of strength capacity, deformation and failure mode. As in [73], the stiffened reinforced walls are those for which the voids of the block units are filled with concrete grout and steel reinforcement. Regarding the axial deformation, unstiffened walls showed a significant settlement at the onset of the loading yielded by the nonlinear progressive closure of the bed-joints. They also observed that the stiffness of the unstiffened wall progressively increased upon loading until about 45% to 55% of the ultimate load. After this load threshold, the wall stiffness exhibited a linear behaviour until near the failure load. Likewise, Lourenço et al. [79] noted that dry-stacked masonry walls exhibited a significant stiffness increase with increasing load, which complies also with the finding of Hongjun et al. [72].

Allaoui et al. [61] investigated the joint closure in mortarless refractory masonries using digital image correlation (DIC). They found that the gap thickness of the dry joints is predominantly owed to the non-planarity of the masonry bed-joints, the roughness playing a second role. As well, they figured out that the bed-joint closure in DSM is nonlinear, strongly heterogeneous, orthotropic, and involves crushing of asperities and surface adjustments.

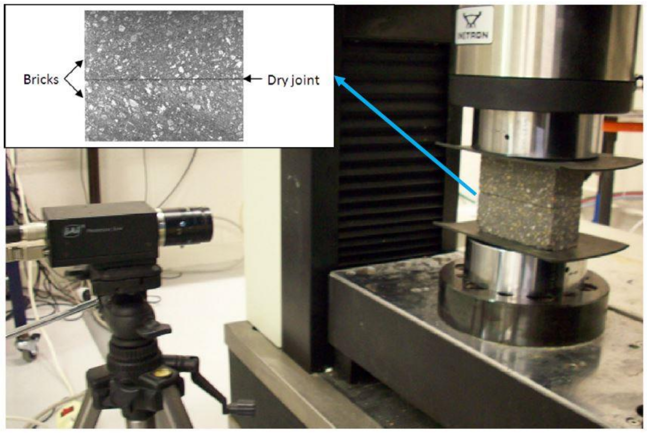

Figure 15. Experimental test device [61]

Prior to these authors, Jaafar et al. [64] also reported the nonlinear response of dry-stacked masonry related to the bed-joint closure and the crushing of the surface asperities.

- **Stress distribution / Load percolation system**

Bigoni et al. [80] exploited a photoelasticity transmission technic to disclose the stress percolation occurring in dry-stacked masonry wall subjected to a vertical compressive load. They found that the load percolation exhibits a sort of 'treelike shape' see Figure 16 and Figure 17. According to these authors, the load transfer from a course to another mainly occurs through the corner and the middle sections of the block units, which results in a highly concentrated stresses in some parts of the wall (Figure 16). They also witnessed that with increasing load, the stress distribution in the wall moves from highly localized to more spread, behaviour imparted to the increase of the actual contact area between the masonry courses. From the experiments, they concluded that the load percolation in a dry-stacked masonry is governed by the actual contact between the masonry blocks. Hence, for the same load conditions, nominally dry-stacked masonry wall identical in terms of height and length could show different load percolation system (in terms of 'treelike shapes') depending on the initial actual contact between the block units. They did not clearly relate the imperfect contact and the potential variation of the load percolation system to the height difference between the block units, but this could be expected like demonstrated by Agaajani et al. [45,66,81].

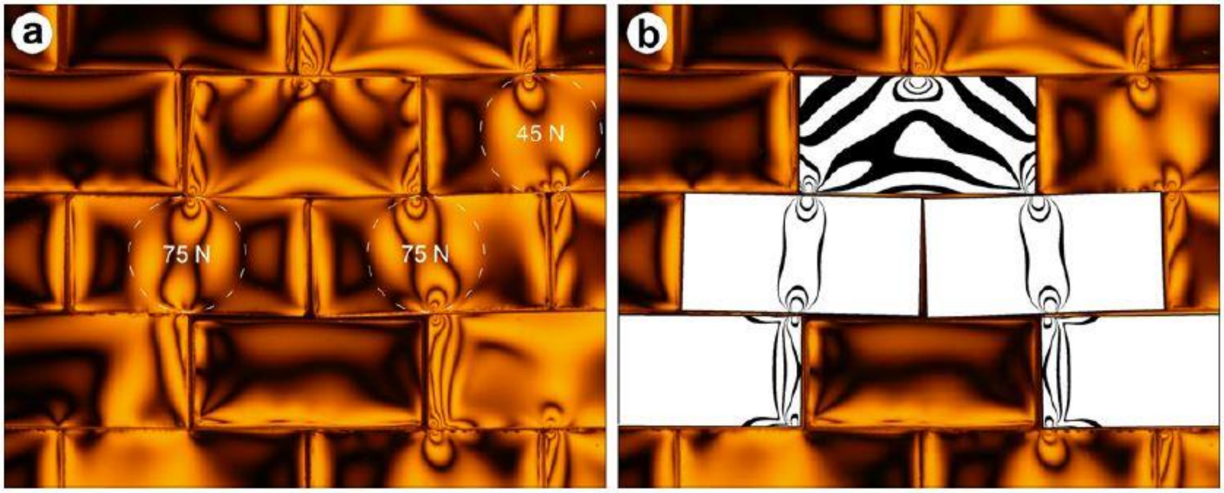

Figure 16. Photo elastic fringes of a model of dry-stacked masonry [80]

Following the experimental investigations reported in [80], Bigoni et al. [82] proposed two analytical models depicting the load percolation system observed during the experimental tests, i.e. (1) the micromechanical approach and (2) the continuum mechanical approach. In the micromechanical approach, they have modelled block units as discrete elements assuming that from a course to another the loads are transferred as punctual forces applied in the middle or in the edge sections of the block units. They also proposed analytical formulae (equation (6) and (7)) predicting the reactions or the punctual forces applied on each block unit. However, in the proposed model, the load redistribution stemming from the increase of the actual contact area between the masonry blocks is ignored. As shown in Figure 17, all the load transmission mechanisms assume that the applied force is transferred through punctual force on the block unit, which therefore do not take into account the increase of the actual contact in the bed-joints. Moreover, the developed approach does not enable to find the overall load-bearing capacity of a DSM wall. In addition, as noticed the authors [82], the punctual forces/reactions predicted with their model are associated to an arrangement of the block units in a wall, which may change from a construction to another.

Load transmission mechanism 1

$$\begin{cases} R_1 = F_1 + 0{,}5F_2 \\ R_2 = 0 \\ R_3 = F_3 + 0{,}5F_2 \end{cases} \tag{6}$$

Load transmission mechanism 2

$$\begin{cases} R_1 = \langle F_1 - F_3 \rangle \\ R_2 = F_1 + F_2 + F_3 - \langle F_1 - F_3 \rangle - \langle F_3 - F_1 \rangle \\ R_3 = \langle F_3 - F_1 \rangle \end{cases} \tag{7}$$

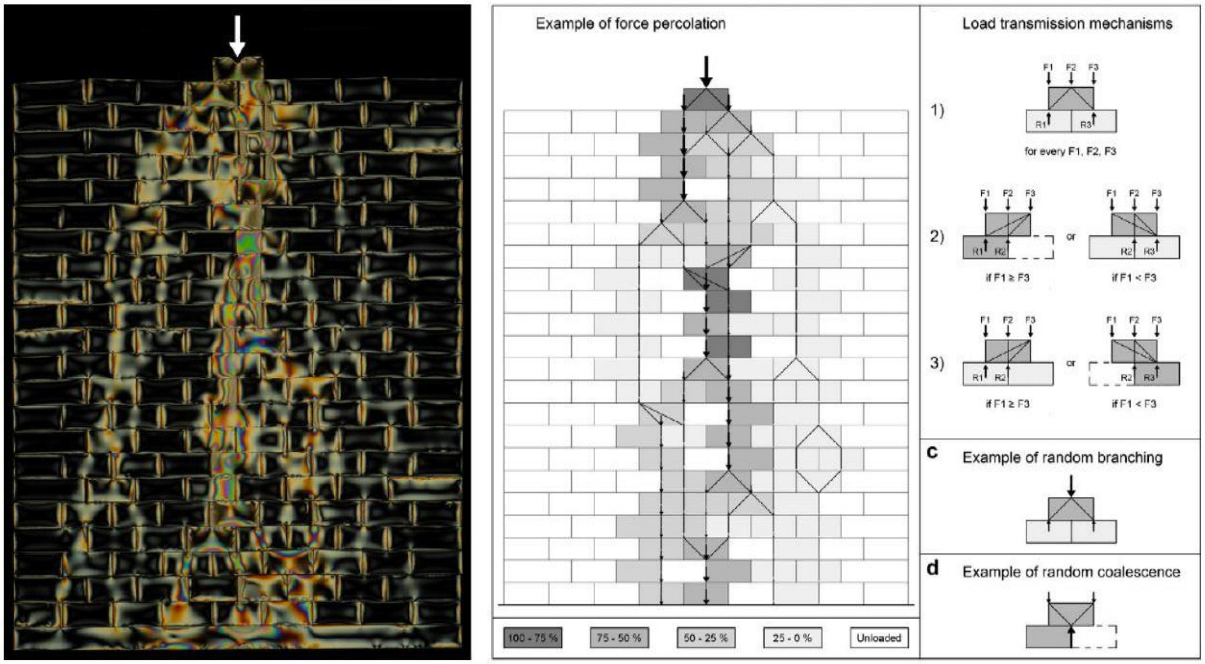

(a) **(b)** **(c)**

Figure 17. Experimental test device [82]

Regarding the continuum mechanical approach, they proposed to model a full dry-stacked masonry wall as a continuous homogeneous material with an extreme orthotropic feature. However, this approach takes out the possibility for considering the various potential load percolation system yielded by the distribution of block units in a wall.

As previously mentioned, Agaajani et al. [45,66,81] measured the actual height of a wide sample of block units. Based on the height distribution of the block units, they developed an analytical concept depicting the 'treelike shape' of the load percolation occurring in a dry-stacked masonry (Figure 18). Considering dry-stacked masonry as discrete structures, they assumed two states for the bed-joints, i.e. the open state and the closed state. The closed state joints are the horizontal joints where the bed-faces of the block units are only separated by the height of the surface asperities. The open state joints in turn are the horizontal joints where the bed-faces of the block units are separated by both the height of the surface asperities and the height difference of the underlying block units. Both bed-joint states (open and closed) were also assumed by Nguyen et al. [71] in the investigation on the mechanical homogenisation of mortarless masonry. In the model developed by Agaajani et al. [45,66,81], the contact was supposed full in the closed state bed-joint and null in the open state bed-joint. As result, the load percolation system was derived from the ‘treelike shape’ yielded by the vertical connection of the closed state bed-joints. Using the developed analytical model to analyse a wall, they inferred that the compressive stress is highly localised in some parts the wall and the latter exhibits several unloaded parts.

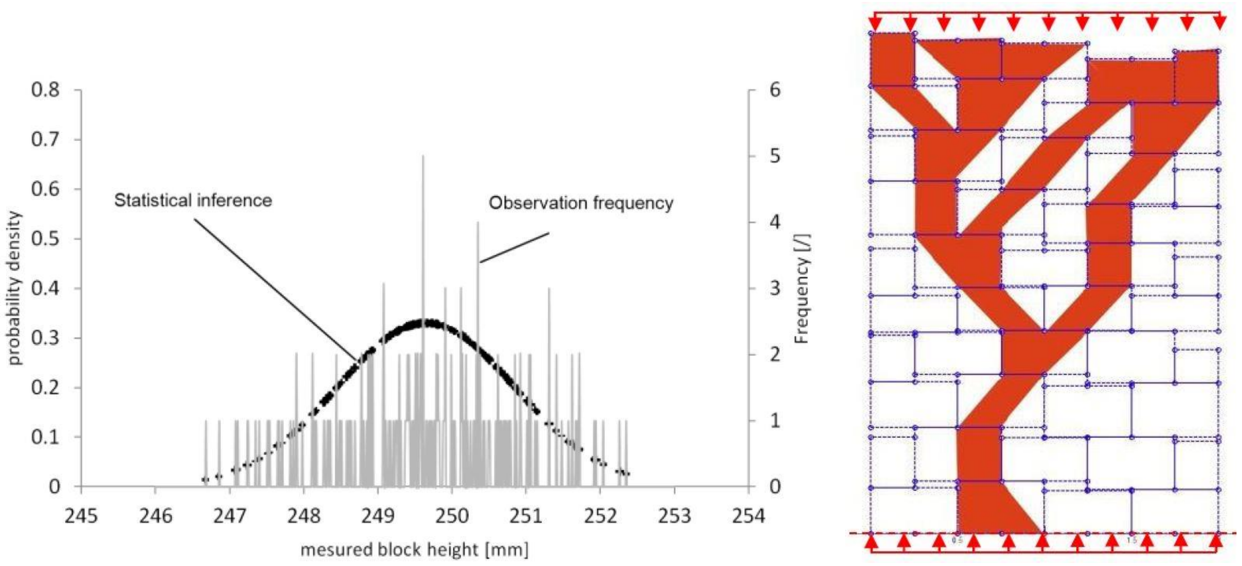

(a) **(b)**

Figure 18. Masonry block’ height distribution according to Agaajani et al. [66]

The Agaajani’s findings line up with those of Bigoni et al. [80,82]. Beside the macroscopic view of the load percolation system in a dry-stacked masonry, very few investigations singularly addressed the stress distribution in the so-called closed bed-joints.

Kang-Ho et al. [60], addressed the behaviour of hollow DSM under compression by means of numerical simulation. They studied a 3-course masonry prism. In order to take into account the influence of the bed-joint roughness in their numerical model, they measured the actual stress-closure in the bed-joints of a 3-course masonry prism and calculated the corresponding local contact stiffness (slope of the stress-deformation curve). They incorporated the measured local contact stiffness in their model and found that the block units of the masonry prism exhibited an asymmetric stress distribution as well as stress peaks close to the compressive strength of the block’ material. The ascertainment of Kang-

Ho et al. [60] join those of Thanoon et al. [7] see Figure 19, Ben Ayed et al. [49], Tatheer et al. [55] and Lourenço et al. [79,83]. Indeed, dry stacked masonry suffers from surface roughness related stress concentration. Using matrix based tactile surface sensors (MBTSS), Tatheer et al. [55,59] properly disclosed the stress distribution in the contact interface of a prism of two dry-stacked masonry blocks. They showed that the stress distribution is unevenly distributed in a closed bed-joint (Figure 20). They also showed that some stress peaks reach 14 times the compressive stress applied on the masonry prism. Lourenço et al. [83] characterized the behaviour of a dry joint by studying a dry-stacked masonry prism under cyclic load. Under a compressive stress of 1,0 N/mm^2, they observed a stress peak of 1,43 N/mm^2 in the bed-joint. Lourenço et al. [79] also investigated the mechanical response of dry joint stone masonry walls subjected to in-plane loading. They inferred that the lack of an interlayer material in the bed-joints led to a stress concentration in some sections of the contact.

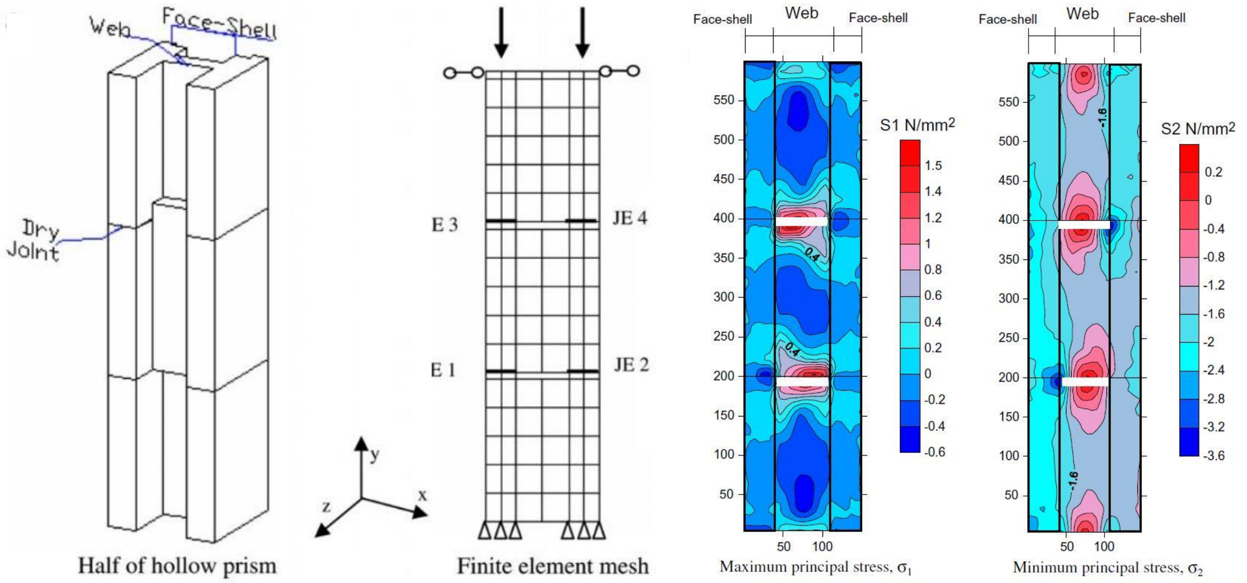

(a) (b) (c)

Figure 19. a) Masonry prism; b) 2D finite element model; b) Principal stress distribution [7]

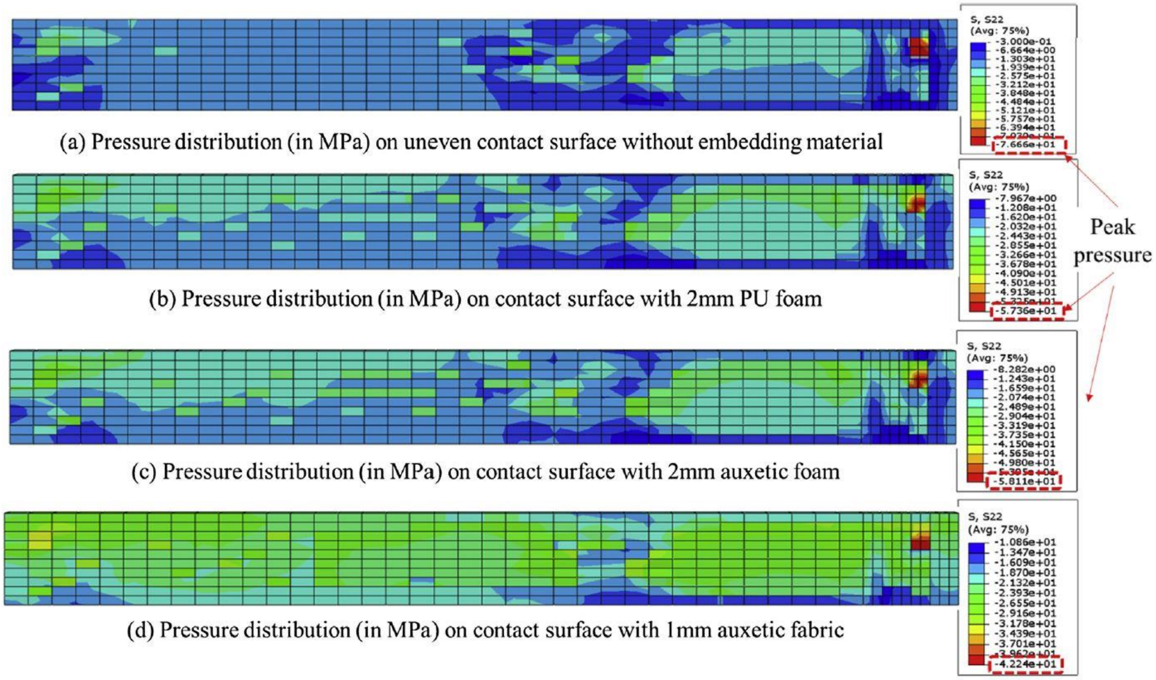

(a) Pressure distribution (in MPa) on uneven contact surface without embedding material

(b) Pressure distribution (in MPa) on contact surface with 2mm PU foam

(c) Pressure distribution (in MPa) on contact surface with 2mm auxetic foam

(d) Pressure distribution (in MPa) on contact surface with 1mm auxetic fabric

Figure 20. Stress distribution at the contact interface of two dry-stacked block units [55].

Among the factors influencing the behaviour of dry-stacked masonry, the bed-joints imperfections play a significant role in governing the actual contact and the load percolation system. All these authors related both the progressive bed-joint closure and the imperfect contact to the roughness of the contacting block faces.

2.4.3.3 Failure mechanisms

An overview of former investigations reveals that dry-stacked masonry exhibits two main failure mechanisms: (i) the development of cracks at the interface between the face-shells and the webs; and (ii) the face-shell splitting and spalling.

- **Cracks at the interface between face-shells and webs**

Drysdale et al. [84] investigated the strength and deformation properties of grouted and ungrouted dry-stacked masonry block. Regarding the failure mechanism of the ungrouted prisms, they observed occurrence of vertical cracks at the interface between the block' face-shells and the webs. Likewise, in an investigation on the strength correlation between a block unit, a masonry prism and a wallet, Mohd et al. [85] observed that dry-stacked masonry collapse following the development of vertical cracks at the interface between the webs and the face-shell of the block units. Agaajani et al. [45] also experienced this failure mechanism when performing compressive tests on dry-stacked masonry prisms, which lines up with the findings reported in [7,8,60,64,69,73,76,86,87]. Indeed, this failure mechanism is strongly related to the loading conditions. As the block units are exclusively loaded and supported on their face-shells, the latter experience compression and induce tensile stresses in the webs. In addition, as the webs are not loaded, shear stresses develop at the interface with the face-shell. The combination of this state of stress yields vertical cracks in the webs as observed in Figure 21.

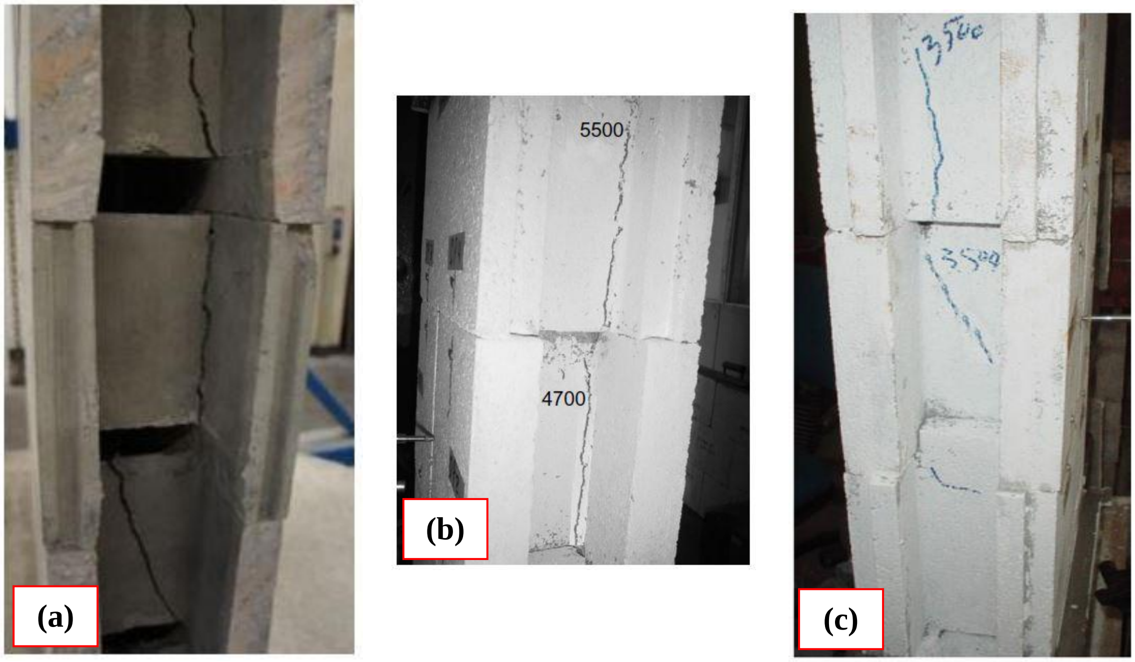

Figure 21. Crack at the interface face-shells / webs. a) Agaajani et al. [45]; b) Jaafar et al. [64]; c) Waleed et al. [7]

- **Splitting and spalling of the block' face-shells**

Mohd et al. [85] performed compressive tests on wallets constructed using dry-stacked masonry blocks. They reported that under compression, the face-shells of the full blocks exhibited vertical cracks aligned with the vertical joints of the wallets. However, they did not argue about this failure mechanism. Likewise, Agaajani [45] conducted compressive tests on full-scale dry-stacked masonry walls and also observed appearance of vertical cracks in the face-shells, aligned with the vertical joints of the wall. Like Agaajani [45], Thanoon et al. [73] also carried out compressive tests on full-scale dry-stacked masonry walls. Similarly as the previous authors, they reported that most of the cracks appearing in the face-shells of the block units were vertical and aligned with the vertical joints of the walls.

Exploiting its analytical model predicting the load percolation system in a dry-stacked masonry, Agaajani [45] showed that this failure mechanism is imparted to a high concentration of the compressive stress in a half part of some full-blocks (Figure 18). The high stress concentration itself stems from the load and support conditions governed by the height difference between the block units. Moreover, the load percolation model proposed by Bigoni et al. [82] further explains the face-shells splitting as they showed that in a dry-stacked masonry, load percolates in form of high localised punctual forces applied in the edges or in the middle sections of the block face-shells (Figure 17).

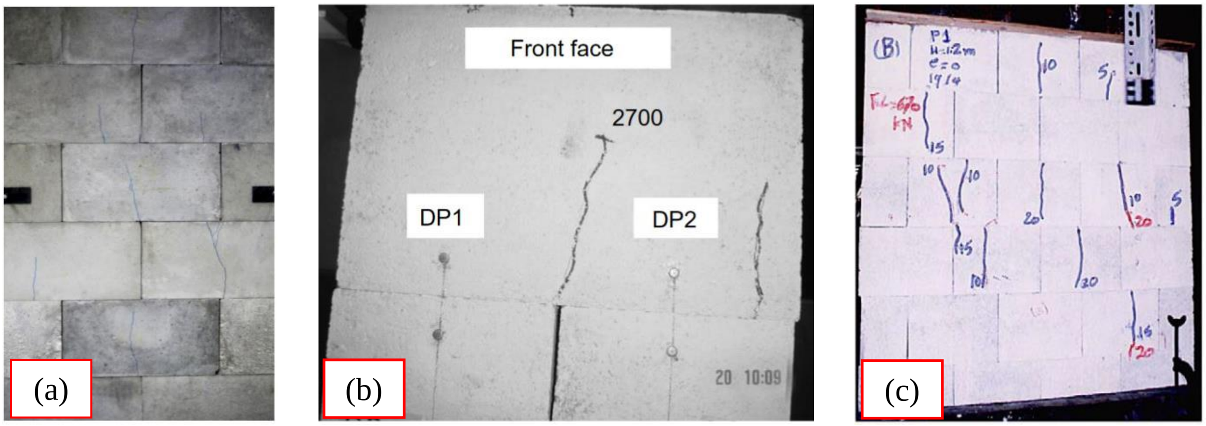

Figure 22. Face-shell splitting in DSM. a) Agaajani [45]; b) and c) Jaafar et al. [64, 85]

Rui et al. [88] focussed on the characterisation of dry-stack masonry made of compressed earth blocks (CEB$_S$) stabilised with alkaline activation. They tested masonry prisms under compression and observed spalling with localised damage in the block' corners. They related this failure mechanism to the stress concentration caused by the bed-joint imperfections of the CEB$_S$ units.

Shrive et al. [89] presented a theory explaining the crack ignition in brittle materials. In brief, they showed that for any brittle material specimen, the crack ignition is governed by factors like the Poisson's ratio, the material cohesive strength, the distribution of surface irregularities, the internal voids, the structure of the internal pores and the macroscopic stress distribution in the specimen. By relating the findings of Shrive et al. [89] to the failure mechanism of dry-stacked masonry, it stems that the crack ignition in a DSM depends on the macroscopic (general load percolation system) and the microscopic (stress distribution in a closed bed-joint) stress distribution in a wall. Indeed, the macroscopic stress distribution i.e. the general load percolation system depends on the height difference between the block units. In turn, the microscopic stress distribution i.e. the stress distribution in a closed bed-joint depends on the bed-joint unevenness of the block units.

2.4.3.4 Load-bearing capacity and strength correlation

Kun Lin et al. [90] experimentally characterized dry-stacked masonry under compression and shear loading. They compared dry-stacked masonry prisms with mortared masonry prisms in terms of the compressive strength. They observed that the compressive strength and the elastic modulus are strongly influenced by the bed-joint imperfections. They showed that in comparison with the mortared masonry prism, the compressive strength of the dry-stacked masonry prism was decreased by roughly 15% as well as the elastic modulus by roughly 62%.

Uzoegbo et al. [76,77] investigated the load capacity of dry-stack masonry walls under in-plane and out-of-plane loading. Based on experimental evidences, regarding the in-plane response in compression, they showed that a dry-stacked masonry wall with a height to thickness ratio of 11 experienced 40% less compressive strength with respect to a similar mortared masonry wall. However, they did not discuss this significant drop of the compressive strength.

Most of the authors investigating on dry-stacked masonry have proposed to relate the compressive strength of wallets and/or prisms to the compressive strength of individual blocks. As part of the in-plane analysis of dry-stacked masonry, Uzoegbo et al. [76,77] tested walls constructed using interlocking blocks of different strength and proposed equation (8) to relate the block compressive strength ($f_{c.block}$) to the wall compressive strength (f_w):

$$f_w = \phi_m \, 0{,}15 \; f_{c.block} + 1 \tag{8}$$

Drysdale et al. [84] investigated the strength and deformation properties of grouted and ungrouted dry-stacked masonry prisms with a h/t ratio of 4,0. They found a prism to block strength ratio of 0,38 for the ungrouted prisms. Sturm et al. [50] conducted experimental tests on interlocking earth blocks, masonry prisms of 0,14 x 0,45 m^2 and wallets of 0,84 x 0,84 m^2 with dry joints. Out of their experiments, they proposed two relationships to link the compressive strength of a wallet (f_w) once to the compressive strength of a masonry prism (f_{mp}) and once to a block unit ($f_{c.block}$). According to Sturm et al. [50], $f_w = 0{,}2 \; f_{c.block}$ block and $f_w = 0{,}6 \; f_{mp}$. However, the scatter of their results concerning the compressive strength of wallets showed a COV of 39%.

Rui et al. [88] focussed on the characterisation of dry-stack masonry made of compressed earth blocks (CEB_S) stabilised with alkaline activation. Along their experimental investigation, they tested individual blocks and masonry prisms with a h/t ratio of 5. They found on average a prism to unit strength ratio of 0,39. In their discussion, they stress out that this strength correlation depends on the type of masonry block, the failure mechanism, and amount of localised stresses induced by the bed-joint imperfections.

Still in the field of interlocking mortarless masonry, Mohd et al. [85] carried out experimental tests in order to correlate the compressive strength of an individual block ($f_{c.block}$) to the compressive strength of a masonry prism (f_{mp}) as well as to a wallet (f_w). They first tested ten masonry prisms of 0,30 x 0,60 m^2 with a h/t ratio of 4, then 4-wallets of 1,20 x 1,20 m^2 with a h/t ratio of 8. Based on the results of the experiments, they found that $f_w = 0{,}39 f_{c.block}$ and $f_{mp} = 0{,}47 f_{c.block}$.

Waleed et al. [73] investigated the structural behaviour of mortarless interlocking grouted and ungrouted masonry under an eccentric compressive loading. They tested prisms with a h/t ratio of 4 and found a prism to block strength ratio of 0,47 (for the ungrouted prism axially loaded). They imparted the reduction of the prism' strength to both the effect of the slenderness and the surface unevenness between the blocks.

Anand et al. [54] performed compressive tests on wallets constructed using solid interlocking blocks (SILBLOCK). They found a prism-to-block strength ratio of 0,7, which is very high compared to the findings made by other authors [50,73,76,77,84,85,88]. However, this is explained by the fact that the SILBLOCK is an almost full block without hollows. A brief summary of the strength correlation found former authors is presented in Table 2.

Table 2. Prism-to-block strength ratio in dry stacked masonry [121]

Authors	Prism height to thickness ratio (h/t)	Net to gross section ratio. NS_r (%)	Relationship found out of the experiments
Sturm et al. [50]	3,0	90%	$f_{c.prism} = 0{,}33\ f_{c.block}$
Uzoegbo et al. [76,77]	2,0	100%	$f_{c.prism} = 0{,}25 - 0{,}32\ f_{c.block}$
	4,0	100%	$f_{c.prism} = 0{,}27 - 0{,}34\ f_{c.block}$
Rui et al. [88]	5,0	90%	$f_{c.prism} = 0{,}39\ f_{c.block}$
Drysdale et al. [84]	4,0	49%	$f_{c.prism} = 0{,}38\ f_{c.block}$
Mohd et al. [85]	4,0	63%	$f_{c.prism} = 0{,}47\ f_{c.block}$
	8,0	63%	$f_{c.prism} = 0{,}39\ f_{c.block}$
Waleed et al. [73]	4,0	63%	$f_{c.prism} = 0{,}47\ f_{c.block}$
Anand et al. [54]	4,0	≈100%	$f_{c.prism} = 0{,}70\ f_{c.block}$
Agaajani [45]	6,3	40%	$f_{c.prism} = 0{,}41\ f_{c.block}$
	6,3	40%	$f^{*}_{c.prism} = 0{,}86\ f_{c.block}$
	10,2	40%	$f_{c.prism} = 0{,}13\ f_{c.block}$
	10,2	40%	$f^{*}_{c.prism} = 0{,}68\ f_{c.block}$
Francis et al. [91]	2	100%	$f^{*}_{c.prism} = 0{,}50\ f_{c.block}$
	2	100%	$f^{**}_{c.prism} = 0{,}21\ f_{c.block}$

$\boldsymbol{f_{c.prism}}$	prism compressive strength. (*) units with polished surfaces; (**) units with saw-cut surfaces
$\boldsymbol{f_{c.block}}$	block compressive strength
NS_r	ratio of the *net section** on the gross section of the block unit. (For a full-solid block, NS_r = 100%).
	* The net section is obtained by removing the section of hollow on the gross section of the block unit.

.

2.4.3.5 Modelling contact in dry-stacked masonry

Out of the experimental test, Lourenço et al. [83] concluded that the Coulomb friction law is adequate for representing the failure of dry joint masonry. They also showed that after a given number of cycles, significant differences could be found between the initial and the final friction angle, the bed-joint roughness being the crucial parameter influencing this variation. Indeed, larger roughness leads to a larger final friction angle. Kun Lin et al. [90] carried out shear-compression tests under cyclic loading and figured out that the Mohr-Coulomb's friction law accurately describes the failure of a dry-joint, which lines up with the finding of Lourenço et al. [83], Zuccarello et al. [92], and Gasser et al. [63].

Hongjun et al. [72] investigated the effects of three interlocking systems, the effect of the compression stress levels and the effect of the loading cycles on the resulting friction coefficient of mortarless brick joint. As in [83], they exploited the Mohr-Coulomb law to describe the shear failure modes observed in the investigated joints. Out of the experiments, they ascertained that the friction coefficient increases with the compressive stress and the smoothening of the contacting surfaces. Indeed, the influence of the compression stress level on the friction coefficient chiefly arises from the rate of the actual contact in the bed-joint. In a dry-stack masonry block, due to the bed-joint imperfections the actual contact increases with the compressive load and the progressive additional contact area induce an increase of the shear force. Aside from the influence of the compression stress, they found that an increase in the loading cycle leads to a decrease in the friction coefficient. In addition, they stressed out that the rate of degradation of the friction coefficient increases with the roughness of the contacting surfaces.

Like Ben Ayed et al. [49], Bui et al. [93] in addressing the in-plane and out-of-plane behaviour of dry-stacked masonry exploited the Mohr-Coulomb friction law for modelling the contact behaviour in the bed-joints.

2.4.4 Strategies to mitigate the effects of the bed-joint imperfections and improve the load bearing capacity of dry-stacked masonry

It has been shown that the behaviour and the compressive strength of a dry stacked masonry is highly affected by the bed-joint imperfections of the block units. Indeed, these imperfections reduce the actual contact area between the courses and lead to high localised stresses in walls. As strategy to face the issues due to the bed-joints imperfections (bed-joint roughness and block height difference), researchers propose different solutions that can be summarized in four points. (*i*) The block's surface polishing, (*ii*) the material embedment in the block's bed-joints, (*iii*) the use of grout for hollow block units, and (*iv*) the increase in block sizes combined to a more stringent manufacturing processes.

(i) The block's surface polishing as strategy

Although levelled concrete surfaces still present a fractal topography [94], manufactured block units may undergo additional process like a grinding of their bed-joints to ensure a good contact between the wall courses. Sez et al. [87], Francis et al. [91], Tatheer et al. [55,78], Agaajani [45] and Thallon et al. [46] experienced with satisfactory results the block surface polishing as strategy mitigating the influence of the geometric imperfections on the stress distribution in a bed-joint and on the masonry compressive strength.

Sez et al. [87], carried out experimental tests to assess the influence of a grinding surface on the load-bearing capacity of masonry prisms of two dry-stacked block units. They carried out experimental tests on prisms with grinded or un-grinded surfaces. They ascertained that the masonry prisms constructed using block units with grinded surfaces offered greater compressive strengths than masonry prisms constructed using raw block units. Sez et al. [87] also revealed that on average, the compressive strength of the masonry prisms with grinded block units increased by 8% as the unit strength was increased by 10%.

Francis et al. [91] investigated the effect of the joint thickness on the compressive strength of brickwork. They tested prisms with a h/t ratio of 2 while varying the mortar layer thickness from 10 to 25 mm. For completeness, they also tested prisms with 0-thickness mortar layer, i.e. dry-stacked prisms. Regarding the latter, they investigated two surface treatments: surfaces polishing and saw-cut surfaces. In terms of compressive strength, they showed that the masonry prisms whose block units have been polished (33 MPa) outperformed the mortared masonry prisms (15 – 20 MPa). In contrast, they observed that the masonry prisms with saw-cut block units exhibited lower resistance (14 MPa) than all the other prisms, including mortared masonry prisms. In addition, they also noticed that spalling and cracking occurred earlier at 14% of the ultimate load in masonry prisms with saw-cut block units. They concluded that this drop of strength could be related to the surface unevenness and the stress concentration in the bed-joint.

Using a finite element model, Tatheer et al. [55,78] investigated both the surface grinding and the embedding of a packing material to mitigate the contact surface unevenness in dry-stack masonry blocks. Firstly, for a given load and using the matrix based tactile surface sensors (MBTSS), they determined the stress distribution in the bed-joint interface of a masonry prism of two dry-stacked block units. They found the stress distribution and a stress peak of 77 MPa (Figure 23). For simulating polished bed-joints, they simply assumed it flat without asperities. They modelled two dry-stacked block units and observed that under the same compressive load as during the experiment, the stress distribution over the entire surface of the bed-joint interface became uniform around 20 MPa (Figure 23). Accordingly, they showed that grinding the contact surface enables to ensure a uniform stress distribution in the dry-joint, decreasing the stress peak by 75%.

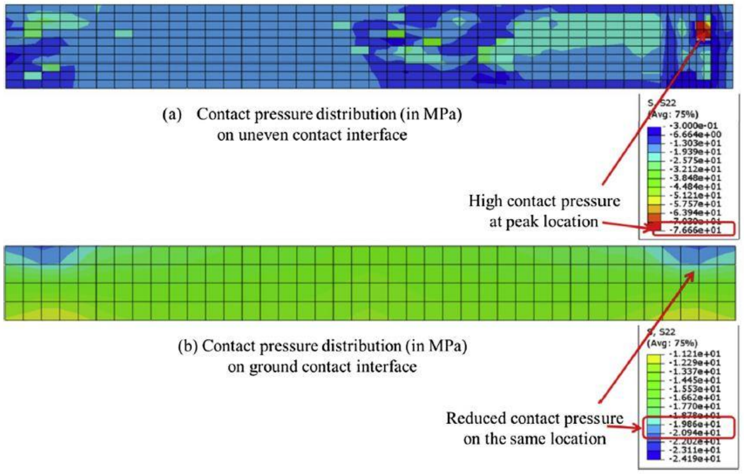

Figure 23. Comparison of stress distribution for raw and polished bed-joints, Zahra et al. [55]

Agaajani [45] also performed compressive tests on conventional mortared masonry (HBN6-24) and on dry-stacked masonry constructed using raw and polished block units. As reported in Figure 24, in terms of compressive strength, they showed that dry-stacked masonry with polished block units outperformed those with raw block units.

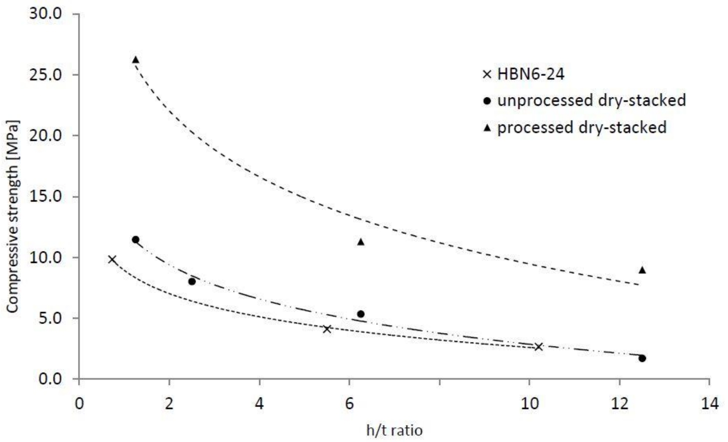

Figure 24. Wall compressive strength with raw and polished block units, Agaajani et al. [45].

However, the grinding process slows the production while increasing the unit cost. In addition, the bed-joint grinding is not always possible on interlocking DSM$_b$ because of their complex shape. Hence, in most cases, the masonry blocks are marketed without undergoing any mechanical treatment of their bed-joints.

(ii) The material embedment in the block's bed-joints as strategy

As previously mentioned, using a finite element model, Tatheer et al. [55,78] also investigated the embedding of a packing material for mitigating the contact surface unevenness in dry-stack masonry blocks. For simulating the bed-joint roughness (Figure 25), they proceeded in three stages. (1) They refined the mesh around the sections where stress peaks have been observed during the experimental test. (2) They selected the nodes in the sections where stress peaks have been observed during the experimental test and raised them up by 0,10 mm by changing their y-coordinate. Finally, (3) they changed the properties of the raised elements to high stiff rock properties with a linear elastic behaviour.

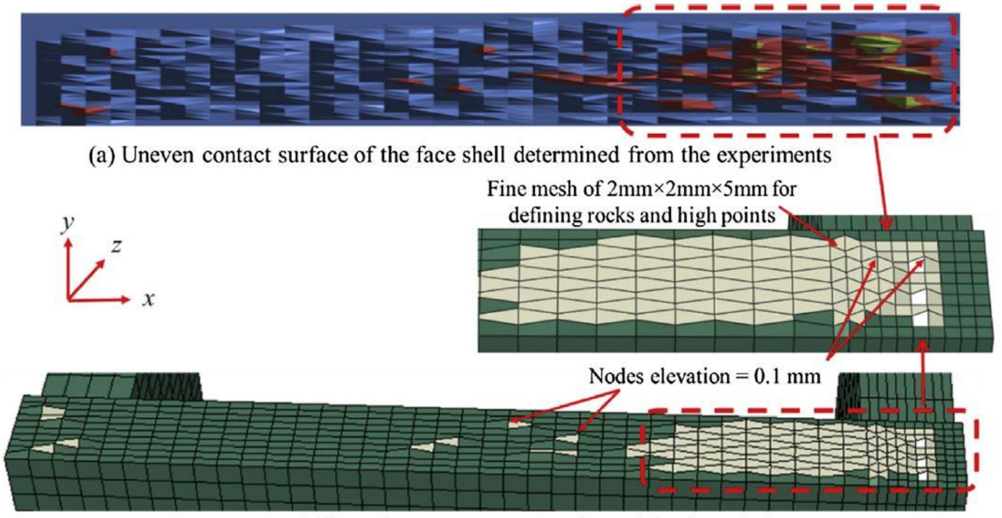

(a) Uneven contact surface of the face shell determined from the experiments

(b) 3D FE modelling of uneven contact surface of the face shell

Figure 25. Modelling of the contact surface unevenness [55]

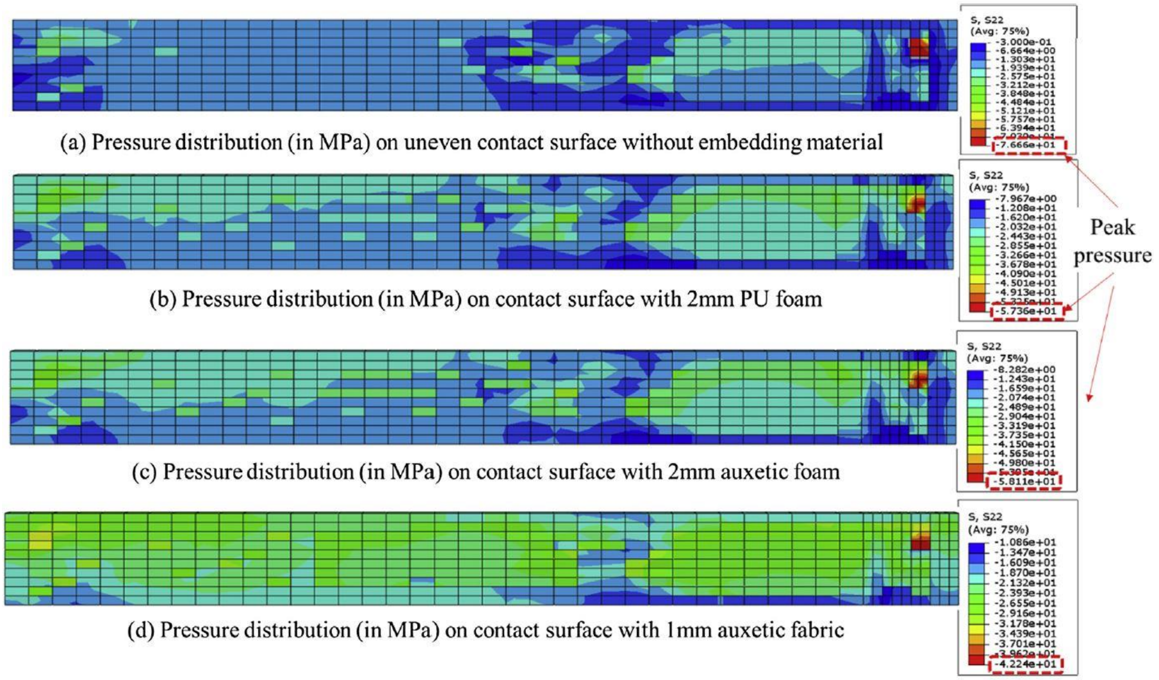

(a) Pressure distribution (in MPa) on uneven contact surface without embedding material

(b) Pressure distribution (in MPa) on contact surface with 2mm PU foam

(c) Pressure distribution (in MPa) on contact surface with 2mm auxetic foam

(d) Pressure distribution (in MPa) on contact surface with 1mm auxetic fabric

Figure 26. Stress distribution at the contact interface with and without embedding materials [55].

As result, under the same compressive load like during the experiment, they observed a stress peak reduction of about 50% by using an auxetic embedding material. They observed that the stress peak decreased from 77 MPa to roughly 60 MPa for both the auxetic and the polyurethane foams as embedding material, and from 77 MPa to 40 MPa for the auxetic fabric (Figure 26). However, they did not perform tests to failure and hence, although these strategy could enable to reduce the stress peaks, they did not verify the correlation with the increase of a wall compressive strength.

(iii) The use of grout as strategy

Instead of treating the contact surface of the block units, other authors rather propose to use grout in hollow block units. Mohd et al. [64,85] investigated the behaviour of interlocking mortarless masonry through experimental tests on masonry prisms of 0,30 x 0,60 m^2. The authors compared grouted and un-grouted masonry prisms. Over three tests carried out for each one, they observed that the former reached an average ultimate load of 392 kN while the latter failed on average to 268 kN. Although they [64,85] did not measure the actual contact between the block units, they attributed the drop of the compressive strength of the un-grouted masonry prisms to the absence of grout and to a low actual contact in the bed-joints. Drysdale et al. [84] investigated the strength and deformation properties of grouted and ungrouted dry-stacked masonry. Like concluded by Mohd et al. [64,85] and Thanoon et al. [8,73], they found that grouted DSM offer greater resistance in compression than ungrouted DSM, due to the stiffening provided by the grout. However, as stated by Kang-Ho et al. [60], although grout may greatly stabilize a finished dry-stacked masonry, the dry contact will still be a parameter influencing the mechanical performance under compression.

Ferozkhan et al. [86] analysed the compressive strength of dry-stacked masonry wallets when wrapped with fibre-reinforced cement composite (FRCC). They found that wrapping a DSM enables to modify the failure mode from a complete block collapse to a fine and uniform cracking. Furthermore, they observed that the FRCC wrapping makes increase the compressive strength of the wallets by roughly 20% with respect to the unwrapped DSM wallets.

Using a FE approach, Alwathaf et al. [69] investigated the use of concrete grout as reinforced strategy (stiffened masonry) for an alternative interlocking mortarless block under concentric and eccentric compressive load. Based on the numerical results, they showed that reinforced dry-stacked masonry walls, i.e. the walls for which the voids of the masonry blocks have been filled with a concrete grout, yield higher compressive strengths than unreinforced ones.

(iv) The increase in block sizes as strategy

As improvement strategy, Agaajani et al. [66] also proposed to increase the masonry block' sizes to reduce the number of joints and accordingly, the geometric imperfections affecting the wall compressive strength. However, they did not perform tests in this purpose. Waleed et al. [73] emphasised the need for a stringent dimensional tolerance for the masonry block to reduce the influence of the bed-joint imperfections. However, Anand et al. [54] have noted this necessity for a stringent dimensional tolerance as being a main limitation of dry-stacked masonry block.

2.5 Theory on contact mechanic between rough surfaces

As outlined in the previous paragraphs, almost all the authors investigating on the behaviour of the dry-stacked masonry concluded that the drop of the compressive strength of the masonry is in part related to the low actual contact in their bed-joints. Several works [95–100] in the field of the contact mechanic correlated the actual contact area to the load transfer and the stress intensity between two solids coming into contact with rough surfaces. Indeed, Greenwood et al. [95], Pasaribu et al. [96], Jeng et al. [97], Chang et al. [98] and Zhao et al. [99,100] have developed analytical relationships linking the load carried by a rough surface and the actual contact area between the considered rough surface and a flat surface coming into contact. When two surfaces are in contact (rough surface on a rough surface / rough surface on a flat surface), only some asperities actually come in contact, which reduces the actual contact area with respect to the nominal contact area. In a dry contact, four main cases may be defined:

- The compression of a non-deformable rough surface on a deformable surface;
- The compression of a deformable rough surface on a non-deformable surface;
- The compression of a deformable rough surface on another deformable one;
- The compression of a non-deformable rough surface on another no-deformable one.

Since the analysis of the contact between surfaces is fundamental to some engineering problems among which those of dry-stacked masonry, the different theoretical approaches are briefly recalled in the forthcoming sections.

2.5.1 Greenwood and Williamson contact model

Greenwood and Williamson [95] have developed a model approaching the mechanical contact between multi-asperities contacting surfaces. Instead of modelling the contact between two rough surfaces, for simplifying needs, they modelled a contact between an equivalent rough surface and an ideal smooth surface. For this purpose, they made some assumptions. (1) The rough surface is represented by a constant distribution of spherical asperities. (2) The asperities are uniformly distributed over the surface with a density D_{sum}. (3) The height of the peaks (z_s) follows a Gaussian distribution with a variance (σ_s). (4) The asperity height varies randomly. (5) All the asperities have the same radius R. (6) Frictionless contact is assumed between the elastic solids.

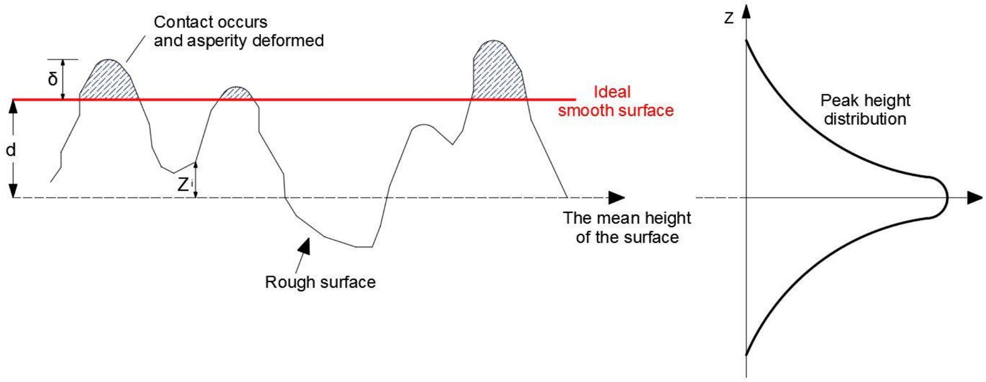

Figure 27. Roughness surface according to Greenwood and Williamson [95].

According to Greenwood and Williamson [95], if the two surfaces are separated by a distance d (Figure 27), the probability that a contact occurs on an asperity with a height of z is given by equation (9). In this relation, $f(z)$ representing the function of the normal standard density is given in equation (10).

$$P(z>d) = \int_{d}^{\infty} f(z)dz \tag{9}$$

$$\mathrm{f}(\mathrm{z_s}) = \frac{1}{\sigma_s (2\pi)^{1/2}} \exp\left(- \frac{z_s^2}{2\sigma_s^2} \right) \tag{10}$$

The number of asperities actually in contact per unit area is given by equation (11). D_{sum} is the density of asperities and A_n represents the nominal contact area.

$$n = A_n\, D_{sum} \int_d^{\infty} f(z) dz \tag{11}$$

When an asperity meets a flat surface, the height of the asperity flattened is given by $\delta = z_s - d$. According to the Hertz's theory, when a spherical asperity with a radius R is compressed on a flat surface, assuming an imposed displacement of δ and an elastic deformation, the actual contact area and the load carried by the asperity are respectively given by equation (12) and (13).

$$A = \pi\, R\, \delta = \pi\, R\, (z_s - d) \tag{12}$$

$$P = \frac{4}{3} E^* R^{1/2} \delta^{3/2} \tag{13}$$

$$E^* = \left(\frac{1 - v_1^2}{E_1} + \frac{1 - v_2^2}{E_2} \right)^{-1} \tag{14}$$

In equation (12) and (13), E_1 and E_2 denote the Young's elastic moduli of the two solids coming into contact, whereas υ_1 and υ_2 denote their Poisson's ratio. Further, the whole actual contact area and the total load carried by the surfaces coming into contact are given respectively by the equation (15) and (16). Greenwood and Williamson neglected the elastic interaction between the deformed asperities.

$$A_t = \pi\, R\, A_n\, D_{sum} \int_d^{\infty} (z - d)\, f(z) dz \tag{15}$$

$$P = \frac{4}{3} E^* R^{1/2}\, A_n\, D_{sum} \int_d^{\infty} (z - d)^{3/2}\, f(z) dz \tag{16}$$

2.5.2 The Chang Model

The Chang's model [98] is similar to the Greenwood and Williamson model, but with the main particularity that asperities conserve their volume during the plastic deformation. In the Greenwood and Williamson model, the contact area is underestimated when a substantial percent of the material in contact enters in the plastic phase. The Chang's model assumes that the deformation of an asperity happens around the surface actually in contact. Beyond a certain pushing due to an imposed displacement (δ), the asperity enters in a non-deformable state. According to Chang, δ_c denotes the maximum vertical displacement beyond which the asperity enters in its plastic phase (Figure 28).

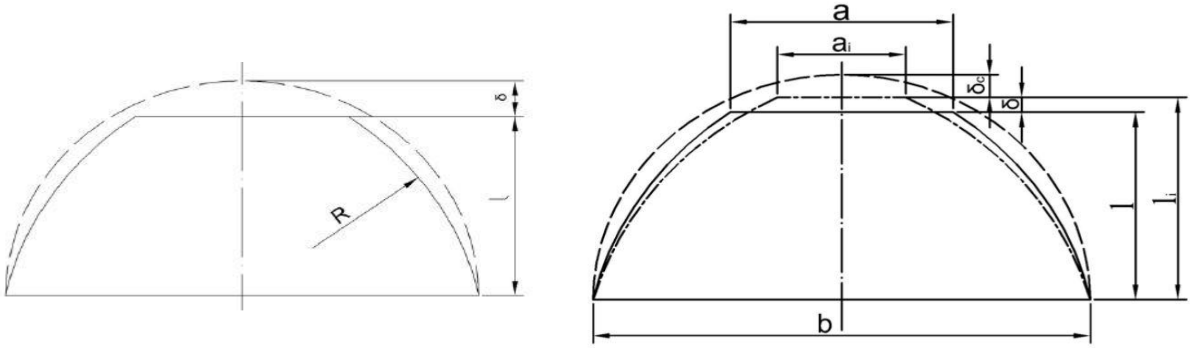

Figure 28. a) Plastically deformed asperity and b) Conservation of asperity volume

In case of a displacement $\delta < \delta c$, the diameter a_i of the actual contact area is found through equation (17).

$$a_i = 2\sqrt{R\delta_c} \tag{17}$$

The contact area and the load carried by an asperity in the plastic-phase are respectively given by equation (18) and (19), kH being the average pressure over the contact area.

$$\overline{A_p} = \frac{\pi a^2}{4} = \pi R\delta\left(2-\frac{\delta_c}{\delta}\right) \tag{18}$$

$$\bar{W} = \pi R\delta\left(2-\frac{\delta_c}{\delta}\right)kH \tag{19}$$

As aforementioned, the model develop by Chang takes into account the elasto-plastic deformation of the asperities. Hence, the whole contact area is given by equation (20).

$$A_t(d) = A_e(d) + A_p(d) \tag{20}$$

$$A_e(d) = \pi\, R\, A_n\, D_{sum} \int_{d}^{d+\delta_c} (z-d)\, f(z)dz \tag{21}$$

$$A_p(d) = \pi\, R\, A_n\, D_{sum} \int_{d+\delta_c}^{\infty} [2(z-d)-\delta_c]\, f(z)dz \tag{22}$$

In addition, the total load supported by the asperities is given by equation (23).

$$P(d) = A_n\, D_{sum}E^{*} \left(\frac{4}{3}R^{1/2}\, A_n\, D_{sum} \int_{d}^{d+\delta_c} (z-d)^{3/2}\, f(z)dz + \pi Rk \frac{H}{E^{*}} \int_{d+\delta_c}^{\infty} [2(z-d)-\delta_c]\, f(z)dz\right) \tag{23}$$

This model is applied to the entire deformation range, from fully elastic to fully plastic, but one shortcoming is that the approach only allows two possible states of deformation for an asperity: either fully elastic or fully plastic, without any transition state.

2.5.3 The Jeng and Wang Model

Jeng and Wang [97] developed an elasto-plastic model tackling the contact between rough surfaces. The Jeng and Wang's model takes into account the elastic phase, the elasto-plastic phase and the fully plastic phase of deformation of the asperity material. As Chang et al. [98], they also took the assumption of a volume conservation of the asperity in the plastic phase. Nevertheless, the variation with all the other models lies on the asperity shape. Indeed, instead of a spherical shape, the Jeng and Wang's model assumes that the asperities have an elliptical shape (Figure 29).

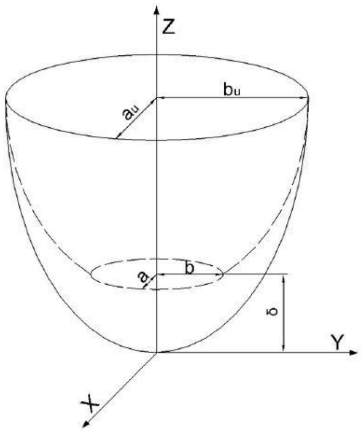

Figure 29. Interference on an elliptical asperity

The boundary between the different deformation phases of the asperities are given by δ_{c1} and δ_{c2} (Figure 30). Asperity remains in the elastic phase when the displacement δ is less than δ_{c1} (Figure 29). Once δ exceeds δ_{c1}, the asperity enters in an elasto-plastic phase, then in a fully plastic phase when δ exceeds δ_{c2}.

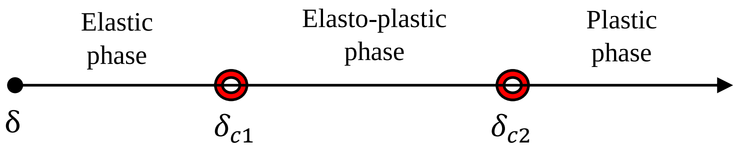

Figure 30. Boundary of the deformation phases of an asperity

In the model proposed by Jeng and Wang [97], the actual contact area and the load supported by the asperities are calculated for each deformation phase. More details on the developed formulae are provided in [97].

- **Elastic phase**

The actual contact area and the load by asperity are respectively given by equation (24) and (25).

$$A_e(\delta) = \pi\, R_m\, \delta\, f_1(e) \quad and \quad f_1(e) = \frac{E(e)}{K(e)(1-e^2)^{0.5}} \tag{24}$$

$$W_e(\delta) = \frac{4}{3} E^* R^{0.5}\, \delta^{0.5}\, f_2(e) \quad and \quad f_2(e) = \frac{\pi\, E(e)^{0.5}}{K(e)^{0.5}(1-e^2)^{0.5}} \tag{25}$$

The critical interference δ_{c1} that marks the border between the elastic phase and the elasto-plastic phase is defined by equation (26).

$$\delta_{c1} = \frac{K(e)\, E(e)}{(\pi/2)^2}\, R_m \left(\frac{H}{E^*}\right)^2 \tag{26}$$

- **Elastoplastic contact**

In the elasto-plastic phase, the equations evaluating the actual contact area and the load carried by the asperities can be retrieved from the equations proposed in the Zhao model [99,100]. Hence, the actual contact area and the load corresponding are respectively given by equation (27) and (29).

$$A_{ep} = \pi R_m \delta * \left\{ f_1(e) + \big(2 f_3(e) - f_1(e)\big) * \left[-2 \left(\frac{\delta - \delta_{c1}}{\delta_{c2} - \delta_{c1}}\right)^3 + 3 \left(\frac{\delta - \delta_{c1}}{\delta_{c2} - \delta_{c1}}\right)^2 \right] \right\} \tag{27}$$

$$W_{ep} = p_m * A_{ep} \tag{28}$$

$$W_{ep} = \left[H - H(1-k) \frac{\ln(\delta_{c2}) - \ln\big(2 f_3(e)\big) - \ln(R_m) - 2\ln(\delta) + \ln(a_l b_l)}{\ln(\delta_{c2}) - \ln(\delta_{c1}) - \ln\big(2 f_3(e)\big) - \ln\big(f_1(e)\big)} \right] * A_{ep} \tag{29}$$

- **Fully plastic contact**

Interference δ_{c2} denotes the border between the elastoplastic phase and the fully plastic phase. In the plastic phase, the actual contact area and the load corresponding are respectively given by the equations (30) and (31).

$$A_p = 2\pi\, R_m \delta\, f_3(\delta) \tag{30}$$

$$W_p = 2\pi\, R_m \delta\, H f_3(\delta) \tag{31}$$

With

$$f_3(e) = \frac{E(e)\, e^2}{2(1-e^2)^{0.5}[E(e) - K(e)(1-e^2)]} \tag{32}$$

According to the Jeng and Wang [97], the total contact area and the total load carried by the asperities are respectively given by the equation (33) and (34).

$$A_t(d) = A_e(d) + A_{ep}(d) + A_p(d) \tag{33}$$

$$W_t(d) = W_e(d) + W_{ep}(d) + W_p(d) \tag{34}$$

2.5.4 The Zhao Contact Model (DCM)

The Zhao's model is also an elasto-plastic model. As in the GW model, they assume a same radius (R) for all the asperities on the contacting interfaces. As in the Jeng and Wang's model, the actual contact area and the corresponding load are calculated for each deformation phase of the material. The critical interferences δ_{c1} and δ_{c2} presented in Figure 30 are also defined in the Zhao's model.

- **Elastic phase**

In the elastic phase, the actual contact area and the load carried by each asperity are respectively given by the equations (35) and (36).

$$A_e = \pi R \delta \tag{35}$$

$$W_e = \frac{4}{3} E^* R^{1/2}\, \delta^{3/2} A_t(d) = A_e(d) + A_p(d) \tag{36}$$

With the interference δ given by equation (37). In this equation, P_a represents the mean contact pressure of the asperity.

$$\delta = \left(\frac{3\pi P_a}{4E^*}\right)^2 R \tag{37}$$

The critical interference δ_{c1} fixing the border between the elastic phase and the elasto-plastic phase is defined by equation (38).

$$\delta_{c1} = \left(\frac{3\pi k H}{4E^*}\right)^2 R \tag{38}$$

- **Elasto-plastic phase**

In this phase ($\delta > \delta_{c1}$), the actual contact area is obtained by equation (39) while the corresponding load is given by equation (40).

$$A_{ep} = \pi R \delta \left[1 - 2\left(\frac{\delta - \delta_{c1}}{\delta_{c2} - \delta_{c1}}\right)^3 + 3\left(\frac{\delta - \delta_{c1}}{\delta_{c2} - \delta_{c1}}\right)^2\right] \tag{39}$$

$$W_{ep} = \left[H - H(1-k)\frac{\ln(\delta_{c2}) - \ln(\delta)}{\ln(\delta_{c2}) - \ln(\delta_{c1})}\right] * \pi R \delta \left[1 - 2\left(\frac{\delta - \delta_{c1}}{\delta_{c2} - \delta_{c1}}\right)^3 + 3\left(\frac{\delta - \delta_{c1}}{\delta_{c2} - \delta_{c1}}\right)^2\right] \tag{40}$$

- **Fully plastic phase**

In the fully plastic phase ($\delta > \delta_{c2}$), the actual contact area and the load corresponding are respectively given by the equations (41) and (42).

$$A_p = 2\pi R \delta \tag{41}$$

$$W_p = 2\pi R\delta H \tag{42}$$

In summary, the total actual contact area (eq. (43)) and the total load supported by the asperities (eq. (44)) are obtained by summing up the values of the elastic, the elasto-plastic and the fully plastic phases.

$$A_t(d) = A_e(d) + A_{ep}(d) + A_p(d) \tag{43}$$

$$W_t(d) = W_e(d) + W_{ep}(d) + W_p(d) \tag{44}$$

2.5.5 The deterministic Contact Model (DCM)

Parasibu and Schipper [96] proposed a deterministic contact model (DCM) analysing the contact between a rough surface and a flat-layered surface, while taking into consideration the different deformation phases of the material. The DCM of Parasibu and Schipper is based on the findings of Gao et al. [101] regarding the determination of an equivalent Poisson's ratio for a layered surface, and on the findings of Bhattacharaya et al. [102] regarding the determination of the effective hardness of a layered surface. The DCM is also based on the findings of Swain et al. [103] regarding the determination of the effective Young's Modulus of a layered surface. In addition, besides the fact that the asperities are assumed of different radius, the DCM is also mainly based on the developments of the Zhao's model. Parasibu and Schipper [96] confute the assumption that the height of the asperities follow absolutely a Gaussian distribution.

For a given layered surface, the effective Poisson's ratio v_{eff}, the effective Young's Modulus E_{eff}, and the effective hardness H_{eff} are respectively given by the equations (45), (46) and (47).

$$v_{eff}(w_i) = v_s - (v_1 - v_s)\, I_1(\xi(w_i)) \tag{45}$$

$$E_{eff}(w_i) = E_s - (E_1 - E_s)\, I_0(\xi(w_i)) \tag{46}$$

$$H_{eff}(w_i) = \begin{cases} H_s + (H_1 - H_s)\, exp\left(-\dfrac{\sigma_{y1}\, E_s}{\sigma_{ys}\, E_1}\left(\dfrac{w_i}{t}\right)^2\right) \quad if \quad H_s > H_1 \\ H_s + (H_1 - H_s)\, exp\left(-\dfrac{(H_1/H_s)}{(\sigma_{y1}/\sigma_{ys})\,(E_{y1}/E_{ys})^{0.5}}\left(\dfrac{w_i}{t}\right)\right) \quad if \quad H_s < H_1 \end{cases} \qquad (47)$$

With I_1 and I_0 respectively given by:

$$I_1(\xi(w_i)) = \frac{2}{\pi} tan^{-1}(\xi(w_i)) + \frac{\xi(w_i)}{\pi} ln \frac{1 + \xi(w_i)^2}{\xi(w)^2} \qquad (48)$$

$$I_0(\xi(w_i)) = \frac{2}{\pi} tan^{-1}(\xi(w_i)) + \frac{1}{2\pi(1 - v_{eff})}\left[(1 - 2v_{eff})\, \xi(w_i)\, ln \frac{1 + \xi(w_i)^2}{\xi(w)^2} - \frac{\xi(w_i)}{1 + \xi(w_i)^2}\right] \qquad (49)$$

$$\xi(w_i) = \frac{t}{\beta^{0.5} w_i^{0.5}} \qquad (50)$$

The analytical formula of the DCM are obtained by inserting the effective Poisson's ratio v_{eff}, the effective Young's Modulus E_{eff} and the effective hardness H_{eff} in the equations (43) and (44) of the Zhao's model. Here, the actual contact area and the load are calculated for each asperity since they are of different radius.

In summary, over the respective developments of the authors [95–100], it is found that the load carried by the asperities in a rough contact is closely related to the actual contact area between the contacting solids.

3 Development of a new interlocking dry-stacked masonry block

3.1 Introduction

The dry-stacked masonry blocks developed around the world vary according to the type (solid and hollow), the interlocking systems (protrusions and grooves) and the constitutive materials. Waleed et al. [44] stated that the designing of a dry-stack masonry block should include three particularities: (1) an efficient interlocking provision for withstanding out of plane loading; (2) a simple interlocking provision for self-alignment and fast construction; (3) a manufacturing process similar or close to the traditional blocks to remain affordable and competitive. Hence, in the current research project, the new dry-stacked masonry block (M-block) was developed in a way to ease the handling for a high productivity. Furthermore, numerical analysis were carried out for correlating the block compressive strength to the material strength.

3.2 Description of the M-block

The M-block can be classified in the category of hollow dry-stacked masonry blocks. It appears as a rectangle box of 350 x 175 x 200 mm (length x width x height). The M-block presents 4 face-shells (2 on both sides of the block in the width direction) interconnected by 3 webs. Both face-shells on the both sides of the block unit are interconnected for stiffening purposes. The block unit presents a gross section of 61.250 mm^2 and a net section of 38.100 mm^2. Protrusions and grooves are provided in the vertical and horizontal axis for ensuring the interlocking mechanisms and the self-alignment process.

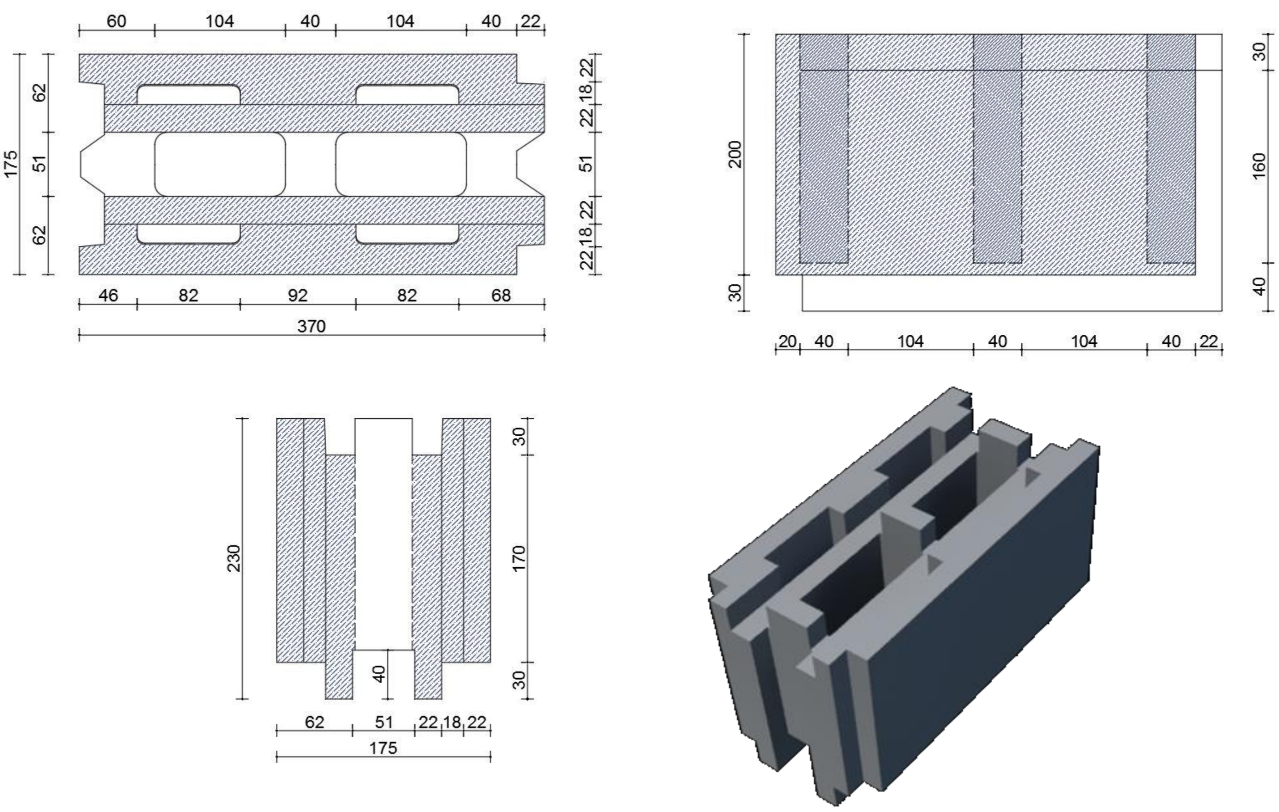

Figure 31. Developed dry-stacked masonry block (M-block)

3.3 Mechanical analysis of the M-block

Once the shape and the interlocking mechanisms designed, a finite element analysis was performed with the aim to predict the compressive strength of the M-block and optimize its face-shell thickness. In addition, the FEM was realised in order to foresee the damage mechanism of the M-block. The finite element modelling was carried out using the FE software ANSYS.

3.3.1 Finite element modelling

The M-block was model on ANSYS using the eight nodes concrete element Solid65 of ANSYS17. Indeed, the used element Solid65 supports cracking and crushing capabilities and is based on the William and Warnke failure criterion [112]. The element Solid65 cracks and loses its stiffness when the ultimate tensile strength of the material is exceeded. Likewise, the element Solid65 fails by crushing when the ultimate compressive strength or the shear resistance of the material is exceeded. In the case of a multiaxial state of stress, four failure modes can be distinguished as defined in the following in function of the principal stresses:

- $0 \geq \sigma_1 \geq \sigma_2 \geq \sigma_3 0 \geq \sigma_1 \geq \sigma_2 \geq \sigma_3$ Compression – compression - compression: the element reaches failure by crushing of concrete.
- $\sigma_1 \geq 0 \geq \sigma_2 \geq \sigma_3$ Traction – compression - compression : the element reaches failure by crushing and appearance of cracks in perpendicular direction to σ_1,
- $\sigma_1 \geq \sigma_2 \geq 0 \geq \sigma_3$ Traction - Traction – compression: cracks appear in the plans perpendicular to the principal stresses σ_1 and σ_2. The element reaches failure by crushing and cracking of concrete.
- $\sigma_1 \geq \sigma_2 \geq \sigma_3 \geq 0$ Traction – Traction – traction: the element reaches failure by appearance of cracks in the plans perpendicular to the principal stresses σ_1, σ_2 and σ_3.

The principal stresses are given according to the uniaxial stress such as follows:

$$\sigma_1 = \max(\sigma_{\text{xp}}, \sigma_{\text{yp}}, \sigma_{\text{zp}}) \text{ and } \sigma_3 = \min(\sigma_{\text{xp}}, \sigma_{\text{yp}}, \sigma_{\text{zp}}) \tag{51}$$

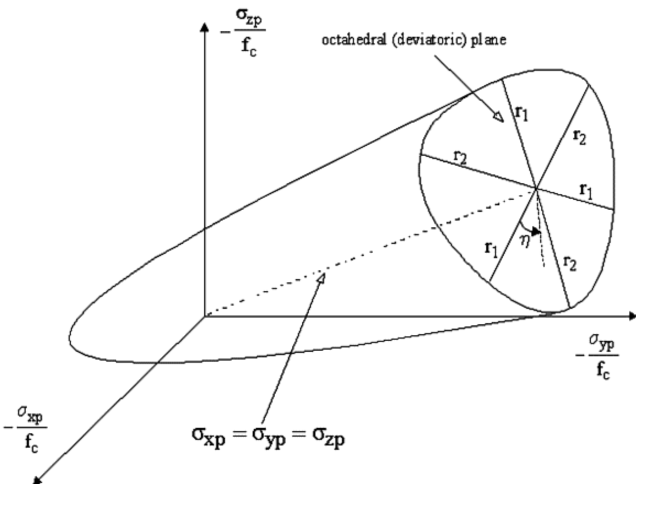

Figure 32. Failure surface according to William and Warnke criterion

The occurrence of a crack in an element of the model results in a weakening of the stiffness matrix of the model. For considering these changes, William and Warnke propose to define a failure surface where the crack appears and introduce shear transfer coefficients in the stiffness matrix of the model. According to William and Warnke [112], 2-shear transfer coefficients are defined, i.e. β_t and β_c, which stands respectively for the open and closed cracks. The values of β_t and β_c vary from 0 to 1. A shear transfer coefficient of 1 denotes a rough crack, i.e. a cracking without absolute loss of shear transfer capacity. Conversely, a shear transfer coefficient of 0 denotes a smooth crack, i.e. a cracking with total loss shear transfer capacity. Throughout the numerical investigation the shear transfer coefficients were set to 0,2 for the open cracks (β_t) and to 0,5 for the closed cracks (β_c), guaranteeing a ratio β_t /β_c of 0,4. In the current research, the used shear transfer coefficients were defined through a calibration using the experimental results of Agaajani [45], and respecting the findings of Uday et al. [9]. Indeed, Uday et al. [9] investigated the influence of the shear transfer coefficients (β_t and β_c) on the variation of the compressive strength predicted for a masonry block using element "SOLID65" provided by ANSYS17. As reported in [9] and shown on Figure 33 and Figure 34, the shear transfer coefficients do not significantly influence the predicted masonry strength for a ratio β_t /β_c of 0,4.

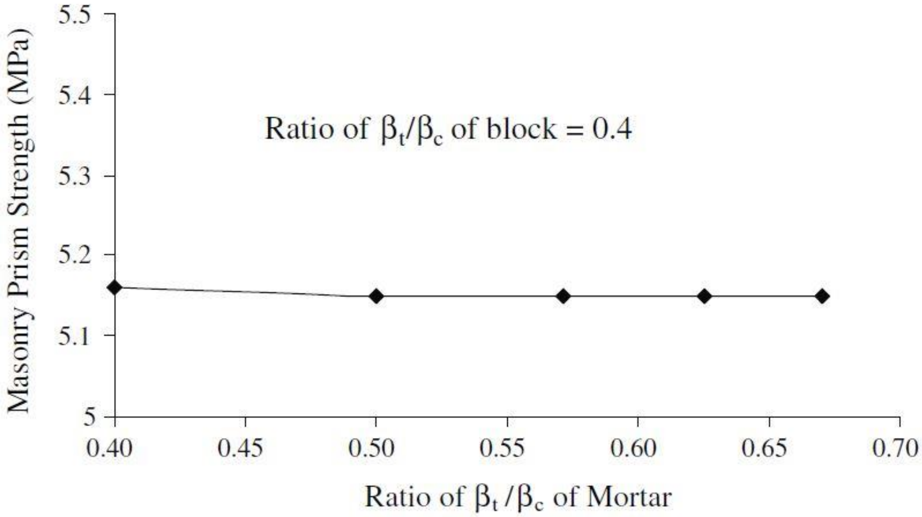

Figure 33. Masonry prism strength in function of the ratio β_t /β_c of the mortar layer and for a constant ratio β_t /β_c of the block unit [9]

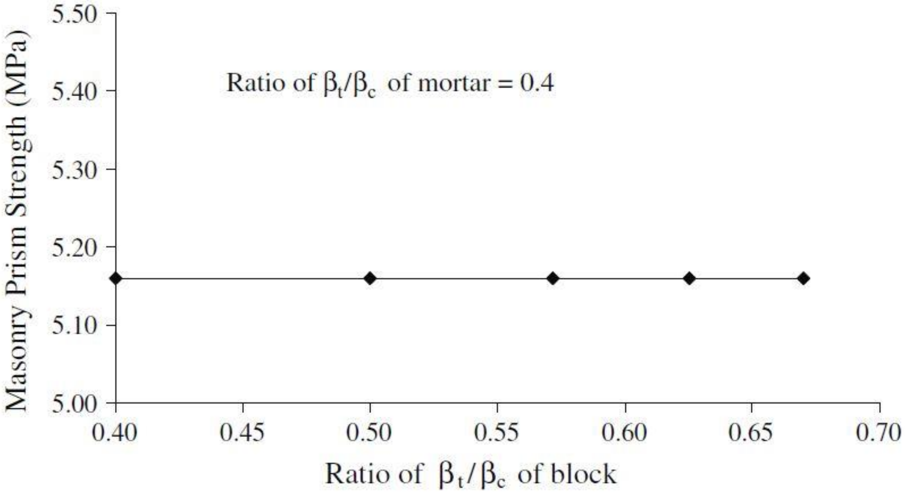

Figure 34. Masonry prism strength in function of the ratio βt /βc of the block unit and for a constant ratio βt /βc of the mortar layer [9]

3.3.2 Strength correlation between the material and the M-block' strength

a) Parameters of the analysis

The strength correlation between the masonry block and the constitutive material was analysed at the same time with a parametric study of the mesh size of the block unit. Regarding the strength correlation, the compressive strength of the masonry block was computed while varying the compressive strength of the constitutive material between 20 and 75 MPa. In addition, the parametric study of the block mesh was carried out before further numerical investigations were realised for purposes of reliability of the FE model in the prediction of the block compressive strength. In this analysis, the block mesh size was analysed for 22, 11 and 5,5 mm side length. These dimensions have been chosen according to the dimensions of the face-shell and webs of the masonry block. Hence, altogether, 24 models were investigated. Figure 35 shows a full 3D regular mesh of the modelled masonry block.

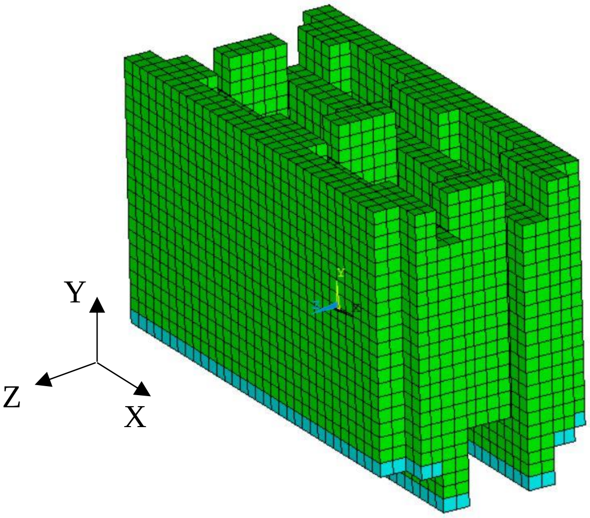

Figure 35. 3D regular mesh of the masonry block

The masonry block was face-shell loaded and bedded, which means that the load was applied exclusively on the face-shells and the masonry block was supported exclusively on the face-shells. The displacements u_y and u_x were restrained on the support faces of the masonry block, whereas the displacements u_x, u_y and u_z were free on the top face (Table 3).

Table 3. Boundary conditions on the nodes

	Displacements	**Node on the y-axis [mm]**	**Node on the z-axis [mm]**	**Boundary conditions**
Top face of the masonry block	u_x, u_y, and u_z	230	[00, 40] and [135, 175]	free
		200	[40, 62] and [113, 135]	free
Support face of the masonry block	u_y and u_x	30	[00, 40] and [135, 175]	restrained
		00	[40, 62] and [113, 135]	restrained

The performance of the masonry block under axial compression was expressed either in terms of gross compressive strength, or in terms of net compressive strength (see Figure 36). Indeed, the gross compressive strength stands for the ratio between the ultimate load and the whole cross section of the masonry block. The net compressive strength in return stands for the ratio between the ultimate load and the cross section of the masonry block minus the hollow section. However, the common parameter used to indicate the performance of a masonry block is the gross compressive strength. Nevertheless, when assuming a perfect contact in the bed-joints, the net compressive strength enables to know roughly the level of stress in the face shells of the masonry block. According to their respective definition, the gross and the net compressive strength of the M-block were obtained with the equations (52) and (53).

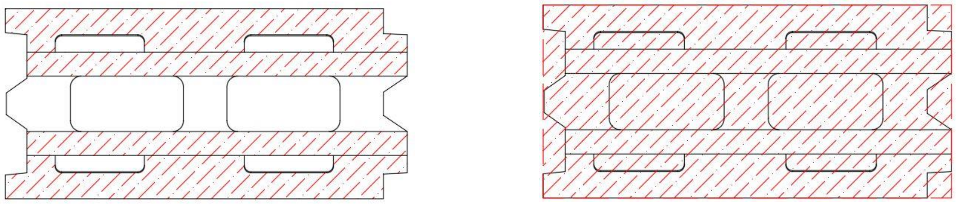

Figure 36. Net (left) and gross (right) section of a masonry block

$$f_{b.\ gross} = \frac{Ultimate\ load}{S_G} \tag{52}$$

$$f_{b.\ net} = \frac{Ultimate\ load}{S_N} \tag{53}$$

S_G gross section of the masonry block (61.250 mm^2)

S_N net section of the masonry block (38.100 mm^2)

b) Strength correlation (masonry block / constitutive material)

The gross compressive of the masonry block is presented in Figure 37 in function of the compressive strength of the block material and the size of the mesh used in the model.

First, regarding the mesh size, it appears that the FE model predicts almost the same compressive strength for a mesh size varying between 11 and 5,5 mm. Nonetheless, less CPU time has been paid using a mesh size of 11 mm with respect to a mesh size of 5.5 mm. The trends towards a convergence of the solution being reached for 11 mm mesh size, the subsequent numerical investigations have been performed using cubic elements Solid65 of 11 mm size.

The findings of Figure 37 also reveal that the compressive strength of the M-block increases linearly with the increase of the constitutive material strength. Furthermore, as concerning the correlation between the gross compressive strength of the masonry block ($f_{b.gross}$) and the compressive strength of the constitutive material ($f_{material}$), it is found that $f_{b.gross}$ could be expressed as $f_{b.gross} = 0{,}41\ f_{material}$.

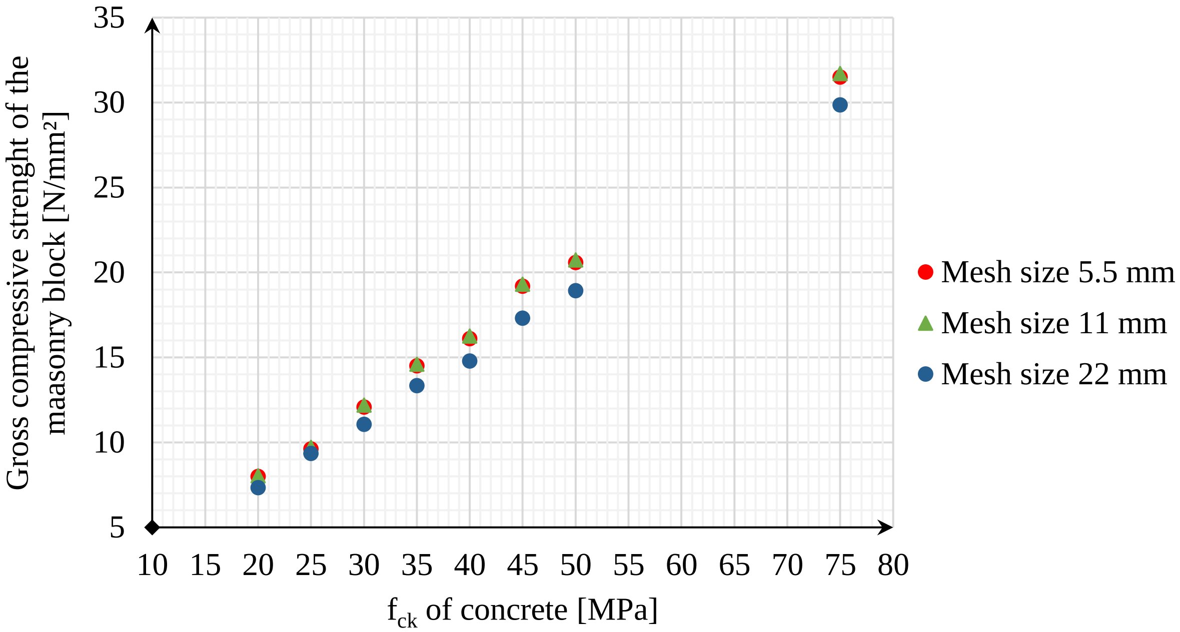

Figure 37. Mesh size influence of the masonry block on the predicted load bearing capacity

c) Stress distribution in the M-block and failure mechanism

Figure 38 shows the stress distribution in the masonry block at 80% of the ultimate load (F_u). The compressive stress is almost uniformly distributed in the face shells and partially transmitted in the webs. In consequence, the webs experience tensile stresses in their upper and lower section. As shown in Figure 39, the compressive stress is measured in the middle height of the face shell and the web of the masonry block. Likewise, the tensile stress is measured in the lower section of the web. Figure 39 shows the increase of both compressive and tensile stresses measured in function of the ratio applied load/failure load (F/F_u).

Figure 39 shows that as the applied load increases, the compressive stress increases almost linearly in the face shell and the tensile stress in the webs follows a non-linear path. Up to 60% of the ultimate load (Fu), the tensile stress increases linearly in the web, then cracks occur for a ratio F/F_u greater that 60%. The occurrence of cracks in the web leads to a stress relaxation in the whole masonry block. The failure of the M-block occurs by a splitting in the weak interfaces I_1 and I_2 (Figure 40). Indeed, the splitting at the interface I_1 is imparted to the exceedance of the tensile strength of the material. The splitting at the interface I_2 could be imparted to the fact that this section represents a weak section with respect to the neighbour face-shells. In addition, the difference in the level between the internal and the external face-shells promotes the development of shear in the interfaces I_2.

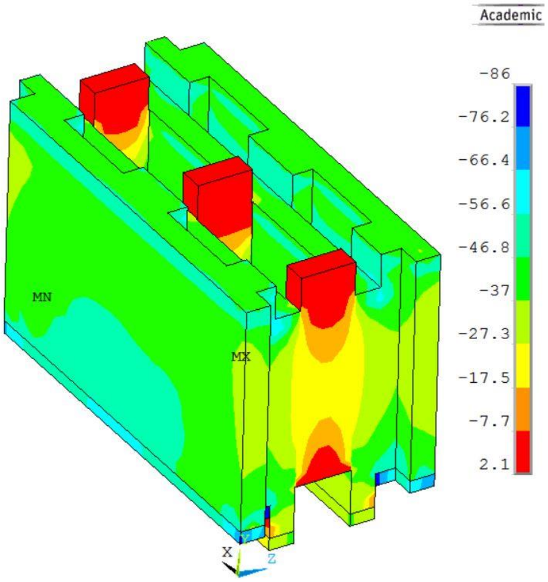

Figure 38. Stress distribution in the M-block at 80% of the ultimate load.

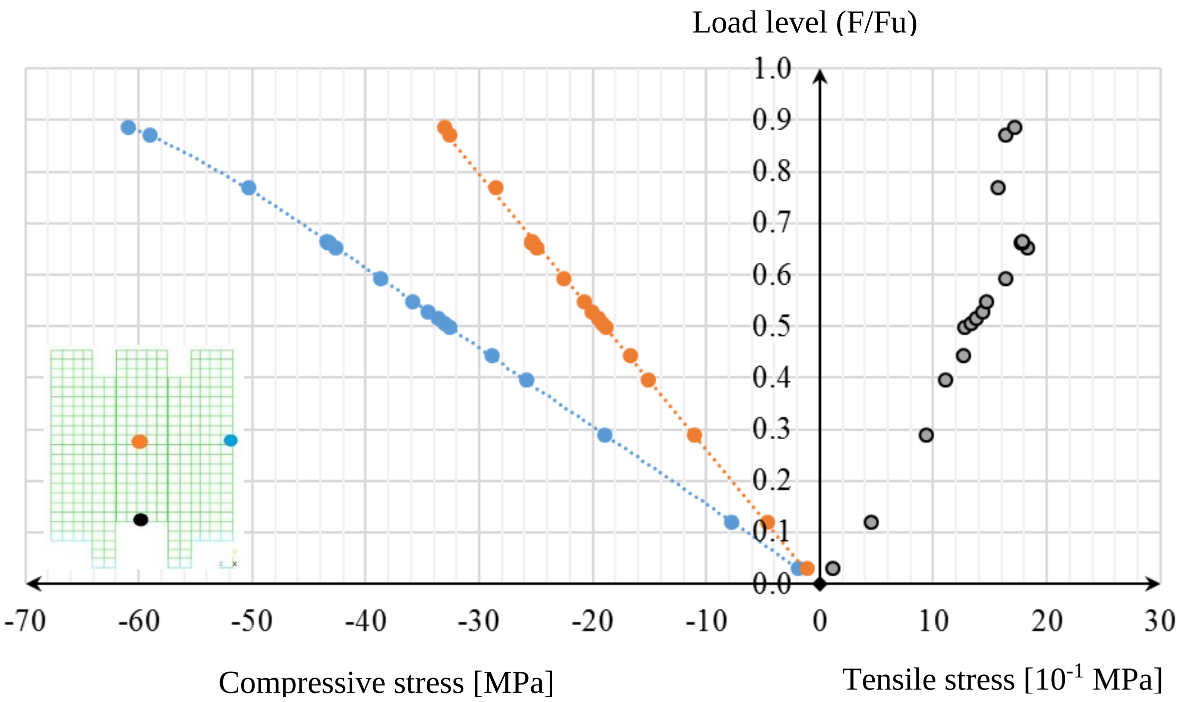

Figure 39. Compressive and tensile stresses in the face-shell and the web, in function of the ratio F/Fu

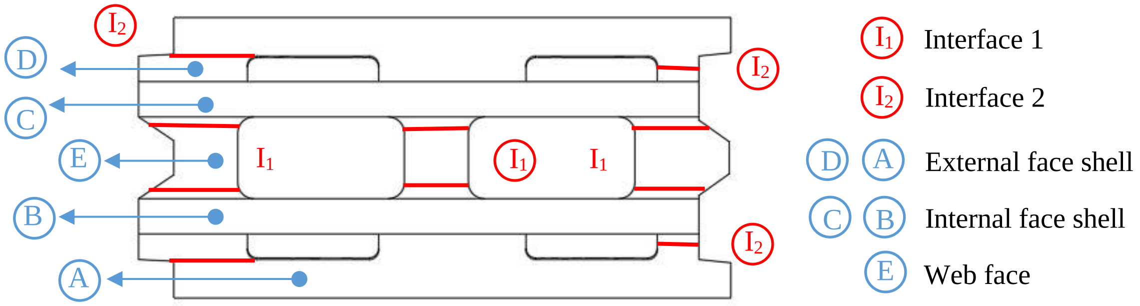

Figure 40. Nomenclature of the parts and interfaces of the masonry block

d) Experimental tests and validation of the FE model

A limited stock of M-blocks (30 samples) were manufactured by Lëtzebuerger Contern using a self-compacting concrete with a compressive strength of 80 MPa. Axial compressive tests were carried out on 4-samples of M-blocks in the laboratory of the University of Luxembourg, for determining the actual compressive strength and furthermore validate the FE model. For the test purposes, the masonry blocks were prepared according to the provision of [1, 67]. Hence, the upper and lower grooves and protrusions were cut and a capping material was provided at the interfaces between the block units and the plates of the press. Indeed, the capping material was provided for ensuring a uniform load transfer and avoid any irregular contact caused by the bed-joint roughness of the block units. In addition, prefabricated stiff metal plates were placed on the upper and lower faces of the masonry block for exclusively applying the load on the face-shells of the masonry block. Figure 41 shows a sketch of the experimental test performed.

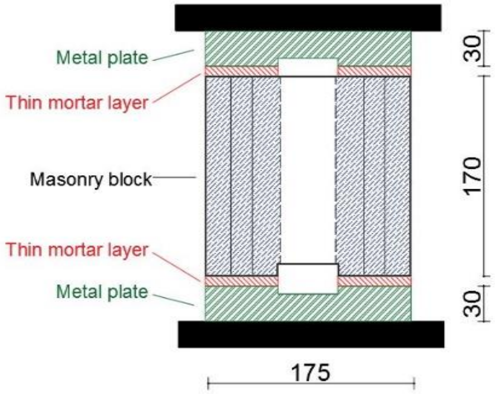

Figure 41. Sketch of the experimental test device used for the single masonry blocks

Table 4 presents the results of the compressive test carried out on single masonry blocks. As previously mentioned the compressive strength of the masonry block is presented in terms of net and gross compressive strength. The experimental tests show that the M-block exhibits a mean failure load of 2168 kN, i.e. a gross compressive strength of 35 MPa with a standard deviation of 11%. According to Atkinson et al. [1], the effect of the friction at the interface with the plates of the press yields an increase of the failure load of about 15% for concrete masonry blocks. The FE model predicted a block compressive strength of 32 MPa for a material compressive strength of 80 MPa, which means a mean accuracy of roughly 92%. In addition, as concerning the correlation between the gross compressive strength of the masonry block ($f_{b.gross}$) and the compressive strength of the constitutive material ($f_{material}$), the results of the experimental tests give $f_{b.gross} = 0,44\ f_{material}$. This actual correlation is close to the one obtained in the numerical model, which provides agreement between the FE model and the experimental test for the prediction of the compressive strength of the masonry block.

Table 4. Compressive strength of the masonry block at 28 days

M-block specimen	Mass [kg]	Failure load [kN]	Net compressive strength [MPa]	Gross compressive strength [MPa]
Sample 1	18,7	2349	62	38
Sample 2	18,2	1852	49	30
Sample 3	18,8	2395	63	39
Sample 4	18,8	2077	55	34
Mean value	18,6	2168	57	35

Aside the 4-samples previously tested, one masonry block was compressed up to 90% of the expected failure load then unloaded for capturing pictures of the developed cracks. Figure 42 shows the crack path in the concerned masonry block. Upon loading and up to the failure load, the masonry block experienced splitting at the interface I_1 and I_2 as predicted in the FE model.

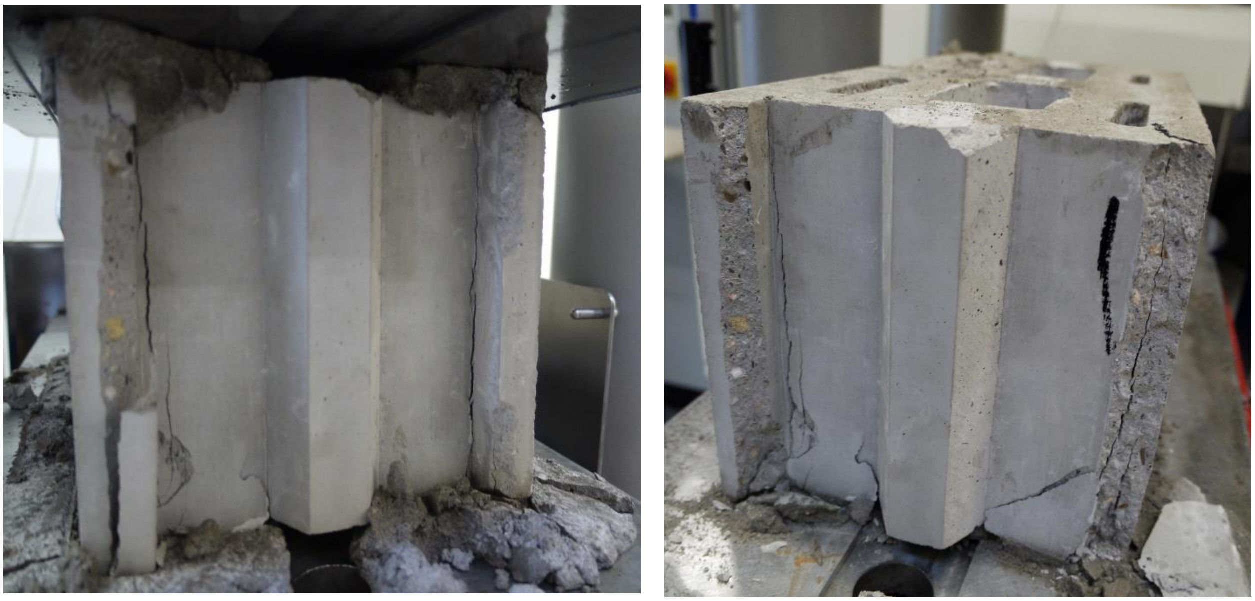

Figure 42. Crack path in masonry block tested under axial compression until 90% of $F_{u.\,Block}$

3.4 Summary

In this chapter, a new dry-stacked masonry block was developed with an efficient interlocking system valuable to facilitate the wall construction and potentially improve the out of plane resistance. The strength correlation between the block compressive strength and the material strength was established. It was found that the new developed dry-stacked interlocking masonry block can withstand compressive loads of about 41% of the ultimate compressive strength of its constitutive material. In the following chapters, the effect of the block imperfections on the in-plane response of dry-stacked masonry will be investigated and presented.

4 Experimental investigation of the effectiveness of a contact layer in dry-stack masonry

This chapter is based on the work published in the following research papers:

- *Gelen Gael Chewe Ngapeya, Danièle Waldmann, Experimental and analytical analysis of the load-bearing capacity P_u of improved dry-stacked masonry, Journal of Building Engineering 27 (2020), 100927.*
- *Gelen Gael Chewe Ngapeya, Danièle Waldmann, Overcome of bed-joint imperfections and improvement of actual contact in dry-stacked masonry, Construction and Building Materials 233 (2020) 117173.*

4.1 Introduction

The following chapter deals with experimental tests on DSM masonry prisms and wallets, with the aim to assess the capacity of the contact layer for overcoming the bed-joint imperfections of block units. For this purpose, first of all, the masonry block used and the materials of the contact layer are presented and characterised on a mechanical perspective. Thereafter, tests on dry-stacked masonry prisms are described, as well as the technical device used for capturing the actual contact area in the bed-joints. Finally, tests on dry-stacked masonry wallets are described and the effectiveness of the contact layer is discussed in terms of improvement of both the actual contact area and the load-bearing capacity.

In this section, a great part of the experimental tests were carried out using a simple block provided by the project partner, as the implementation of the industrial production process of the M-block was still under development/implementation. An overview of the experimental tests carried out on single blocks, on masonry prisms and on wallets is presented in the Summary table 1.

Summary table 1. Overview of aspects investigated for each type/group of masonry blocks.

		Experimental approach
Single block	M-block	Compressive strength
	Simple block	Compressive strength
Masonry prisms (with the simple block)	P-group 1 (no add. layer)	Load-bearing capacity, contact surface, stress-strain behaviour
	P-group 2 (layer mix A)	Load-bearing capacity, contact surface, stress-strain behaviour
	P-group 3 (layer mix B)	Load-bearing capacity, contact surface, stress-strain behaviour
	P-group 4 (layer mix C)	Load-bearing capacity, contact surface, stress-strain behaviour
	P-group 5 (layer mix D)	Load-bearing capacity, contact surface, stress-strain behaviour
	P-group 6 (layer mix E)	Load-bearing capacity, contact surface
Masonry wallets (with the simple block)	W-group 1 (no add. layer)	Load-bearing capacity, contact surface.
	W-group 2 (layer mix A)	Load-bearing capacity, contact surface.
	W-group 3 (layer mix B)	Load-bearing capacity, contact surface.
	W-group 4 (layer mix C)	Load-bearing capacity, contact surface.
	W-group 5 (layer mix D)	-
	W-group 6 (layer mix E)	Load-bearing capacity, contact surface.
Masonry prisms (with the M-block)	P-group 7 (layer mix F)	Contact area.
	P-group 8 (layer mix G)	Contact area.
	P-group 9 (layer mix H)	-
	P-group 10 (layer mix I)	-

4.2 Materials

4.2.1 Dry-stack masonry block (DSM_b)

The investigations to improve the rate of the actual contact area between the DSM_b and the load-bearing capacity of a dry-stacked masonry wall has been carried out on the DSM_b provided by a local producer. The masonry block used within this study is composed out of two face-shells intended to bear the loads and interconnected through two webs. The masonry block has a nominal length of 500 mm, a height of 200 mm, a width of 200 mm and a face-shell thickness of 22 mm. Figure 43 shows a perspective view of the masonry block. At the onset of the study, uniaxial compressive tests have been performed on single masonry blocks to disclose their load-bearing capacity. From the 10 samples tested, the mean ultimate strength found was about 1300 kN.

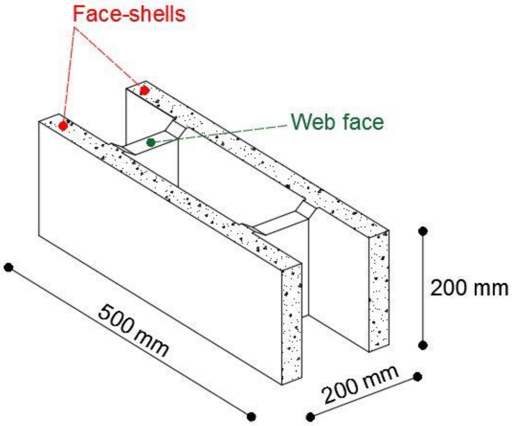

Figure 43. Perspective view of the masonry block [122]

The improved DSM_b ($I.DSM_b$) were manufactured by adding a contact layer of 10 mm [26,33,65,105–111] on the head of the face-shell of the raw dry-stack masonry blocks ($R.DSM_b$). The assumption of 10 mm was taken based on the findings of Feng et al. [49] who showed that this thickness is the optimum mortar joint thickness leading to the least effect on the masonry's strength. To apply the contact layers on the raw masonry blocks, formworks (Figure 44) having the shape of the raw masonry block have been manufactured with a height being 10 mm higher than the nominal height of the raw masonry block. The gap of 10 mm forecasted on the top face of the raw masonry blocks was filled by hand with the materials of the contact layer and the whole was vibrated before being unmoulded to avoid air gaps. The improved masonry blocks were stored for 28 days. Figure 45 shows the raw dry-stack masonry block (R.DSM$_b$) and the improved dry-stack masonry block (I.DSM$_b$).

Figure 44. Sample of the wood formwork used to apply the contact layers [122]

(a) (b)

Figure 45. (a) Raw dry-stack masonry block R.DSM$_b$; (b) Dry-stack masonry block improved with a contact layer on its head (I.DSM$_b$) [122]

4.2.2 Materials of the contact layer

Four different materials have been chosen for the experimental study of the contact layer. The material selection was based on the results of Tatheer [9, 10] showing that the embedment of a compressible material in the contact interface enables to reduce the stress peaks. The material selection was also based on the results of Vasconcelo [50] demonstrating that the bed-joint closure in a dry-stacked wall is proportional to the material's stiffness. The materials were selected in a way to analyse the cases of a contact layer with a conventional material of medium stiffness (mix A, mix B, mix C and mix D), and the case of a contact layer with an auxetic material of low stiffness (mix E).

Indeed, auxetic materials [41-48], which are classified in three groups i.e. crystals, foams and fibres, are materials having a negative Poisson's ratio. Hence, conversely to conventional materials, which extend laterally under a compression, they rather compress (see Figure 46). As shown in Figure 47, the internal structure of auxetic material presents nodules connected by fibres [42-46] that tighten the nodules when the material is subjected to compression. Hence, under compression, the tightening effect of the fibres mitigates the lateral tensile stress, which differs from conventional materials where the dilatation yields a lateral tensile stress.

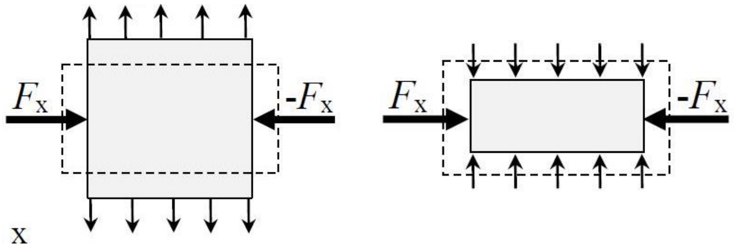

(a) (b)

Figure 46. (a) Conventional and (b) auxetic materials' behaviour under uniaxial compression [46]

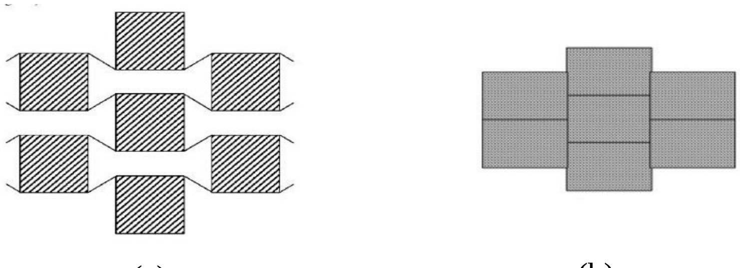

(a) (b)

Figure 47. Internal structure of an auxetic material like mix E (a) before and (b) after a compression [43, 47]

Four different materials of a common stiffness but of different stress-strain responses (mixtures A, B, C and D) are compared to a more compressible and low stiffness material (mix E). Mix E is a 99% mineral material with a porous structure, a density of 200 kg/m^3. Mixtures A, B and C are materials composed of 1/3 of cement, 2/3 of sand and crush polymer. Mix C is a specific variation of the blend of mix A and B. Mix D is a common mortar cement used in masonry.

The mechanical properties (compressive strength and stress-strain behaviour) of each material used to build the contact layer were assessed by performing compressive tests on prism samples of 4x4x16 cm size. The prisms were tested under axial compression at 28 days of hardening. In addition to the compressive strength, the stress-strain behaviour of each material was recorded to determine the Young's modulus. Table 5 summarizes the ultimate compressive strength found in each sample of material and Figure 49 shows the mean stress-strain response recorded. Based on the stress-strain relationships of the materials shown in Figure 49, the Young's Modulus of the mixes A, B, C, D and E are respectively about 11500 MPa, 10500 MPa, 7000 MPa, 3000 MPa and 150 MPa.

Table 5. Compressive strength and Young's Modulus of the contact layer mixtures

Mixture Type	Test	Compressive strength [N/mm²]	Mean compressive strength [N/mm²]	Young's Modulus [MPa]
Mix A	1	36,0	37,0	11500
	2	38,0		
	3	37,8		
Mix B	1	34,0	34,0	10500
	2	33,8		
	3	34,1		
Mix C	1	39,0	38,0	7000
	2	36,9		
	3	38,0		
Mix D	1	5,0	5,2	3000
	2	5,2		
	3	5,3		
Mix E	1	1,2	1,3	150
	2	1,4		
	3	1,2		

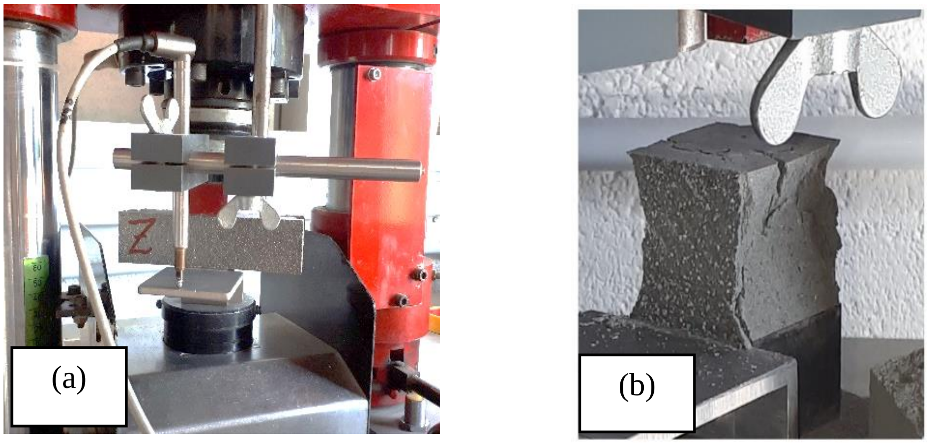

Figure 48. Mixture prisms tested [121]

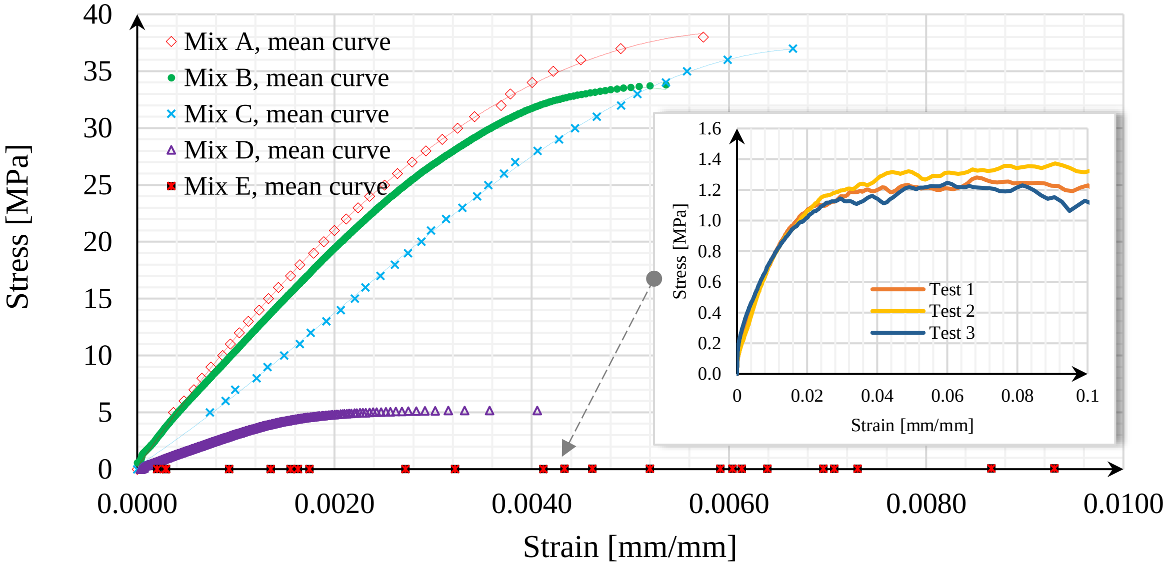

Figure 49. Stress-strain behaviour of the mixtures at 28 days of hardening

4.3 Bed-joint roughness measurement

The actual surface bed-joint roughness of a DSM-block was measured on a finite section element of 1,7 x 1,7 mm^2 using a profilometre with a 3D capability. Indeed, the profilometre used is the DektakXT^R capable for measuring a surface roughness of the order of a nanometre. The DektakXT^R is constituted of a platform placed under a needle (Figure 50.a). For performing a surface roughness measurement, the sample is placed on the platform so that the surface to be studied is directly under the needle. During the measurement, the platform is discontinuously displaced following one axis (x-axis or y-axis) and respecting a specified displacement steps Δx (Figure 50.b). Then, for each discontinuous displacement step, the roughness profile is continuously measured following the axis perpendicular to the discontinuous displacement axis. Accordingly, the bed-joint roughness measurement is delivered as a series of parallel profiles measured at each step of imposed displacement (Figure 50.b). The quality of the 3D roughness profile is strongly dependant on the imposed displacement step Δx. The smaller Δx is, the better is the 3D roughness profile. The needle of the DektakXT^R is capable for measuring a maximum height variation of ±0,50 mm. Figure 50.a shows a sketch of the device used to measure the roughness on a surface. The sample is placed on a movable platform. During the moving of the platform, the needle measure the unevenness of the surface. Figure 50.b shows a top view of a sample with the different roughness profiles measured over the surface.

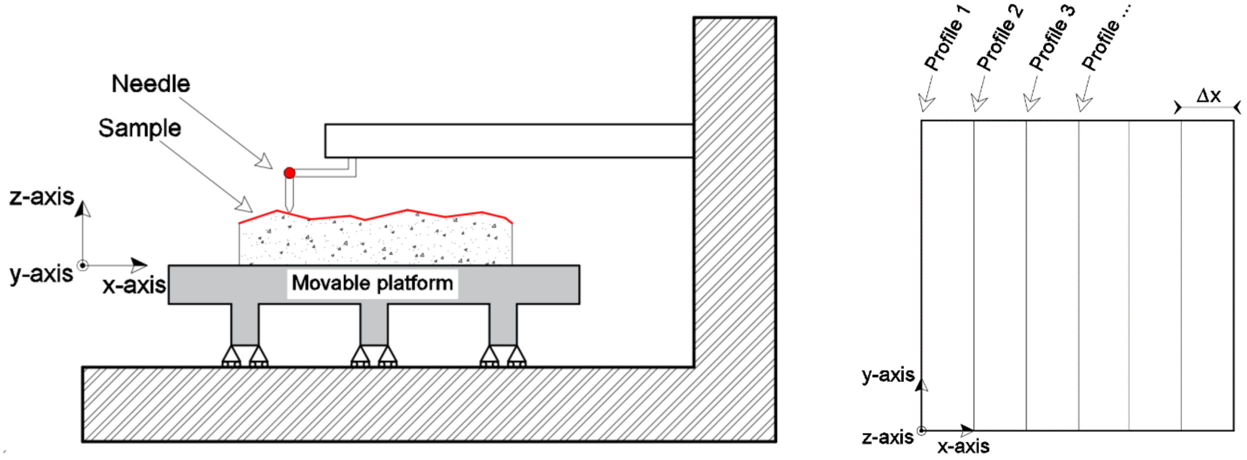

a) b)

Figure 50. Illustration of the measurement device

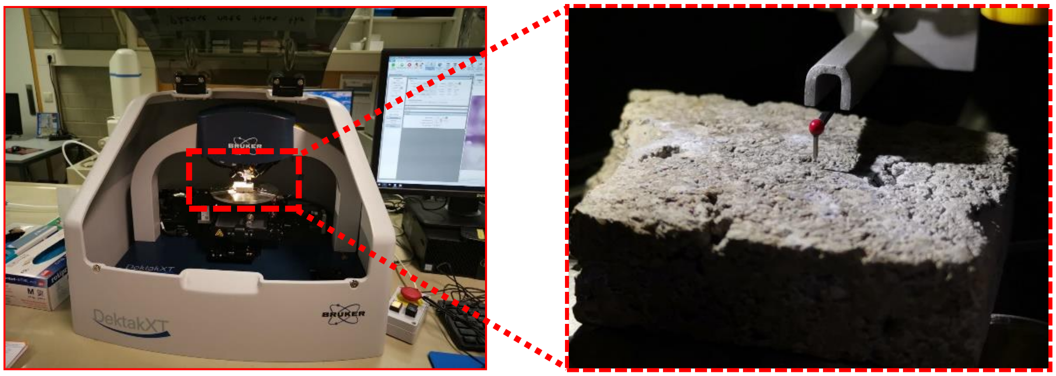

Figure 51. Actual measurement of a surface bed-joint roughness

The actual surface roughness measured on the finite section element is presented on Figure 52. The maximum height between the peaks and the valleys was found around 0,18 mm, which is in accordance with the range of the bed-joint closure (0,03 to 0,25 mm) measured by former researchers [60-64]. Nevertheless, this measure was done on the surface sample while avoiding the depth holes for not trapping the needle of the instrument in a depth hole and break it during the moving of the platform.

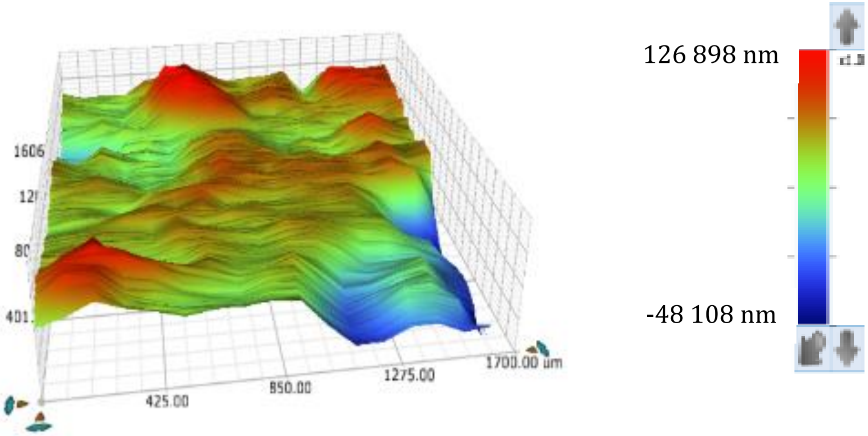

Figure 52. Actual surface roughness on a finite section element of 1,7 x 1,7 mm^2

4.4 Experimental tests on masonry prisms

4.4.1 Description

The aim of the analysis is to assess the efficiency of the I.DSM$_b$ as strategy to improve both the load-bearing capacity and the actual contact in the bed-joints of a DSM. The footprint of the actual contact in the bed-joints was recorded by using Prescale Fujifilm. The used contact sensors are composed of two sheets (X and Y). Sheet Y is constituted of very small bubbles that burst under the effect of a defined stress to release the ink. The released ink impregnates the underlying sheet (sheet X) thereby enabling to record an actual contact area. The burst of the bubbles occurs progressively as the load increases, causing the appearance of red nuances on the sheet X, which then enables to identify the contact intensity.

As shown in Figure 53, each tested masonry prism was composed of three dry-stacked masonry blocks assembled between the two plates of the hydraulic press. The compressive load generated by the six hydraulic pistons was applied exclusively on the face-shells of the masonry blocks. In order to ensure a uniform contact between the plates of the hydraulic press and the masonry blocks, a thin mortar layer was placed on their contact interfaces. Moreover, an experimental test was carried out by inserting also contact sensors between the masonry blocks and the plates of the press to check the uniform contact. The last experiment revealed a full contact at these interfaces.

At the onset of the experiments, the masonry prisms were prepared according to the following manufacturing process: A quick hardening mortar layer was placed on the bottom press plate and the masonry blocks were dry-stacked in the hydraulic press (Figure 54) following the scheme of Figure 53. The contact sensors able to record a compressive stress up to 50 MPa were inserted in the bed-joints during the prism erection and a layer of the quick hardening mortar was placed on the top face of the device. A hardening time of 24 hours was left to enable the upper and the lower mortar layers to develop their strength. During the loading tests, the axial compressive load was progressively applied on the face-shells, with a rate of 1 kN/s, until the collapse of the masonry prism. In fact, the load was increased slowly in order to allow a progressive deformation of the contact layer.

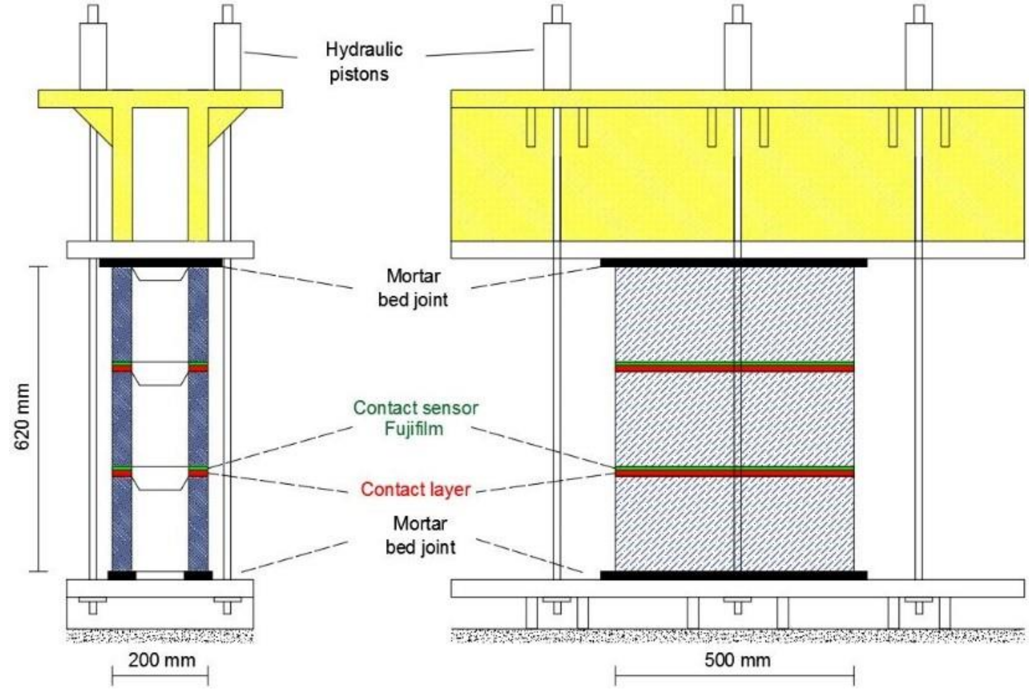

Figure 53. Side and transversal view of the experimental test device [121]

Figure 54. Perspective view of the experimental test on the field

In addition as shown in Figure 55, six displacement gauges of 20 mm deformation length have been used to measure the bed-joint closure (D1L, D1R, D2L, D2R) and the lateral expansion near the bed-joints (D3, D4). The displacement gauges (D1 and D2) were asymmetrically disposed in order to identify an eventual in-plane rotation of the masonry block. The displacement gauges were removed at around 250 - 300 kN of applied load to avoid destroying them at failure of the masonry prism.

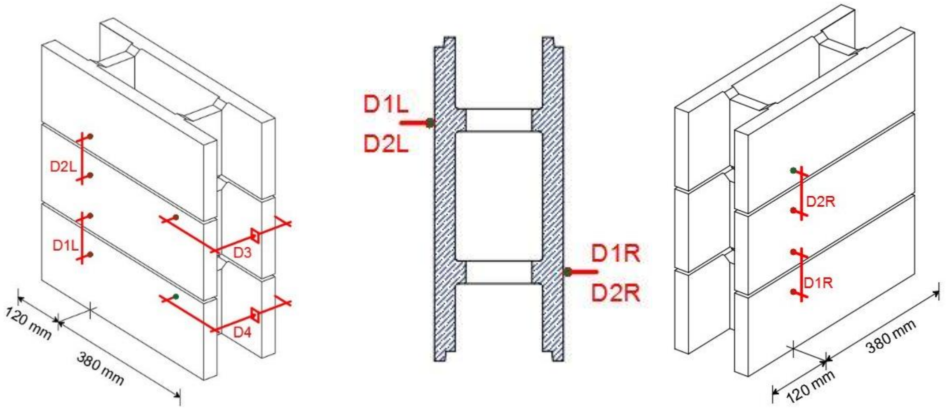

Figure 55. Disposition of the gauges (D1-D2 for vertical displ. and D3-D4 for horizontal displacement) [122]

Table 6. Masonry block prisms ranged by P-group [122]

Test group	Mixture of the masonry block's contact layer	Masonry prisms tested
P-group 1	Without contact layer	5
P-group 2	mix A	5
P-group 3	mix B	5
P-group 4	mix C	5
P-group 5	mix D	-
P-group 6	mix E	5

For comparison purposes, the experimental test was performed on twenty-five masonry prisms subdivided into in five P-groups as indicated in Table 6. Following the experimental tests, the sheets of the contact sensors were scanned, converted in black and white and then analysed with a MATLAB code. Indeed, the digital band resulting from the scanning of the contact sensors are bands containing millions of pixels characterised by a RGB (Red-Green-Blue) triplet. The pixels with a RGB triplet of “0-0-0” represent the areas where the bubbles of sheet have burst, i.e. the actual contact area. Conversely, the pixels with a RGB triplet of “255-255-255” represents the areas where the bed-joints of the DSM$_b$ did not come into contact. Therefore, the MATLAB code scans the digital band, counts the number of pixels having a RGB triplet different of “255-255-255” and reports this number to the whole number of pixels of the digital band. The resulting ratio represents the percentage of the actual contact area with respect to the scanned nominal area.

4.4.2 General behaviour and failure modes

Out of the five P-groups of masonry prisms tested, two main failure modes have been observed. The first failure mode is the one observed by several researchers [6, 7, 13] in the field of dry-stacked masonry blocks, i.e. the appearance and the development of cracks in the webs of the masonry blocks (Figure 56) at about 60% of the ultimate load.

(a) (b) (c)

Figure 56. Failure mode in the masonry prisms of P-group 1 to 4. (a)-(c) cracks in the webs; (b) actual contact [122]

Upon the loading of the masonry prisms (P-group 1 to 4), a closure of the bed-joints is observed at the onset, followed by the development of the masonry prism resistance. As observed in former numerical investigations [6, 7, 18], the load applied on the face-shells is partly transferred on the webs leading there to a concave stress distribution, which creates a tensile stress zone and finally cracks in the webs. In addition, the lateral expansion of the contact layer due to the positive Poisson's ratio of the material makes also increase the lateral tensile stress in the masonry blocks. Once the cracks arise in the webs, the horizontal displacements of the bed-joints increase faster and the DSM-prism collapses by lateral instability. The lateral expansion of the contact layer followed by a loss of the material between the face-shells leads to a stress concentration on a reduced surface around the bed-joints. This also contribute to a development of cracks in the face-shells (Figure 57).

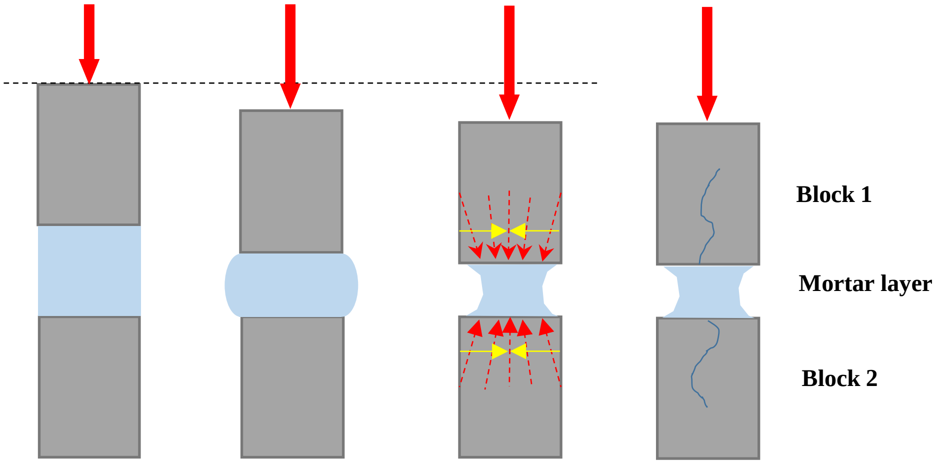

Figure 57. Sequence of crack development in a bed-joint

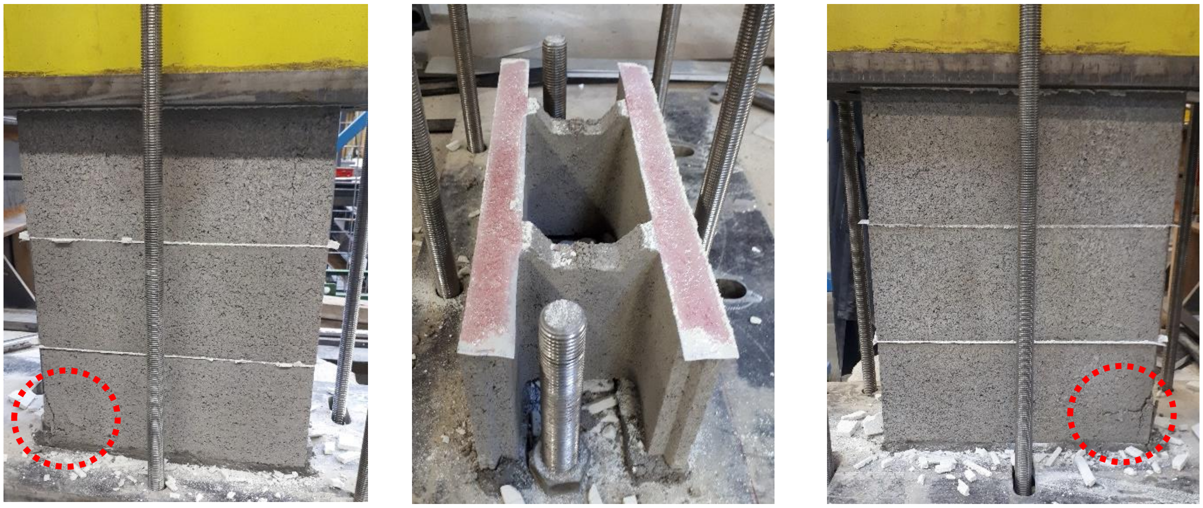
(a)

(b)

(c)

Figure 58. Failure mode in the masonry prisms of P-group 6. (a)-(c) crushing of the face-shells; (b) actual contact in the bed-joints [122]

The second failure mode was observed in the DSM-prisms of P-group 6 (Figure 58). In these prisms, the collapse happens both with the development of micro-cracks in the webs and more by a sudden crushing of the face-shells. During the experimental tests, it has been observed that the masonry prisms of P-group 6 clearly exhibited less lateral expansion (Figure 59) compared to the masonry prisms of the other P-groups (1 to 4). This reduced lateral expansion is the result of the lateral expansion of the block units and the lateral retraction of the auxetic contact layer made of of mix E. Hence, instead of a significant lateral expansion of the contact layers as in the I.DSM$_b$ of P-groups 2 to 4, the contact layer of the masonry blocks of P-group 6 rather compress in the direction perpendicular to the loading, which explain the lower lateral expansion. In addition, as observed in Figure 58, the compressibility of the mix E enabled to reach a full contact in the bed-joints, which in turn led to a uniform load transfer between the masonry blocks. Thanks to a full contact and a uniform load transfer between the masonry blocks, the face-shells of the masonry blocks have been able to leverage their entire strength to the benefit of the masonry prisms. Hence, the masonry prisms of P-group 6 only collapsed due to an exceeding of the face-shell stiffness.

Figure 59 reports the displacement monitored with the displacement gauge D3. Figure 60 shows the force–displacement relationship recorded during the experimental test on the masonry prism number 3 of each P-group. It is worth to remind that the displacement gauges were removed around 250-300 kN of applied load to avoid destroying them at ultimate loading. However, to show properly the difference in the failure load reached by the prism of each P-group, the failure load is represented on each graph by extending the force–displacement curve exploiting the stiffness of the masonry prisms between 50-90% of the ultimate load. Waleed et al. [6] and Mohd et al. [13, 14] who have used a similar masonry block respectively showed that the in plane deformation is no more influenced by the bed-joint imperfection after 45% and 57% of the ultimate load. After the initial non-linear phase due to the closure of the bed-joints, dry-stacked masonry walls exhibit an almost linear behaviour [52-54] until brittle failure.

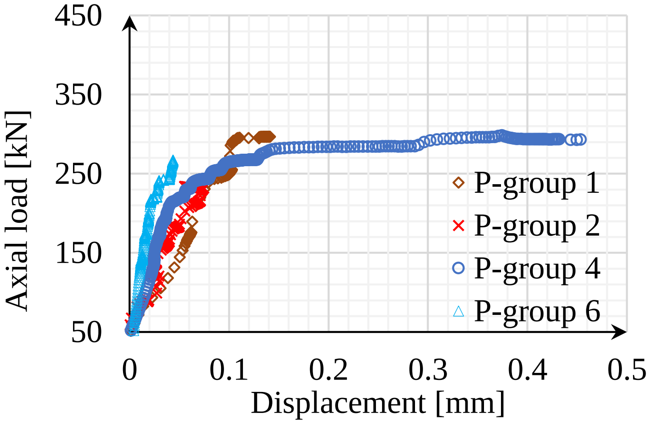

Figure 59. Lateral displacement (D3) at the bed-joint in function of compressive loading (test 3) [122]

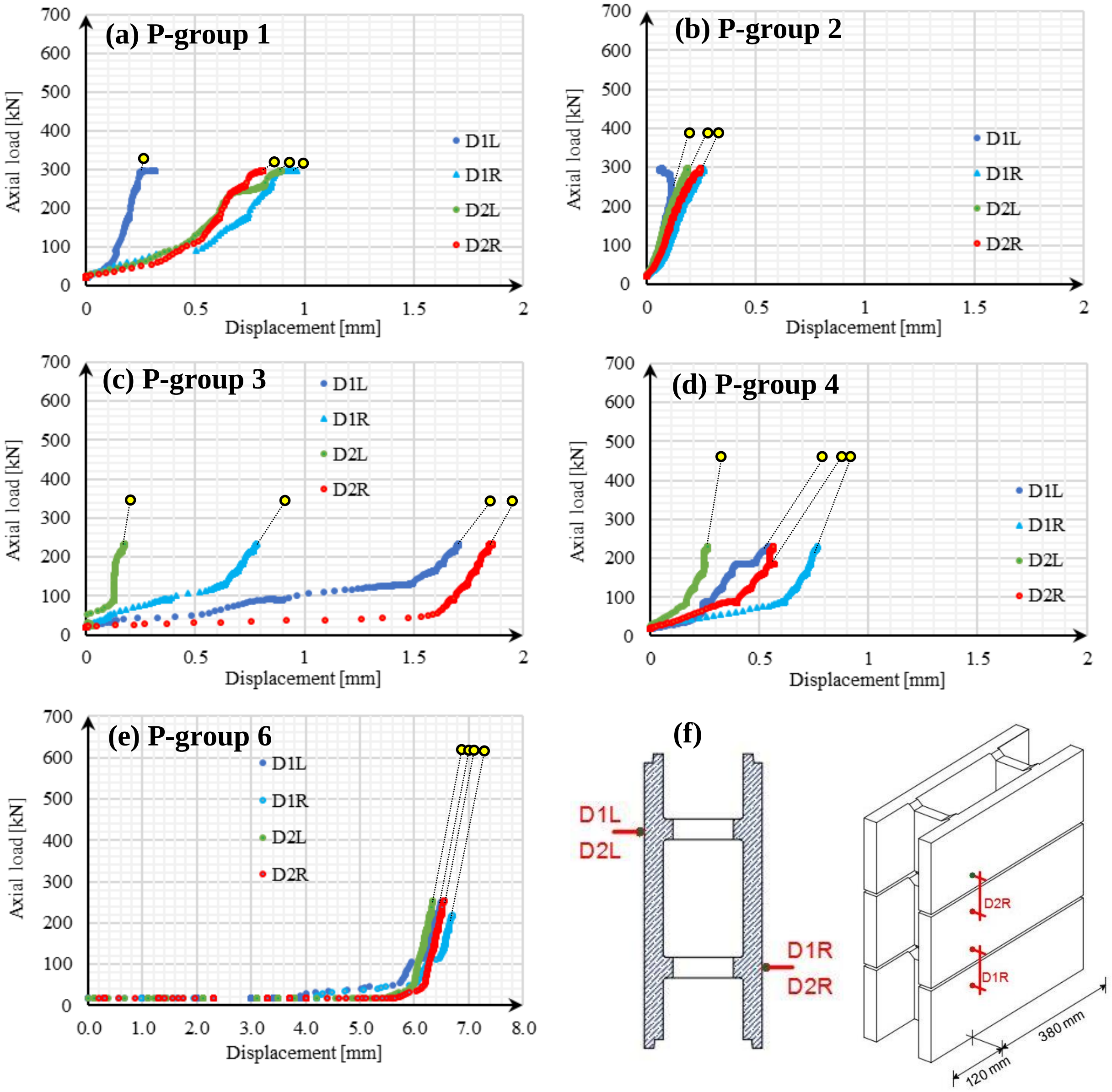

Figure 60. Compressive load against the close-up deformation. (a) P-group 1 - raw DSM$_b$; (b) P-group 2 - DSM$_b$ improved with mix A; (c) P-group 3 - DSM$_b$ improved with mix B; (d) P-group 4 - DSM$_b$ improved with mix C; (e) P-group 6 - DSM$_b$ improved with mix E; (f) Displacement gauges [122]

The dispersion of the force–displacement relationships observed on each prism (D1L with respect to D1R and D2L with respect to D2R) is owed to the magnitude of the bed-joint imperfections, i.e. the roughness and the non-planarity of the surfaces coming in contact. In addition, as highlighted by Allaoui [8], a dry joint opening instead of closing sometimes happens due to a motion of the masonry block caused by the bed-joint imperfections. As former authors [5-8, 12-15] observed, the initial settlement occurring at the onset of the loading leads to a densification of the bed-joint contact and an increase of the reaction to compression. The gradual closure of the gaps between the DSM_b is therefore responsible for a nonlinear progressive stiffening of the interface.

4.4.3 Actual contact and load-bearing capacity

In order to coordinate the discussion of the results in terms of actual contact area, the bed-joints of the masonry blocks were labelled in the vertical and the horizontal axis. Following the vertical axis, the lower bed-joints were named “bed-joint 1” while the upper bed-joints were named “bed-joint 2”. Following the horizontal axis, the bed-joints were referenced by the acronym A for the left side of the masonry block and B for the right side. Figure 61 shows the identifications used in the bed-joints.

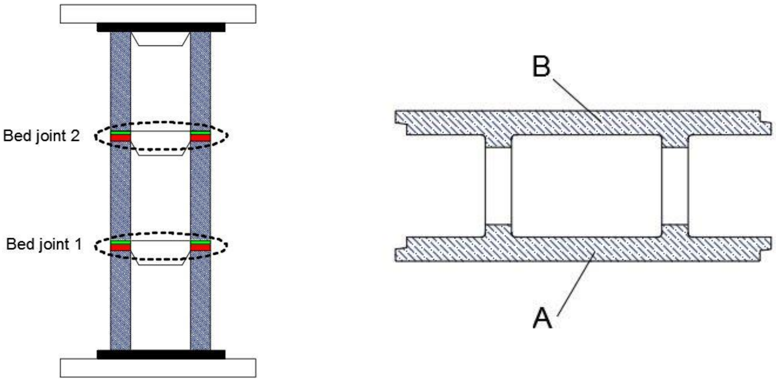

Figure 61. Bed-joints identification in a DSM_b [122]

The results of the twenty-five experimental tests are summarized in Table 7. In this table, the rate of the actual contact area in the bed-joints and the failure load reached is given for each tested masonry prism. In the same table, the mean rate of the actual contact and the mean value of the failure load are calculated for each P-group of masonry prisms. In the last column of Table 7, an improvement factor gained by the contact layer is calculated by reporting the mean failure load of the masonry prisms to the mean failure load of the masonry prisms of P-group 1.

$$\text{Improvement factor} = \left(\frac{\text{Mean failure load of the masonry prisms with I.DSMb}_{\,2,\,3,\,4,\,6}}{\text{Mean failure load of the masonry prisms with R.DSMb}}\right) \qquad (54)$$

4.4.3.1 Prisms with the R.DSM$_b$ (P-group 1)

In order to weigh the influence of the contact layer on both the actual contact in the bed-joints and the load-bearing capacity of the dry-stacked masonry prisms, the experimental tests were firstly performed on the prisms built with the raw dry-stacked masonry blocks. As shown in Table 7 P-group 1, the mean rate of the actual contact reached in the bed-joints is about 23%, which means that the load uniformly applied on the top face of the masonry blocks is transferred from one block to another through a cross-section reduced by 77%. This means that the compressive stress is on average amplified by 4,3 (1/0,23) in the contact interfaces of the masonry blocks because of the reduction of the useful section. The low rate of the actual contact is due to the geometric imperfections of the bed-joints and the low crushing or the hardening of the asperities in the contact interfaces. Indeed, the intrinsic properties of the materials coming in contact play a significant role in the increase of the actual contact in the bed-joints upon the loading. At the onset of the loading, only the pics of the bed-joints come in contact and the actual contact area increases with the compressive load. However, since the stiffness of the faces coming into contact is equal and very high, the surface asperities barely deform and the actual contact area increases slowly with the loading. This induces a local stress concentration in a few points of the masonry blocks, which at the end leads to an early collapse of the prisms at roughly 320 kN. Figure 62 (a) shows in red patches the distribution of the actual contact surfaces in the bed-joints of a masonry prism (test 3) of P-group 1. Among all the studied specimens, the higher level of actual contact reached is about 32% (Table 7). One can deduce that the low evolution of the actual contact is related to the intrinsic properties of the materials coming into contact, especially their Young's Modulus. Indeed, the high Young's Modulus of the surfaces coming into contact restrains the deformation of the bed-joints [12], which ultimately limits the accommodation of the DSM$_b$.

Table 7. Actual contact at the failure and ultimate load of the masonry prisms [122]

Mixture of the contact layer	Test number	Rate of the actual contact area "R_{ac}" [%]				Failure load [kN]	Mean actual contact [%]	Mean failure load [kN]	$\left(\frac{F_I}{F_N}\right)$
		1A	1B	2A	2B				
P-group 1 (without CL)	Test 1	32	24	25	22	323	23	320	-
	Test 2	22	32	22	24	315			
	Test 3	20	21	18	21	313			
	Test 4	22	20	19	18	318			
	Test 5	24	25	23	23	332			
P-group 2 (mix A)	Test 1	45	44	50	48	371	50	373	+ 1,16
	Test 2	43	45	46	47	367			
	Test 3	46	63	63	54	388			
	Test 4	58	52	49	64	380			
	Test 5	42	44	42	46	361			
P-group 3 (mix B)	Test 1	45	40	39	35	345	50	366	+ 1,14
	Test 2	44	51	53	55	350			
	Test 3	61	50	59	50	348			
	Test 4	52	52	71	60	411			
	Test 5	47	46	51	40	375			
P-group 4 (mix C)	Test 1	50	53	53	48	432	55	439	+ 1,37
	Test 2	53	49	64	57	446			
	Test 3	56	68	75	69	461			
	Test 4	52	49	52	49	425			
	Test 5	51	48	51	52	430			
P-group 6 (mix E)	Test 1	99	96	98	99	623	98	631	+ 1,97
	Test 2	99	99	99	96	664			
	Test 3	99	97	98	99	614			
	Test 4	99	97	98	97	625			
	Test 5	99	96	98	99	631			

Nomenclature used in this table:

F_N : Mean failure load of the R.DSM_b

F_I : Mean failure load of the considered P-group of I.DSM_b

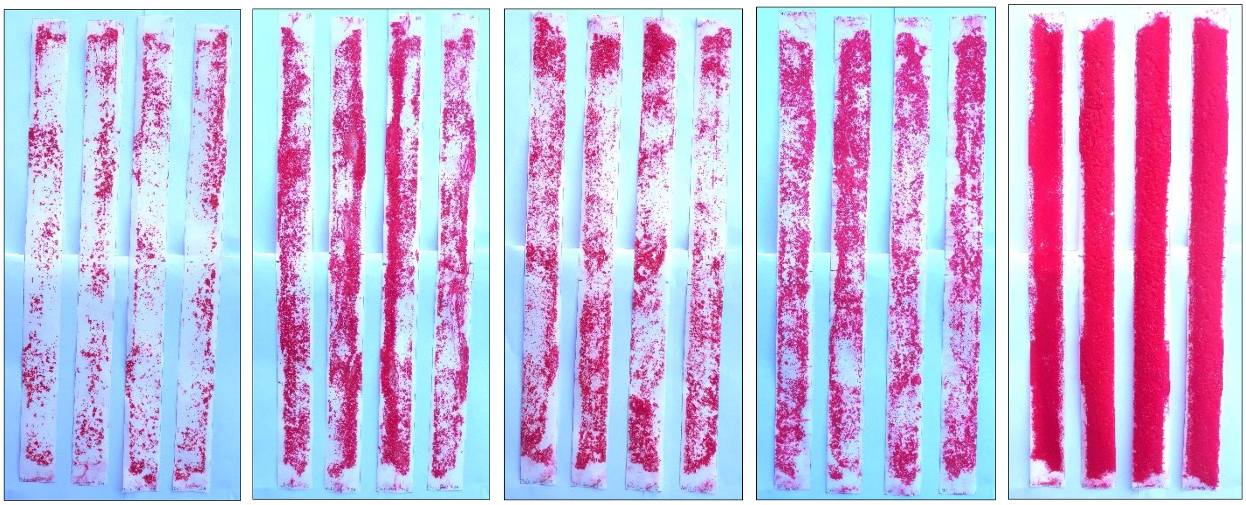
(a) (b) (c) (d) (e)

Figure 62. Actual contact in the bed-joints at the failure load (test 3).
(a) R.DSM$_b$; (b) improved with the mix A; (c) improved with the mix B; (d) improved with the mix C; (e) improved with the mix E [122]

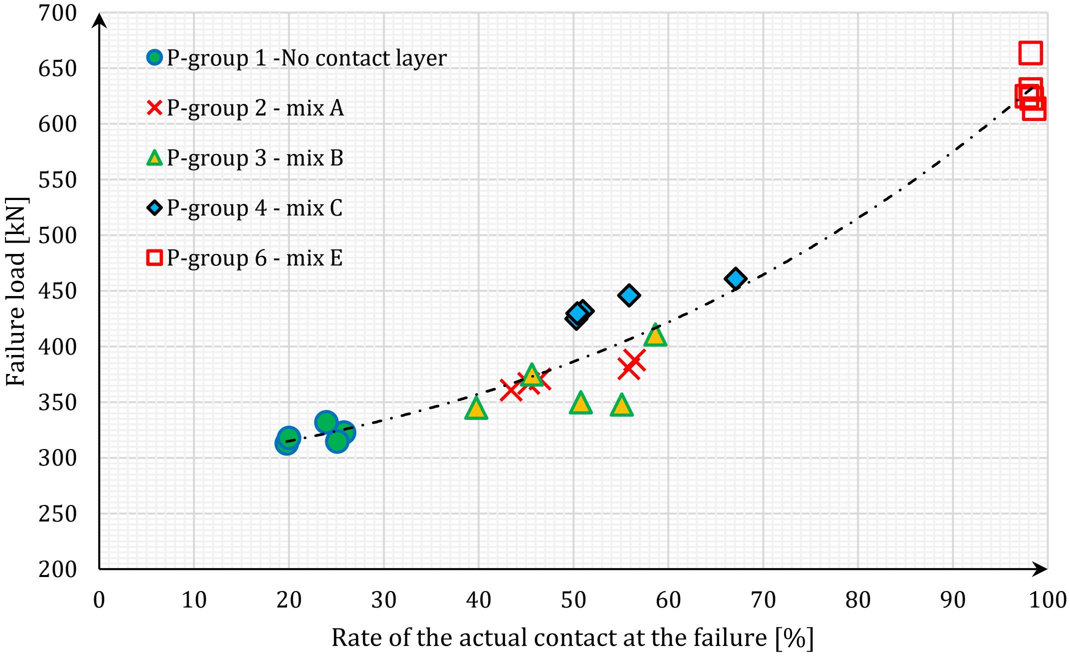

Figure 63. Failure load in function of the material of the contact layer – Mean rate of the actual contact in the bed-joints of the masonry prisms [122]

4.4.3.2 Prisms with the I.DSM$_b$

Following the tests on the masonry prisms built with the R.DSM$_b$, the same experimental tests were undertaken on the prisms built with the improved dry-stacked masonry blocks. For the masonry prisms of P-group 2 and 3, Figure 62 (b) and (c) show each a sample of the contact sensors with the footprints of the actual contact area in the bed-joints of the masonry blocks. The measurement of the actual contact area at the failure load shows that, when compared with the findings made on the prisms of P-group 1, a contact layer made with the mix A or mix B enables to double the rate of the useful section between the dry-stacked masonry blocks. Indeed, as shown in Table 7, a mean actual contact of 50% is reached in the bed-joints at the failure load. In other words, the compressive stress on the top course of the prisms is on average amplified in the bed-joint interfaces by a factor of 2,0 (1/0,50). The stress amplification factor in the bed-joints of the prisms of P-group 2 and 3 is reduced from 4,3 (P-group 1) to 2,0, thanks to the potential of the contact layer to easily deform under loading. However, in the bed-joints of the prisms of P-group 2 as in the bed-joints of the prisms of P-group 3, there is a relative variation of the actual contact between 40% and 60%. This amplitude of the variation comes from the irregular and non-repetitive roughness of the bed-joints of the masonry blocks from a masonry prism to another. Thus, depending on whether the surfaces coming in contact are more or less rough, the contact layer, by its intrinsic properties (especially its Young's Modulus), overcomes a part of the imperfections and thereby enlarges the actual contact surfaces. The improvement of the rate of the actual contact has a repercussion on the load-bearing capacity of the masonry prisms that is improved by 16% and 14% respectively in the P-group 2 and 3. As shown in Table 7, a mean failure load of 373 kN is reached for the prisms of P-group 2 and 366 kN for the prisms of P-group 3.

Concerning the masonry prisms of P-group 4, the mean rate of the actual contact reached in the bed-joints is slightly better than the one reached in the masonry prisms of P-group 2 and 3. Indeed, the explanation of this fact comes from the stress-strain behaviour of the mix C. Figure 49 shows that for a given compressive load, the deformation in the loading plane is greater for the mix C than for the mixtures mix A and mix B. This leads to the fact that during the loading, the asperities in the bed-joints of the prisms of P-group 4 flatten slightly faster than in the masonry prisms of P-group 2 and 3, and of course faster than in the masonry prisms of P-group 1. The crushing of the surface asperities leads to a reduction of the geometric imperfections, which contributes to an improvement of of the prisms' load-bearing capacity. The mean actual contact reached in the bed-joints of the masonry prisms of this P-group is about 55%, which thus limits the stress amplification factor in the contact interfaces of the masonry blocks to 1,8 (1/0,55) instead of 4,3 compared to the masonry prisms of P-group 1. Once again, the increase of the actual contact in the bed-joints has enabled to improve the load-bearing capacity of the masonry prisms to a mean value of 439 kN obtained out of five experimental tests. In comparison with the masonry prisms of P-group 1, the use of mix C in the contact layer led to an increase of the compressive strength by roughly 37%.

Regarding the masonry prisms of P-group 6, under loading, the contact layer completely levelled the surface unevenness, thereby ensuring an almost full contact between the dry-stacked masonry blocks. As shown in Table 7, from all the five tested masonry prisms and despite the irregular and the non-repetitive character of the surface roughness, the rate of the actual contact recorded in the bed-joints at the failure load of each prism is greater than 95% with a mean value of 98%. Figure 62 (e) shows an almost full contact reached in all the bed-joints of the masonry prisms thanks to a contact layer made of mix E. This also means that the compressive stress applied on the top faces of the masonry prisms was almost not amplified by the geometric imperfections in the bed-joints since the latter are well resorbed. The stress amplification factor in the bed-joints was roughly 1,02 (1/0,98) and the mean failure load reached about 631 kN, i.e. almost the double of the compressive strength of the masonry prisms of P-group 1. However, although ensuring the higher performance in compression compared to the masonry prisms of P-group 1 to 4, the masonry prisms of P-group 6 exhibited a significant settlement at the onset of the loading. Of course, the significant axial deformation at the onset of the loading is owed to the mix E whose 10 mm layer has been reduced to roughly 3 mm at the failure load. Indeed, the optimal height of the layer of P-group 6 has still to be investigated since 10 mm of mix E per joint give large vertical deformations.

Figure 63 reports the failure load of DSM-prisms in function of the mean rate of the actual contact in the bed-joints. As already mentioned, it is well established that the actual contact in the bed-joints has a great influence on the load-bearing capacity of the masonry prisms. Indeed, the load-bearing capacity of a masonry prism and the rate of the actual contact in the bed-joints exhibits a non-linear relationship. In a general overview, the increase of the actual contact in the bed-joint alleviates the stress concentration in the masonry blocks, which in turn enable the block units to better withstand the loads for a greater resistance of the masonry prisms.

4.5 Experimental tests on wallets

4.5.1 Description

DSM-wallets better reflect the actual behaviour of dry-stacked masonry wall compared to masonry prisms, as they include beside the effects of the bed-joint roughness also the blocks' height variation. These two effects are the main shortcomings of a dry-stacked system (Gumaste et al. [2], Fonseca et al. [3]). In this regards, the experimental tests in the first section were carried out on wallets constructed using dry-stacked masonry blocks (DSM_b). A local producer provided the raw DSM_b and the mixtures used to make the contact layer.

In sum, twenty (20) dry-stacked masonry wallets constructed using either raw or improved DSM_b were tested under axial compression for assessing the load-bearing capacity (P_u) and the load at which the first crack appears in the face-shells (P_{crack}). The complete test program on the wallets is given in Table 8. A first group of 4 DSM-wallets of 1,00 x 0,80 m^2 (W-group 1) constructed using raw masonry blocks were tested under axial compression for determining the reference load-bearing capacity P_u. Afterwards, sixteen (16) similar DSM wallets arranged in 4 W-groups of 4 wallets each depending on the contact layer material of the block units were also constructed and tested under axial compression. The results of the overall twenty (20) tested DSM wallets were compared to assess the effectiveness of the strategy in improving P_u of a wall. All the tested wallets were constructed following the scheme of Figure 64.a with 2 block units in the length and 4 courses, leading to a height to thickness ratio h/t of 4.

A thin capping material was placed on the top and the bottom faces of the wallets to ensure a uniform load transfer between the press plates and the tested wallets. Before subjecting each wallet to the axial compressive load, a hardening time of 24 hours was given for enabling the material developing its strength. Afterwards, the axial compressive load was generated using six hydraulic pistons capable of developing each up to 300 kN. An instrument control and a data acquisition software was also set up to support the testing machine. The compressive load was applied gradually at a rate of 1kN/s until the wallet failure.

Table 8. Test matrix on the wallets

Wallet group	Mixture of the masonry block's contact layer	Number of wallets tested
W-group 1	Without contact layer	4
W-group 2	mix A	4
W-group 3	mix B	4
W-group 4	mix C	4
W-group 5	mix D	4
W-group 6	mix E	-

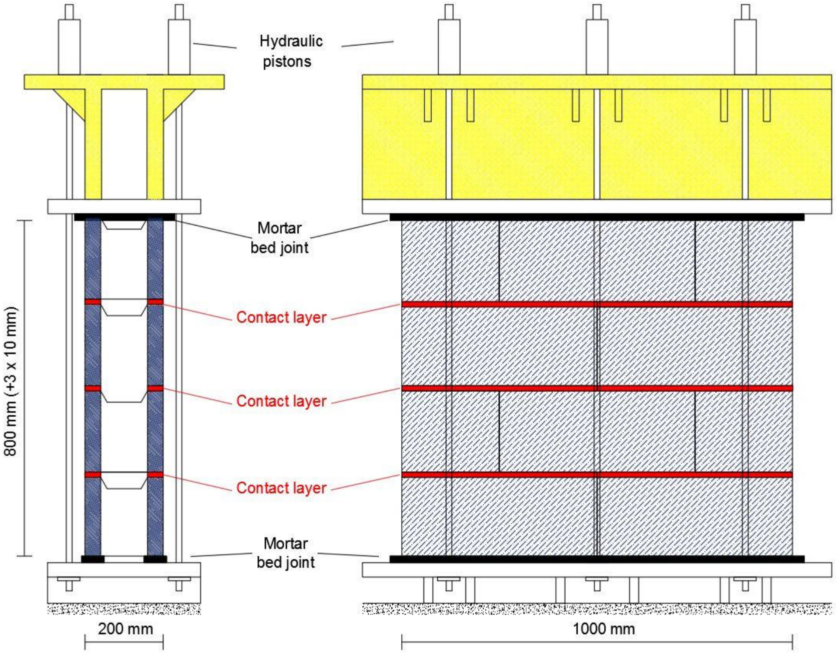

a) Sketch of the wallets tested

b) Walls tested in the laboratory

Figure 64. Experimental test [121]

4.5.2 Failure mechanism

Throughout the experimental tests, three damage mechanisms were observed in the wallets. In the following, the three damage mechanisms are presented and discussed in their order of appearance upon loading.

The first damage mechanism observed was the face-shell splitting, i.e. the appearance of first vertical cracks in the middle of the face-shells of the full masonry blocks. Figure 65.a-b shows the appearance of the first crack, corresponding to a face-shell splitting. This damage mechanism meets the one observed in [45,64,85] and is caused by the height variation of the block units. Indeed, the height variation between the masonry blocks in a course yields an uneven contact with the overlying course, which in turn leads to a stress concentration in some masonry blocks [70], predominantly in the middle of the face-shells [80,82] according to the overlapping of the blocks from one row to the next. As discussed in the next section, the face-shell splitting occurs between 17% and 92% of the load-bearing capacity of the wallets, depending on the material of the contact layer.

The second damage mechanism noticed was the ignition of vertical cracks mainly at the interface between the face-shells and the web-faces (Figure 65.c). This damage mechanism (web splitting), proper to the hollow dry-stacked masonry blocks, has been disclosed in a former numerical investigation [70]. Indeed, since the masonry blocks are loaded exclusively on their face-shells, shearing occurs at the interface between the face-shells and the web-faces. In addition, the lateral deformation of the face-shells in the bed-joints makes arise a tensile stress in the web-faces, which speed up the growing of the vertical crack at the interface between the webs and the face-shell. This damage mechanism occurs near the collapse of the wallets, almost at the same time as the third damage mechanism presented in Figure 65.d.

Finally, the third damage mechanism observed is the spalling of some sections of the face-shells around the bed-joint interfaces (Figure 65.d). Regarding the third damage mechanism, Figure 65.d also shows that the spalling of the face-shells mainly occur in the upper part of the bed-joint interfaces. The reason of the latter behaviour can be explained by the fact that the lateral expansion of the contact layer was less restricted on the top face than on the lower face due to the bonding between a masonry block and the underside of its associated contact layer [114]. In addition, this damage mechanism is caused by a local exceedance of the block material compressive strength, itself caused by the local stress concentration steaming from the "treelike" load percolation system [66,70,80,82] and the reduction of the actual contact in the bed-joints [49,55,62]. Indeed, as shown in Figure 66, DSM generally experiences local stress concentration related to the height difference between the block units. This local stress concentration explains the local face-shell spalling observed in Figure 65.d.

The damage mechanism observed was expected for dry-stacked masonry structures as the masonry courses were unevenly in contact and therefore unevenly loaded because of the height variation between the blocks. However, as discussed in the upcoming section, the timing of occurrence of the first crack was delayed for the wallets constructed with improved DSM_b. Nevertheless, this tendency was changed for the wallets for which the contact layer of the masonry blocks was made with the mix D. In the latter case, the second damage mechanism (crack at the interface web/face-shell) was predominant due to the significant lateral expansion of the low strength contact layer.

Figure 67 shows the failure mechanism of a wallet following the block unit damaging. In this singular test videotaped (aside the 20 other DSM wallets tested), contact sensors (Prescale Fujifilm strips) have been inserted in the dry bed-joints between the block units. The Prescale Fujifilm strips were inserted in this test for experimenting the treelike load percolation system. By analysing the Prescale Fujifilm strips retrieved after the wallet collapsing, it has been observed that some block units were only supported on a half of their length. This means that DSM actually suffers from a treelike load percolation system that can exist up to the failure load. In addition, as shown on Figure 67, the wallet has collapsed owing to the ignition and the progressive widening of cracks in the webs.

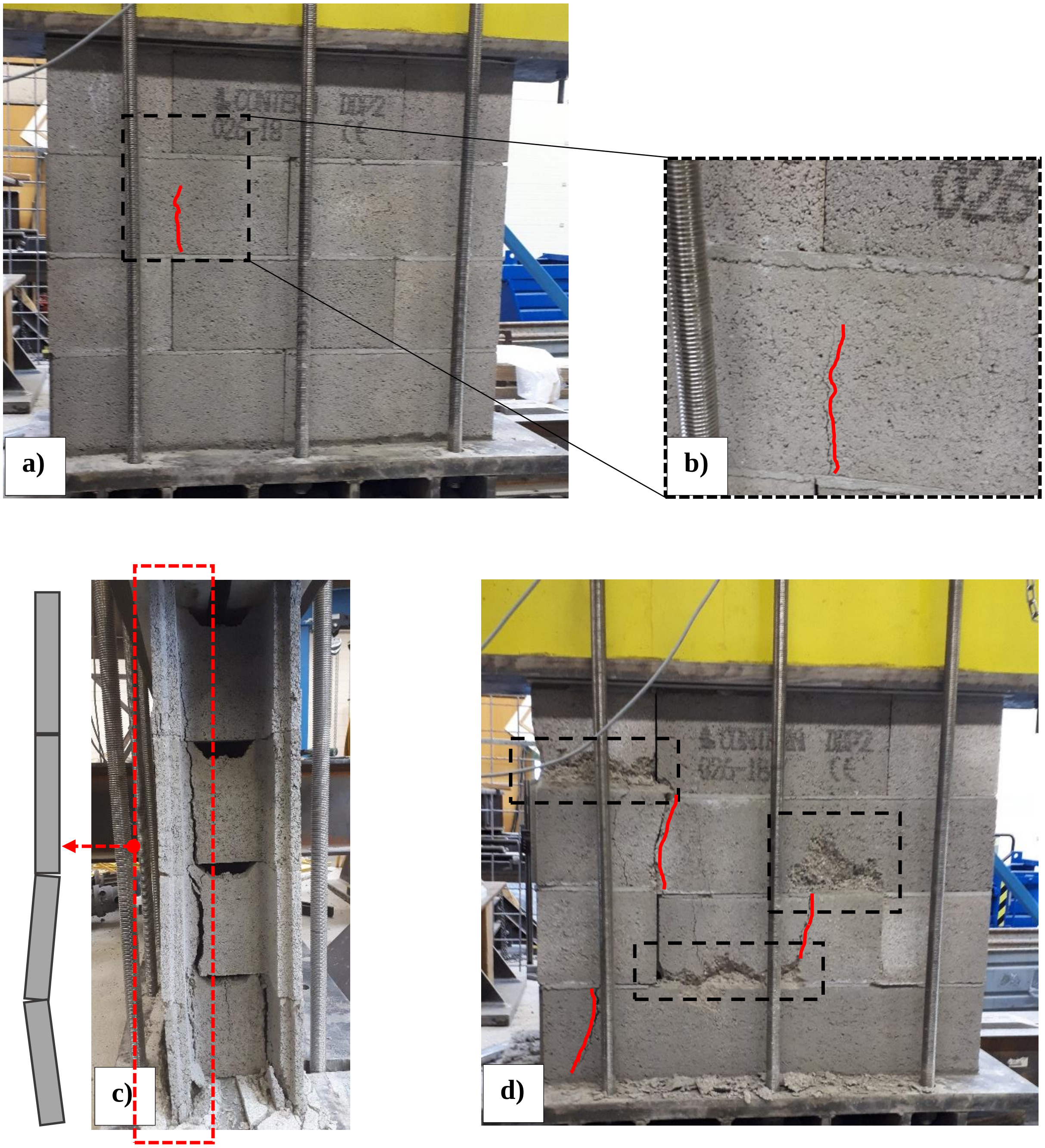

Figure 65. Damage mechanisms of the raw and the improved dry-stacked masonry wallets [121]

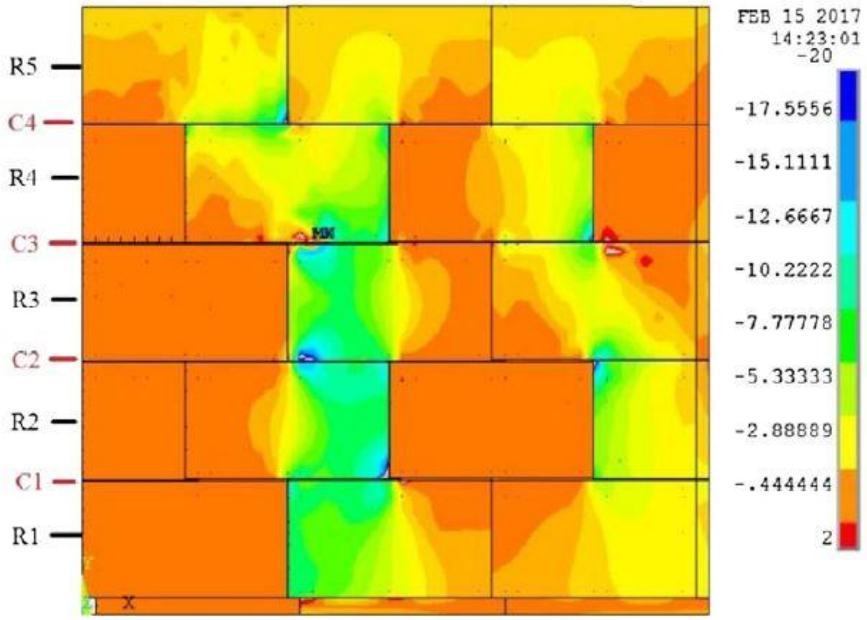

Figure 66. Treelike load percolation system in DSM [70]

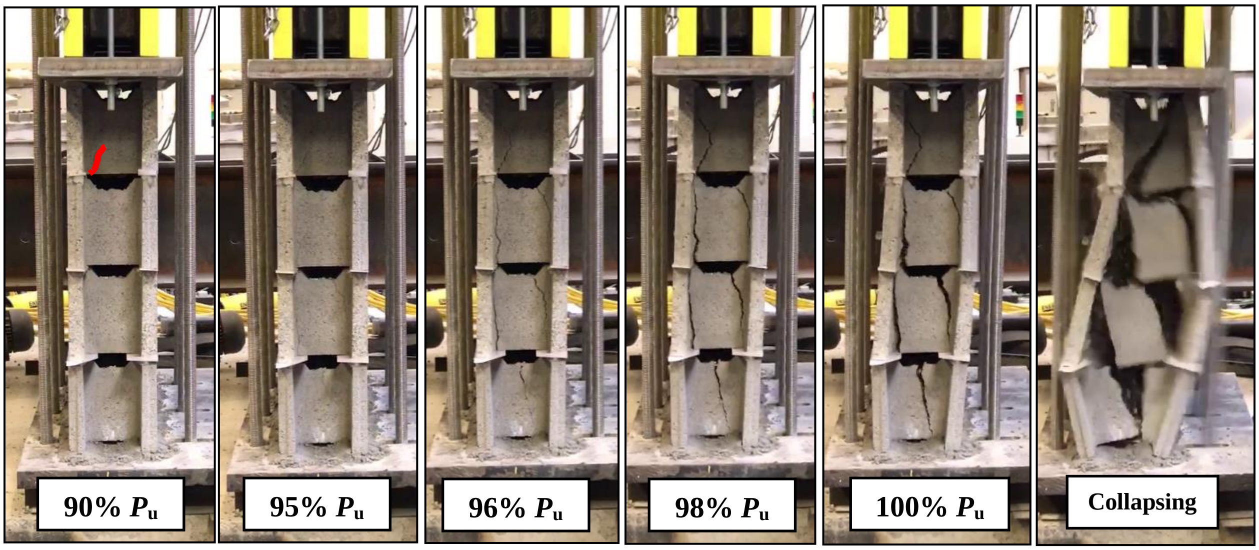

Figure 67. Failure mechanism of a dry-stacked masonry wallet [121]

4.5.3 Load-Bearing capacity

Table 9 presents the load-bearing capacity (P_u) reached by each tested wallet, as well as the load at which the first mechanism was observed, i.e. the face-shell splitting load (P_{crack}). The mean load-bearing capacity, the mean face-shell splitting load and their respective coefficient of variation (COV) were calculated for each W-group of four wallets and the results are also summarized in Table 9. Furthermore, an efficiency factor (Table 10) was calculated by reporting the mean load-bearing capacity and the mean face-shell splitting load of the wallets of W-groups 2-6 to the ones of W-group 1.

As shown in Table 9, the results of the experiments show that the wallets of W-group 1 exhibit a face-shell splitting load P_{crack} varying between 0,60 N/mm^2 and 3,60 N/mm^2, which represents 17 to 92 % of P_{u}. In addition, when compared to the wallets of the other W-groups, it is observed that the wallets of W-group 1 exhibit the lowest face-shell splitting load (17 % of P_{u}) and the highest coefficient of variation of P_{crack} (COV of 80,3 %). The wide range of variation of P_{crack} results from the unmitigated effect of the random height variation between the adjacent masonry blocks in the wallet courses. Indeed, as highlighted in [70,80], the unpredictable height variation between the DSM$_{\text{b}}$ imposes an initial load percolation system in the wallet. The initial distribution of the masonry block's height could be more or less tight, reducing the actual contact in the bed-joints from a full contact to a point contact [80] and leading finally to a stress concentration in some masonry blocks. This phenomenon explains the premature face-shell cracking observed in some cases. The face-shell cracking is followed by a differential settlement in the wallet courses, which in turn leads to an increase of the actual contact in the bed-joints and a load redistribution in the wallet. The wallets of W-group 1 showed a mean load-bearing capacity of 3,66 N/mm^2 which is taken as reference load-bearing capacity throughout the discussion.

Like for the block compressive strength [17,18], the Young's modulus of the contact layer has two opposite effects on the load-bearing capacity of DSM. (1) The decrease in the Young's Modulus of the contact layer increases the axial deformation in the bed-joints, accordingly higher bed-joint imperfections levelling, higher actual contact, better stress distribution and higher load-bearing capacity of DSM wall are expected. At the same time, (2) the decrease in the Young's Modulus of the contact layer increases the lateral tensile stress induced in the block units and, consequently, is expected to reduce the load-bearing capacity of DSM wall.

In regards to the wallets of W-group 2 made with the DSM$_{\text{b}}$ improved with mix A, it is observed that the average strength at which the face-shells cracked is about 2,09 N/mm^2

with a COV of 10,1 %. These wallets reached a mean load-bearing capacity of roughly 3,70 N/mm^2, i.e. almost the same with respect to the wallets of W-group 1. This means that the use of mix A in the contact layer has no influence or solely a very slight influence on the ultimate load-bearing capacity of the wallet. Indeed, it is deduced that the improvement in the stress distribution generated by the levelling effect of the contact layer of a medium Young's Modulus (11500 MPa) was cancelled by the lateral tensile stress induced in the blocks by the same contact layer. However, if the face-shell splitting loads of the wallets of W-group 2 are reported to their respective ultimate load-bearing capacity, it is found that the first crack in the face-shells occurred around 51% to 62% of P_u.

Concerning the wallets of W-group 3 made with the DSM$_\mathrm{b}$ improved with mix B, the mean face-shell splitting load P_crack reached 2,79 N/mm^2 with a COV of 14,4 %, i.e. on average 43% of improvement with respect to the wallets of the first group (W-group 1). Over the four wallets tested in W-group 3, it is observed that P_crack varies from 66% to 78 % of P_u. When comparing this latter range (66 to 78 % of P_u) to the one observed in W-group 1 (17 to 92 % of P_u), one may state that the use of a contact layer made of mix B enabled increasing the actual contact area in the bed-joints of the wallets. This has also been observed regarding the DSM-prisms of W-group 3 (section 4.4.3). Indeed, the Young's Modulus of mix B (10500 MPa) enables increasing the axial deformation of the contact layer, which leads to a better levelling of the bed-joint imperfections and an increase of the actual contact in the bed-joints. The increase of the actual contact area leaded to a better stress distribution in the wallets, which has delayed the face-shell splitting and slightly improved the load-bearing capacity. Indeed, it is observed that the wallets of W-group 3 showed a mean load-bearing capacity of about 3,88 N/mm^2 with a COV of 6,7 %, i.e. a mean increase of 6,1 % with respect to the wallets of W-group 1. Once again, the positive effect of the contact layer's Young's Modulus on the increase of the actual contact, on the improvement of the stress distribution and therefore on the load-bearing capacity, was altered by the lateral tensile stress induced in the block units.

Regarding the wallets of W-group 4 made with the DSM$_\mathrm{b}$ improved with mix C, one notes that the face-shell splitting of the masonry blocks occurred on average at 3,94 N/mm^2, i.e. at around 82 % of P_u. Over the four wallets tested, it is observed that P_crack varies between 74 and 87 % of P_u. Once again, the increase of the lower bound of the P_{crack} / P_u ratio witnesses the effectiveness of a contact layer of well-defined properties in improving the actual contact area in the bed-joints for a more uniform stress distribution in the wallets. This ascertainment supports the observation made in W-group 2 and 3 regarding the trend of evolution of the P_{crack} / P_u ratio. In terms of load-bearing capacity, the wallets of W-group 4 have reached on average 4,83 N/mm^2 with a COV of 8,3 %, i.e. a mean increase of 31,9 % with respect to the wallets of W-group 1. Indeed, the positive effect of the contact layer's Young's Modulus (7000 MPa) on the increase of the actual contact, on the improvement of the stress distribution and therefore on the load-bearing capacity, was more significant than its negative effect of inducing lateral tensile stresses in the block units.

In regards to the wallets of W-group 5 made with the DSM_b and improved with mix D, the face-shells splitting occurred at around 1,51 N/mm^2, i.e. earlier than in the wallets of W-group 1. In addition, the wallets of W-group 5 collapsed at a compressive stress of 2,15 N/mm^2, i.e. 41,3% below the load-bearing capacity of the wallets of W-group 1. This drop of resistance is a consequence of the significant lateral tensile stresses induced in the block units by the low strength material of the contact layer. Indeed, as similarly observed in the field of bonded masonry [18,20,21,24,43,115,116], weak mortars yield significant localised tensile stresses in the block units, which weakens the load bearing capacity of the overall masonry wall. Indeed, the positive effect of the contact layer's Young's Modulus (3000 MPa) on the increase of the actual contact and furthermore the load-bearing capacity, was far below the negative effect of inducing significant lateral tensile stresses in the block units.

Table 9. Load-bearing capacity of the wallets with the raw and the improved DSM_b [121]

Wallet - Mixture of the contact layer	Test number	P_{crack} [N/mm^2]	Average(1) P_{crack} [N/mm^2]	COV^a	P_u [N/mm^2]	Average(2) P_u [N/mm^2]	COV^b	P_{crack} / P_u
W-group 1 Without CL	1	2,95	1,94	80,3%	3,47	3,66	4,9%	53%
	2	0,60			3,60			
	3	0,63			3,68			
	4	3,60			3.90			
W-group 2 CL - Mix A	5	2,00	2,09	10,1%	3,57	3,70	3,0%	56%
	6	2,40			3,83			
	7	2,05			3,67			
	8	1,93			3,73			
W-group 3 CL - Mix B	9	2,55	2,79	14,4%	3,75	3,88	6,7%	72%
	10	2,40			3,60			
	11	3,30			4,20			
	12	2,90			3,96			
W-group 4 CL - Mix C	13	3,63	3,94	6,1%	4,61	4,83	8,3%	82%
	14	4,02			5,40			
	15	4,20			4,80			
	16	3,90			4,52			
W-group 5 CL- Mix D	17	0,60	1,51	40,2%	1,95	2,15	10,6 %	70%
	18	1,80			1,97			
	19	1,83			2,41			
	20	1,81			2,28			
W-group 6 CL- Mix E	-	-	-	-	-	-	-	-
	-	-			-			
	-	-			-			
	-	-			-			

P_{crack} : face-shell splitting load , e.g. load at which a vertical crack appears in a face-shell

P_u : ultimate load-bearing capacity

COV $^{a, b}$: coefficient of variation of the mean value of P_{crack} and of P_u

Table 10. Wallets efficiency [121]

	W-group 1 Without CL	W-group 2 CL – mix A	W-group 3 CL – mix B	W-group 4 CL – mix C	W-group 5 CL – mix D	W-group 6 CL – mix E
Face-shell splitting load P_{crack}	reference load	+7,7 %	+43,8 %	+ 103%	- 22,2%	-
Load-bearing capacity P_{u}	reference load	+1,0 %	+6,1 %	+ 31,9%	- 41,3%	-

4.6 Summary

In the current chapter, the actual contact between the block units and in-plane load-bearing capacity of dry-stacked masonry have been investigated. The use of a precast contact layer placed on the bed-joint faces of the raw masonry blocks was considered as mitigation strategy to overcome the effects of the block imperfections. The experimental investigations on dry-stacked masonry prisms and wallets made of raw and improved block units have evidenced the substantial capacity of a contact layer to (1) overcome the bed-joints imperfections, (2) improve the actual contact area in dry-stacked masonry, and (3) improve the resulting load-bearing capacity. The experimental tests also emphasised the capacity of a contact layer for delaying the occurrence of vertical cracks in the face-shell of the block units in DSM. Furthermore, it has been found that auxetic low strength material is very effective to fully mitigate the effects of the block imperfections and to significantly increase the load-bearing capacity of DSM. In addition, it has been also confirmed that conventional low strength material significantly reduces the load-bearing capacity of masonry structures in general. More insights on the effects of the block imperfections will be provided in the finite element analysis presented in the following chapter.

5 Numerical investigation of the effectiveness of a contact layer in dry-stack masonry

This chapter is based on the work published in the following research paper:

- *Gelen Gael Chewe Ngapeya, Danièle Waldmann, Frank Scholzen, Impact of the height imperfections of masonry blocks on the load bearing capacity of dry-stack masonry walls, Construction and Building Materials 165 (2018), 898-913.*

5.1 Introduction

Numerical models provide an efficient means for predicting the mechanical response of a dry-stack masonry system without the need for several experiments. In this section, a 3D finite element model (3D FEM) developed and performed on the software ANSYS.17 (APDL) is exploited for computing the load-bearing capacity of dry-stacked masonry systems, while including the impact of the blocks imperfections (bed-joint roughness and height variation). The 3D FEM is also exploited for analysing the impact of the block imperfections on the stress distribution in a dry-stacked masonry system. Furthermore, the 3D FEM is used for investigating the capacity of an additional layer (labelled the contact layer) placed on top of the DSM-blocks in order to level the block imperfections and to regulate the stress distribution in a wall increasing ultimately its load-bearing capacity. In a general overview and as pointed out by K. Andreev et al. [24], the stress needed to close the gaps in the bed-joints is proportional to the material stiffness: the higher the material stiffness, the higher is the stress needed to close the gaps. Finally, the 3d FEM is exploited to capture the local behaviour of the bed-joints in a dry-stacked masonry system and provide more explanation to the damage and the failure mechanisms observed during the experimental tests. The numerical analysis was performed on another masonry as the one that has been developed with the industrial partner "Lëtzebuerger Contern", because there was not yet enough M-Blocks (the developed block) to perform all the experimental tests. An overview of the numerical investigations carried out on single blocks, on masonry prisms and on wallets is presented in the Summary table 2.

Summary table 2. Overview of aspects investigated by numerical analysis.

		Finite element approach
Single block	M-block	Compressive strength
	Simple block	Compressive strength, load cases
Masonry prisms (with the simple block)	P-group 1 (no add. layer)	Load-bearing capacity, contact surface, stress distribution, stress-strain behaviour, imperfections
	P-group 2 (layer mix A)	Load-bearing capacity, contact surface, stress distribution, stress-strain behaviour, imperfections
	P-group 3 (layer mix B)	Load-bearing capacity, contact surface, stress distribution, imperfections
	P-group 4 (layer mix C)	Load-bearing capacity, contact surface, stress distribution, stress-strain behaviour, imperfections
	P-group 5 (layer mix D)	Load-bearing capacity, contact surface, stress distribution, stress-strain behaviour, imperfections
	P-group 6 (layer mix E)	Load-bearing capacity, contact surface, stress distribution, imperfections
Masonry wallets (with the simple block)	W-group 1 (no add. layer)	Load-bearing capacity, contact surface, stress distribution, imperfections.
	W-group 2 (layer mix A)	-
	W-group 3 (layer mix B)	-
	W-group 4 (layer mix C)	Load-bearing capacity, contact surface, stress distribution, imperfections.
	W-group 5 (layer mix D)	Load-bearing capacity, contact surface, stress distribution, imperfections.
	W-group 6 (layer mix E)	-
Masonry prisms (with the M-block)	P-group 7 (layer mix F)	Contact area, stress distribution, imperfections
	P-group 8 (layer mix G)	Contact area, stress distribution, imperfections
	P-group 9 (layer mix H)	Contact area, stress distribution, imperfections
	P-group 10 (layer mix I)	Contact area, stress distribution, imperfections

5.2 Finite element Modelling

5.2.1 Failure criterion and concrete damage model

The Finite Element analysis is done through a 3D modelling of the dry-stacked masonry block on the software ANSYS, using the cubic element Solid65 which is suitable to define the damage model of reinforced and unreinforced concrete.

5.2.2 Masonry block modelling

The masonry block was modelled using the script language "ANSYS Parametric Design Language", known in the short name APDL. Since the software does not imposed default units, the length units were set in millimetres [mm] and the stress in Newton per millimetres square [N/mm^2]. The geometric characteristics of the masonry block used in the experimental tests being already defined, solely the height of the masonry was parametrized to be able to define a specific height to each block. Thus, the parameter ΔH was used to define the difference between the nominal height and the actual height of a masonry block. As shown in Figure 68, the parameter ΔH can be positive or negative, depending on whether the actual height of the masonry block is higher or lower than the nominal height.

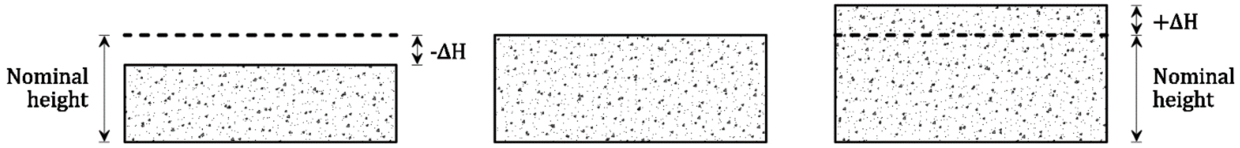

Figure 68. Contact pairs and link elements in the bed-joints of DSM

5.2.3 Contact interface modelling

One of the main features of the horizontal joints of the dry-stacked masonry blocks is the variation of the rate of the actual contact between the superposed courses. In order to take into account this feature, the contact interfaces between the masonry blocks were modelled using both the springs (LINK180) and the contact elements (Conta174/Targe170) of the ANSYS software (Figure 70 and Figure 69).

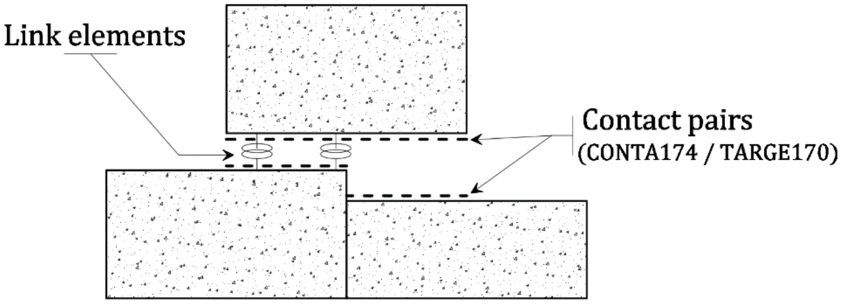

Figure 69. Contact pairs and link elements in the bed-joints of DSM

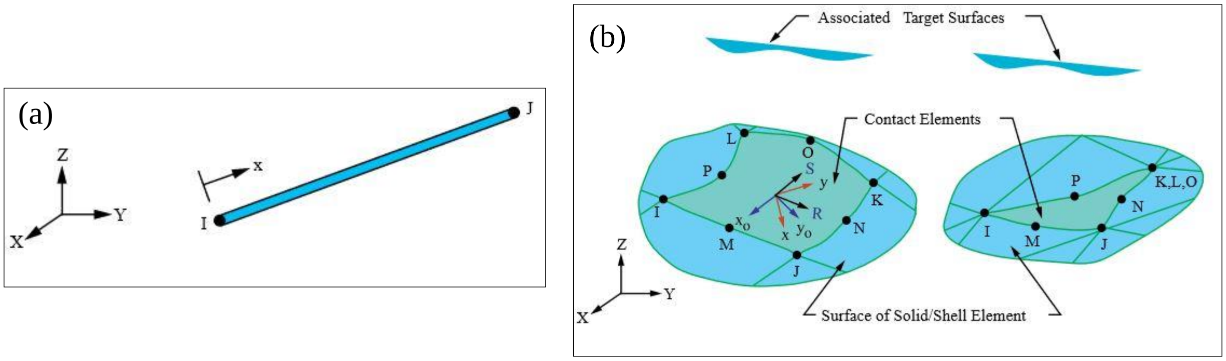

Figure 70. Spring (a) and Contact (b) elements [113]

- Contact pairs (Conta174/Targe170)

The paired contact elements (Conta174/Targe170) were defined between the faces of the masonry blocks intended to come into contact upon loading. The contact elements Conta174 were affected to the deformable surfaces while the target elements Targe170 were affected to the rigid surfaces. The contact pairs supplies a scheme for ensuring a proper load transfer between the DSM-blocks coming into contact, according to the normal and the tangential stiffness. The normal contact stiffness of each element of the contact pair (CONTA174 and TARGE174) was identical to the normal stiffness of the body to which the contact element belong. The tangential contact stiffness for representing the sliding was governed by the Mohr-Coulomb criterion [49, 63, 72, 83, 90, 92]. The paired contact elements support the Coulomb friction and allow sliding when the shear stress exceeds τ_{lim}. The threshold beyond which the sliding occurs is defined by $\tau_{\text{lim}} = \mu\sigma + c$, where μ represents the friction coefficient, σ the normal contact stress and c the contact cohesion. However, as the investigations address the behaviour of DSM-walls, the contact cohesion was set close to zero ($c = 0{,}01$). The friction coefficient was set to $\mu = 0{,}6$ [72, 119-120].

- Link elements (Link180)

In addition to the contact pairs, link elements were purposely added in the initial “closed bed-joints” of the DSM-walls. This was done for connecting the masonry blocks and for taking into account the opening existing in the “closed bed-joints” before the loading. LINK180 is a uniaxial tension compression element with two nodes, including plasticity, rotation and large strain capabilities. Each node of the element offers three degrees of freedom in translation following the main axes (x, y, and z) of the 3D model. The stress-strain response of the link element (LINK180) was set in a way to provide a very low compression strength and a null tensile strength (Figure 71). Thereby, although connected with each other, in case of existence of gaps in the bearing face, a masonry block of the wall has the possibility to rotate in the loading plane without being held by the spring elements.

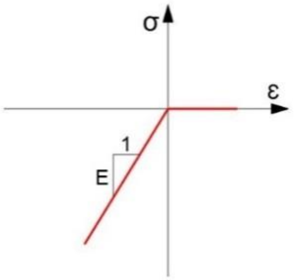

Figure 71. Shows the stress-strain behaviour defined for the link element LINK180 [70].

Like in the investigations of Ben Ayed et al. [49], Gasser et al. [63], Hongjun et al. [72], Lourenço et al. [83], Zuccarello et al. [92] and Bui et al. [93], the Mohr-Coulomb’s friction law was used for modelling the contact behaviour in the bed-joints. Indeed, as shown in section 2.4.3.5, it accurately describes the dry-joint behaviour in dry-stacked masonry.

5.2.4 Modelling sequence

The modelling sequence used for studying both masonry prisms and wallets is depicted in Figure 72. Different written function scripts using the APDL language have been defined for modelling the masonry blocks and meshing them, for adding the link elements in the close bed-joints and for defining the contact pairs in the bed-joints of the wallets. For capturing the progressive damage of the masonry, the applied load was progressively increased in load steps. The failure criterion was checked for each finite cubic element following a loading step. Then, the stiffness of each finite cubic element whose failure criterion has been exceeded was defined as zero before moving to the next loading step. For this analysis, a function script was also written.

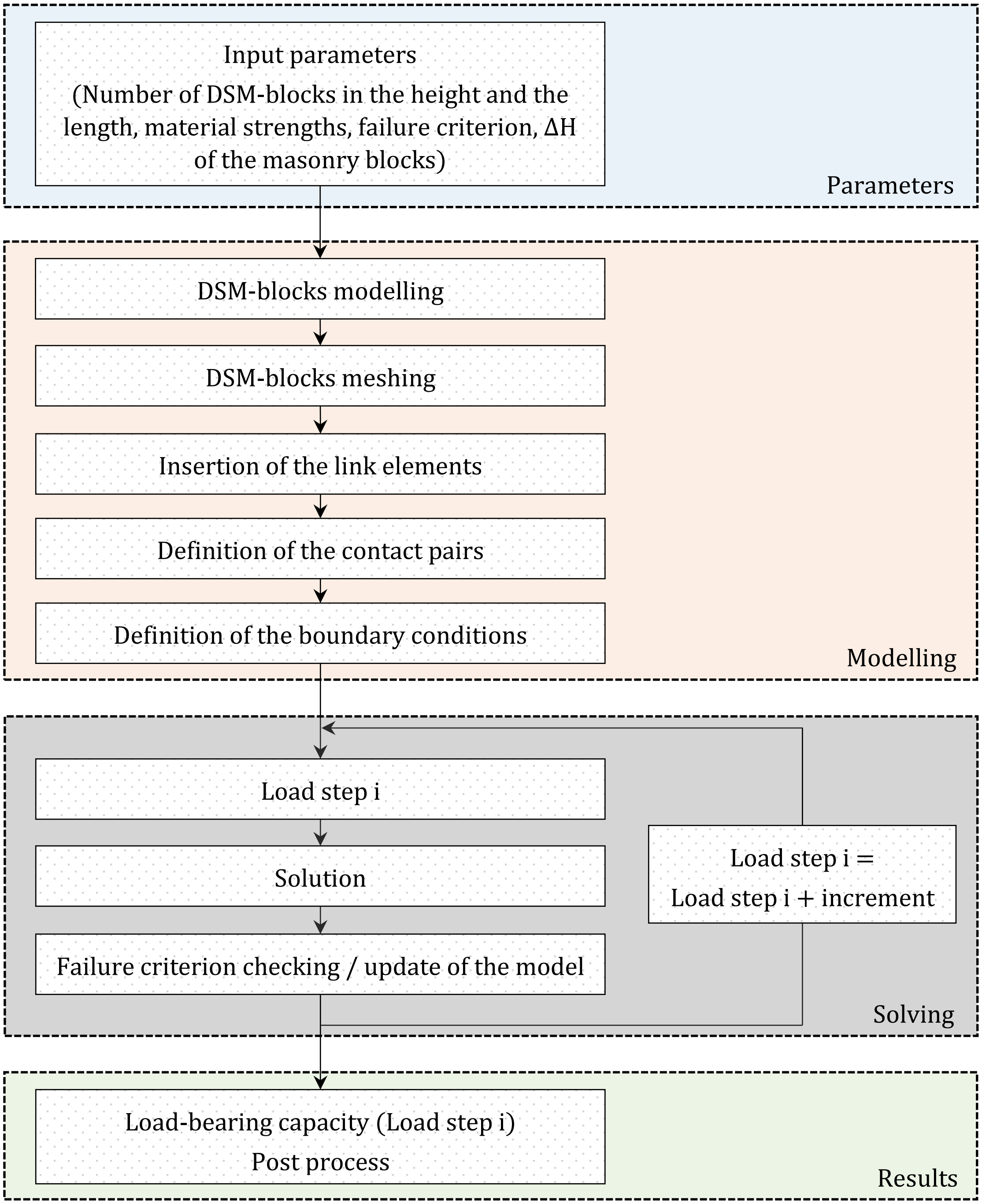

Figure 72. Sequence of the finite element simulation

5.3 Effect on the bed-joint roughness – Finite element model of masonry prisms

5.3.1 Model design

The numerical investigation aims to study both the influence of the bed-joint roughness on the stress distribution in dry-stacked masonry and the capacity of a contact layer for levelling this imperfection. For this purpose, the masonry prism previously tested was modelled. The material properties of the different contact layer have been defined in section 4.2.2 (Table *5*).

In order to carry out a comparative analysis of the capacity of the contact layer for levelling the bed-joint roughness, a basic bed-joint roughness was defined in the first and the second course interface for all the masonry prisms studied. In addition, for reducing the CPU-time and considering the symmetry behaviour of the masonry block, a quarter part of the masonry prism was modelled and a symmetry-plane was defined about the x-axis at x = 250 mm, and about the z-axis at z = 100 mm (Figure 73).

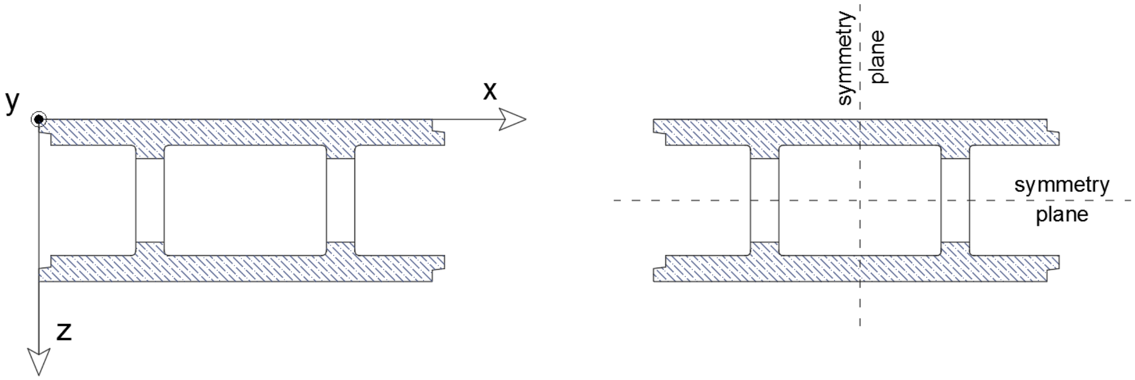

Figure 73. Ground view of the masonry prism with the symmetry planes

The modelling of the bed-joint roughness of the masonry blocks (Figure 74) was realised as follows:

1. The maximum height of the asperity peaks was defined with the parameter z_S.
2. The asperity peaks were defined at a regular distance of 10 mm over the block contact surfaces.

3. The height of the asperity peaks was randomly generated without exceeding the maximum height z_s.
4. The asperity was defined by raising some nodes of the contact faces of the masonry blocks [55].

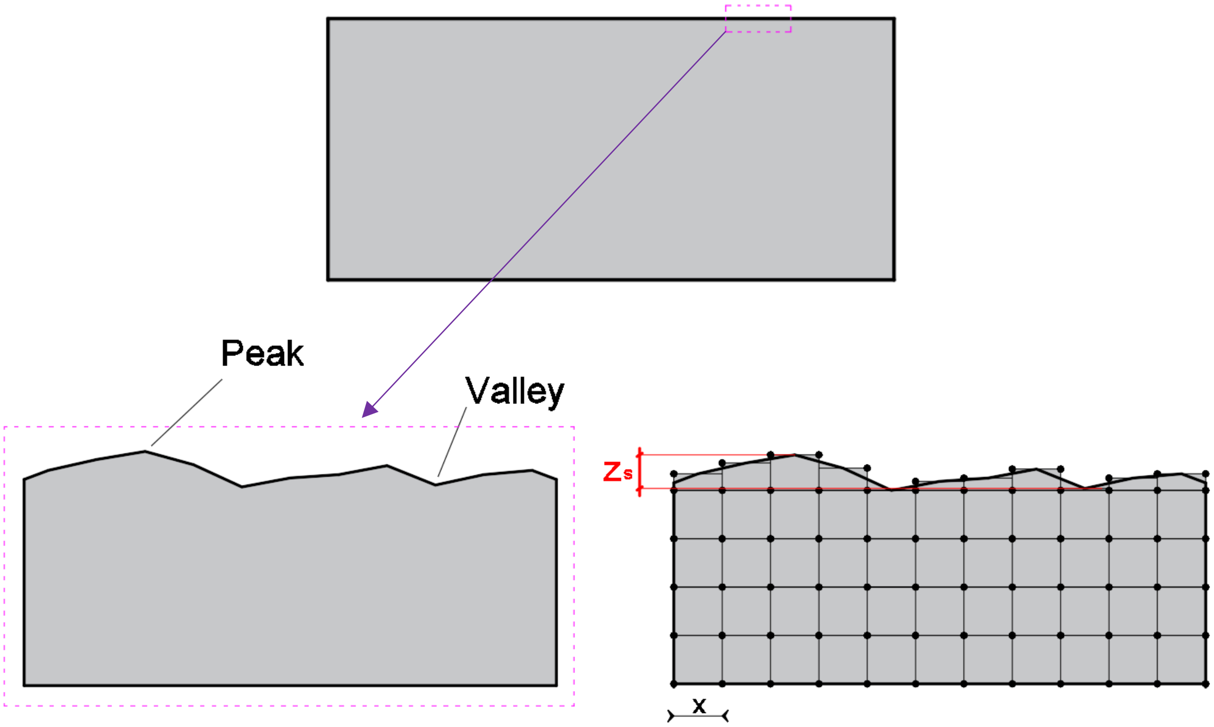

Figure 74. Illustration of the periodic distribution of the asperities forming the surface roughness on a masonry block

Figure 75 shows a masonry prism with its bed-joints and the gaps generated by the bed-joint roughness of the masonry blocks. A basic contact layer thickness of 10 mm was defined as in the experimental tests.

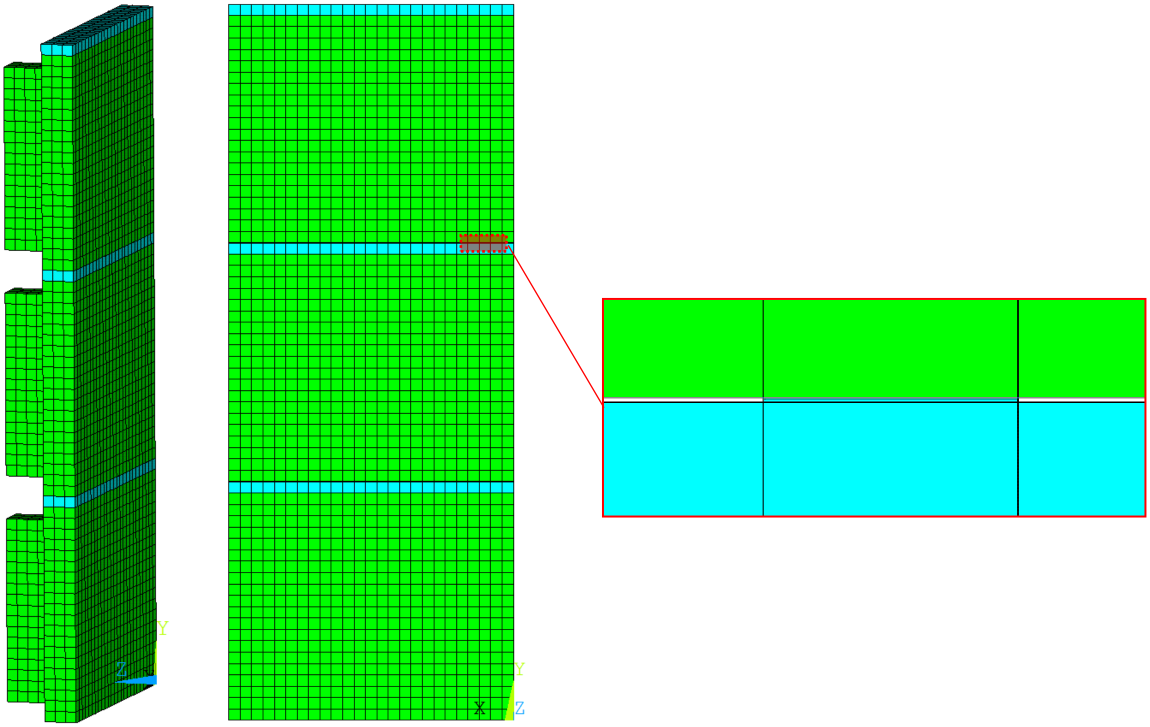

Figure 75. Dry-stacked masonry prism with uneven contact generated by the bed-joint roughness

The normal displacement was restrained at the base of the masonry prism ($u_y = 0$), as well as the displacements u_x and u_z on the edge nodes. A uniform load was applied on the top face of the masonry prism. Paired-contact surface elements Conta174 and Targe170 of the ANSYS 17 package [113] were used for defining the contact interfaces in the bed-joints.

5.3.2 Numerical results

For the sake of clarity in the discussion of the results, the reference masonry prism is taken as being the masonry prism made with the raw DSM-blocks. The load-bearing capacity of the masonry prism experimentally and numerically determined are respectively labelled $P_{\text{u. EXP}}$ and $P_{\text{u. FE}}$. In addition, the load-bearing capacity of the reference masonry prism (i.e. the masonry prism of P-group 1) is labelled $P_{\text{u. EXP-Réf}}$ and $P_{\text{u. FE-Réf}}$. The discussion is conducted between the masonry prisms of P-group 1, 4 and 6, as the masonry prisms of P-group 2, 3 and 5 did not present valuable improvements for engineering purposes. Nevertheless, the results regarding the masonry prisms of P-group 2, 3, and 5 are also presented in Table 11 (stress peaks, maximum actual contact and load-bearing capacity).

5.3.2.1 Influence of the contact layer on the stress distribution

The state of the actual contact area in the interfaces of the masonry prism of P-groups 1, 4 and 6 at 95% of $P_{\text{u. FE. Réf}}$ is presented in Figure 76. The resulting stress distribution in the contact interfaces is presented in Figure 77 and in Figure 78. In Figure 77, the stress distribution is presented by using for all figures the scale imposed by the masonry prism of P-group 1. This enables to compare the intensity of the stress peaks and the stress distribution in the contact interfaces of the masonry prisms of P-groups 4 and 6 with respect to the masonry prism of P-group 1. In Figure 78, the same stress distribution in the contact interfaces is presented, however here a scale normalised per group of masonry prism is used. This enables to well highlight the actual stress distribution and the stress pics for each P-group of masonry prism.

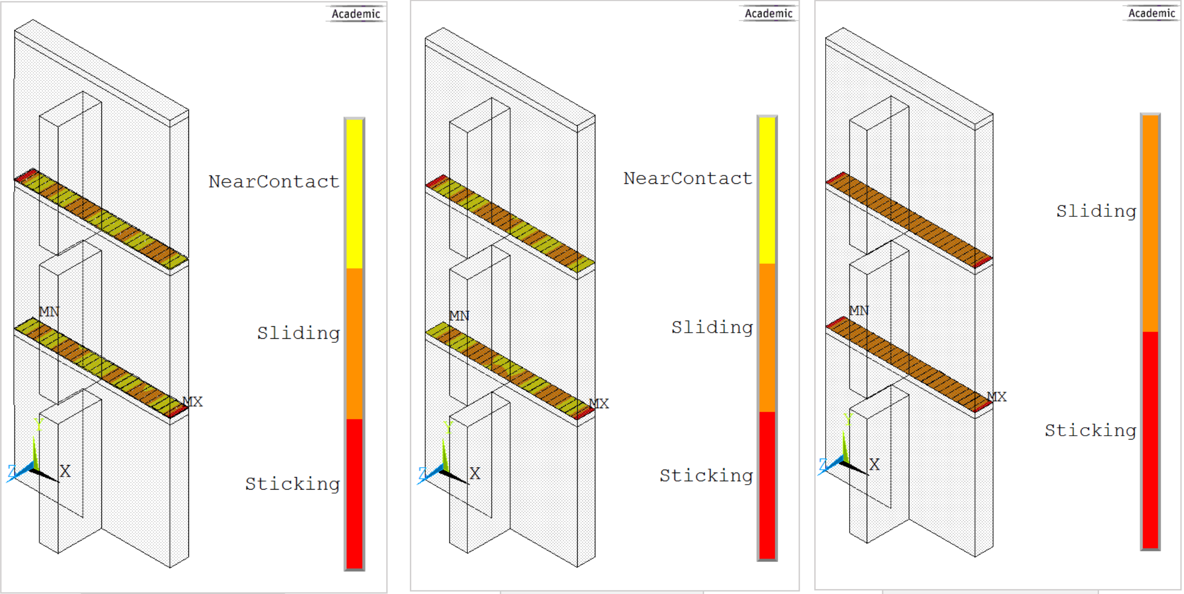

P-group 1

P-group 4

P-group 6

Figure 76. State of the actual contact in the DSM-prisms at 95% of $P_{\text{u. FE-Réf}}$

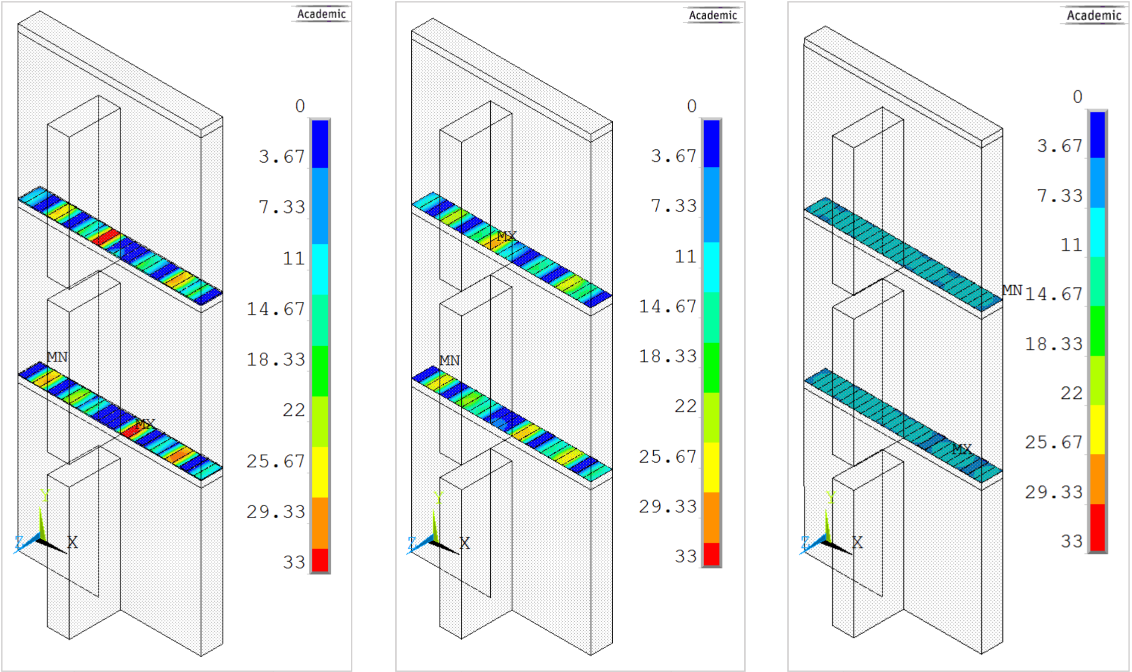

P-group 1 P-gGroup 4 P-group 6

Figure 77. Stress distribution in the contact interfaces of the DSM-prisms at 95% of $P_{\text{u. FE-Réf}}$

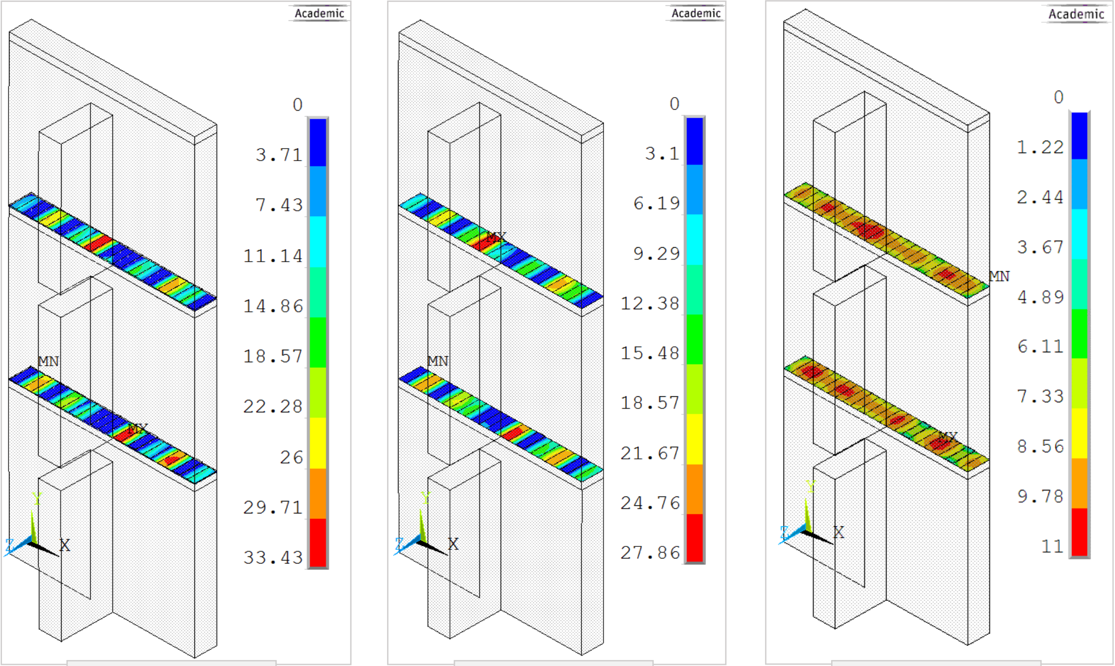

P-group 1 P-group 4 P-group 6

Figure 78. Stress distribution in the contact interfaces of the DSM-prisms at 95% of $P_{\text{u. FE-Réf}}$.
(Scale normalised for each group of masonry prism)

Finally, the stress distribution over the whole height of the masonry prism of P-group 1, 4 and 6 is presented in Figure 79.

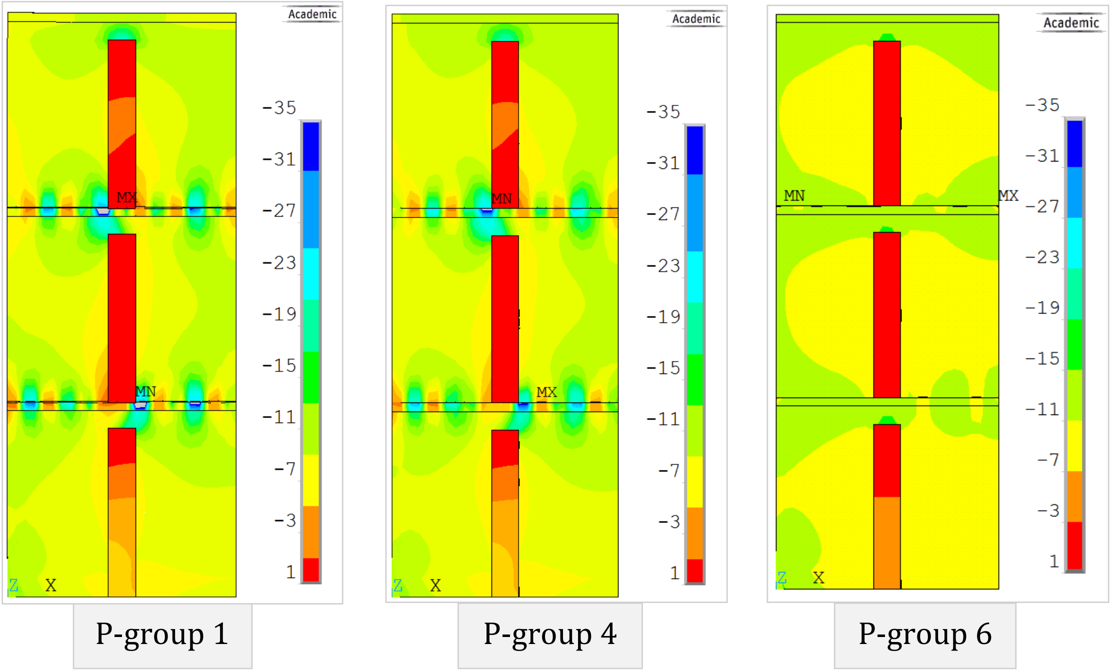

Figure 79. Stress distribution over the height of the DSM-prism at 95% of $P_{\text{u. FE-Réf}}$

- Masonry prism of P-group 1 (without contact layer).

It is observed that the compressive stress is strongly unevenly distributed in the bed-joints, because of a very low actual contact between the DSM-blocks. Indeed, as the masonry blocks are dry-stacked and without any contact layer, only few asperity peaks come into contact. Then, under loading, as the contacting materials have a high and a similar Young's Modulus, the asperity peaks coming into contact only slightly deform, which results in a limited closure of the bed-joints. Accordingly, the actual contact remains low in the bed-joint (around 38% of the full surface) and the stress peaks arise in the few contacting surfaces. Up to 95% of $P_{\text{u. FE-Réf}}$, a wide variation of the compressive stress is still observed over the contact interfaces. The stress peaks almost reach the compressive strength of the material of the masonry blocks. This means that the bed-joint roughness of the raw DSM-blocks still significantly influences the stress distribution in the masonry prisms until failure.

- Masonry prisms of P-group 4 (contact layer made of mix C).

At 95% of $P_{\text{u. FE-Réf}}$, a slight increase of the actual contact area from 38% to 44% is observed in the interfaces of the masonry prism of P-group 4. This increase in the actual contact is a result of a more important axial deformation of the contact layer, itself yielded by the Young's Modulus of the mixture used (mix C). Indeed, as the contact layer of the DSM-blocks is made with a material having a lower Young's modulus (7000 MPa) than the stiffen part of the blocks, the contact mechanic in the bed-joints is similar to a contact between a deformable and a non-deformable surface. The progressive increase of the actual contact area makes decrease the stress concentration over the contact interfaces between the DSM-blocks. This explains why the maximum stress peaks presented in Figure 78 has decreased by roughly 17% with respect to the masonry prism of P-group 1. At the ultimate load-bearing capacity of the masonry prism of P-group 4, i.e. at 1,32 $\mathrm{P}_{\text{u. FE-Réf}}$, the maximum actual contact was found equal to 64%.

- Masonry prism of P-group 6 (contact layer made of mix E).

In the masonry prism of P-group 6, the full contact was already reached before 95% of $\mathrm{P}_{\text{u. FE-Réf}}$ (Figure 76), which means that the initial bed-joint roughness is well levelled. The full levelling of the bed-joint roughness is due to the expected performance of the contact layer made of mix E. Indeed, mix E presents a very low Young's Modulus (150 MPa) with respect to the stiffen part of the masonry block. Hence, under compression, the contact layer of the DSM-blocks undergoes a large axial deformation, fulfils the gaps and thereby reduces the contact discontinuity in the bed-joints. The filling of the gaps causing the contact discontinuities thus leads to an increase of the actual contact in the bed-joints, which results in an improvement of the stress distribution over the contact interfaces (Figure 77). However, despite a full contact between the DSM-blocks, some stress peaks are still observed (Figure 78) in the contact interface at the sections where the initial contact occurred. This comes from the fact that upon loading, because of a gradual deformation, the asperity peaks and the sections around the asperity peaks experienced a material densification. The local densification of the material generates a local stiffening in the contact interface. This local stiffening around the asperity peaks creates preferential surfaces for the load transfer between the DSM-blocks, which explains the appearance of some stress peaks. Nevertheless, the range of variation between the minimum and the maximum stress peaks is significantly reduced from the masonry prism of P-group 1 (0 MPa - 33 MPa) to the masonry prism of P-group 6 (5 MPa – 11 MPa).

Table 11 shows the comparison between the numerical and the experimental results obtained on the masonry prisms (the actual contact in the bed-joints and the load-bearing capacity). Based on these results, it is observed that the numerical model slightly overestimates the maximum actual contact area and the load-bearing capacity of the masonry prisms. Indeed, this overestimation can be imparted to the effect of the bed-joint roughness, which varies from one masonry block to another.

Table 11. Comparison between the finite element and the experimental results

	Numerical			Experimental		
	Stress peak [MPa] *Measured at P_u	Max. actual contact	Ultimate load [kN]	Stress peak [MPa] *Measured at P_u	Max. actual contact	Ultimate load [kN]
Mas. Prism. P-group 1	33,4	38%	$P_{\text{u. FE-Réf}} = 348$ kN	/	23%	$P_{\text{u. EXP-Réf}} = 320$ kN
Mas. Prism. P-group 2	28,4	56%	1,12 x $P_{\text{u. FE-Réf}}$	/	50%	1,16 x $P_{\text{u. EXP}}$
Mas. Prism. P-group 3	28,8	55%	1,11 x $P_{\text{u. FE-Réf}}$	/	50%	1,14 x $P_{\text{u. EXP-Réf}}$
Mas. Prism. P-group 4	27,8	64%	1,32 x $P_{\text{u. FE-Réf}}$	/	55%	1,37 x $P_{\text{u. EXP-Réf}}$
Mas. Prism. P-group 5	11,6	60%	0,75 x $P_{\text{u. FE-Réf}}$	/	40%	0,70 x $P_{\text{u. EXP-Réf}}$
Mas. Prism. P-group 6	10,7	100%	1,72 x $P_{\text{u. FE-Réf}}$	/	98%	1,97 x $P_{\text{u. EXP-Réf}}$

5.3.2.2 Influence of the bed-joint roughness on the close-up deformation

The results of the compressive load against the close-up deformation of the masonry prisms of P-group 1, 2, 4, 6 are presented in the Figure 80 to Figure 83. Based on these results, it has been observed that the global stiffness of the DSM-prisms does no more vary after roughly 11% to 46% of $P_{\text{u. FE-Réf}}$, which lines up with the findings of Thanoon et al [7] and Jaafar et al [64, 85].

Indeed, the threshold from which the global stiffness of the DSM-prisms no longer varies is about 24% to 46% of $P_{\text{u. FE-Réf}}$ in the masonry prism of P-groups 1, 2 and 4, and about 11% of $P_{\text{u. FE-Réf}}$ in the masonry prism of P-group 6. The difference between the thresholds of variation in these P-groups comes from the intrinsic behaviour of the materials of the contact layer. In the masonry blocks of P-group 6, mix E has a very low compression strength and Young's Modulus as explained in section 5.3.2.1, which makes it possible for compensating the contact discontinuities at the earlier stage of the loading. The full contact in the bed-joints therefore enables the DSM-prisms to develop their actual stiffness. Regarding the DSM-prisms of P-group 1, 2 and 4, the non-linearity in the bed-joints closure is more extended over time because of the stiffness and the progressive deformation of the contacting materials. It is also observed that in these P-groups of DSM-prisms (1, 2 and 4), the local stiffness slightly varies from a section to another, which is of course due to the contact discontinuity in the bed-joints.

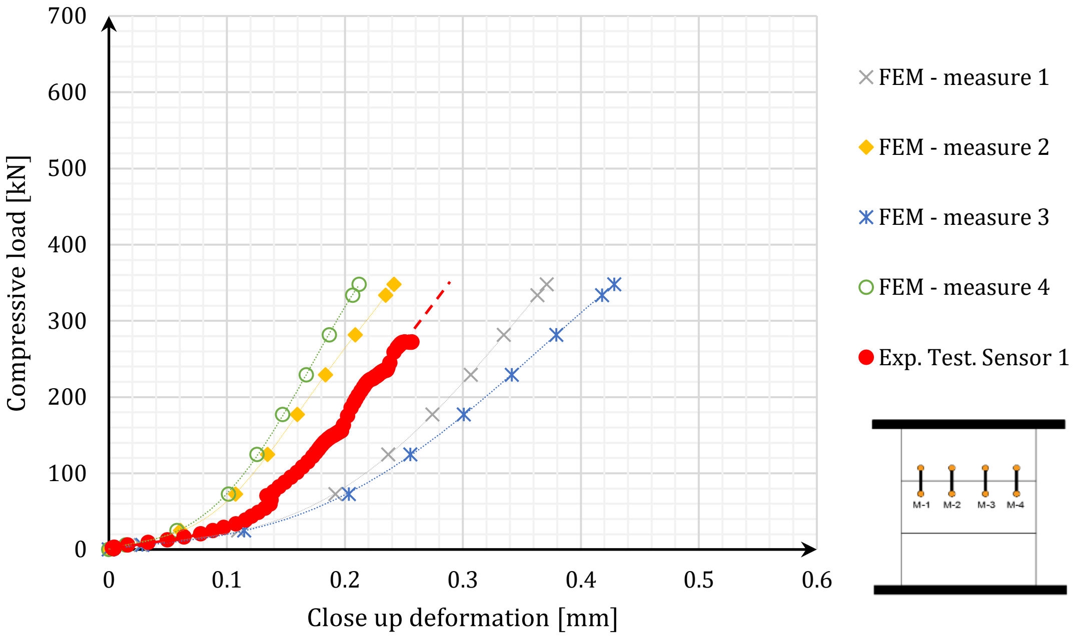

Figure 80. Close-up deformation of the dry-joint against the compressive load in DSM-prism of P-group 1 (without contact layer)

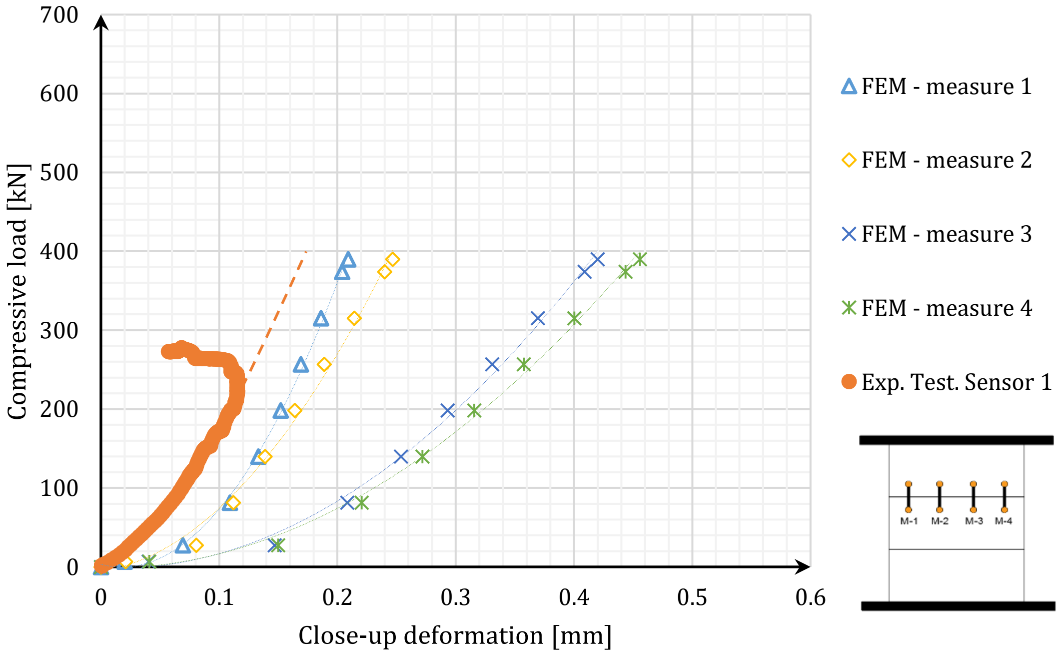

Figure 81. Close-up deformation of the dry-joint against the compressive load in DSM-prism of P-group 2 (contact layer – mix A)

In Figure 81, a reopening of the bed-joint was observed in the experimental test. This bed-joint reopening is due to a local crushing of the face-shells on one side of the blocks, which led to a rigid body motion of the masonry prism. Allaoui et al. [61] observed a similar behaviour by using the digital image correlation for measuring the mortarless joint closure in refractory masonry. In addition, the finite element calculation did not really depicted the actual load-close up deformation of the experimental test. This is due to variation of the actual bed-joint roughness from one masonry block to another. In Figure 83, instead of 4 curves of the load against the close-up deformation, a mean curve was presented because the 4 curves were overlapping.

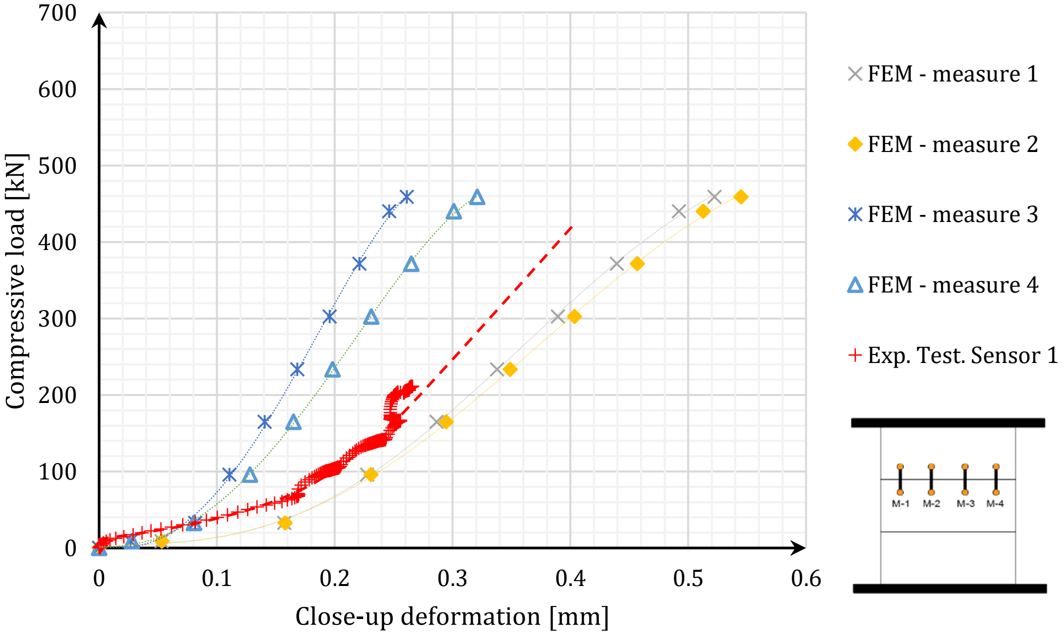

Figure 82. Close-up deformation of the dry-joint against the compressive load in DSM-prism of P-group 4 (contact layer – mix C)

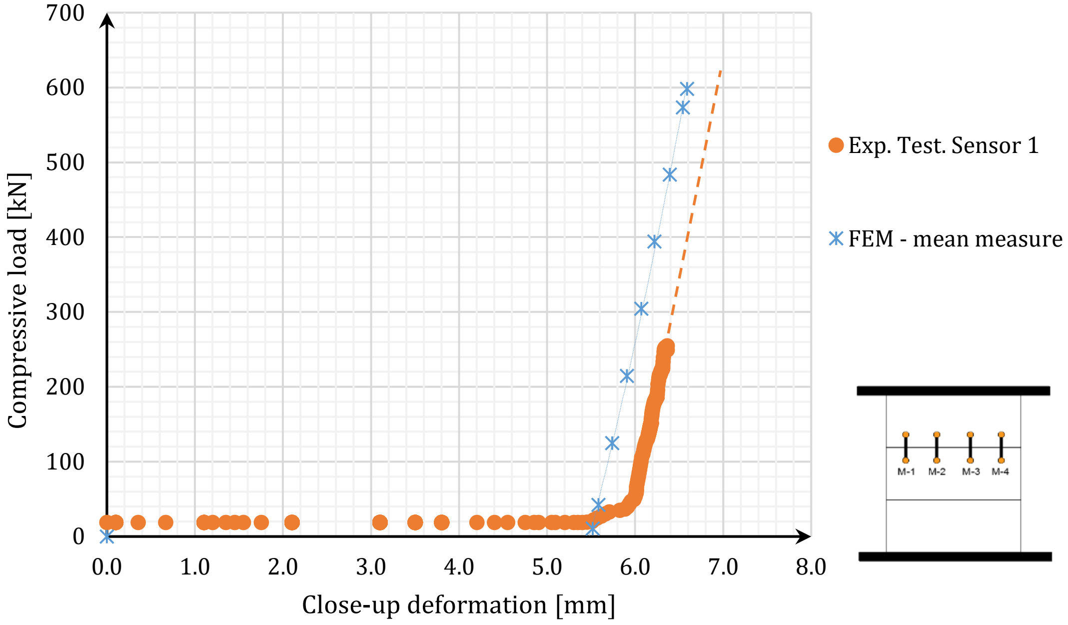

Figure 83. Close-up deformation of the dry-joint against the compressive load in DSM-prism of P-group 6 (contact layer – mix E)

5.3.2.3 Influence of the height of the surface asperities on the stress distribution

Another parameter of relevant interest is the influence of the height of the asperities forming the bed-joint roughness on the stress distribution in DSM. For addressing this issue, the bed-joint roughness was model while varying the height of the asperities within the range of variation [0 to z_S]. The maximum height of the asperities z_S was successively set equal to 0,1 then to 0,3 mm, respecting the range of variation reported in the literature [60-64]. Figure 84 to Figure 87 show the stress distribution at $y = 200$ mm and $z = 0$ mm, in the DSM-prisms of P-groups 1, 2, 4 and 6, at 95% of $P_{\text{u. FE-Réf}}$.

It is observed that in the DSM-prisms of P-group 1 and 2 (Figure 84 and Figure 85), the reduction of the height of the asperities only leads to a slight decrease of the stress peaks. However, in the DSM-prism of P-group 4 (Figure 86), the same reduction of the height of the asperities is accompanied by a more significant reduction of the stress peaks and a better redistribution over the length of the masonry block. Regarding the DSM-prism of P-group 6, there is almost no influence of the height of the asperities on the stress distribution over the length of the masonry block. Indeed, the level of influence of the height of the asperities is mitigated by the deformation capacity of the contact layer material. In the case of a very large (P-group 6) or a medium (P-group 4) axial deformation capability of the contact layer, the unevenness of the bed-joints is even more levelled as the height of the asperities is decreased. However, for a low axial deformation (P-group 2) or a very low axial deformation (P-group 1) of the contact layer, as the asperities deform much less, the unevenness of the bed-joints is not significantly levelled.

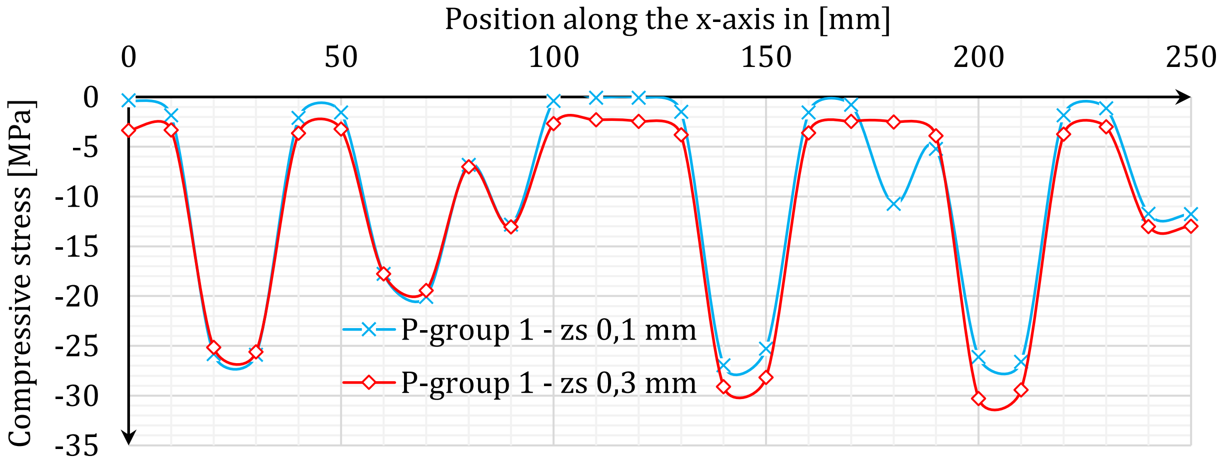

Figure 84. Stress distribution at 95% of $P_{\text{u. FE-Réf}}$ in the masonry prisms of P-group 1 and for a maximum height of the asperity of $z_s = 0{,}1$ mm and $z_s = 0{,}3$ mm

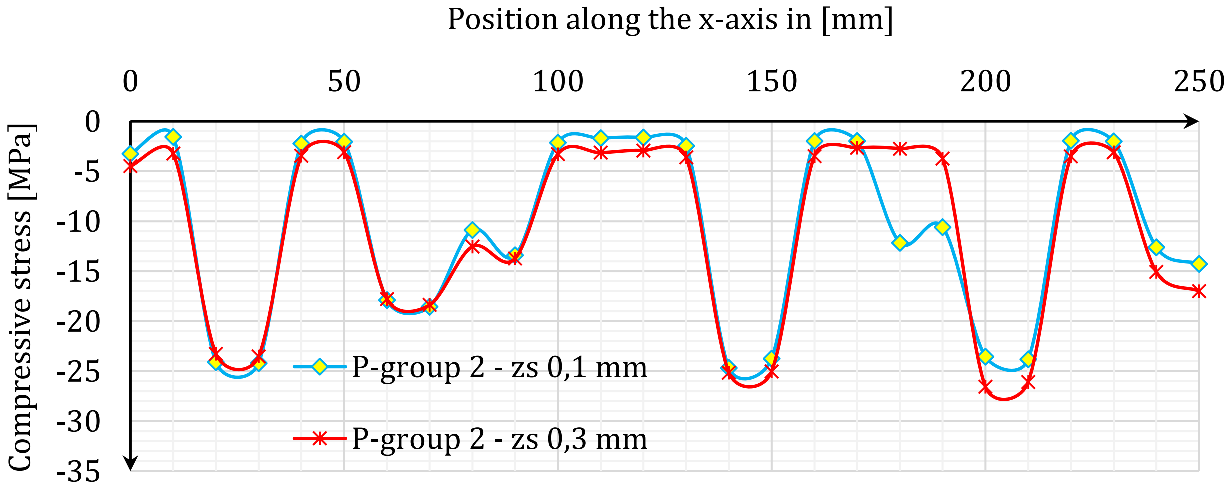

Figure 85. Stress distribution at 95% of $P_{\text{u. FE-Réf}}$ in the masonry prisms of P-group 2 and for a maximum asperity heights of $z_s = 0{,}1$ mm and $z_s = 0{,}3$ mm

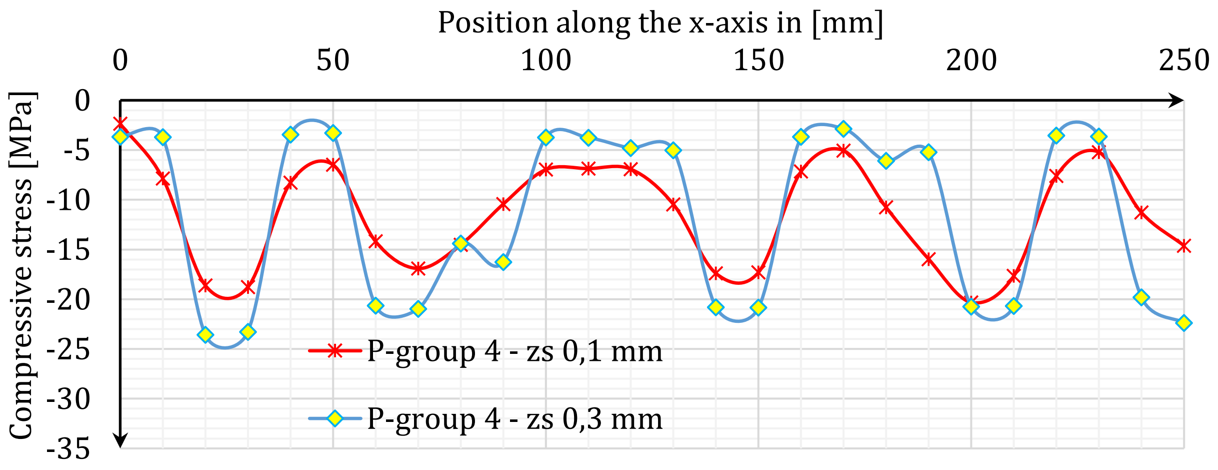

Figure 86. Stress distribution at 95% of $P_{\text{u. FE-Réf}}$ in the masonry prisms of P-group 4 and for a maximum asperity height of $z_s = 0{,}1$ mm and $z_s = 0{,}3$ mm

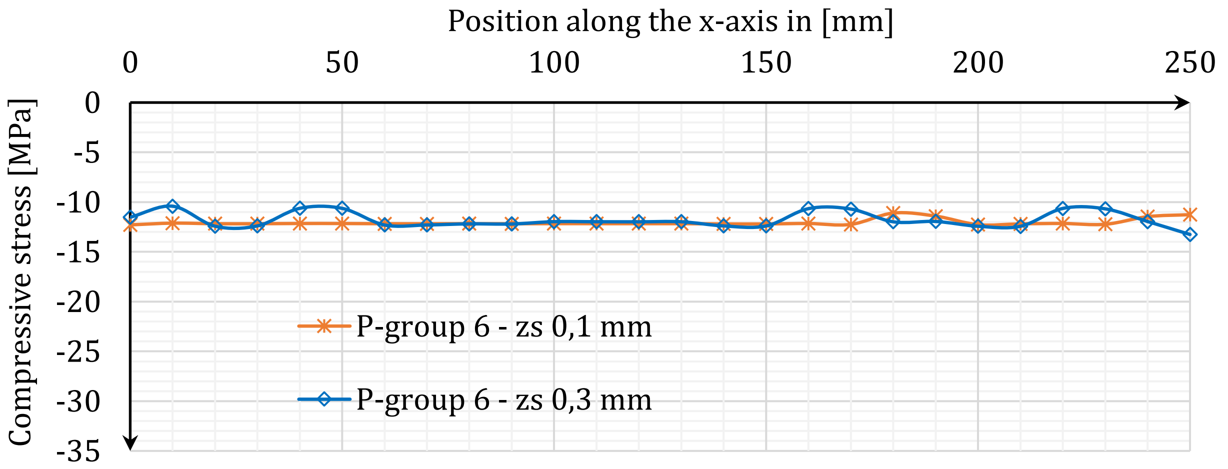

Figure 87. Stress distribution at 95% of $P_{\text{u. FE-Réf}}$ in the masonry prisms of P-group 6 and for a maximum asperity height of $z_s = 0{,}1$ mm and $z_s = 0{,}3$ mm

5.3.3 Additional investigation on the M-block

In this additional section, four materials of decreasing Young's Modulus have been investigated: mix F, G, H and I, with a respective young's Modulus of 42800, 3000, 2000 and 1600 MPa. Mixture F is the one used to cast the M-blocks, while mixtures G, H and I are the one purposely defined to analyse their influence in the contact layer.

5.3.3.1 Material and approach

The numerical investigation aims at studying the influence of the roughness and of the intrinsic material properties of the contact layer on the evolution of the actual contact area between two bodies coming into contact. Indeed, the entire model consists of two bodies, a stiff and a deformable one coming into contact. The stiff body represents the stiff-core of the masonry block, while the deformable body represents the contact layer. Considering the computational time needed to study the whole bed-joint of a masonry block while taking into account the roughness of its faces, the bed face of the contact layer is assumed flat while the bed face of the stiff body is assumed rough which leads to the needed simplification of the contact model [14-16, 21]. In addition, during the production process, the formwork of the masonry blocks is filled from the top to the bottom, a smooth metal sheet is forecasted in the bottom side and the pressure is applied on the upper side. Hence, the bottom side of the masonry blocks is much more flatten than the upper side.

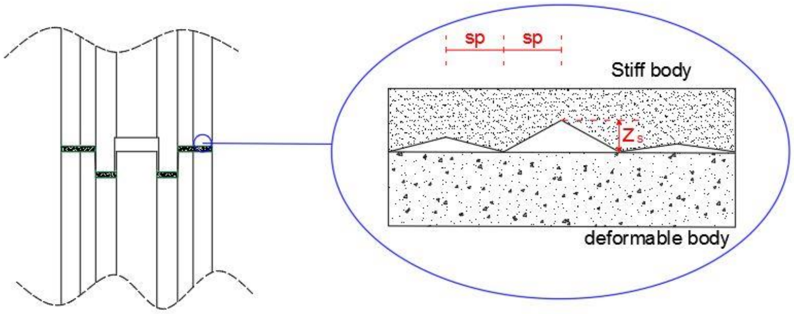

Figure 88. Contact layer in random contact to the stiff body

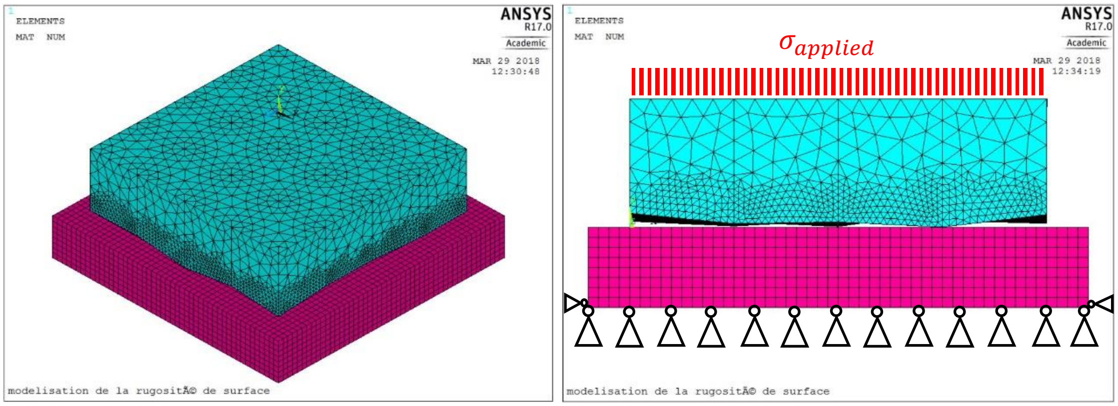

Figure 89. Modelling of an contact layer and a stiff body

The length and the width of the contact layer are fixed to 5 mm whereas its thickness is fixed to 10 mm. Concerning the modelling of the rough surface, the maximum height of the peaks is given by z_s and the asperity peaks are at a regular distance of 1,25 mm. The regular space between the asperity peaks was set in a way to get a density of 1 asperity/mm^2. The height of each asperity is defined by means of a random value generator RAND (0, z_s) which takes as input the minimum and the maximum height of the peaks. The maximum height of the peaks of the asperities (z_s) was set successively to 0,2 mm, 0,4 mm and 0,8 mm. Figure 88 and Figure 89 show a zoom on a bed-joint interface with the stiff body lying on the contact layer.

At the base of the contact layer, the normal displacements were restrained ($u_y = 0$), as well as the displacements u_x and u_z on the edge nodes on one side. A uniform stress ($\sigma_{applied}$) was applied on the top face of the stiff body. At the interface between the contact layer and the stiff body, the paired surface elements Conta174 and Targe170 of the ANSYS 17 package [113] were used to define the mechanical contact pairs. In the script of the modelling, the stress-strain response of the involved materials was set through a multi-linear stress-strain relationship. The mesh size was refined on the bed-joint to ease the solution convergence and improve the accuracy of the results. The behaviour of the three-dimensional finite element model was simulated using a concrete model of ANSYS (CONCR

SOLID65) [113] that includes the failure mechanism of tensile cracking and compressive crushing.

In each numerical computation, the contact layer was flattened due to load increase on the stiff body and the rate of the actual contact area was recorded in function of the applied stress. For each value of z_s, the gathered data set are displayed on a figure having the rate of the actual contact area (R_{ac}) on the y-axis and the stress applied on the x-axis. The comparison of the functions $R_{ac} = f(\sigma_{applied})$ enables to point out the influence of the intrinsic properties of the material of the contact layer, as well as the influence of the roughness of the bed-joint on the evolution of the actual contact area.

5.3.3.2 Results and discussion

The results presented in the Figure 90, Figure 91, and Figure 92 show the evolution of the actual contact area in a bed-joint in function of the material of the contact layer and the stress applied on the layer. The first main observation is that whatever the roughness, the constitutive material of the contact layer strongly influences the evolution of the actual contact area on a bed-joint. Each of the figures shows that with the decrease of the Young's Modulus of the constitutive material, the full actual contact under compression is increased. At the onset of the loading, the constitutive material of the contact layer is in the elastic phase and solely the peaks of the asperities are actually in contact with the underlying flat surface. Hence, due to a low rate of the actual contact area, the applied stress is amplified on the bed-joint and the weak Young's Modulus of the material ease a gradual deformation close to the asperities. These combined phenomenon lead to the increase of the rate of the actual contact area.

Table 12 provides the rate of the actual contact area and the stress amplification factor in a bed-joint of an contact layer modelled with $z_s = 0{,}2$ mm. While Table 12 presents the data at two load steps for a clear discussion, Figure 90 shows the whole tendency during the loading up to 30% of the ultimate load of a single masonry block. As the stress applied on the contact layer increases, the rate of the actual contact increases and the stress amplification factor in the bed-joint decreases. The increase of the applied stress enables to bridge some gaps and the Young's Modulus of the material enhances the effect. At 3 MPa of the applied stress, the rate of the actual contact area (R_{ac}) is about 30% with mix G, 52% with mix H and almost 78% with mix I. This improvement of the R_{ac} reduces the stress amplification factor in a bed-joint from 3,3 to respectively 1,9 and 1,3. Furthermore, at 5 MPa, more bed-joint imperfections are levelled thanks to the contact layer. The stress amplification factor varies from 3,3 to 1,8, from 1,9 to 1,1 and from 1,3 to 1,0 for the contact layer modelled with respectively mix G, H and I.

Table 12. Actual contact area and stress amplification factor in a bed-joint* (*$z_s = 0{,}2$ mm)

	Stress applied = 3 MPa				**Stress applied = 5 MPa**			
	Mix F	Mix G	Mix H	Mix I	Mix F	Mix G	Mix H	Mix I
Rate of the actual contact (R_{ac})	7%	30%	52%	78%	13%	55%	90%	100%
Stress amplification factor on the bed-joint ($1/R_{ac}$)	14,3	3,3	1,9	1,3	7,7	1,8	1,1	1,0

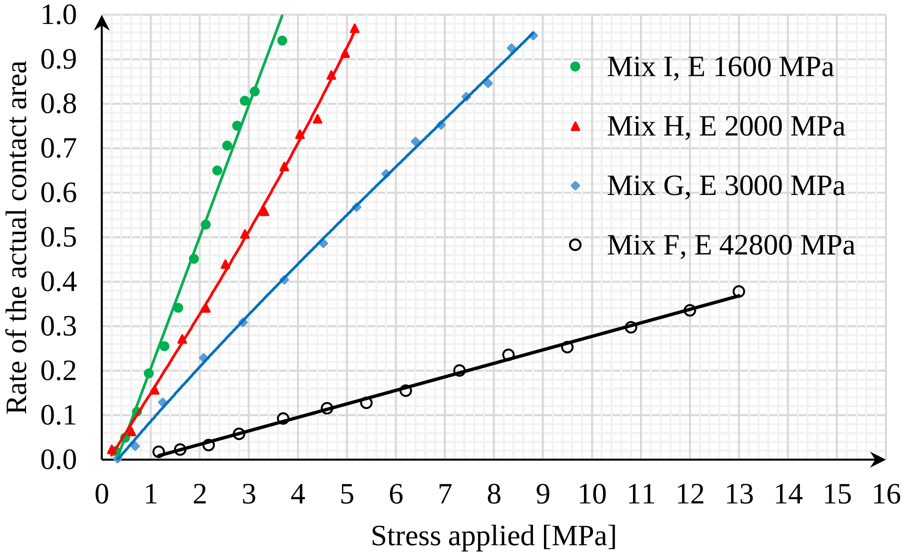

Figure 90. Stress-contact relationship for $z_s = 0{,}2$ mm

Figure 91 shows the R_{ac} in function of both the applied stress and the material of the contact layer modelled with $z_s = 0{,}4$ mm. When the maximum height of the peaks (z_s) of the rough surface is increased from 0,2 mm to 0,4 mm, the slope of the stress-contact curves becomes less steep, i.e. the rate of the actual contact area increases more slowly with the applied stress. Table 13 reports again the R_{ac} and the stress amplification factor in the bed-joint at 3 MPa and 5 MPa of the applied stress. For comparison purposes, the increase of the stress amplification factor according to the study in Table 12 is also reported in brackets. First, it is observed that at the same load level (3 and 5 MPa), the R_{ac} has decreased compared to the study in Table 12 and Figure 90. Indeed, the decrease of the rate of the actual contact area is owed to the roughness of the bed-joint: the higher the height of the asperities, the lower the actual contact area. Due to the more significant roughness and therefore less significant actual contact area, the stress amplification factor in the bed-joint has increased. This highlights the importance of the bed-joint texture in a DSM_b and shows that the more the geometric imperfections are significant; the lower will be the contact surfaces available for the load transfer between the block courses.

Nevertheless, although the R_{ac} has decreased because of the roughness, the influence of the constitutive material of the contact layer remains similar. At 3 MPa of applied stress, while the R_{ac} is about 27% with material mix G, the materials mix H and mix I enable to reach respectively 40% and 62% of the actual contact area in the bed-joint. The resulting stress amplification factor in the bed-joint are respectively 3,7, 2,5 and 1,6, which means that the intrinsic properties of the material of the contact layer have enabled to overcome some geometric imperfections and to limit the stress concentration in the bed-joint. At 5 MPa of applied stress, the stress amplification factor in the bed-joint decreases from 3,7 to 2,3, from 2,5 to 1,6 and from 1,6 to 1,0 for the contact layer modelled with respectively material mix G, mix H and mix I. Nonetheless, these stress amplification factors are higher than those obtained on the bed-joint with $z_s = 0{,}2$ mm (Table 12).

Table 13. Actual contact area and stress amplification factor in a bed-joint* (*$z_s = 0{,}4$ mm)

	Stress applied = 3 MPa				Stress applied = 5 MPa			
	Mix F	Mix G	Mix H	Mix I	Mix F	Mix G	Mix H	Mix I
Rate of the actual contact (R_{ac})	7%	27%	40%	62%	12%	43%	63%	100%
Stress amplification factor on the bed-joint (1/ R_{ac})	14,3 (+0,0)	3,7 (+0,4)	2,5 (+0,6)	1,6 (+0,3)	8,3 (+0,6)	2,3 (+0,5)	1,6 (+0,5)	1,0 (+0,0)

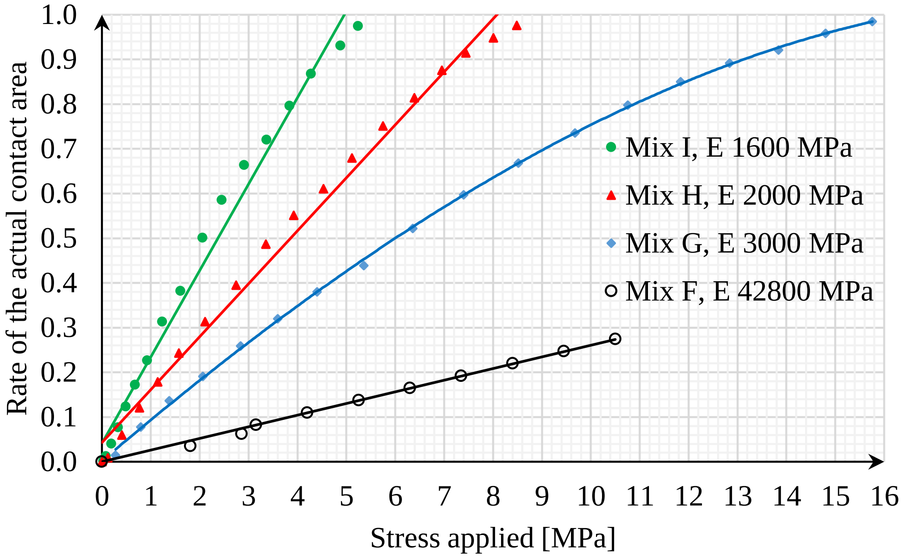

Figure 91. Stress-contact relationship for $z_s = 0{,}4$ mm

When the maximum height of the asperity peaks is one more time increased and set to 0,8 mm (Figure 92), similar phenomena are observed: the slope of the stress-contact curves decreases, the stress amplification factors increases and the low Young's Modulus enables still to overcome the geometric imperfections faster. This supports the previous observations stating that as the roughness increases, the rate of the actual contact decreases.

Table 14. Actual contact area and stress amplification factor in a bed-joint* (*$z_s = 0{,}8$ mm)

	Stress applied = 3 MPa				**Stress applied = 5 MPa**			
	Mix F	Mix G	Mix H	Mix I	Mix F	Mix G	Mix H	Mix I
Rate of the actual contact (R_{ac})	7%	18%	34%	56%	11%	30%	58%	92%
Stress amplification factor on the bed-joint ($1/R_{ac}$)	14,3 (+0,0)	5,5 (+2,3)	2,9 (+1,0)	1,8 (+0,5)	9,1 (+1,4)	3,3 (+1,5)	1,7 (+0,6)	1,1 (+0,1)

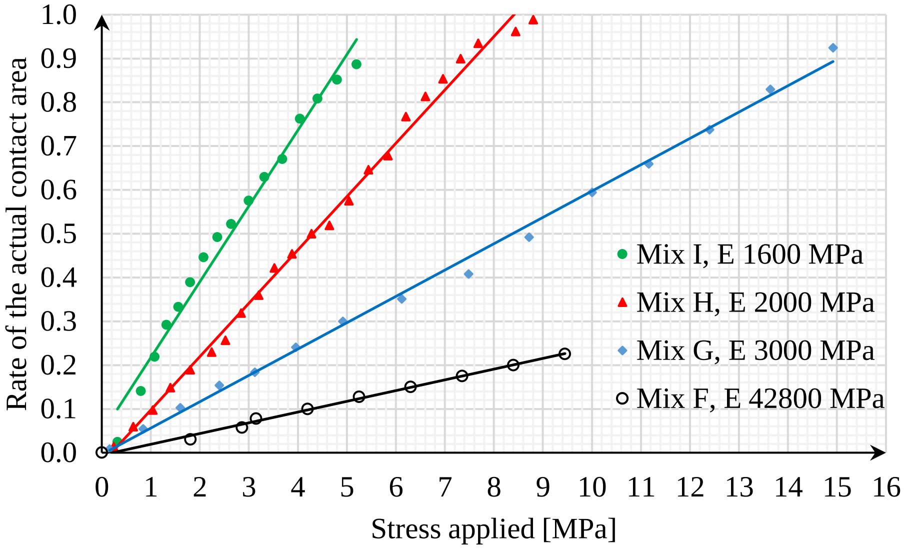

Figure 92.Stress-contact relationship for z_s = 0,8 mm

In a general overview and as pointed out by K. Andreev et al. [24], the stress needed to close the gaps in the bed-joints was found to be proportional to the material stiffness: the higher the material stiffness, the higher is the stress needed to close the gaps. As observed by Xiaomei et al. [25], the results of Figure 90, Figure 91, and Figure 92 show that the relationship between the applied stress and the actual contact area is almost linear. The coefficient of proportionality between the applied stress and the resulting actual contact area depends on the material properties. As the compressive load increases, the asperities of the bed-joints deform and crush, which leads progressively to a levelling of the bed-joint imperfections and the increase of the actual contact area. Vasconcelos et al. [26] also observed this phenomenon during their experimental characterization of stone masonry in shear and compression. However, as the Young's Modulus of the materials coming into contact increases, the asperities deform much less, which in return provide a small useful section for the load transfer. This finding could explain the earlier cracking observed by former authors [7, 12, 27, 28] during their experimental tests on various shapes of DSM_b. In addition, at a same load level, the rate of the actual contact area decreases as the bed-joint became rougher.

5.3.3.3 Experimental tests and finite element model on prisms with M-blocks

Similar investigations were performed on the M-Block where a dry-stack masonry prism was considered. A contact layer made of mix G was placed on the top face of the full masonry block (improved block unit). The actual contact captured in the bed-joint interfaces during the experimental tests is presented in the following as well as the results of the finite element model.

A series of six dry-stacked masonry prisms of 350 x 400 x 175 mm (length x height x thickness) were tested under axial compressive loads in the lab for capturing the actual contact in the bed-joint interface (Figure 93). For this purpose, Prescale Fujifims presented in chapter 4 were inserted in the bed-joint interfaces and the DSM prisms were compressed up to 5% and 15% of the ultimate load of a single block ($F_{u.\,Block}$). Following the experimental tests, the strips of Prescale Fujifilms were processed to determine the rate of the actual contact recorded in the bed-joints.

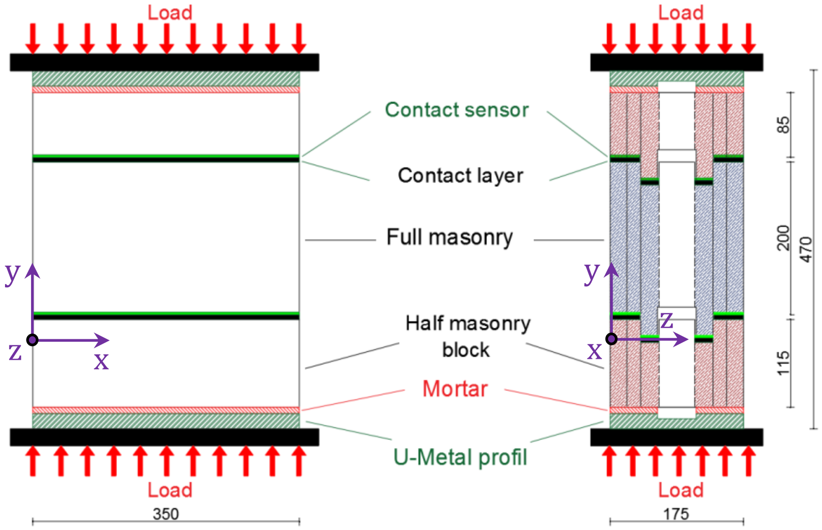

Figure 93. Sketch of the DSM prism tested.

Next to the experimental test, a 3D finite element model was performed to have an insight on the effect of the contact layer on both the rate of the actual contact area and the stress distribution in the M-Block. For this purpose, two models of the DSM prisms have been studied. In the first one, the DSM prism is modelled without a contact layer on the block units.

In the second model, the DSM prism is modelled with block units having a contact layer made of mix G. Considering the CPU time needed due to the rough shape of the dry contact interface, a quarter part of the tested masonry prism was modelled and a symmetry plane was defined about the z-axis at z = 87,5 mm. The block bed-joint roughness was modelled as previously detailed in section 5.3.1. A compressive load was applied on the flat top face of the overlying masonry block and the normal displacements were restrained on the bottom face of the studied masonry block. Regarding the contact interface, paired contact elements Conta174 and Targe170 [23] were used for defining the surfaces intended to come into contact upon the loading.

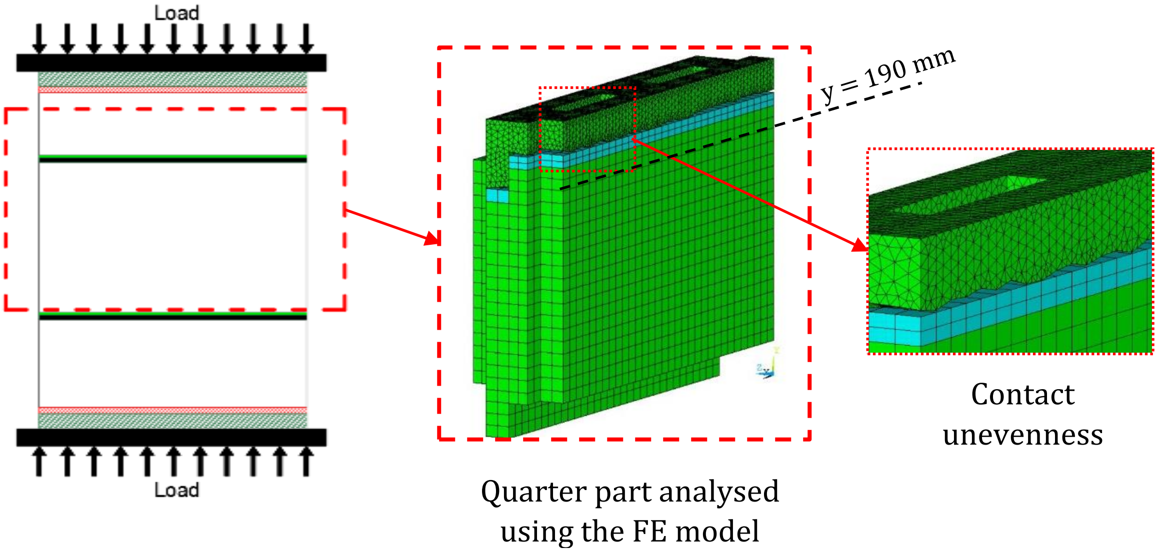

Figure 94. Sketch of the DSM prism tested.

5.3.3.4 Analysis of the results

To assess the effect of the contact layer on the improvement of the rate of the actual contact, the distribution of the normal stress along the x-axis at y = 190 mm and z = 0 mm (please refer to the coordinate system in Figure 93) is reported on Figure 95. It has been observed that the stress distribution is almost uniform along the face shell for the DSM masonry prism made with improved block units. However, the reverse phenomenon is observed in the masonry prism made with raw block units. In the latter, the stress distribution follows a kind of saw tooth curve with a wide amplitude of variation.

At 5% of the $F_{u.\,Block}$, which corresponds to a nominal compressive stress of roughly 5,4 MPa, one observes that the stress distribution along the face shell of the masonry prism with row blocks exhibits a significant range of variation. Indeed, there are high stress peaks at some points along the face shell ($0 < x$ [mm] < 40 and $230 < x$ [mm] < 290) while the others are less solicited. In this case, the overall stress distribution varies between -2,3 and -12,7 MPa. Of course, the occurrence of the stress peaks can be explained by a low levelling of the surface unevenness in the bed-joint. The stress peaks occur where the contact face of the upper masonry block encounters the underlying one. In addition, as the load increases, a hardening of the asperities occurs [29] and this leads to a further stress amplification around the initial contacting sections (Figure 96). Regarding the DSM prism with improved block unit, at 5% of the $F_{u.\,Block}$, the compressive stress along the face shell varies between -3,8 and -6,2 MPa. The promising reduction of the range of variation of the compressive stress is once again owed to the capacity of the contact layer to resorb a part of the bed-joint imperfections.

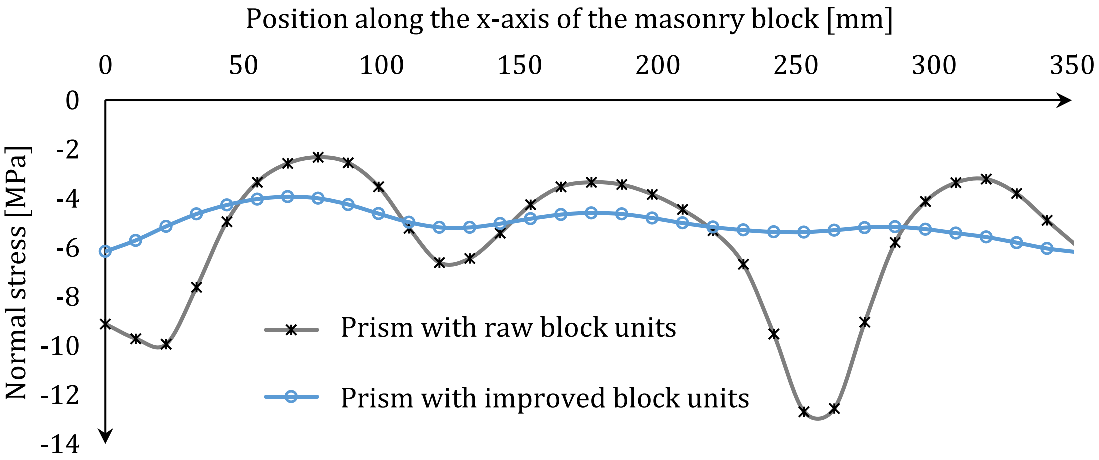

Figure 95. Stress distribution in the masonry block at 5% of $F_{u.\,Block}$ (at $y = 190$ mm, $z = 0$ mm)

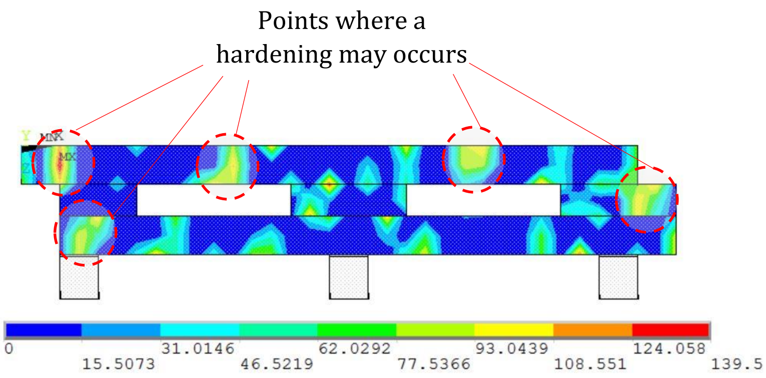

Figure 96. Contact points where a hardening may occur in the $N.DSM_b$

Figure 97 shows the state of the closure of the bed-joint at 5% and 15% of $F_{u. Block}$, for the raw DSM block and the improved DSM block. It is clearly highlighted that the closure of the bed-joint is proportional to the stiffness of the contacting material. At 15% of $F_{u. Block}$, the prim with raw block units still presents significant stress peaks with respect to the prism with improved block units, because of the low deformation of the asperities.

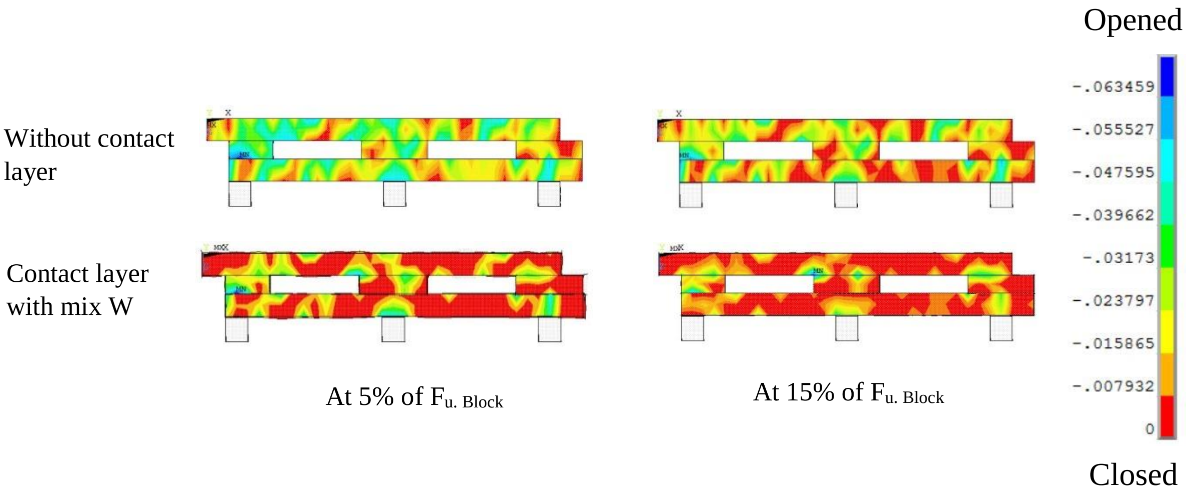

Figure 97. State of closure and actual contact area in the bed-joint of the masonry block

Figure 98 and Figure 99 show once the actual contact area measured during the experimental test. A comparison has been made between the rate of the actual contact computed using the FE model and the rate of the actual contact area measured during the lab tests. It has been observed that at 15% of $F_{u. Block}$, the FE model predicts a rate of actual contact area of about 30% in the DSM prism with raw block units, while the experimental tests provides around 39%. Regarding the DSM prism with improved block units, the FE model predicts roughly 85-90% of actual contact area whereas the experimental tests provided a mean value of 75%.

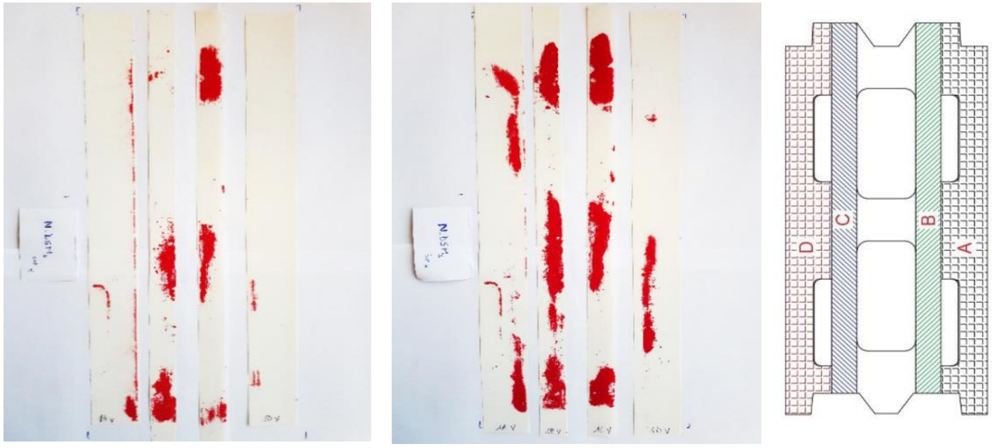

Figure 98. Actual contact area in the bed-joints of the DSM prims with raw block units, at 5% and 15% of $F_{u.\,Block}$

Figure 99. Actual contact area in the bed-joints of the DSM prims with improved block units, at 5% and 15% of $F_{u.\,Block}$

For a given roughness, the higher the stiffness of the contacting materials, the lower are the deformation and the crushing of the asperities in the bed-joint. Conversely, the lower the stiffness of the contacting materials, the higher are the deformation and the crushing occurring in the bed-joint, which contributes for improving the actual contact in the involved bed-joints.

5.4 Effects of the height difference between the masonry blocks

5.4.1 Wall modelling

To study the effect of a height variation of the masonry blocks on the mechanical response of a dry-stacked wall, several walls were modelled with masonry blocks of different heights. All along the following discussion, ΔH^* refers to the deviation of the actual height of a masonry block with respect to the nominal height, while ΔH_D refers to the height difference between two adjacent masonry blocks. The numerical construction of the walls has been done as follows:

- An external csv.data file containing the height deviation (ΔH^*) of each masonry block is read. It should be noted that the height deviation in the csv.data file was sometimes done randomly, sometimes in a controlled manner, depending on the specific purpose of the current numerical investigation.
- The coordinates (Px, J) of the “virtual” origin point of each masonry block are defined (see Figure 100).
- The right ordinate (J+VDy) of the “actual” origin point of each masonry block is calculated based on the coordinates of its “virtual origin point” and its height deviation is defined in the csv.data file.
- Having defined the parameters ΔH^*, J, Px and VDy for each masonry block, each one is modelled by calling the predefined function “Masonry.txt”.

Figure 100 shows for instance a dry-stacked wall with three courses and three full-masonry blocks in the length. The random height difference between the masonry blocks ΔH_D is amplified to differentiate and well depict the “virtual” and the “actual” origin point used to build the wall.

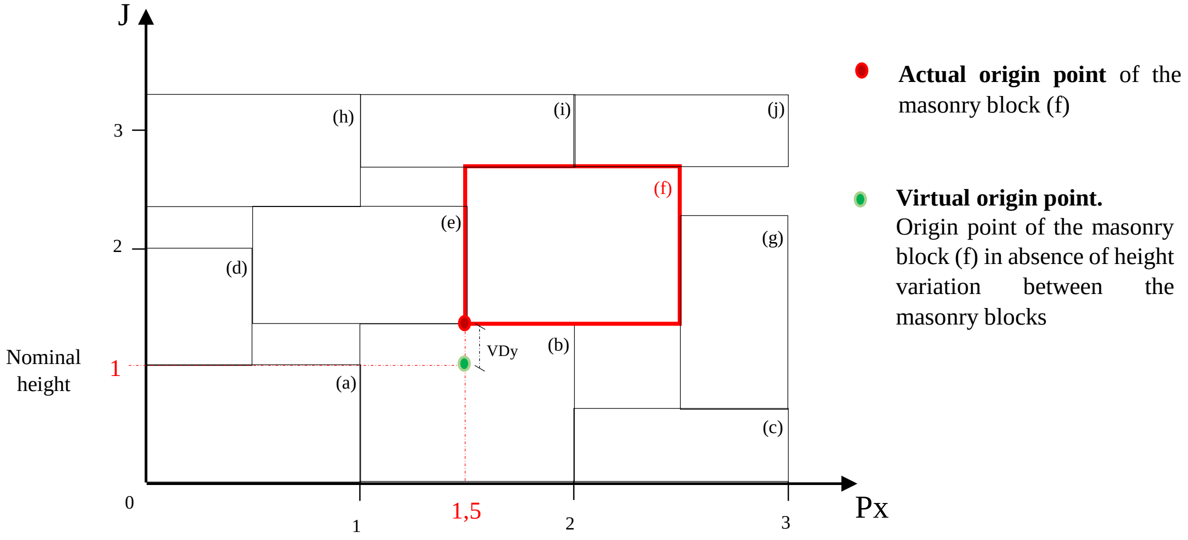

Figure 100. Origin points of a dry-stacked masonry block (f) in a wall.

5.4.2 Raw dry-stacked masonry blocks (R.DSM$_b$)

5.4.2.1 On the level of a single masonry block

Agaajani [45] has observed during his experimental investigation that the height distribution of a sample of manufactured masonry blocks follows a Gaussian distribution. Based on the tolerance of production (+/-2 mm) extracted from the Gaussian distribution, a dry-stacked wall is erected using masonry blocks of various heights (Figure 101). The height distribution of the masonry blocks in the wall courses exhibits the five main load cases that may occur in a dry-stacked masonry block. Indeed, the height variation of the masonry blocks from one course to the underlying one defines how each block will be loaded and supported. Figure 101 shows the different possible scenarios in case of a submission of a wall to an axial compressive load.

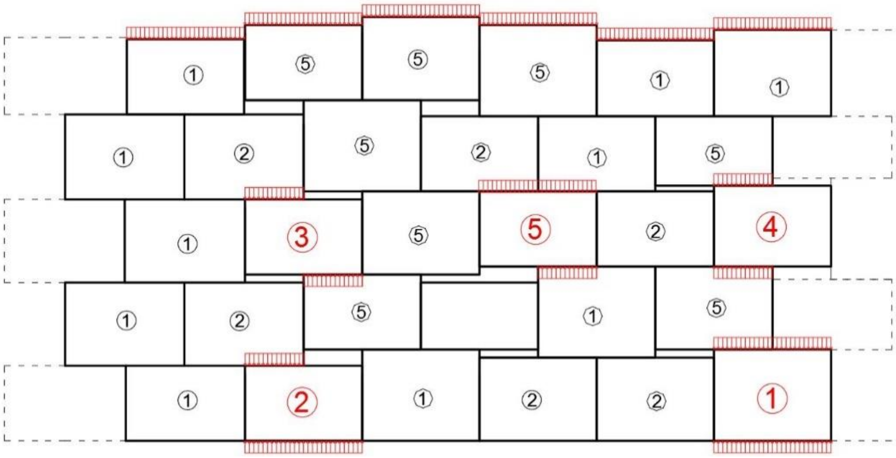

Figure 101. Load cases (1 to 5) induced by the height variation of the masonry blocks [70]

In order to compare the mechanical response of the masonry blocks in function of their actual load case, they were separately modelled and submitted to a same unit load. Thus, a constant load of 100 kN was applied on the top face of the masonry block, exclusively on the available loading areas according to the load case. The stress distribution in the masonry block of each load case is represented in Figure 103.

In the first load case, the masonry block is loaded and supported on its whole contact areas. In this case, the applied load follows an almost vertical path, which results in a uniform distribution of the compressive stresses in the bottom face of the masonry block (Figure 103). In this perfect case, the masonry block develops its whole resistance and the cracks appear only along the height of the two web faces. The lateral displacement (uz) along the upper face of the face shell is almost uniform in the whole masonry block. This load case occurs when all the masonry blocks of a wall have exactly the same height, i.e. $\Delta H^* = 0$ mm, or when a mortar layer is inserted between the courses of masonry blocks to level the height differences.

Instead of a perfect vertical load percolation as in the first load case, the numerical analysis shows a specific non-uniform stress distribution in the masonry blocks subjected to the load cases 2, 3, 4 and 5. In the load case 2, the masonry block is loaded on one-half section and supported on its whole bottom face. As highlighted in Figure 103, 34% of the cross section carries about 62% of the applied load whereas 16% of the cross section carries 18% of the applied load. The remaining load passes through the second half part of the cross section. Due to the non-uniform stress state in the two half parts of the face shell of the masonry block, a shear stress is developed over the height of the face shell, which leads to premature cracking. Also, due to the non-uniform stress state in the two half parts of the face shell, the lateral displacement (uz) of the web face occurs only on the loaded side of the masonry block. The non-uniform lateral displacement of the whole masonry block leads to the development of cracks in the web face on the loaded side (Figure 102.b along the interface with the face shell). The ultimate strength of the masonry block is thus reduced by 60%.

In the third load case, the masonry block is loaded on a half cross section and supported on the opposite half cross section. Due to the asymmetrical disposition of the loaded area with respect to the support area, one might think that the masonry block is likely to spin instantly upon loading. Indeed, although occurring, this movement is more or less limited or prevented by the neighbouring masonry blocks of the considered course (Figure 104.a and b). Nevertheless, as the considered masonry block will gradually deform and remain supported on two small sections (the middle section and one of the left or the right edge section), a load redistribution will occur. Considering the initial load and support conditions, the masonry block was modelled in a way to respect the real boundary conditions by limiting the displacement along the x-axis. On the left and right sides of the masonry block, contact and spring elements were put in place to simulate the resistance to horizontal displacements imposed by the neighbouring masonry blocks. The spring elements were designed to provide a compressive strength and a null tensile strength (Figure 71), thus allowing a rigid motion of the masonry blocks like an uplift. Upon loading, a slight spin of the masonry block occurs and a great part of the applied load is carried by a small part of the lower cross section. As it can be observed in Figure 103 (load case 3), a uniform load applied on top of the masonry block produces a stress concentration at the lower contact face. Moreover, it is observed that 60% of the applied load is transferred through solely 18% of the cross section of the masonry block. The remaining 40% of the applied load is transmitted across 32% of the cross section. The stresses concentration is heightened in the middle of the cross section, which results in (1) a fast increase of the shear intensity in the critical section and in (2) a development of cracks (Figure 102.a). Nevertheless, the continuous deformation of the masonry block allows at a certain moment to increase the actual contact surface at the base of the block, which then enables a better load distribution. This load case is the most unfavourable compared to the four other. The compressive strength of the masonry bock is reduced by 86% and the applied load follows an oblique path of at most 63° (α = tan-1[length/ height]).

In the fourth load case, the masonry block is loaded and supported on a half cross section of the masonry block. Here, the full masonry block behaves like two distinct half blocks, the first being uniformly loaded and supported on its whole contact area, the second being not loaded. As highlighted in Figure 103 (load case 4), the applied load is uniformly distributed on one-half cross section. In this load case, premature cracking appears in the middle of the masonry block, as a straight line along the height of the face shell. The out of plane displacement of the upper side of the face shell is irregular along the masonry block. The out-of-plane displacements occurring on the loaded side of the block intensifies the cracking of the web face of this side. These phenomena reduce the compressive strength of the masonry block by 60%.

The last load case is the one where the masonry block is loaded on its whole cross section and supported on a half cross section. In this load case as in the third load case, one might think that the block will simply spin, but the flexibility of a masonry block to spin is depending on the position of the masonry block in the wall (in the upper course or elsewhere). Indeed, as shown on Figure 104, a spin of any masonry block requires vertical and horizontal displacement of the block. However, each masonry block is not fully free to move along the x-axis due to its neighbouring blocks (Figure 104.b). In addition, in all the courses other than the upper course of the wall, the masonry block is only able to spin if on one side at least the weight of all the overlying courses can be lifted. Theses combined effects of the weight and the interaction between the blocks in a course limits the movability of a masonry block in a wall. Nevertheless, as in the previous cases, the increase of the in plane displacement will finally lead to an increase of the contact surface between the courses. This load case produces a load concentration at the middle of the masonry block. As it is shown on Figure 103 (load case 5), 30% of the applied load passes through 10% of the cross section and the remaining load is distributed on 40% of the cross section. Due to the load concentration in the middle section of the masonry block, high shear stresses are developed, which gives rise to cracking. As for load case 2, the stresses follow a vertical path above the supported side and an oblique path of at most 63° in the unloaded side of the masonry block. The premature occurrence of cracks is responsible of a reduction of 75% of the compressive strength of the masonry block.

Figure 104 shows a reduced model of a wall with the contact and spring elements provided to model the vertical and horizontal interaction between the masonry blocks. Figure 104.a shows an initial positioning of the masonry blocks before loading, while Figure 104.b shows the vertical and horizontal interactions with the rotation that may occur if the blocks were fully free to rotate. The spring and contact elements defined on the vertical and horizontal edge faces of the masonry blocks (Figure 104.a and b) enable to ensure the vertical load transmission as well as the horizontal interaction between the blocks in the load cases 3 and 5.

Table 15. Ultimate load of the masonry block in function of the load case [70].

Load case	Ultimate load [kN]	Load reduction compared to load case 1 [%]
Case 1	2031	100,0
Case 2	804	39,6
Case 3	270	13,3
Case 4	810	39,9
Case 5	506	24,9

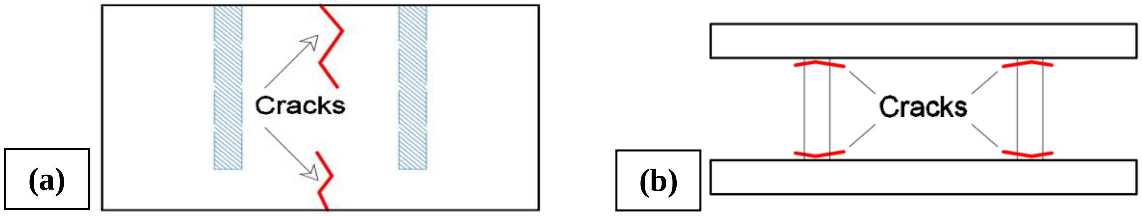

Figure 102. Crack in the middle of the block unit and at the interface face-shell / web

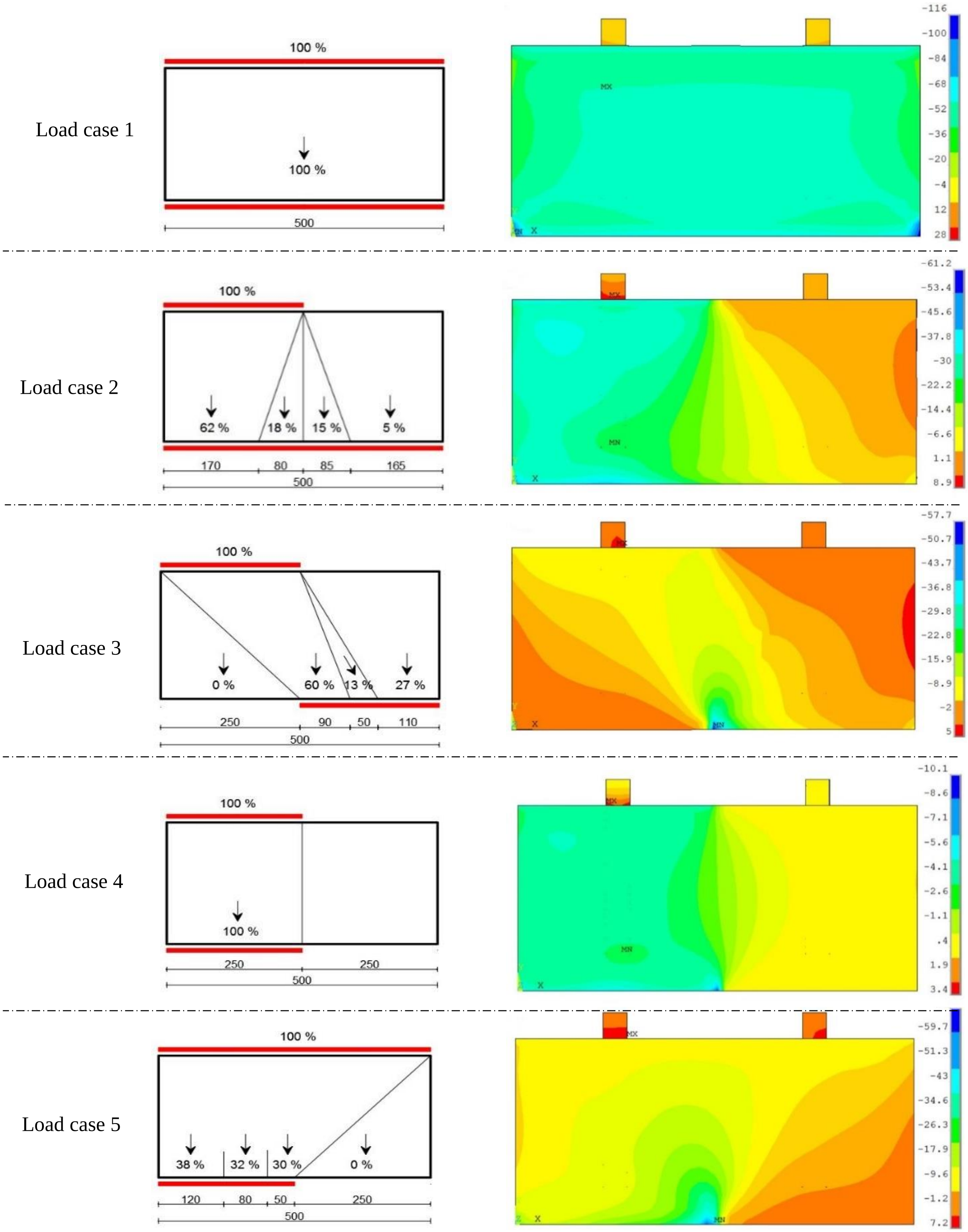

Figure 103. Stress distribution [MPa] in the masonry block in function of the load case [70]

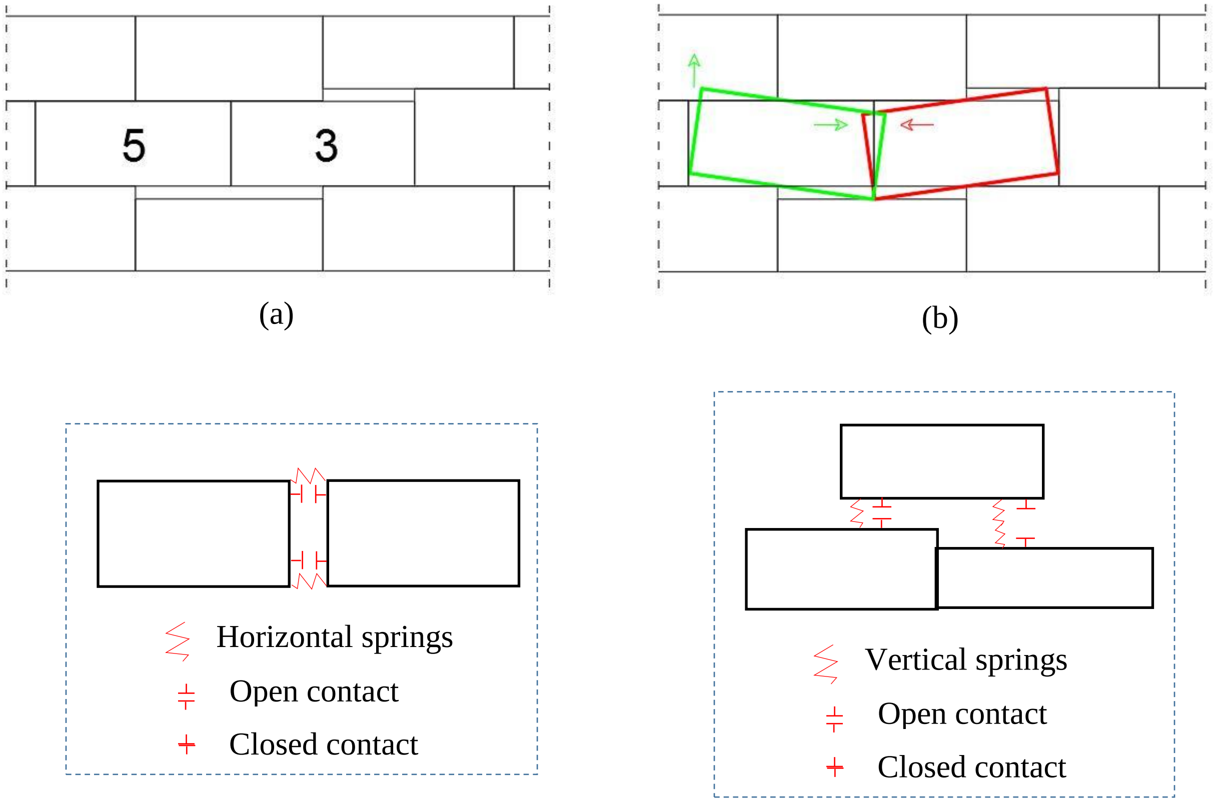

(a) (b)

(c) (d)

Figure 104. Loading and boundary conditions schemes for the load cases 3 and 5. (a) Initial positioning of the masonry blocks; (b) interaction occurring between the masonry blocks under loading; (c, d) contact and spring elements on the edge faces of the masonry blocks [70]

5.4.2.2 On the level of a dry-stacked masonry wall

a) Study of a raw dry-stacked masonry wall

A finite element analysis was performed on a random wall built with masonry blocks of random height and selected within the statistical height distribution measured on manufactured blocks. Table 16 sets the material properties used to model the wall and the latter was gradually loaded on the top face. Given that the computation time of a large-scale wall is very important, an x-y plane of symmetry was defined and the size of the studied walls limited to three masonry blocks in the length and five in the height. Figure 105 shows a random load percolation system among many others that could occur in such a wall. This model was used as example to perceive the effect of the height difference between the masonry blocks on the mechanical response of a wall. In Figure 105, ΔH* [mm] represents the height deviation of each masonry block with respect to the nominal height. The block bed-joint roughness was not included in the wall modelling. Indeed, as stated in the introduction, the block imperfections have been studied apart.

Table 16. Material properties of concrete [70]

Ultimate compressive strength [MPa]	75
Ultimate tensile strength [MPa]	7
Young's modulus [N/mm^2]	41500
Poisson's ratio	0,2
Shear transfer coefficient for open crack, β_t	0,2
Shear transfer coefficient for closed crack, β_c	0,5

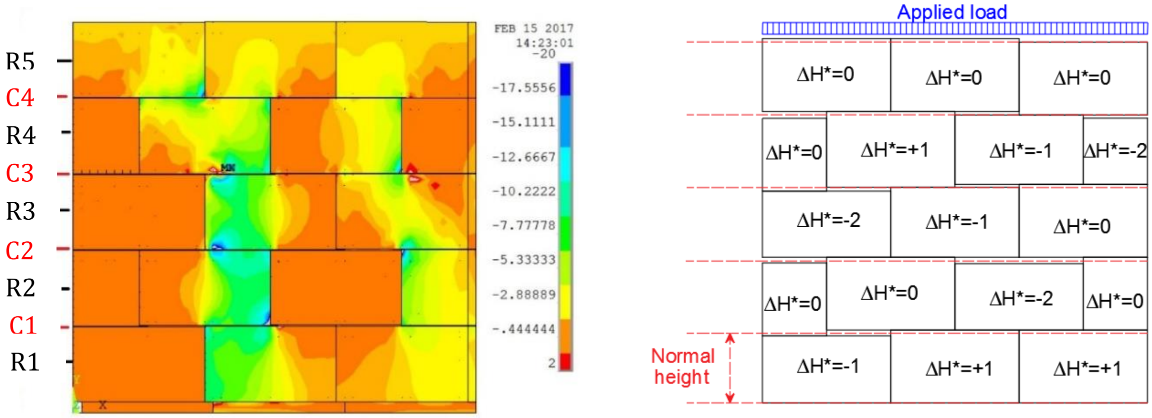

a) Stress distribution

b) Height deviation in [mm]

Figure 105. a) Stress distribution σ_y [MPa] in the wall [70] and b) height deviation of the masonry blocks ΔH* in [mm]

Figure 105 also highlights the load percolation in the wall, while showing the different load cases of single masonry blocks described in section 5.4.2.1. Due to the height difference between adjacent masonry blocks, the wall cracked at 24% of the ultimate load of a same wall without imperfections. Based on the initial load cases of the masonry blocks in the wall, one can describe the stress distribution.

In the following discussion, the gross compressive stress (σ) on the top course (R5 in Figure 105.a) is defined has being the ratio between the applied force and the contact area. The three masonry blocks of course R5 are uniformly loaded and their load cases are similar to load case 5. This being, premature cracking occurs and according to findings in section 5.4.2.1 - Table 15, the failure of these masonry blocks is predicted at 24% of the ultimate load of an isolated masonry block. In the contact area C4, the applied load percolates through one and a half block. Instead of a cross section of 1000 x 175 mm^2, the load passes through an actual section of 525 x 175 mm^2, which induce a local gross compressive stress of 2,0 σ. Due to the height imperfection of the masonry blocks, the actual contact area C4 is reduced and the stress is almost doubled in the course R4. This phenomenon explains the increase of the stress intensity observed in the masonry blocks of course R4 where only two blocks participate to the load percolation. The load case of the first masonry block corresponds to load case 5, while the load case of the second masonry block corresponds to load case 4.

Once more, because of the height imperfection of the masonry in the underlying course R3, the actual contact in C3 is reduced to a cross-section of 350 x 175 mm^2 (two half blocks). The drop of the cross section implies an increase of the gross compressive stress from 2,0 σ to 3,0 σ in the course R3. Between the three masonry blocks of the course R3, only two participate to the load percolation. The first masonry block is loaded according to load case 4 and the second masonry block according to load case 3. In this course (R3), the cracking of the face shells of the two bearing masonry blocks is predicted in the middle of the masonry block (Figure 102.a), at 12% of the ultimate load of an isolated masonry block. Moreover, in this course, the compressive stress in the top face of the masonry block is no longer evenly distributed, which plays a part to amplify the load concentration at the base of the masonry block. In the joint C2, the cross section available for the load percolation is the same as in C3, thus the gross compressive stress remains steady from course R3 to course R2. However, the stress peak observed in the joint C2 highlights the effect of the concentrated load coming from the above block.

The effect of the concentrated load appears on the left upper corner of the second masonry of course R3 as a local stress peak followed by a cracking (Figure 106). The same observation is established on the second branch of the load percolation system. The third masonry block of the fifth course partly transfers its load by a concentrated load applied on the right upper corner of the second full block of course R4. This point load is almost transferred from the upper corner to the lower corner and the cracking of the third masonry block of course R3 (Figure 106) highlights the intensity of the point load. The transfer of the load through contact area C1 is carried out without special features, as the cross section remains the same from C2 to C1. Finally, in course R1, only two masonry blocks bear the whole applied load. Each of these blocks is similar to the masonry defined in load case 2: only 50% of the support area of each masonry block support 80% of the applied load. One observes that the stress intensity in the two masonry blocks of this last course is slightly lower than the one observed in course R2, merely because of the increase of the actual contact area on the bottom faces. Nevertheless, the stress intensity of these masonry blocs remains higher and far from the one of the masonry blocks in course R5. On Figure 106, the ignition of cracks at low load level (9% of the ultimate load) in the face shells of the masonry blocks point out the harmful effect of the height variation of the blocks. This premature development of cracks limits the serviceability load of dry-stacked masonry walls.

Table 17 displays the results of Figure 105 for the masonry blocks taken individually. It represents the contact stress, the actual contact area as well as the different load cases of the masonry blocks of course R1, R3 and R5. The analysis of the results of Figure 105 grouped together in table 4 enables to highlight some key findings:

- For a constant load applied on the top course of a wall, the height difference between adjacent masonry blocks induces a stress amplification.
- The applied load is more concentrated in the intermediate and the bottom courses than in the upper course of the wall;
- The height imperfection of the masonry blocks in a course governs the load case of each masonry block, which therefore governs the load percolation system and finally the load-bearing capacity of the wall.

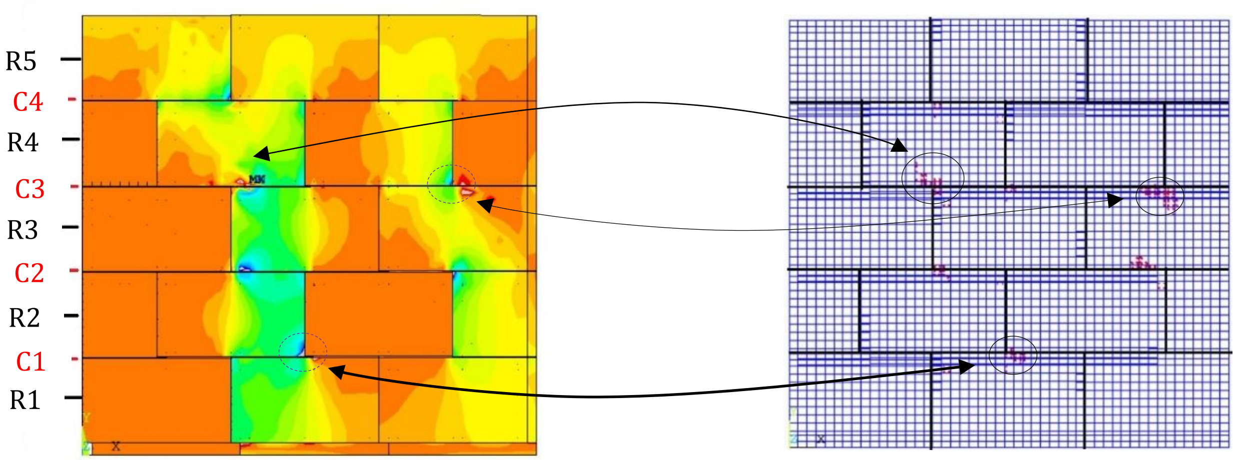

Figure 106. Stress distribution and crack path in wall A at 9% of ultimate load [70].

Table 17. Load cases and actual contact area in the wall for the masonry course R1, R3 and R5 at 9% of the ultimate load [70]

Wall A										
		Masonry block 1			Masonry bloc 2			Masonry bloc 3		
Course		Load case	Actual contact area* [%]	Max. gross stress [MPa]	Load case	Actual contact area [%]	Max. gross stress [MPa]	Load case	Actual contact area [%]	Max. gross stress [MPa]
R5	top	5	100%	1,48	5	100%	1,48	5	100%	1,48
	bottom		50%	2,97		50%	2,97		50%	2,97
R3	top	-	0%	0	4	50%	2,97	3	50%	2,97
	bottom		0%	0		50%	5,94		50%	2,97
R1	top	-	0%	0	2	50%	5,94	2	50%	2,97
	bottom		0%	0		100%	2,97		100%	1,48

*Actual contact area * - the actual contact here defined do not take into account the block bed-joint roughness*

In Figure 107, the curves C1 to C4 show the compression stress distribution over the length of the wall and in each of the four contact interfaces. These specific curves illustrate how the load is unevenly transferred within the wall. On curves C2 and C4, one observes the stress peaks, which come from the concentrated loads, resulting themselves from the load and support conditions of the overlying blocks.

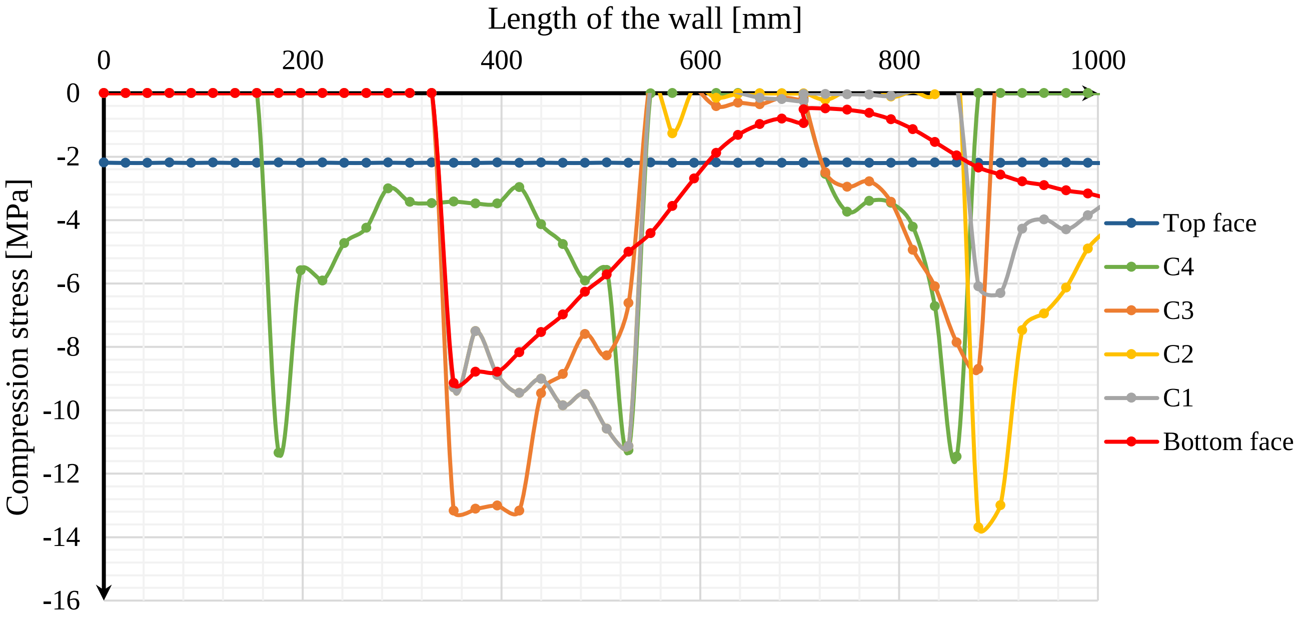

Figure 107. Compression stresses at each contact layer and on the top and the bottom faces of the wall [70]

b) Prediction of the stress amplification in a dry-stacked masonry

It has been observed that dry-stacked masonry suffers from stress concentration related to the actual load percolation system, which is in turn related to the height difference between the masonry blocks. In addition, a different disposition of the masonry blocks in a same basic dry-stacked masonry wall can leads to different load percolation systems. The existence of several load percolation systems in a basic wall induces the possibility of having several degree of stress concentration in the same wall. Thus, the need for the determination of the maximum stress peak in a statistical reliable way is of significant relevance.

In order to take into account the effect of the height difference ΔH* between adjacent masonry blocks, it is worth to define the useful section of a dry-stacked masonry wall. In this purpose, to predict an optimal useful section, it is necessary to gather and study all the load percolation systems that can occur in a wall. From the latter systems, the most probable systems are deduced as well as their influence on the stress amplification in the wall. In addition, it should be noted that the appearance of cracks in the face shells of the masonry blocks is likely to change the load percolation system of a wall. In the following, the stress amplification factor due to the height difference between adjacent masonry block will be evaluated for walls in the un-cracked state. The approach consists in defining an equivalent section coefficient k_{uE} calculated on the basis of all the possible load percolation systems in a wall of a given height and length. For a given wall with x masonry blocks in the length and y in the height, there is a large range of possible load percolation systems. From an analysis of the combinations of the load percolations systems, it has been observed that the number of load percolation systems (N) follows a logarithmic evolution with the increase of the height and length of the wall. Figure 108 shows the number of load percolation systems in function of the height and the length of a wall.

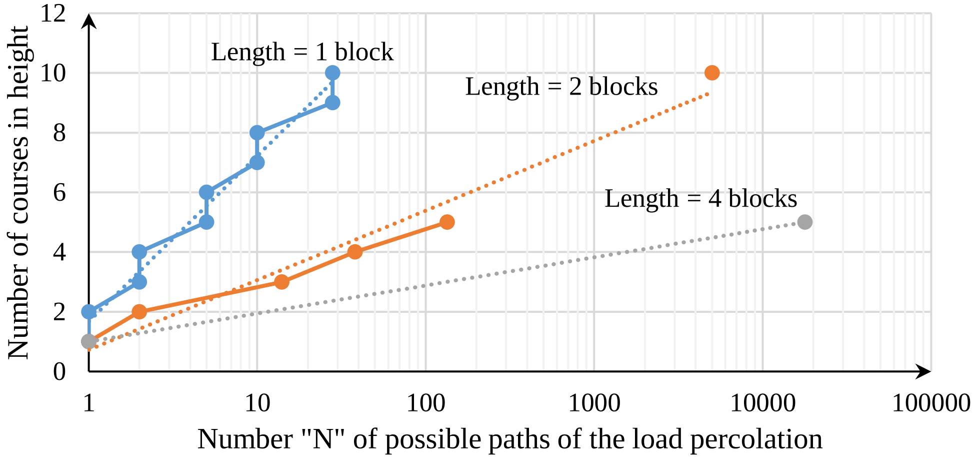

Figure 108. Number of load percolation systems depending on the height and length of a wall [70]

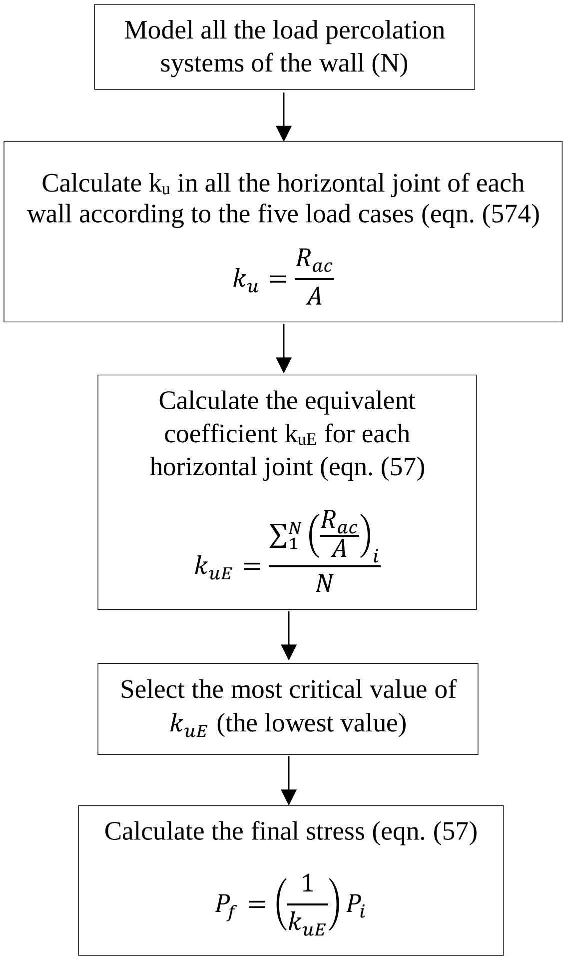

Figure 109. Algorithm for the determination of the amplified stress due to the geometric imperfections of the DSM blocks for N-load percolation systems (based on [70])

In a wall, the different load cases of the masonry blocks enable to draw the load percolation system from which the rate of the actual contact (R_{ac}) between the course is deduced. Figure 109 shows the flowchart of the algorithm for the determination of the equivalent useful section coefficient k_{uE}, leading to the maximum stress in the wall by taking into consideration the imperfections ΔH*. The useful section coefficient k_u in each horizontal joint of each load percolation system is given by the ratio of the actual contact area (R_{ac}) on the whole contact area (A), equation 54. Once the useful coefficient k_u calculated for each load percolation system, the equivalent coefficient k_{uE} is defined as being the mean value of k_u over the N-load-percolation systems considered see equation 55. The reliability of the equivalent coefficient k_{uE} is related to the number of load percolation systems studied. Indeed, the greater the number of load-percolation systems considered, the more reliable the mean value of k_{uE} is. This specific aspect is addressed in the design model in chapter 6, using a developed MATLAB program enabling to model the possible load-percolation systems in a wall. Following the calculation of the coefficient k_{uE} at each horizontal layer, the lowest value is selected to calculate the maximum stress amplification factor (see equation 56).

To show the interest of the method, a basic wallet built up of two block units in the length and three block units in the height has been studied. A uniform load of 9 N/mm^2 was applied on the top face of the wallet. It is worth to remind that the aim of the investigation was to predict the intensity of the amplified stress in the wall using the flowchart defined in Figure 109 and compare it to the stress peak predicted using the finite element model.

In a first approach, all possible load percolation systems were investigated using the finite element model (Figure 110) and the distribution of the compression stress was recorded at the base of all the wallets for the same load level (Figure 111). Furthermore, an envelope curve (green curve) covering the effect of all the load percolation systems has been drawn by linking all the stress peaks obtained over the studied models (Figure 111). Based on the shape of the envelope curve, it can be observed that the maximum stress intensity reached 25 N/mm^2, which is strongly increased compared to the applied load of 9 N/mm^2. The stress amplification factor goes up to 2,7 times the uniform applied load (25/9 N/mm^2). The FE approach permits to predict the crack pattern and the actual behaviour of the wall, but it requires much computational time, which will still become more important for an increased wall size.

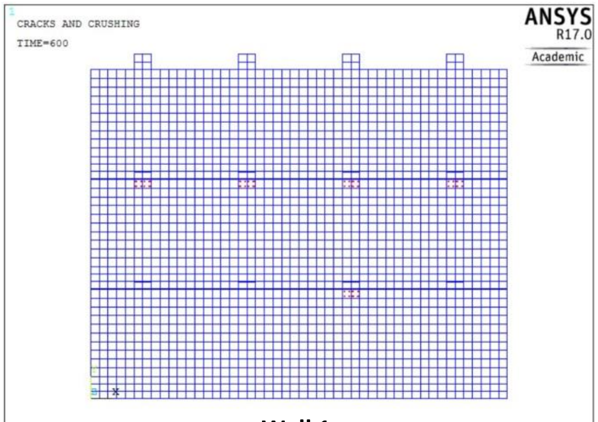

Wall 1

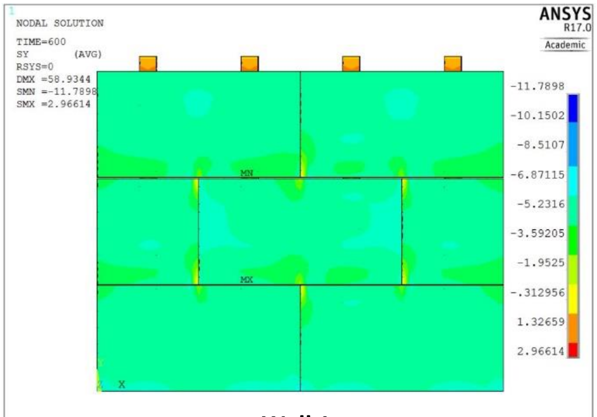

Wall 1

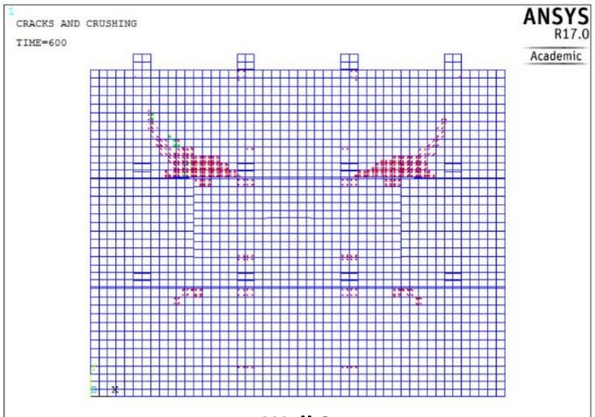

Wall 2

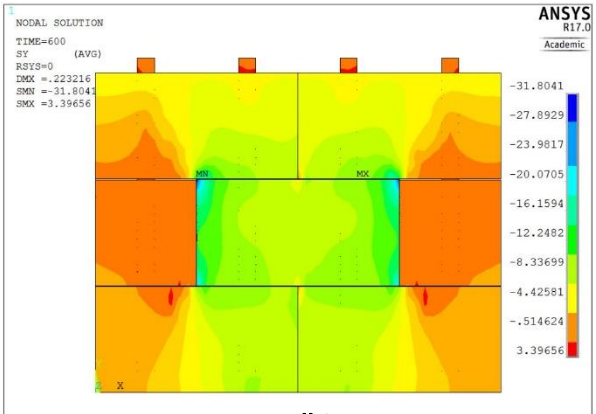

Wall 2

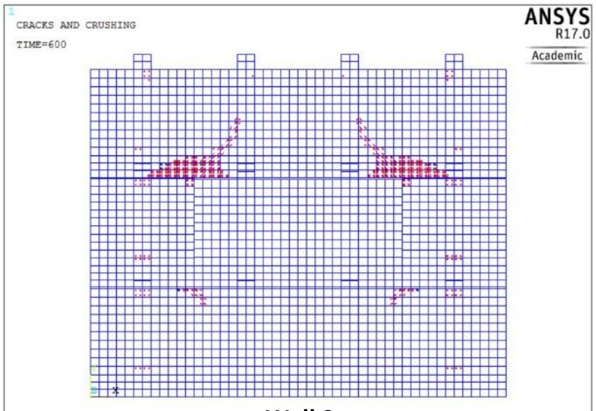

Wall 3

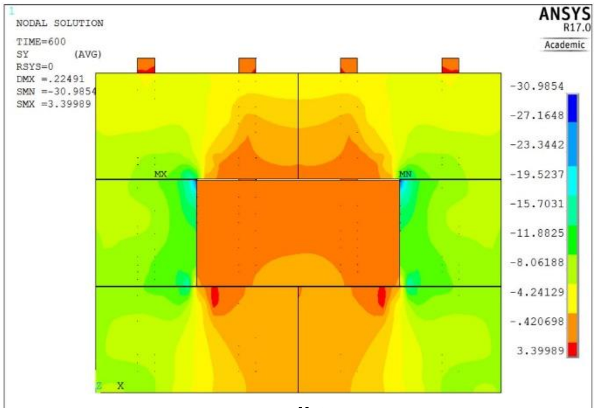

Wall 3

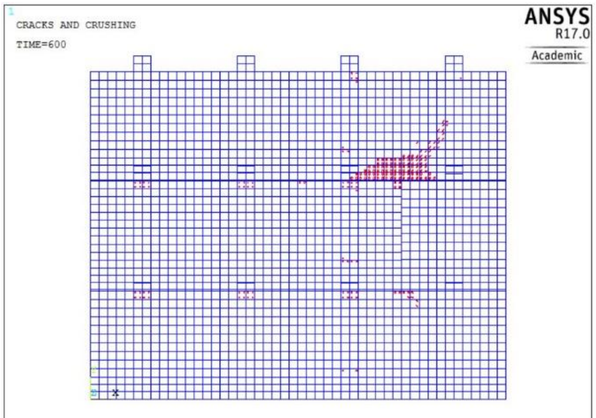

Wall 4

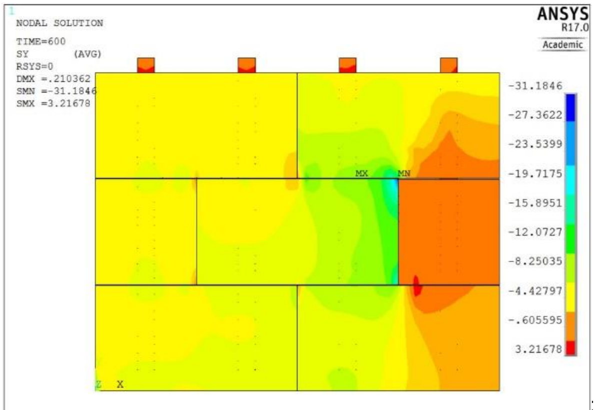

Wall 4

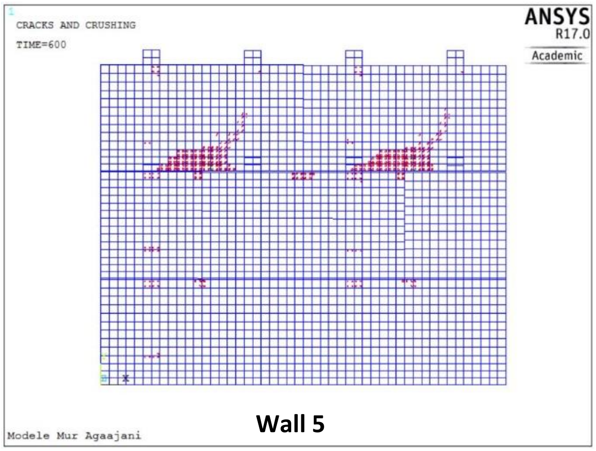

Wall 5

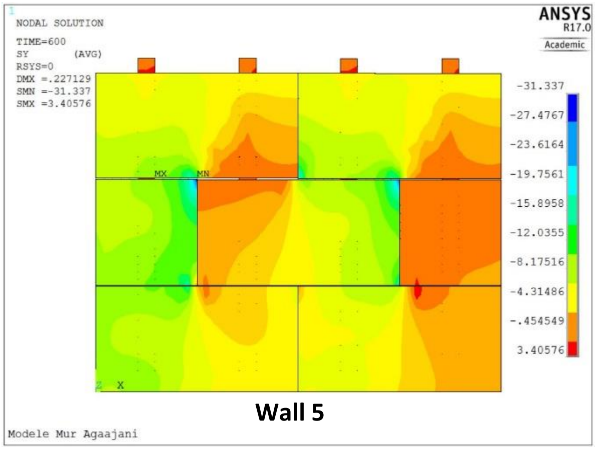

Wall 5

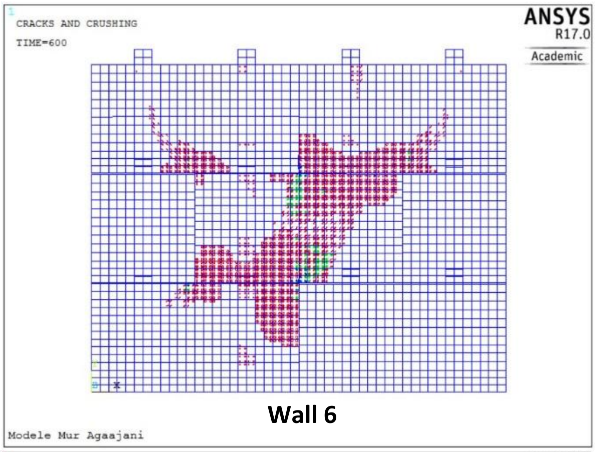

Wall 6

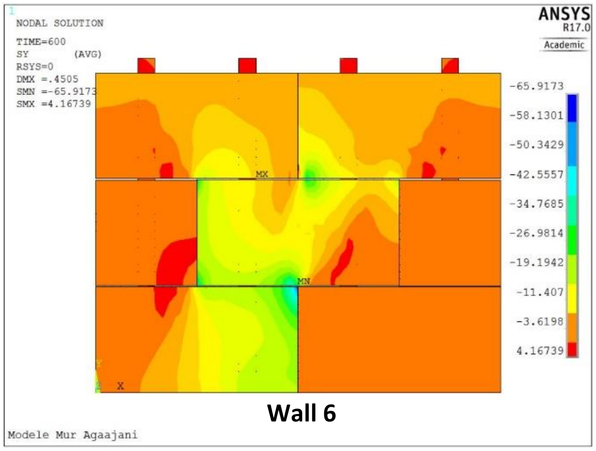

Wall 6

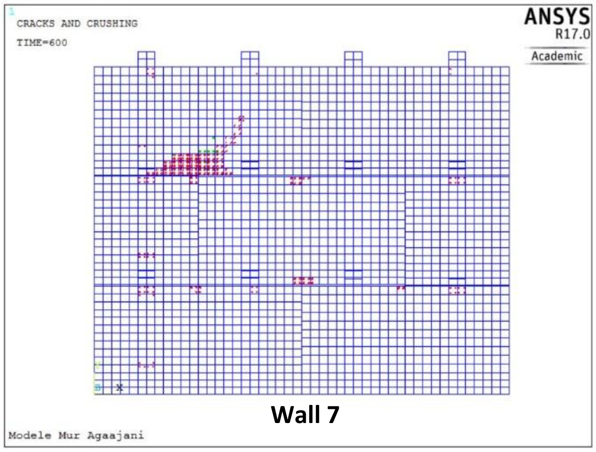

Wall 7

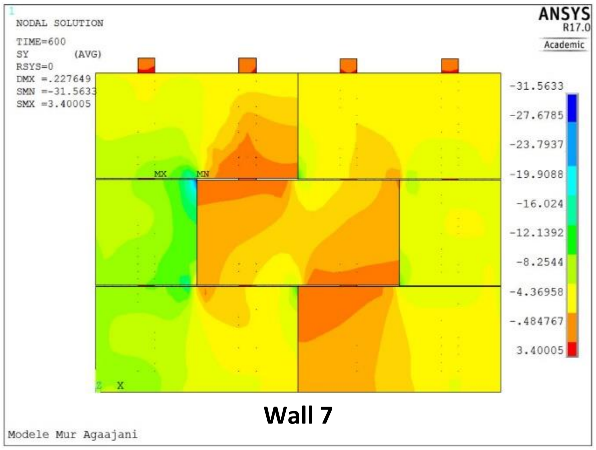

Wall 7

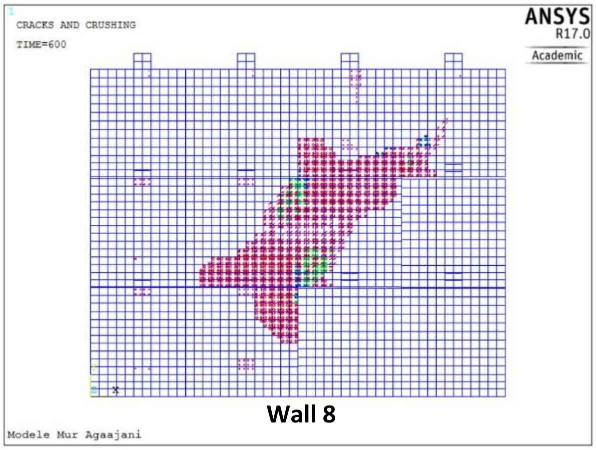

Wall 8

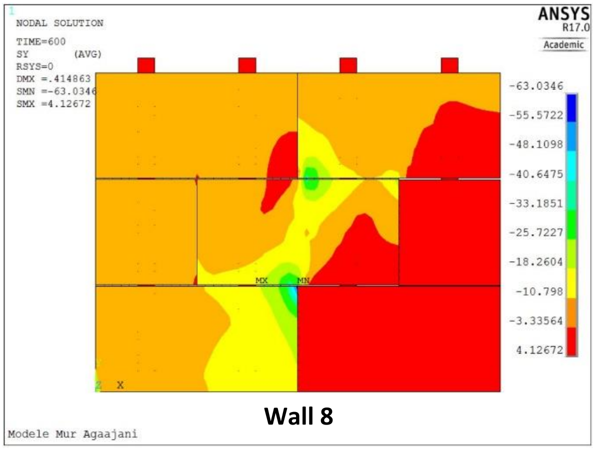

Wall 8

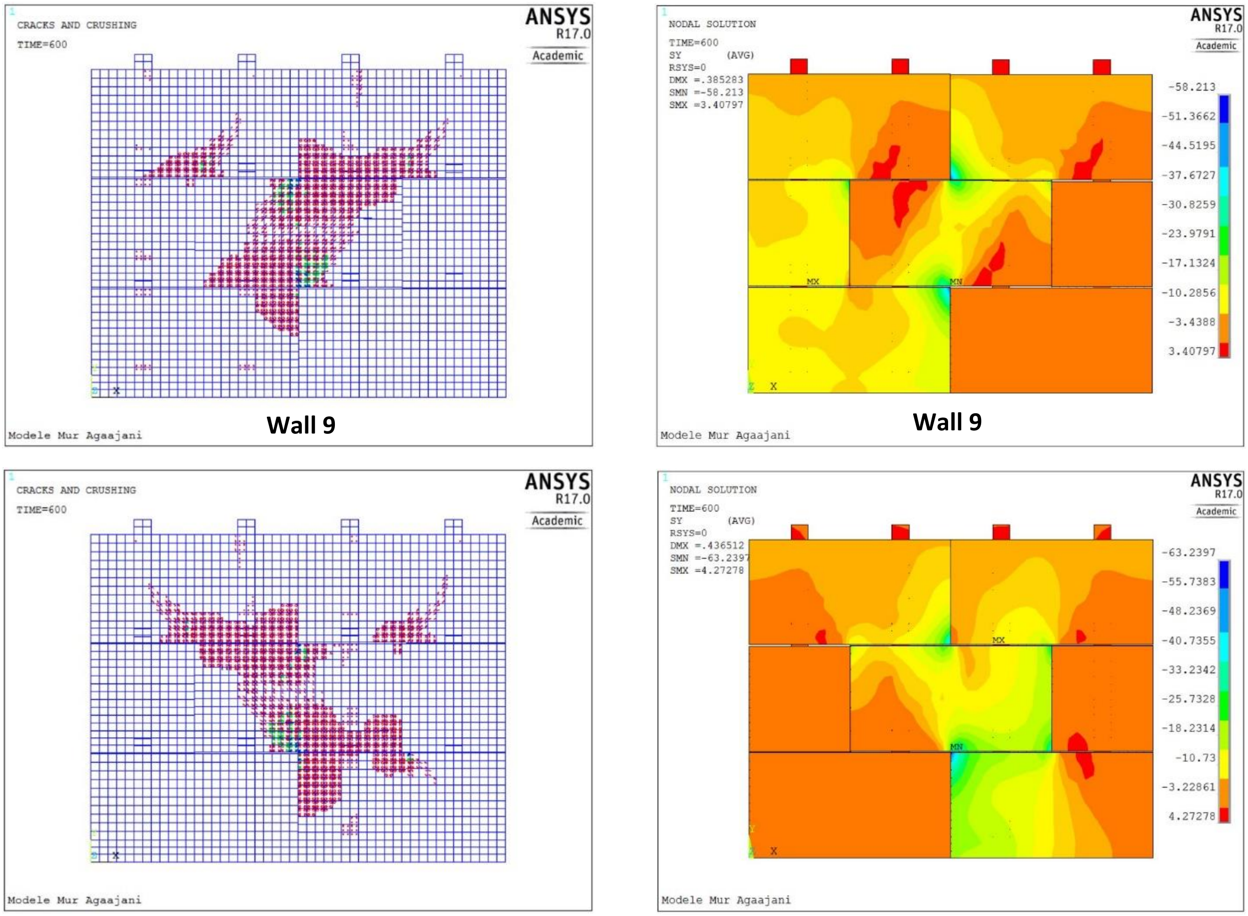

Wall 10 **Wall 10**

Figure 110. Crack path and σy stress distribution [MPa] shown for all possible load percolation systems of the studied wallet.

The crack path and the load bearing capacity of the dry-stacked masonry wall are governed by the load cases of its masonry blocks, themselves governed by the imperfections ΔH. As an illustration, compared to the ideal wall number 1, the walls 2, 3, 4 and 5 reach failure respectively at 46%, 48%, 49% and 65% of the ultimate load of wall 1. In the same way, walls 6, 7, 8, 9 and 10 reach failure respectively at 34%, 65%, 39%, 39% and 33% of the ultimate load of the ideal wall. Indeed, the geometric imperfections, especially the height variation of the blocks, impose a path to the load percolation, which very often lead to a concentration of the load in some masonry blocks of the wall. Thus, the failure load of some masonry blocks is reached despite the fact that the load applied on the top of the wall is far from the ultimate load of the masonry block.

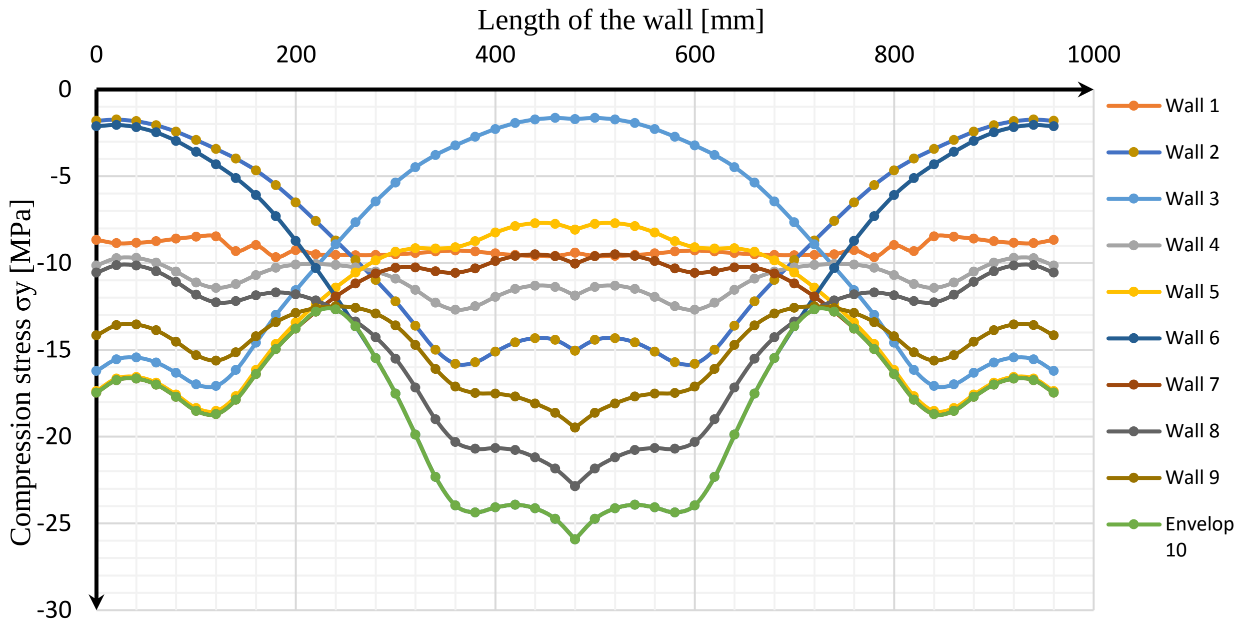

Figure 111. Compression stress intensity recorded on the support area of the wall in function of different wall configurations and wall lengths [70]

In the second approach, the flowchart defined in Figure 109 to predict the maximum stress in the wall is applied. Respecting the provisions of the flowchart in Figure 109, the useful section coefficient k_u in each horizontal joint was calculated for each of the ten load percolation systems, and then the equivalent useful coefficient k_{uE} was deduced. Table 18 summarizes the obtained results. Using this approach, the critical value of the coefficient k_{uE} was found equal to 0,47, which gives a stress amplification factor of 2,1 (1/0,47).

Table 18. Calculation of the equivalent useful section of a wallet of 2 blocks in the length and 3 in the height [70]

	k_u										k_{uE}	Critical k_{uE}
	Wall 1	Wall 2	Wall 3	Wall 4	Wall 5	Wall 6	Wall 7	Wall 8	Wall 9	Wall 10		
#3	1	1	1	1	1	1	1	1	1	1	1	0,47
#2	1	0,5	0,5	0,75	0,5	0,5	0,75	0,75	0,5	0,5	0,52	
#1	1	0,5	0,5	0,75	0,75	0,25	0,75	0,5	0,5	0,25	0,47	
#0	1	1	1	1	1	1	1	1	1	1	1	

The numerical analysis enables to find a multiplier factor of 2,7 with a maximum compression stress of 25 N/mm^2, while, the analytical approach enables to find a multiplier factor of 2,1 with a maximum compression stress of 19,2 N/mm^2.

5.4.3 Improved dry-stacked masonry blocks (I.DSM$_b$)

This sub-section presents the finite element modelling of the mitigation strategy used to overcome the effects of the height difference encountered in dry-stack masonry. The numerical investigation in section 5.4.2.2 have shown that the height difference ΔH_D between adjacent masonry blocks leads to a significant stress concentration in DSM walls that can exceed 2 times the uniform load applied. From a structural perspective, such a stress amplification increases the safety hazards and therefore should be reduced as much as possible. Based on the results of the experimental tests, the masonry blocks of groups 4 and 6 were found as being those that can offer a structural benefit to dry-stacked masonry. Accordingly, they have been selected for the parametric study of the effect of the contact layer against the height difference between the masonry blocks. The mechanical properties of the contact layer materials determine in chapter 4 have been exploited in the finite element analysis.

5.4.3.1 Wall model and studied parameters

For a consistent comparison of DSM walls modelled with DSM blocks of different groups, the basic wallet tested in the lab was modelled while purposely inserting and distributing the same height difference ΔH_D between the masonry blocks from one model to another (Figure 112). The representation of the height difference between the masonry blocks in Figure 112 is amplified only for good visualisation purposes. The finite element model of the basic wallet is also presented in Figure 113. The vertical displacement was restrained at the base of the wallet ($u_y = 0$ at $y = 0$) and a symmetry plane was defined about the z-axis at z = 100 mm. A uniform compressive load was applied on the top face of the wallet. The constant height difference ΔH_D between the masonry blocks was set successively equal to 0,5 mm, 1,0 mm and 2,0 mm.

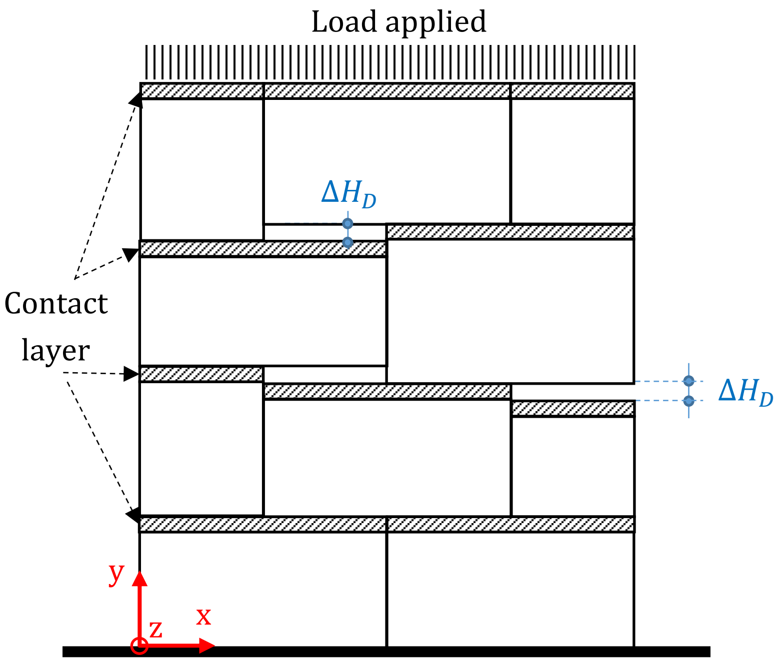

Figure 112. Basic DSM wallet with the height difference ΔH_D between the masonry blocks

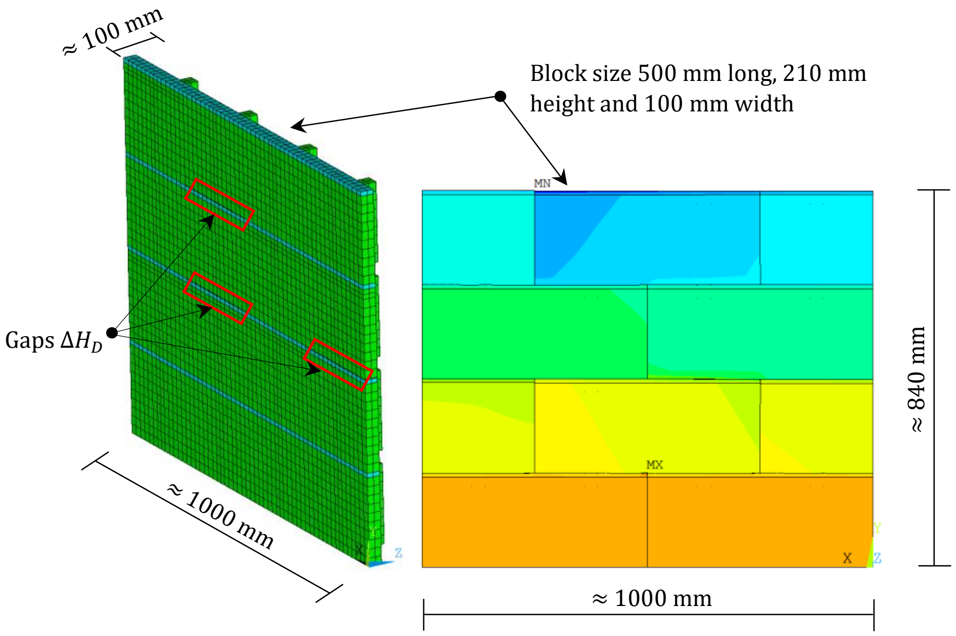

Figure 113. FE model of the basic DSM wallet with the contact layer

5.4.3.2 Finite element results

Figure 114 and Figure 115 show respectively the normal stress distribution and the state of the actual contact area in the wallets of W-groups 1, 4 and 6, at 95% of $P_{\text{u. FE-Réf}}$, and for a height difference ΔH_D of 1,0 mm between the masonry blocks.

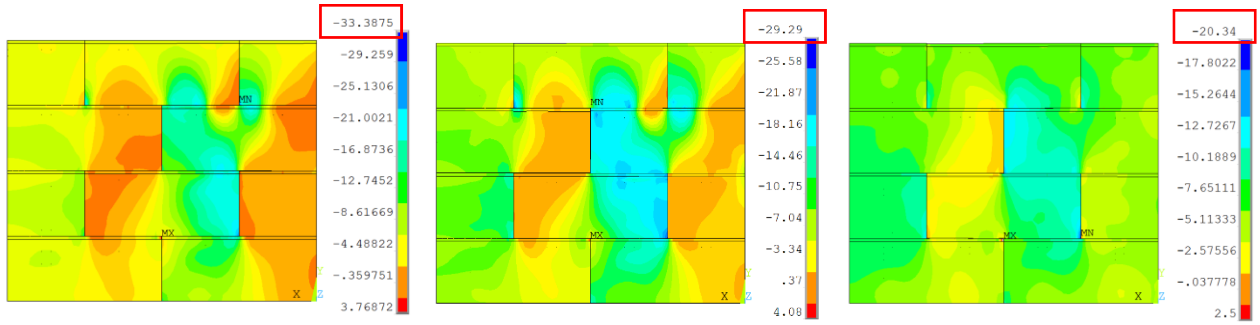

W-group 1
(No contact layer)

W-group 4
(Contact layer – mix C)

W-group 6
(Contact layer – mix E)

Figure 114. Stress distribution in the dry-stacked masonry wallets of W-groups 1, 4 and 6 at 95% of $P_{\text{u. FE-Réf}}$ and for a height difference ΔH_D of 1,0 mm

The DSM wallet of W-group 1 (without contact layer) clearly exhibits the maximum stress amplification around the ultimate stage of the loading (Figure 114 – W-group 1). This is related to the limited actual contact between the masonry blocks. Indeed, as the masonry blocks undergo only a slight deformation, the height difference ΔH_D of 1,0 mm limits the actual contact between the block units (Figure 115), which limits the load distribution and explains the local stress amplification. Regarding the DSM wallet of W-group 4, despite the height difference ΔH_D of 1,0 mm between adjacent masonry blocks, they experienced lower vertical stresses. The DSM wallet of W-group 4 shows a stress peak reduction of roughly 12% with respect to the DSM wallet of W-group 1. This reduction results from the slight increase in the actual contact, which led to a slightly wider load distribution in the wallet. Concerning now the DSM wallets of W-group 6, faced with the same height imperfections as the wallet of W-group 1, they exhibited a significant stress peak reduction of about 39%. This substantial reduction of the stress peak is due to the significant improvement of the actual contact in the bed-joints. As shown in Figure 115, the masonry blocks in the wallet of W-group 1 experience a continuous contact in the bed-joints, which results in a better load distribution from one course to another one. Nevertheless, despite the full contact, the masonry blocks in the DSM wallet of W-group 1 still present a non-uniform stress distribution due to a differential strain experienced by the block units. However, the amplitude of variation of stress is less important than in the DSM wallet of W-group 1.

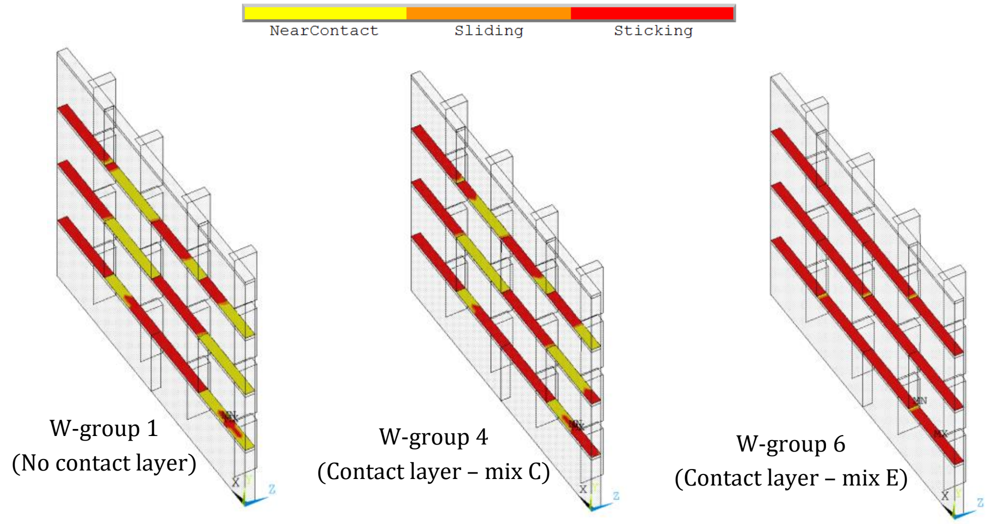

W-group 1
(No contact layer)

W-group 4
(Contact layer – mix C)

W-group 6
(Contact layer – mix E)

Figure 115. State of the actual contact in the dry-stacked masonry wallets of W-groups 1, 4 and 6 at 95% of $P_{\text{u. FE-Réf}}$ and for a height difference ΔH_D of 1,0 mm

Table 19 summarises the stress peaks, the rate of the actual contact area and the ultimate load-bearing capacity of the wallets of W-group 1, 4 and 6, for a height difference ΔH_D of 0,5 mm, 1,0 mm and 2,0 mm respectively. The data of Table 19 are also presented in Figure 116, Figure 117 and Figure 118, for discussing apart the effects of the height difference ΔH_D on the stress peak, the actual contact area and the ultimate load-bearing capacity of dry-stacked masonry.

Table 19. Stress peak, rate of the actual contact and load bearing capacity of DSM wallet for a height difference ΔH_D of 0,5 mm, 1,0 mm and 2,0 mm.

		DSM W-group 1	DSM W-group 4	DSM W-group 6
$\Delta H_D = 0{,}5$ mm	Stress peak [MPa]	-24,7	-24,7	-18,6
	Actual contact rate [%]	61%	87%	99%
	Ultimate strength [N/mm^2]	3,7	4,4	6.0
$\Delta H_D = 1{,}0$ mm	Stress peak [MPa]	-33,4	-29,3	-20,3
	Actual contact rate [%]	58%	64%	99%
	Ultimate strength [N/mm^2]	3,3	4,2	5,9
$\Delta H_D = 2{,}0$ mm	Stress peak [MPa]	-36	-30,1	-22.0
	Actual contact rate [%]	52%	61%	90%
	Ultimate strength [N/mm^2]	3,0	3,8	5,7

- Height difference ΔH_D and rate of the actual contact area

Figure 116 shows the variation of the rate of the actual contact area in the wallet in function of the height difference (ΔH_D) between adjacent masonry blocks. For the wallet of W-group 1 as for the wallets of W-group 4 and 6, although the contact layer enables for reaching higher actual contact area in the bed-joints, it is observed that the actual contact area decreases as the height difference (ΔH_D) between the masonry blocks increases. In addition, it is also observed that the capacity of the contact layer for improving the actual contact area is reduced for ΔH_D equal or greater than 1,0 mm. As it is observed in Figure 116, for $\Delta H_D = 0{,}5$ mm, the actual contact area in the wallet of W-group 4 is increased by 26% with respect to the wallet of W-group 1. For $\Delta H_D \geq 1{,}0$ mm, the improvement of the actual contact area is limited to 6-9%.

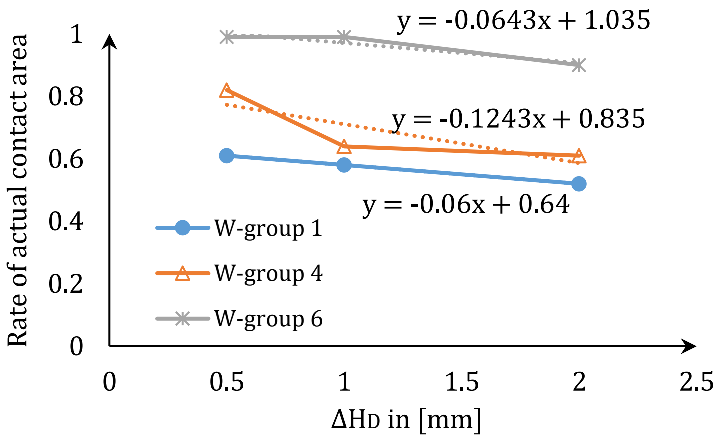

Figure 116. Height difference and rate of the actual contact area in the DSM wallets

- Height difference ΔH_D and stress peaks

Figure 117 shows the variation of the maximum stress peak in the wallet in function of the height difference ΔH_D between adjacent masonry blocks. It is observed that the intensity of the stress peak increases with the increase of the height difference ΔH_D. Indeed, this trend of increase is a direct consequence of the decrease of the rate of the actual contact area in the bed-joint. At any given constant load, the lower the actual contact area between two courses, the higher the resulting stress in the contact interface. However, it is also observed that the slope of the curves of increase of the stress peak is steeper for the wallet of W-group 1 (raw block units) than for the wallet of W-group 4 and 6 (improved blocks). This is a result of the capacity of the contact layer to partly overcome the height difference between the masonry blocks.

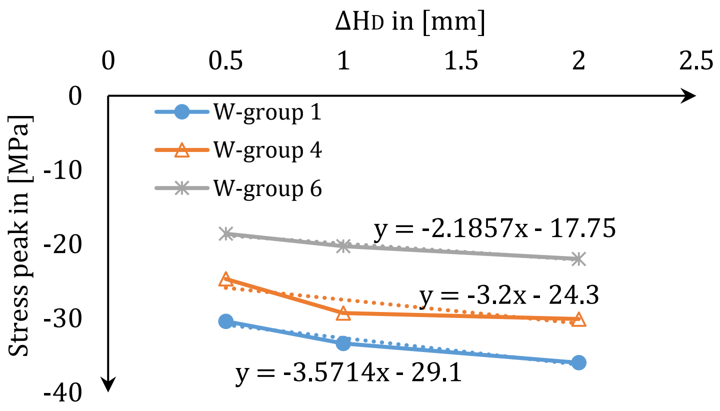

Figure 117. Height difference and stress peak in the DSM wallets

- Height difference ΔH_D and load-bearing capacity of the wallet

Figure 118 shows the variation of the load-bearing capacity of the wallet in function of the height difference ΔH_D between adjacent masonry blocks. It is observed that the load-bearing capacity of dry-stacked masonry decreases with the increase of the height difference between the masonry blocks. Indeed, this reduction of the load-bearing capacity is related both to the decrease of the actual contact area and the increase of the stress peak in the wallet.

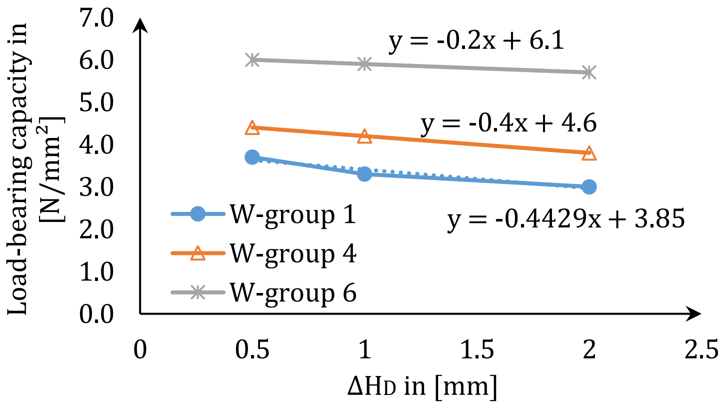

Figure 118. Height difference and load-bearing capacity of the DSM wallets

5.5 Summary

Within this chapter, the proposed mitigation strategy consisting in placing an additional layer on the top face of the raw DSM blocks was investigated considering varying the bed-joint roughness and the height difference between the block units as well as the contact layer materials used in the experimental investigations.

It has been found that the block imperfections yield significant and non-permissible stress concentration in raw dry-stacked masonry. However, the contact layer has been shown to reduce the stress peaks and improve the stress distribution in dry-stacked masonry. The masonry blocks of W-group 6 using mix E was found very effective for reducing the stress peaks by overcoming the bed-joints roughness and the height difference between adjacent blocks units, although they might be expensive and practically challenging in use on construction sites since they exhibit very large axial deformations not allowed in buildings. The masonry blocks of W-group 4 were also found to marginally reduce the stress peaks in dry-stacked masonry, however with very much less axial deformations than in the DSM of W-group 6. The finite element analysis underscored the capability of the improved dry-stacked masonry blocks to overcome up to 2,0 mm of height difference between adjacent masonry blocks in a wall.

In a general statement, it has been deduced that the reduction of the stress peak yielded by the increase of the actual contact area helps for reducing the extent of local failure in the bed-joints, which ultimately enables DSM for withstanding more loads. Following the numerical investigations, a design model has been developed for engineering purposes, considering both the effects of the block bed-joint roughness and the height difference between adjacent masonry block in the prediction of the load-bearing capacity of DSM. This topic is addressed in the following chapter.

6 Design model for predicting the load-bearing capacity of a dry-stacked masonry

This chapter is based on the work published in the following research paper:

- *Gelen Gael Chewe Ngapeya, Danièle Waldmann, Experimental and analytical analysis of the load-bearing capacity P_u of improved dry-stacked masonry, Journal of Building Engineering 27 (2020), 100927.*

6.1 Introduction

This chapter tackle the development of a design model capable for predicting the load-bearing capacity of dry-stacked masonry. The proposed model was designed based on the equations recommended by EN 1996-1-1 [1] for mortared masonry (eq (58)). In the formula of equation (58), γ_M stands for the safety factor, ϕ includes the slenderness effects, t stands for the block thickness and K is a coefficient to be apply in function of the material used to make the blocks (clay, concrete, etc). Furthermore, f_b represents the normalized block compressive strength and f_m the mortar compressive strength respectively. α and β are powers varying for thick and thin mortar joints in masonry.

The models proposed to predict the load-bearing capacity of a dry-stacked masonry while considering the impact of the geometric imperfections of its block units are given in the equations (59) and (60). Equation (59) is designed for the raw DSM_b and equation (60) for the improved blocks (blocks with an additional layer). In the proposed approach, the coefficients α and β of equation (58) are modified and the impact of the block imperfections are introduced through two new factors, i.e. δ_h for the height variation and δ_r for the bed-joint roughness. The constant α, which has been increased with respect to the value proposed by EN 1996-1-1 [1], is a constant allowing to introduce the participation of the own compressive strength of the block units on the final compressive strength of a wall. As concluded Kang-Ho et al. [60], DSM strength can approach the material strength if the bed-joint imperfections are well levelled. Indeed, as a higher DSM wall exhibits more bed-joints than smaller walls, the influence of the bed-joint imperfections was then introduced in the proposed design model for predicting the load-bearing capacity of dry-stacked masonry. Within the development of the proposed models (eq (59) and (60)), as the effects of the imperfections are coupled, the mathematical expression and the power of the different coefficients was defined to fit the best with the experimental results and this was then validated with the results of other experiments of the literature.

$$N_{Rd.\ EN1996-1-1} = \frac{1}{\gamma_M}\left(\phi\ t\ K\ f_b^{\alpha}\ f_m^{\beta}\right) \tag{58}$$

α = 0,85 and β = 0 for thin mortared masonry
α = 0,7 and β = 0,3 for mortared masonry;

$$N_{Rd.\ proposed} = \frac{1}{\gamma_M}\left(\phi\ t\ K\ f_b^{0.95}\right)\delta_h{}^{0.85(1-\delta_r)} \tag{59}$$

$$N_{Rd.\ proposed} = \frac{1}{\gamma_M}\left(\phi\ t\ K\ f_b^{0.85}\ f_m^{0.2}\right)\delta_h{}^{0.85(1-\delta_r)} \tag{60}$$

δ_h	reduction factor due to the height variation
δ_r	reduction factor due to the bed-joint roughness

The factors δ_h and δ_r were determined through experimental measures and statistical modelling presented in the upcoming sub-section.

6.2 Determination of factor δ_r

The influence of the bed-joint roughness was indirectly measured. Factor δ_r is defined as being the mean rate of the maximum actual contact area in the bed-joints of two dry-stacked masonry blocks. Indeed, δ_r is obtained by reporting the maximum reachable actual contact area to the nominal face-shell area of a block unit. The actual values of δ_r reported in Table 20 were experimentally measured (Figure 119) on twenty-five (25) dry-stacked masonry prisms constituted of 3-courses of blocks. To do so, masonry prisms were built using randomly selected raw and improved DSM$_b$. The masonry prisms were axially compressed to failure and the maximum actual contact area in the bed-joints were measured using Prescale Fujifilm strips. The Prescale Fujifilm strips were then digitalised and processed on

MATLAB for calculating the rate of the recorded actual contact. Since the actual bed-joint unevenness varies from a block unit to another, the actual contact area was measured on twenty (20) full face-shell bed-joints for each P-group of masonry prisms. The coefficients of variation presented in Table 20 show that δ_r barely varies in each P-group.

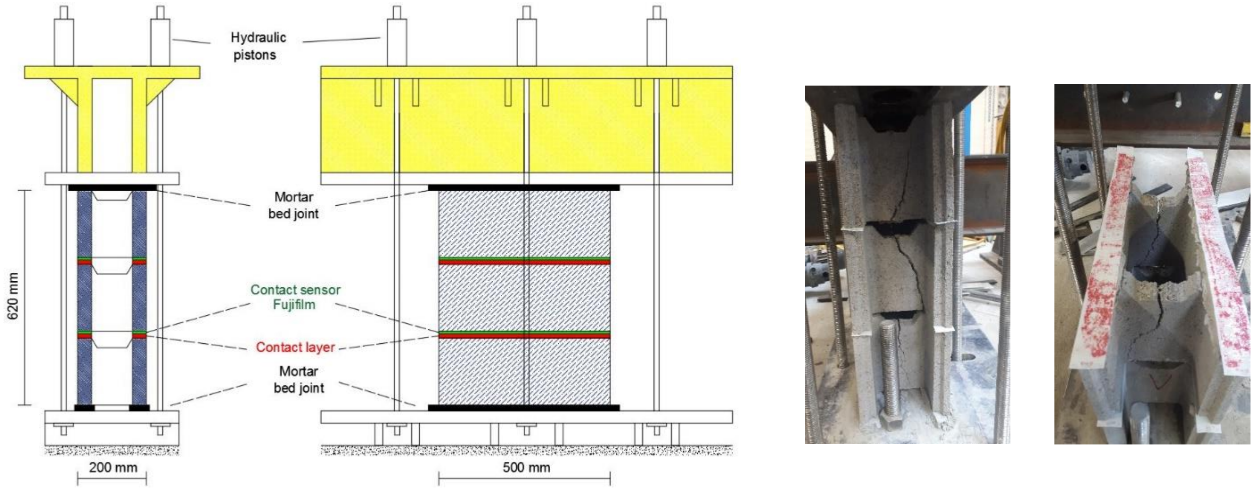

Figure 119. Test measuring the maximum actual contact area in the bed-joints of DSM [121]

Table 20. Factor δ_r due to the block bed-joint roughness [121]

Masonry prisms tested	Factor (δ_r)	Coef. of variation
P-group 1 – block units without contact layer – raw blocks	23%	4%
P-group 2 – block units with a contact layer – mix A	50%	7%
P-group 3 – block units with a contact layer – mix B	50%	8%
P-group 4 – block units with a contact layer – mix C	55%	8%
P-group 5 – block units with a contact layer – mix D	40%	7%

6.3 Determination of factor δ_h

Factor δ_h depicts the overall reduction of the useful section of the wall yielded by the height deviation (ΔH^*) of block units. As shown in Figure 120, the height difference (ΔH_D) between adjacent masonry blocks in a course yields two types of 'bed-joint status' in the horizontal joints: the open bed-joints and the closed bed-joints. Both bed-joint status were also assumed by Nguyen et al. [71] and Agaajani et al. [66]. The open bed-joints are the horizontal joints where the bed-faces of the block units are separated by the height difference (ΔH_D) between adjacent block units. Regarding the closed bed-joints, two sub-status are defined. There is (1) the closed bed-joints with useful sections, i.e. the horizontal joints where the bed-faces of the block units are in contact and the applied load percolates. There is also (2) the closed bed-joints with useless sections, i.e. the horizontal joints where the bed-faces of the block units are in contact but where the applied load does not transit because the overlying block unit is not loaded. Nonetheless, the closed bed-joint defined throughout the paper is based on the hypothesis of a full contact without any influence of the bed-joint roughness.

The actual height of 110 masonry blocks used in the current investigation has been measured to the nearest tenth of a millimetre. The data exhibited a Gaussian distribution with a mean value of 200,2 mm and a standard deviation of 1,0, see Figure 121. For a same wall, the arrangement of the block units randomly varies from a construction to another. Accordingly, the rate of the useful face δ_h and the load percolation system [70,80,82] also vary from a construction to another. Thus, for the determination of the most likely value of the useful face δ_h, a statistical reliable approach was developed. The flowchart for the determination of the useful section of a dry-stacked masonry wall was defined in [70] and recalled in section 5.4.2.2.

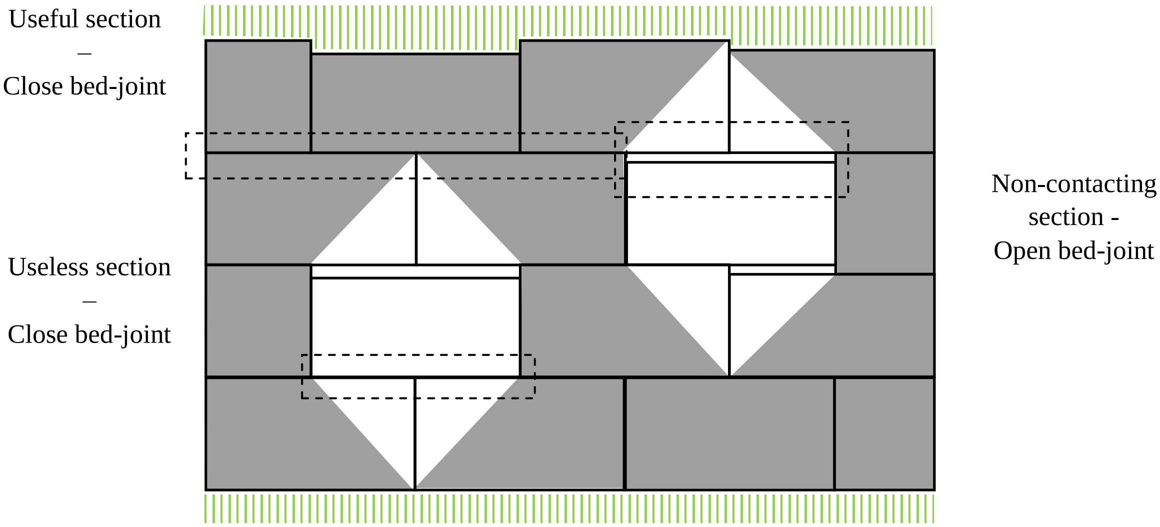

Figure 120. Type of contact status occurring between courses in dry-stacked masonry [121]

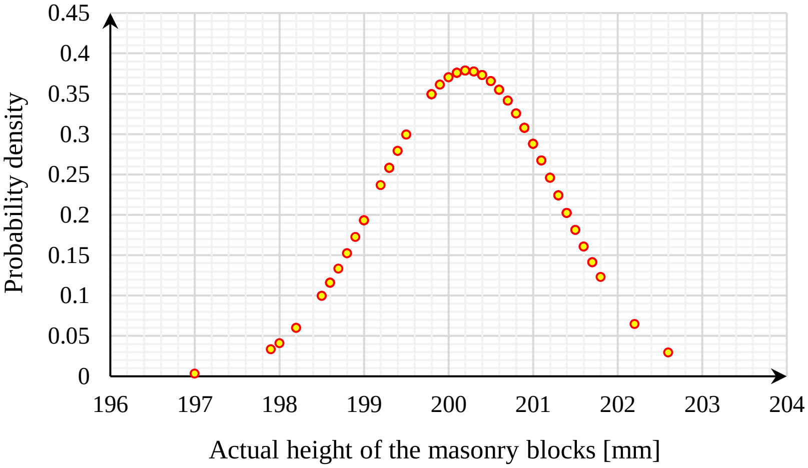

Figure 121. Probability density of the block height [121]

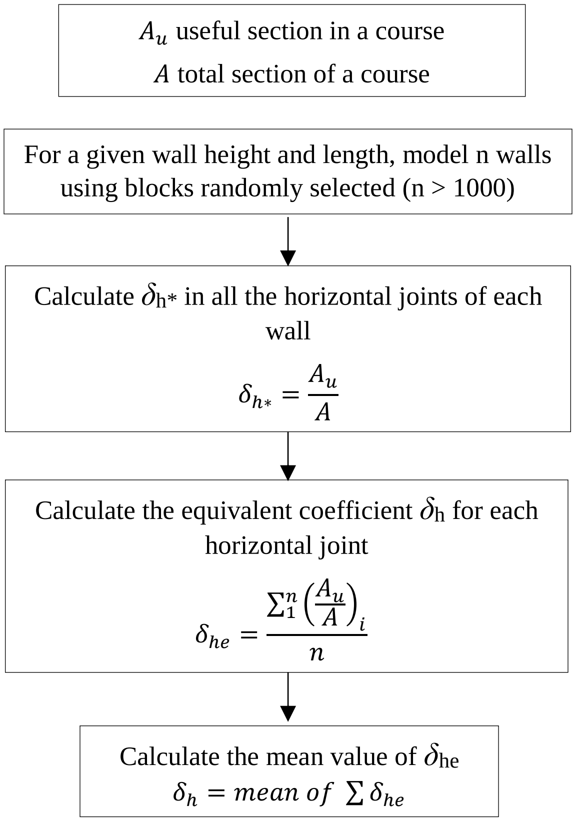

Figure 122. Algorithm for the determination of δ_h derived from [70].

Figure 122 shows the flowchart for the determination of δ_h. In this flowchart, for a given wall, A_u represents the useful section of a bed-joint, i.e. the section through which the load percolates (see Figure 120). A represents the total section of a bed-joint, regardless of the height difference between the masonry blocks. For determining δ_h, n random load percolation systems are firstly modelled, then the ratio (δ_{h*}) between the useful section and the total section is calculated in each horizontal joint for each load percolation system modelled. Following that, an equivalent coefficient (δ_{he}) is calculated in each horizontal joint by considering all the load-percolation systems modelled. Finally, the factor δ_h is obtained by calculating the mean value of δ_{he} over the height of the wall. In the current investigation, the flowchart defined in [70] and in section 5.4.2.2 was slightly modified in the way of calculating δ_h. Instead of using the smallest value of δ_{he}, δ_h represents the mean value of δ_{he} over the wall height except the top and the bottom faces. The modified flowchart (Figure 122) was then implemented in MATLAB to carry out a statistical analysis and to bring out the most likely value of δ_h for a given wall. Figure 123 presents the user interface of the MATLAB program developed to ease the calculation of δ_{he} and finally δ_h. The MATLAB program takes 5 parameters as inputs: (1) the number of masonry blocks in height, (2) the number of masonry blocks in length, (3) the maximum height recoverable, (4) the number of walls modelled and (5) the number of cracks. The first and the second parameters are obtained by dividing respectively the height and length of the wall to the height and length of the block unit. The third parameter enables to predict δ_{he} while considering a reduction of the height difference between the block units. It is worth to precise that the height difference ΔH_D is the difference between the actual height of two adjacent masonry blocks, while the height recoverable is the amount of height difference that a masonry block can overcome. The reduction of the height difference could be generated by a grinding process or by the axial deformation of the block unit upon loading. The fourth parameter (n) refers to the number of walls randomly constructed for calculating the mean value of δ_{he} per course. The fifth parameter enables to update δ_{he}, considering the block rearrangement following a full face-shell splitting. In addition to the 5 input parameters, a user can still add the actual height distribution of its block units.

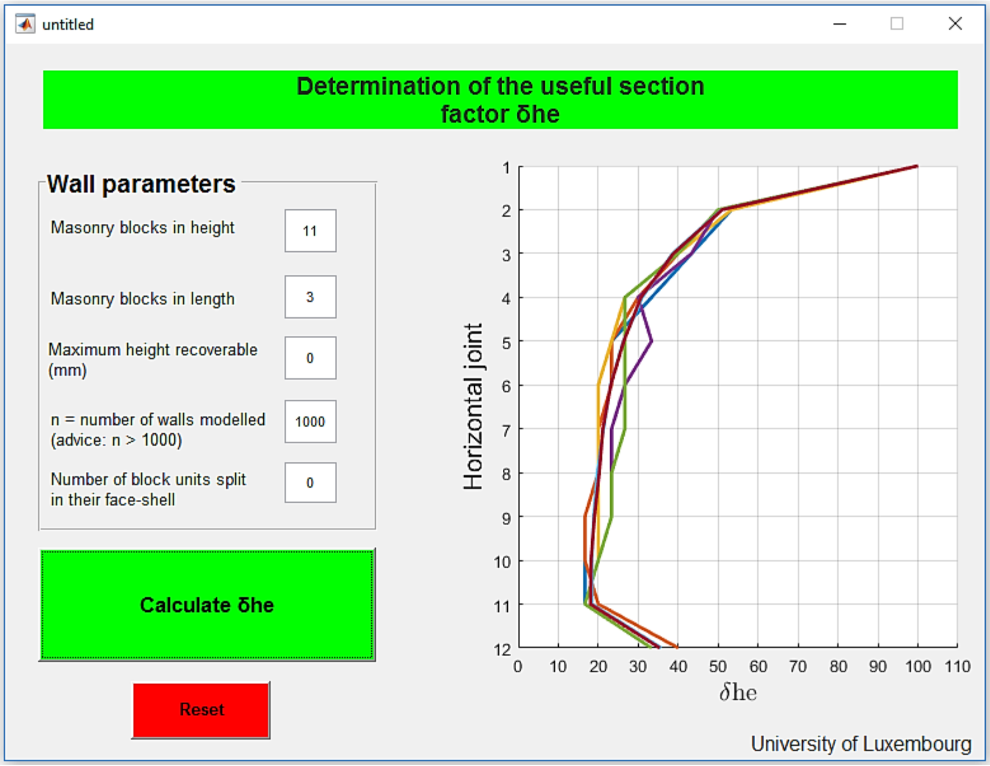

Masonry blocks in height: 11

Masonry blocks in length: 3

Maximum height recoverable (mm): 0

n = number of walls modelled (advice: n > 1000): 1000

Number of block units split in their face-shell: 0

Figure 123. User interface of the flowchart implemented on MATLAB R2017 [121]

Figure 124 shows the mean value of δ_{he} for a nominal wall with 11 block units in the height, 3 block units in the length and different values of n. In Figure 124, a model is defined as being the mean value of δ_{he} per course, obtained following the random construction of n walls. Accordingly, it has been observed that for the calculation of δ_{he}, different models (model 1, 2, etc.) are found for $n << 1000$ (e.g. n=5). This stems from the fact that different arrangements of block units may occur during the construction of a same nominal wall. However, for n greater than 1000, it has been observed that δ_{he} converges toward a steady value regardless the model. From a statistical point of view, this means that there is a tendency of repeatability, which has been exploited for defining δ_h in the proposed design model. It was also observed that δ_{he} depends on the height and the length of both block unit and wall. Indeed, for a given block unit, as the wall height increases, the number of added joints leads to an increase of imperfections, which makes decrease δ_{he}. In addition, for a given wall height and length, the smaller the dimensions of the masonry block, the more there are vertical and horizontal joints, which means again more imperfections and a lower value for δ_{he}.

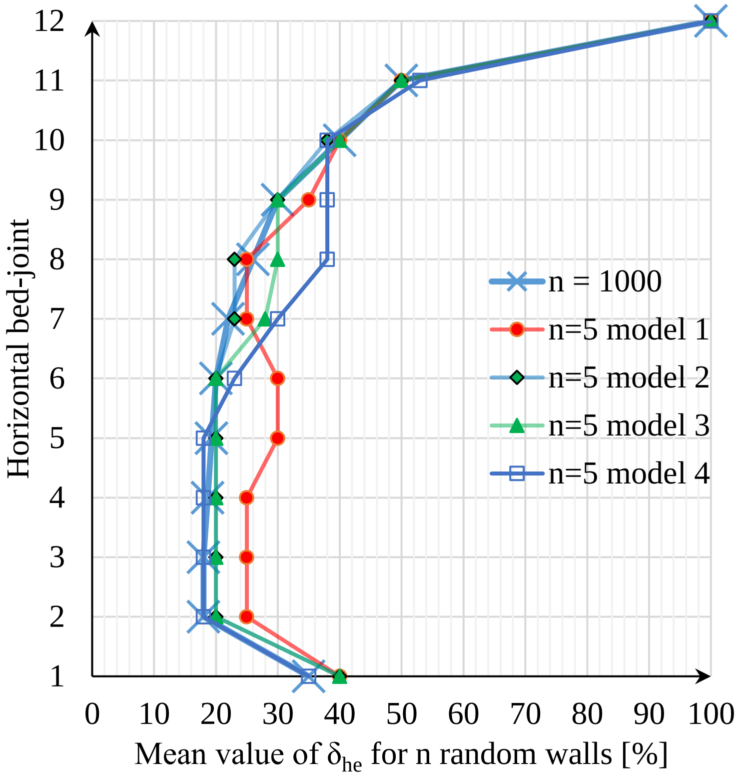

Figure 124. Calculation of factor δ_{he} for a wall with 11 courses and 3 full-blocks in the length. (δ_{he} for n = 5 and δ_{he} for n = 1000) [121]

Exploiting the developed MATLAB code, a designer's diagram was established for determining the factor δ_h (using n = 1000 walls). As shown in Figure 125, the factor δ_h is given in function of the number of block units in the height and length of a DSM wall.

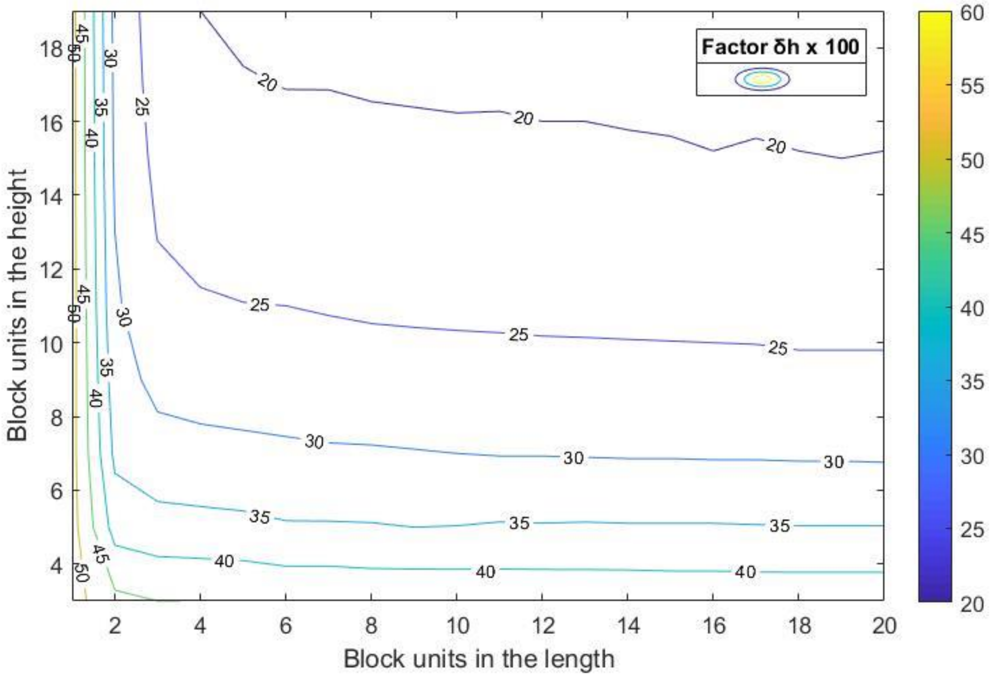

Figure 125. Factor δ_h in function of the number of block units in the height and length of a DSM wall [121]

6.4 Implementation

The mathematical model proposed in the current investigation (eq. (59), (60)) has been used to calculate the load-bearing capacity of dry-stacked masonry walls whose data of the experimental tests were collected in the literature [45,50,73,84,85,88]. Likewise, the standards EN 1996-1-1 [1] for mortared masonry (eq. (58)) was also used to predict the load-bearing capacity of the same dry-stacked masonry walls. The parameters used for the calculation with the proposed model and the standards EN 1996-1-1 [1] are presented in Table 21. The shape factor presented in Table 21 is defined by EN 772-1 [117] in function of the height and the width of a block unit. Indeed, the shape factor is multiplied by the air-dry compressive strength of a block unit for determining its normalized compressive strength. The coefficient K presented in Table 21 is a constant defined in EN 1996-1-1 [1] in function of the material of the block units (concrete, clay, etc) and their classification according to their ratio of hollows. The results of the two approaches, summarized in Table

22, were compared each with the experimental measures. All along the calculation, the safety factor for the material concrete γ_M of equations (58), (59) and (60) has been taken equal to 1,0 as the predicted values of the load-bearing capacity were compared to the experimental ones. A factor for the 'prediction accuracy' defined as being the ratio between the predicted and the experimental value is plotted in Figure 126 for the standards EN1996-1-1 [1] and the proposed model, both in function of the compressive strength of the block units.

The analysis of the results shows that the proposed model predicts accurately the load-bearing capacity (P_u) of a dry-stacked masonry wall. Regarding the raw DSM_b (rows 1-8 of Table 22), the proposed model predicts P_u with a mean accuracy of 93% and a standard deviation of about 12%. For the same category (raw DSM_b), the standards EN 1996-1-1 [1] for masonry with a thin mortar layer predicts P_u with a mean accuracy of 137% and a standard deviation of about 29%. Regarding the improved DSM_b (rows 9-12 of Table 22), the proposed model predicts P_u with a mean accuracy of 106% and a standard deviation of roughly 10%. At the same time, the standards EN 1996-1-1 [1] predicts P_u with a mean accuracy of 124% and a standard deviation of about 9%.

Table 21. Parameters for the calculation of the load-bearing capacity of a wall [121]

	Rui et al. [88]	Rui et al. [88]	Sturm et al. [50]	Drysdale et al. [84]	Mohd et al. [85]	Waleed et al. [73]	Agaajani [45]	**Current investigation**				
								W-group 1	**W-group 2**	**W-group 3**	**W-group 4**	**W-group 5**
Factor δr due to the block bed-joint roughness	0,23	0,23	0,23	0,23	0,23	0,23	0,23	0,23	0,50	0,50	0,55	0,40
Factor δh due to the block height variation	0,52	0,52	0,30	0,52	0,37	0,27	0,37	0,41	0,41	0,41	0,41	0,41
Shape factor – EN 772-1 [117]	0,9	0,9	0,9	1,15	1,25	1,25	1,25	1,15	1,15	1,15	1,15	1,15
Factor K – EN 1996-1-1 [1]	0,75	0,75	0,75	0,65	0,65	0,65	0,65	0,65	0,45	0,45	0,45	0,45

Table 22. Load-bearing capacity with the proposed model, with the standard for mortared masonry and following the experimental tests [121]

		Height (Thickness) [mm]	**Block strength [N/mm^2]**	**Load-bearing capacity in [n/mm^2]**			**Accuracy (%)**	
				Experimental (P_u)	EN 1996-1-1 [1]	Proposed model	EN 1996-1-1 [1]	Proposed model
Rui et al. [88]		500 (140)	8,80	3,30	3,68	2,95	112%	89%
Rui et al. [88]		500 (140)	12,00	4,60	4,61	3,95	100%	86%
Sturm et al. [50]		810 (140)	1,96	0,53	1.02	0,50	192%	94%
Drysdale et al. [84]		812 (203)	10,30	3,90	4,72	3,93	121%	101%
Mohd et al. [85]		1200 (150)	15,20	5,90	6,56	4,56	111%	77%
Waleed et al. [73] & **Alwathaf et al.** [69]		3000 (150)	17,20	3,89	5,67	3,02	146%	78%
Agaajani [45]		1250 (200)	26,30	5,35	8,40	5,64	157%	105%
Current investigation	**W-group 1**	800 (200)	13	3.66	5,72	3,76	156%	114%
	W-group 2	840 (200)	13	3,70	4,95	3,85	134%	111%
	W-group 3	840 (200)	13	3,88	4,83	3,79	124%	104%
	W-group 4	840 (200)	13	4,83	5.01	4,05	104%	92%
	W-group 5	840 (200)	13	2,15	2,76	2,39	128%	120%

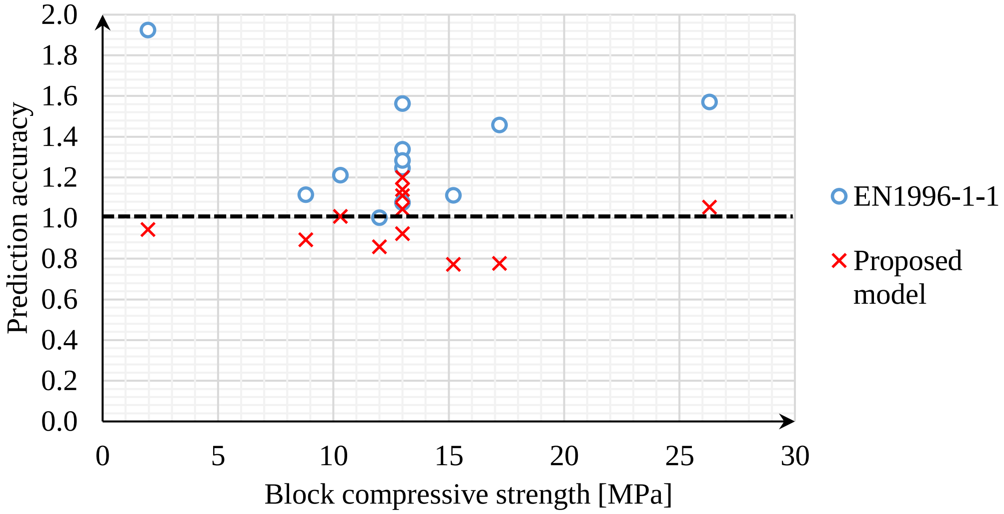

Figure 126. Accuracy factor of the prediction [121]

In a general overview (Figure 126), it is found that the standards EN 1996-1-1 [1] applied to dry-stacked masonry consistently overestimates the actual bearing capacity under axial compressive load, which constitutes a safety hazard if it is exploited for designing of DSM. This overestimation could be explain by the fact that the standards EN 1996-1-1 [1] was designed for mortared masonry structures. Indeed, in the latter structures, the horizontal mortar layer inter alia acts as surface and row leveller, which enables avoiding stress concentration suffered by dry-stacked masonry. On the other hand, as shown in Figure 126, the proposed mathematical model estimates quite well the load-bearing capacity of dry-stacked masonry walls regardless the compressive strength of the block units.

6.5 Summary

This chapter has reported the formulation of a design model considering the effect of the block imperfections for predicting the load-bearing capacity of dry-stacked masonry. The effect of the bed-joint roughness has been considered by capturing, through experimental tests, its impact on the reduction of the actual contact in the ultimate load stage of DSM prisms. The effect of the height difference between adjacent masonry blocks in a DSM wall has been considered by a statistical reliable prediction of its effect on the overall reduction of the actual contact between the block courses in a wall. It has been observed that the developed design model is effective for predicting the load-bearing capacity of dry-stacked masonry wall. In brief, it has been observed that:

1. The standards EN 1996-1-1 for masonry overestimate the load-bearing capacity of dry-stacked masonry (relative to experiments) and accordingly cannot be safely used in structural designing of such a masonry system.
2. The proposed mathematical model enables predicting the load-bearing capacity P_u of the raw dry-stacked masonry with a mean accuracy of 93% and a standard deviation of 12%. In addition, it enables predicting P_u for the developed improved DSM with a mean accuracy of 106% and a standard deviation of 10%

7 Conclusion

7.1 Summary and core findings

In dry-stacked masonry, the block unit imperfections (i.e. the bed-joint roughness and the height deviation) are the key factors leading both to premature cracking and to walls underperformance in compression. The current thesis was devoted to address this issue and propose a mitigation strategy for improving the in-plane response of dry-stacked masonry.

Experimental evidences

The work investigated a strategy for improving the load-bearing capacity of DSM by using an additional layer (called contact layer) placed on the top face of the raw masonry blocks. Five materials were experimented for manufacturing the contact layer. Four conventional materials were compared to an auxetic material. The efficiency of the strategy was discussed in terms of improvement of the actual contact area and the load-bearing capacity experimentally measured on dry-stacked masonry prisms and wallets. All along the investigations, 25 DSM masonry prisms of 0,50 x 0,60 m and 20 DSM masonry wallets of 1,00 x 0,80 m constructed with raw and improved block units were tested under axial compression. In summary, the key findings from the research are highlighted in the following bullets:

1. The actual contact in the bed-joint interface of raw dry-stacked masonry blocks ($R.DSM_b$) is limited to barely a quarter (≈ 23%) of the nominal surface of the face-shells.
2. The contact layer of the DSM-prisms of P-group 2 (mix A), P-group 3 (mix B), P-group 4 (mix C) and P-group 6 (mix E) enables to ensure a mean actual contact of respectively 50%, 50%, 55% and 98% of the nominal surface of the face-shell, compared to solely 23% for the DSM-prisms of P-group 1 (without contact layer).
3. The increase of the actual contact owed to the contact layer significantly affects the load-bearing capacity of a masonry prism since the mean compressive strength of the

masonry prisms of P-group 2, 3, 4, and 6 were respectively enhanced by 16%, 14%, 37%, and 97% in comparison to the masonry prisms of P-group 1.

4. The use of an auxetic material (P-group 6 - mix E) significantly mitigates the lateral expansion near the bed-joints, which delays the splitting of the webs and increases the load-bearing capacity.
5. The rate of increase of the actual contact area is the more significant the more the Young's Modulus and the stiffness of the material of the contact layer decrease. Indeed, the yield strength of the material eases the deformation and ultimately the crushing of the asperities in the bed-joint interfaces.
6. The rate of the actual contact area in the bed-joints of the DSM_b is a function of three parameters: the material properties of the contact layer; the roughness or the unevenness of the bed-joints coming into contact and the level of the compressive load applied on top of the DSM.
7. Improved dry-stacked masonry blocks with well-defined properties were more efficient than raw dry-stacked masonry blocks in terms of load-bearing capacity. The use of mix A (W-group 2), mix B (W-group 3) and mix C (W-group 4) in the contact layer of the $I.DSM_b$ makes it possible to improve the load-bearing capacity of wallets of 1,00 x 0,80 m by roughly 1,0%, 6,1% and 31,9% respectively.
8. Although the compressibility of a low strength material like mix D (W-group 5) is good for improving the actual contact between the masonry blocks, the strong lateral expansion due to a positive Poisson' ratio yields tensile stresses that weakens the performance of wall in compression. The use of mix D leaded to a reduction of the reference load-bearing capacity by 41%.
9. The predominant failure mechanisms of DSM are the development of vertical cracks in the face-shells around on average 53% to 82% of P_u, followed by the ignition of cracks at the interfaces webs/face-shells around 90% to 95% of P_u, then finally the face- shell spalling around the bed-joint interface at roughly more than 90% of Pu.

Numerical investigations

The effectiveness of the contact layer for overcoming the block imperfections and improve the stress distribution in dry-stacked masonry was evidenced. In summary, it was found that:

- The geometric imperfections of the block units leads to a significant stress concentration in dry-stacked masonry, as they generate contact discontinuities in the bed-joints.
- The rate of increase of the actual contact area is the more significant as the Young's Modulus and the strength of the material of the contact layer decrease. Indeed, the yield strength of the material eases the deformation and ultimately the crushing of the asperities in the bed-joint interfaces, which contributes to improve the actual contact area.
- Independently from the material of the contact layer and the roughness of the bed-joints, the increase of the compressive load enables to increase the rate of the actual contact in the bed-joint of the DSM.
- The use of auxetic material in the contact layer of improved block units enables to achieve full contact in the bed-joints and to ensure a uniform stress distribution in DSM despite the presence of the block imperfections.
- The use of a contact layer enables to reduce the intensity of the stress peaks occurring in DSM, which ultimately leads to an improvement of their load-bearing capacity.

The comparison between the FE model and the experimental tests showed that the numerical approach enables to well depict the actual response of DSM. A summary of all the combinations investigated using the experimental and the finite element approach has been outlined in the Introduction. The few combinations which have not been experimentally investigated have still been analysed through finite element modelling.

Design model

In the current research project, a design model was proposed for predicting the load-bearing capacity of dry-stacked masonry while taking into consideration the effects of the block imperfections. The influence of the block imperfections on the reduction of the actual contact area in DSM was introduced through two new factors, the first one for the block bed-joint roughness and the second one for the height difference between adjacent masonry blocks. The first factor was defined by measuring the maximum actual contact area in the bed-joints of dry-stacked masonry prisms. The second factor was defined through a statistical and reliable estimation of the most likely rate of the actual contact area in a DSM, considering the reduction of the actual contact area generated by the height difference between block units. The proposed design model was validated using the results of former experimental tests on dry-stacked masonry collected in the literature. The prediction of the proposed design model was also compared to the prediction based on the current European standards for masonry structures. In a brief, the main findings can be summarised as follows:

1. The current European standards for masonry significantly overestimate the actual load-bearing capacity of dry-stacked masonry.
2. The proposed design model is more conservative in the prediction of the load-bearing capacity of dry-stacked masonry.

7.2 Outlook

The outcomes of the present research can be the base for further research project in the field of dry-stacked masonry.

First, the effectiveness of the contact layer herein evidenced on dry-stacked masonry prisms and wallets can be experimentally tested on full-scale DSM walls. Extensive experimental tests on full-scale walls with different type of masonry blocks can be realized for correlating the effectiveness of the contact layer to the masonry type.

Furthermore, the development of a material mixing as much as possible the features of auxetic materials to the features of medium strength mortar can constitute a full research project. The objective being to provide sufficient axial deformations for covering the block imperfections without generating lateral stresses and very large axial deformations.

References

[1] EN 1996-1-1, Eurocode 6: Design of masonry structures – Part 1-1: General rules for reinforced and unreinforced masonry structures. London: British Standards Institution, 2005.

[2] K.S. Gumaste, K.S.N. Rao, B.V.V. Reddy, K.S. Jagadish, Strength and elasticity of brick masonry prisms and wallettes under compression, Mater. Struct. Constr. 40 (2007) 241–253. doi:10.1617/s11527-006-9141-9.

[3] Fernando S. Fonseca ; Gihad Mohamad; Paulo B. Lourenço; Humberto R. Roman; A. T. Vermeltfoort, Deformation and failure mode of masonry, in: 12th North Am. Mason. Conf., 2015.

[4] J.A. Thamboo, M. Dhanasekar, Correlation between the performance of solid masonry prisms and wallettes under compression, J. Build. Eng. 22 (2019) 429–438. doi:10.1016/j.jobe.2019.01.007.

[5] S.R. Sarhat, E.G. Sherwood, The prediction of compressive strength of ungrouted hollow concrete block masonry, Constr. Build. Mater. 58 (2014) 111–121. doi:10.1016/j.conbuildmat.2014.01.025.

[6] M.H. Dhanasekar, R; Ferozkhan, M; Dhanasekar, Behaviour of dry stack concrete masonry blocks under eccentric compression, in: 14th Int. Brick Block Mason. Conf., 2008.

[7] W.A.M. Thanoon, A.H. Alwathaf, J. Noorzaei, M.S. Jaafar, M.R. Abdulkadir, Finite element analysis of interlocking mortarless hollow block masonry prism, Comput. Struct. 86 (2008) 520–528. doi:10.1016/j.compstruc.2007.05.022.

[8] W.A. Thanoon, A.H. Alwathaf, J. Noorzaei, M.S. Jaafar, M.R. Abdulkadir, Nonlinear finite element analysis of grouted and ungrouted hollow interlocking mortarless block masonry system, Eng. Struct. 30 (2008) 1560–1572. doi:10.1016/j.engstruct.2007.10.014.

[9] C.V.U. Vyas, B.V.V. Reddy, Prediction of solid block masonry prism compressive

strength using FE model, Mater. Struct. Constr. 43 (2010) 719–735. doi:10.1617/s11527-009-9524-9.

[10] A. Drougkas, P. Roca, C. Molins, Numerical prediction of the behavior, strength and elasticity of masonry in compression, Eng. Struct. 90 (2015) 15–28. doi:10.1016/j.engstruct.2015.02.011.

[11] A. Zucchini, P.B. Lourenço, A micro-mechanical model for the homogenisation of masonry, Int. J. Solids Struct. 39 (2002) 3233–3255. doi:10.1016/S0020-7683(02)00230-5.

[12] A. Anthoine, Derivation of the in-plane elastic characteristics of masonry through homogenization theory, Int. J. Solids Struct. 32 (1995) 137–163. doi:10.1016/0020-7683(94)00140-R.

[13] Anthoine, Homogenisation of periodic masonry: plane stress, generalised plane strain or 3D modelling?, Numer. Methods Eng. 13 (1997) 319–326.

[14] S.B. Bati, G. Ranocchiai, G. Ranocchiai, L. Rovero, A micromechanical model for linear homogenization of brick masonry, Mater. Struct. 32 (2006) 22–30. doi:10.1007/bf02480408.

[15] B. Panasenko, Homogenization: averaging processes in periodic media, Kluwer Acad. Publ. (1989).

[16] K.F. Abdulla, L.S. Cunningham, M. Gillie, Simulating masonry wall behaviour using a simplified micro-model approach, Eng. Struct. 151 (2017) 349–365. doi:10.1016/j.engstruct.2017.08.021.

[17] G. Mohamad, P.B. Lourenço, H.R. Roman, Mechanics of hollow concrete block masonry prisms under compression: Review and prospects, Cem. Concr. Compos. 29 (2007) 181–192. doi:10.1016/j.cemconcomp.2006.11.003.

[18] E.H. Fahmy, T.G.M. Ghoneim, Behaviour of concrete block masonry prisms under axial compression, Can. J. Civ. Eng. 22 (2010) 898–915. doi:10.1139/l95-107.

[19] M.N.D. Abrams, Mechanics of masonry in compression, J. Struct. Eng. 111 (1985)

857–870.

[20] A. Drougkas, E. Verstrynge, R. Hayen, K. Van Balen, The confinement of mortar in masonry under compression: Experimental data and micro-mechanical analysis, Int. J. Solids Struct. 162 (2019) 105–120. doi:10.1016/j.ijsolstr.2018.12.006.

[21] A. Zucchini, P.B. Lourenço, Mechanics of masonry in compression: Results from a homogenisation approach, Comput. Struct. 85 (2007) 193–204. doi:10.1016/j.compstruc.2006.08.054.

[22] T. Zahra, M. Dhanasekar, A generalised damage model for masonry under compression, Int. J. Damage Mech. 25 (2016) 629–660. doi:10.1177/1056789516656745.

[23] A. Costigan, S. Pavía, O. Kinnane, An experimental evaluation of prediction models for the mechanical behavior of unreinforced, lime-mortar masonry under compression, J. Build. Eng. 4 (2015) 283–294. doi:10.1016/j.jobe.2015.10.001.

[24] G. Mohamad, F.S. Fonseca, A.T. Vermeltfoort, D.R.W. Martens, P.B. Lourenço, Strength, behavior, and failure mode of hollow concrete masonry constructed with mortars of different strengths, Constr. Build. Mater. 134 (2017) 489–496. doi:10.1016/j.conbuildmat.2016.12.112.

[25] Ž. Radovanović, R. Sindić, S. Dimovska, N. Serdar, N. Vatin, V. Murgul, The mechanical properties of masonry walls - Analysis of the test results, Procedia Eng. 117 (2015) 865–873. doi:10.1016/j.proeng.2015.08.155.

[26] F. Tang, Effect of mortar joint thickness on the compressive strength of autoclaved flyash-lime brick masonry, Appl. Mech. Mater. 190–191 (2012) 462–466.

[27] Julian Ajith Thamboo; M. Dhanasekar; C. Yan, Effects of Joint Thickness , Adhesion and Web Shells To the Face Shell Bedded Concrete, Aust. J. Struct. Eng. 14 (2013) 291–302.

[28] R.E.C. and A.G. Timms, Effect Of Mortar Strength And Strength of Unit On The Strength Of Concrete Masonry, ACI J. 28 (1932) 551–562.

[29] K. FM, Factors Influencing Compressive Strength of Concrete Masonry Prisms, Mag. Concr. Res. 48 (1996) 95–101. doi:10.15623/ijret.2013.0213070.

[30] R.R.R. HR, Compressive strength of grouted and ungrouted concrete block masonry, Br. Mason. Soc. 9 (2002) 399–404.

[31] R.K.S.V.A. R, Compressive strength prediction of hollow concrete block masonry prisms, ACI Struct. J. 91 (2000) 61–67.

[32] P. Andolfato, J.S. Camacho, M.A. Ramalho, Brazilian Results on Structural Masonry Concrete Blocks, ACI Mater. J. 104 (2007) 33–39.

[33] Clàudius S. Barbosa; Paulo B. Lourenço; Joao B. Hanai, On the compressive strength prediction for concrete masonry prisms, Mater. Struct. 43 (2010) 331–344. doi:10.1617/s11527-009-9492-0.

[34] R.J. J., The effect of different test procedures upon the indicated strength of concrete blocks In compression, Mag. Concr. Res. 25 (1968) 87–98.

[35] A.M. Redmond TB, Compressive strength of composite brick and concrete masonry walls. Masonry: past and present., ASTM STP. 589 (1975) 195–232.

[36] H.A. Drysdale RG, Behavior of concrete block masonry under axial compression, ACI J. 76 (1976) 707–721.

[37] H.A. Drysdale RG, Capacity of concrete block masonry prisms under eccentric compressive loading, ACI J. 80 (1983) 102–108.

[38] G.P.W.K.S. C;, Influence of mortar bedding on masonry prism behaviour, 1987.

[39] C.G.D. RG;, Influence of test conditions on the compressive strength and behaviour of face shell mortar bedded concrete block prisms, in: 5th Can. Mason. Symp., 1989: pp. 651–660.

[40] K.F.H.A.F. DR, Study of the compressive strength of blockwork masonry, ACI Struct. J. 91 (1994) 367–376.

[41] S.M.D.R.K. MM, Influence of block geometry and grout type on compressive strength

of block masonry, in: 7th Can. Mason. Symp., 1995: pp. 1116–1127.

[42] N.N. Thaickavil, J. Thomas, Behaviour and strength assessment of masonry prisms, Case Stud. Constr. Mater. 8 (2018) 23–38. doi:10.1016/j.cscm.2017.12.007.

[43] Q. Zhou, F. Wang, F. Zhu, X. Yang, Stress–strain model for hollow concrete block masonry under uniaxial compression, Mater. Struct. Constr. 50 (2017). doi:10.1617/s11527-016-0975-5.

[44] W.A. Thanoon, M.S. Jaafar, M.R. Abdul Kadir, A.A. Abang Ali, D.N. Trikha, A.M.S. Najm, Development of an innovative interlocking load bearing hollow block system in Malaysia, Constr. Build. Mater. 18 (2004) 445–454. doi:10.1016/j.conbuildmat.2004.03.013.

[45] Shahriar Agaajani, Development and investigation of a new dry-stacked wall system, University of Luxembourg, 2015.

[46] Thallon R, Dry-Stack Block, Fine Homebuilding Mag. (1983) 50–57.

[47] A.K. Abang Ali, Strength properties and structural performance of interlocking hollow block walls, J. Inst. Jurutera Malya. 53 (1987) 25–35.

[48] Haener, Stacking Mortarless Block System, Eng. Des. Man. (1984).

[49] H. Ben Ayed, O. Limam, M. Aidi, A. Jelidi, Experimental and numerical study of Interlocking Stabilized Earth Blocks mechanical behavior, J. Build. Eng. 7 (2016) 207–216. doi:10.1016/j.jobe.2016.06.012.

[50] T. Sturm, L.F. Ramos, P.B. Lourenço, Characterization of dry-stack interlocking compressed earth blocks, Mater. Struct. Constr. 48 (2015) 3059–3074. doi:10.1617/s11527-014-0379-3.

[51] Cetholic, Mortarless Masonry - The Mecano System, Hous. Sci. 12 (1988) 145–157.

[52] N.A.A. Bari, N.A. Abdullah, R. Yusuff, N. Ismail, A. Jaapar, Environmental Awareness and Benefits of Industrialized Building Systems (IBS), Procedia - Soc. Behav. Sci. 50 (2012) 392–404. doi:10.1016/j.sbspro.2012.08.044.

[53] K.B. Anand, K. Ramamurthy, Laboratory-Based Productivity Study on Alternative Masonry Systems, J. Constr. Eng. Manag. 129 (2003) 237–242. doi:10.1061/(asce)0733-9364(2003)129:3(237).

[54] K. Anand, K. B.,Ramamurthy, Development and performance evaluation of interlocking block masonry, J. Archit. Eng. 6 (2000) 45–51.

[55] T. Zahra, M. Dhanasekar, Characterisation and strategies for mitigation of the contact surface unevenness in dry-stack masonry, Constr. Build. Mater. 169 (2018) 612–628. doi:10.1016/j.conbuildmat.2018.03.002.

[56] M.J. Greve, M.S. Dersch, J.R. Edwards, C.P.L. Barkan, H. Thompson, T.R. Sussmann, M.T. McHenry, Examination of the Effect of Concrete Crosstie Rail Seat Deterioration on Rail Seat Load Distribution, Transp. Res. Rec. J. Transp. Res. Board. 2476 (2015) 1–7. doi:10.3141/2476-01.

[57] A. Ghosh, M.J. Greve, M.S. Dersch, J.R. Edwards, C.P.L. Barkan, Analyzing Rail Seat Load Distributions on Concrete Sleepers using Matrix Based Tactile Surface Sensors, in: 11th World Congr. Railw. Res., 2016: pp. 1–7.

[58] Fujifilm, https://www.fujifilm.eu/fr/produits/produits-industriels/prescale, (n.d.).

[59] T. Zahra, Z. Yin, M. Dhanasekar, Experimental investigation of dry joint surface and closure characteristics of interlocking blocks under compression, Brick Block Mason. (2016) 2003–2009. doi:10.1201/b21889-263.

[60] Kang-Ho Oh; Harry G. Harries; Ahmed A. Hamid, Behavior of Interlocking Mortarless Masonry Under Compressive Loads, Seventh Can. Mason. Symp. (1995) 340–352.

[61] S. Allaoui, A. Rekik, A. Gasser, E. Blond, K. Andreev, Digital Image Correlation measurements of mortarless joint closure in refractory masonries, Constr. Build. Mater. 162 (2018) 334–344. doi:10.1016/j.conbuildmat.2017.12.055.

[62] K. Andreev, S. Sinnema, A. Rekik, S. Allaoui, E. Blond, A. Gasser, Compressive behaviour of dry joints in refractory ceramic masonry, Constr. Build. Mater. 34 (2012) 402–408. doi:10.1016/j.conbuildmat.2012.02.024.

[63] A. Gasser, K. Terny-Rebeyrotte, P. Boisse, Modelling of joint effects on refractory lining behaviour, Proc. Inst. Mech. Eng. Part L J. Mater. Des. Appl. 218 (2004) 19–28. doi:10.1243/146442004322849881.

[64] Mohd Saleh Jaafar; Ahmed Alwathaf; Waleed Thanoon; J. Noorzaei; M. R. Abdulkadir, Behaviour of interlocking mortarless block masonry, Constr. Mater. 159 (2006) 111–117.

[65] J.A. Thamboo, Development of thin layer mortared concrete masonry, Queensland University of Technology, 2014.

[66] S. Agaajani, D. Waldmann, F. Scholzen, A. Louge, Numerical analysis for the determination of stress percolation in dry-stacked wall systems, Mason. Int. 29 (2016) 27–38.

[67] EN 771-3: (2003); Specification for masonry units. Aggregate concrete masonry units (dense and lightweight aggregates), n.d.

[68] F.S. Fonseca, E.B. Murray, Axial Capacity of Dry-Stacked Endura Masonry Walls, 15th Int. Brick Block Mason. Conf. (2012).

[69] A.H. Alwathaf, W.A. Thanoon, M.S. Jaafar, Finite-element analysis of an alternative masonry wall system, Proc. Inst. Civ. Eng. - Struct. Build. 168 (2014) 237–250. doi:10.1680/stbu.13.00068.

[70] G.G. Chewe Ngapeya, D. Waldmann, F. Scholzen, Impact of the height imperfections of masonry blocks on the load bearing capacity of dry-stack masonry walls, Constr. Build. Mater. 165 (2018) 898–913. doi:10.1016/j.conbuildmat.2017.12.183.

[71] T.M.H. Nguyen, E. Blond, A. Gasser, T. Prietl, Mechanical homogenisation of masonry wall without mortar, Eur. J. Mech. A/Solids. 28 (2009) 535–544. doi:10.1016/j.euromechsol.2008.12.003.

[72] H. Liu, P. Liu, K. Lin, S. Zhao, Cyclic behavior of mortarless brick joints with different interlocking shapes, Materials (Basel). 9 (2016) 1–12. doi:10.3390/ma9030166.

[73] W.A. Thanoon, M.S. Jaafar, J. Noorzaei, M.R.A. Kadir, S. Fares, Structural Behaviour of

Mortar-Less Interlocking Masonry System under Eccentric Compressive Loads, Adv. Struct. Eng. 10 (2007) 11–24. doi:10.1260/136943307780150832.

[74] M.G.K. G, Experimental Investigation of Long-Term Behavior of Dry-Stacked Masonry, Mason. Soc. J. 20 (2002) 9–22.

[75] K. Andreev, S. Sinnema, A. Rekik, E. Blond, A. Gasser, Effects of dry joints on compressive behaviour of refractory linings, InterCeram Int. Ceram. Rev. (2012) 63–66.

[76] H. C. Uzoegbo; R. Senthivel; J. V. Ngowi, Loading capacity of dry-stack masonry walls, Mason. Soc. J. 25 (2007) 41–52.

[77] H. C. Uzoegbo; J. V. Ngowi, Structural Behaviour of Dry-stack Interlocking Block Walling Systems subject to In-plane Loading, Concr. Bet. 103 (2003) 9–13.

[78] T. Zahra, Strategies for Improving the Response of Drystack Masonry to Compression, 2017. https://eprints.qut.edu.au/109907/1/Tatheer_Zahra_Thesis.pdf.

[79] P.B. Lourenço, D. V. Oliveira, P. Roca, A. Orduña, Dry Joint Stone Masonry Walls Subjected to In-Plane Combined Loading, J. Struct. Eng. 131 (2005) 1665–1673. doi:10.1061/(asce)0733-9445(2005)131:11(1665).

[80] D. Bigoni, G. Noselli, Localized stress percolation through dry masonry walls. Part I - Experiments, Eur. J. Mech. A/Solids. 29 (2010) 291–298. doi:10.1016/j.euromechsol.2009.10.009.

[81] Agaajani Shahriar; Waldmann Danièle, Stabilite de systemes de murs en blocs de beton emtoitables sans joints en mortier, in: Regroupement Francoph. Pour La Rech. La Form. Sur Le Bét., 2012.

[82] D. Bigoni, G. Noselli, Localized stress percolation through dry masonry walls. Part II - Modelling, Eur. J. Mech. A/Solids. 29 (2010) 299–307. doi:10.1016/j.euromechsol.2009.10.013.

[83] P.B. Lourenço, L.F. Ramos, Characterization of Cyclic Behavior of Dry Masonry Joints,

J. Struct. Eng. 130 (2004) 779–786. doi:10.1061/(asce)0733-9445(2004)130:5(779).

[84] R.. Drysdale, E.. Gazzola, Strength and Deformation Properties of a Grouted, Dry-Stacked, Interlocking, Concrete Block System, Brick Block Mason. (1991) 164–171.

[85] M.S. Jaafar, W.A. Thanoon, A.M.S. Najm, M.R. Abdulkadir, A.A.A. Ali, Strength correlation between individual block, prism and basic wall panel for load bearing interlocking mortarless hollow block masonry, Constr. Build. Mater. 20 (2006) 492–498. doi:10.1016/j.conbuildmat.2005.01.046.

[86] I. Brick, B.M. Conference, Behaviour of Drystack Masonry Wallettes Under Axial Compression, (2004) 1–10.

[87] S. Atamturktur, B.E. Ross, J. Thompson, D. Biggs, Compressive Strength of Dry-Stacked Concrete Masonry Unit Assemblies, J. Mater. Civ. Eng. 29 (2016) 06016020. doi:10.1061/(asce)mt.1943-5533.0001693.

[88] R.A. Silva, E. Soares, D. V. Oliveira, T. Miranda, N.M. Cristelo, D. Leitão, Mechanical characterisation of dry-stack masonry made of CEBs stabilised with alkaline activation, Constr. Build. Mater. 75 (2015) 349–358. doi:10.1016/j.conbuildmat.2014.11.038.

[89] T. 1N4 N. G. Shrive, Professor The University of Calgary, Civil Engineering Oepartment, 2500 University Orive, N.W., Calgary, Alberta, Canada, COMPRESSIVE STRENGTH ANO STRENGTH TESTING OF MASONRY, (n.d.) 699–710.

[90] K. Lin, Y.Z. Totoev, H. Liu, C. Wei, Experimental characteristics of dry stack masonry under compression and shear loading, Materials (Basel). 8 (2015) 8731–8744. doi:10.3390/ma8125489.

[91] A. J. Francis; C.B. Horman; L.E. Jerrems, The effect of joint thickness and other factors on compressive strength of brickwork, in: Proc. 2nd Int. Brick Mason. Conf., 2017: pp. 31–37.

[92] F.A. Zuccarello, G. Milani, R.S. Olivito, A. Tralli, A numerical and experimental analysis

of unbonded brickwork panels laterally loaded, Constr. Build. Mater. 23 (2009) 2093–2106. doi:10.1016/j.conbuildmat.2008.08.031.

[93] T.T. Bui, A. Limam, V. Sarhosis, M. Hjiaj, Discrete element modelling of the in-plane and out-of-plane behaviour of dry-joint masonry wall constructions, Eng. Struct. 136 (2017) 277–294. doi:10.1016/j.engstruct.2017.01.020.

[94] L. Courard, Two different techniques for the evaluation of concrete surface roughness, (2006) 1015–1020.

[95] J.A. Greenwood, J.B.P. Williamson, Contact of nominally flat surfaces, Proc. R. Soc. London. Ser. A. Math. Phys. Sci. 295 (2006) 300–319. doi:10.1098/rspa.1966.0242.

[96] H.R. Pasaribu, D.J. Schipper, Application of a Deterministic Contact Model to Analyze the Contact of a Rough Surface Against a Flat Layered Surface, J. Tribol. 127 (2005) 451. doi:10.1115/1.1866163.

[97] Y.-R. Jeng, P.-Y. Wang, An Elliptical Microcontact Model Considering Elastic, Elastoplastic, and Plastic Deformation, J. Tribol. 125 (2003) 232. doi:10.1115/1.1537744.

[98] D.B.B. W. R. Chang, An Elastic-Plastic Model for the Contact of Rough Surfaces, J. Tribol. 109 (1987) 257–263.

[99] Y. Zhao, D.M. Marietta, L. Chang, Closure to "Discussion of 'An Asperity Microcontact Model Incorporating the Transition From Elastic Deformation to Fully Plastic Flow' " [ASME J. Tribol., 122, No. 2, p. 479 (2000)], J. Tribol. 122 (2002) 480. doi:10.1115/1.555389.

[100] Y. Zhao, L. Chang, A Model of Asperity Interactions in Elastic-Plastic Contact of Rough Surfaces, J. Tribol. 123 (2002) 857. doi:10.1115/1.1338482.

[101] C.C. and J.L. H. Gao, Elastic Contact Versus Indentation Model of Multi-Layered Material, Int. J. Solids Struct. 29 (1992) 2471–2492.

[102] A.K. Bhattacharya, W.D. Nix, Analysis of elastic and plastic deformation associated with indentation testing of thin films on substrates, Int. J. Solids Struct. 24 (1988)

1287–1298. doi:10.1016/0020-7683(88)90091-1.

[103] C. Scientific, M. Engineering, Mechanical property characterization of thin films using spherical tipped indenters, Thin Solid Films. 253 (2006) 204–211.

[104] R. Hayen, K. Van Balen, D. Van Gemert, Triaxial interaction of natural stone, brick and mortar in masonry constructions, Build. Mater. Build. Technol. to Preserv. Built Heritage, WTA Schriftenr. (2009) 333–352.

[105] V. Alecci, M. Fagone, T. Rotunno, M. De Stefano, Shear strength of brick masonry walls assembled with different types of mortar, Constr. Build. Mater. 40 (2013) 1038–1045. doi:10.1016/j.conbuildmat.2012.11.107.

[106] N. Augenti, F. Parisi, Constitutive modelling of tuff masonry in direct shear, Constr. Build. Mater. 25 (2011) 1612–1620. doi:10.1016/j.conbuildmat.2010.10.002.

[107] F.M. Khalaf, New test for determination of masonry tensile bond strength, J. Mater. Civ. Eng. 17 (2005) 725–732.

[108] S. Pavía, R. Hanley, Flexural bond strength of natural hydraulic lime mortar and clay brick, Mater. Struct. Constr. 43 (2010) 913–922. doi:10.1617/s11527-009-9555-2.

[109] G. Sarangapani, B. V. Venkatarama Reddy, K.S. Jagadish, Brick-Mortar Bond and Masonry Compressive Strength, J. Mater. Civ. Eng. 17 (2005) 229–237. doi:10.1061/(asce)0899-1561(2005)17:2(229).

[110] B. V. Venkatarama Reddy, R. Lal, K.S. Nanjunda Rao, Enhancing Bond Strength and Characteristics of Soil-Cement Block Masonry, J. Mater. Civ. Eng. 19 (2007) 164–172. doi:10.1061/(asce)0899-1561(2007)19:2(164).

[111] T. Zimmermann, A. Strauss, K. Bergmeister, Structural behavior of low-and normal-strength interface mortar of masonry, Mater. Struct. Constr. 45 (2012) 829–839. doi:10.1617/s11527-011-9801-2.

[112] K William; E D Warnke, Constitutive model for the triaxial behaviour of concrete, in: Int. Assoc. Bridg. Struct. Eng., 1975.

[113] A. Inc, ANSYS18 Europe, ANSYS Theory reference, n.d.

[114] K.I.S.A. Kabeer, A.K. Vyas, Experimental investigation on utilization of dried marble slurry as fine aggregate in lean masonry mortars, J. Build. Eng. 23 (2019) 185–192. doi:10.1016/j.jobe.2019.01.034.

[115] Vladimir Haach; Graça Vasconcelos; Paulo Lourenço, Assessment of compressive behaviour of concrete masonry prisms partially filled by general mortar, J. Mater. Civ. Eng. 26 (2014) 04014068 1–12. doi:10.1061/(ASCE)MT.

[116] F. Zeng, F.-B. Lin, K. V. Subramaniam, Experimental Investigation on Granite Masonry Behavior under Compression, Am. Soc. Civ. Eng. (2009) 1–9. doi:10.1061/41031(341)180.

[117] BS EN 772-1:2000, Methods of test for masonry units – Part 1: Determination of compressive strength, n.d.

[118] Atkinson and Kingsley, A comparison of the behaviour of clay and concrete masonry in compression, Masonry Buildings Research, N°1 (1985), USA-JAPAN.

[119] M.A. Hossain, Y.Z. Totoev, M.L. Masia, Friction on mortarless joint in semi interlocking masonry, Brich Block Mason. (2016) 1635-1644. doi:10.1201/b21889-203.

[120] A.H. Alwathaf, W.A.M. Thanoon, J. Noorzaei, M.S. Jaafar, M.R. Abdulkadir, Shear characteristic of interlocking mortarless block masonry joint, Brich Block Mason. 18(3) (2005) 139-146.

[121] G. G. Chewe Ngapeya, Danièle Waldmann, Experimental and analytical analysis of the load-bearing capacity P_u of improved dry-stacked masonry, Journal of Building Engineering 27 (2020), 100927. doi.org/10.1016/j.jobe.2019.100927.

[122] G. G. Chewe Ngapeya, Danièle Waldmann, Overcome of bed-joint imperfections and improvement of actual contact in dry-stacked masonry, Construction and Building Materials 233 (2020), 117173. doi.org/10.1016/j.conbuildmat.2019.117173.

List of figures

List of tables

List of abbreviations

Abbreviations

DSM	Dry-stacked masonry
DSM_b	Dry-stacked masonry block
FEM	Finite element model
MBTSS	Matrix based tactile sensor system
R_{ac}	Rate of the actual contact area
δ_h	Reduction factor due to the block height variation
δ_r	Reduction factor due to the block bed-joint roughness
ΔH^*	Deviation of the actual height of a masonry block with respect to the nominal height
ΔH_D	Height difference between two adjacent masonry blocks

Annexes

Annex A1

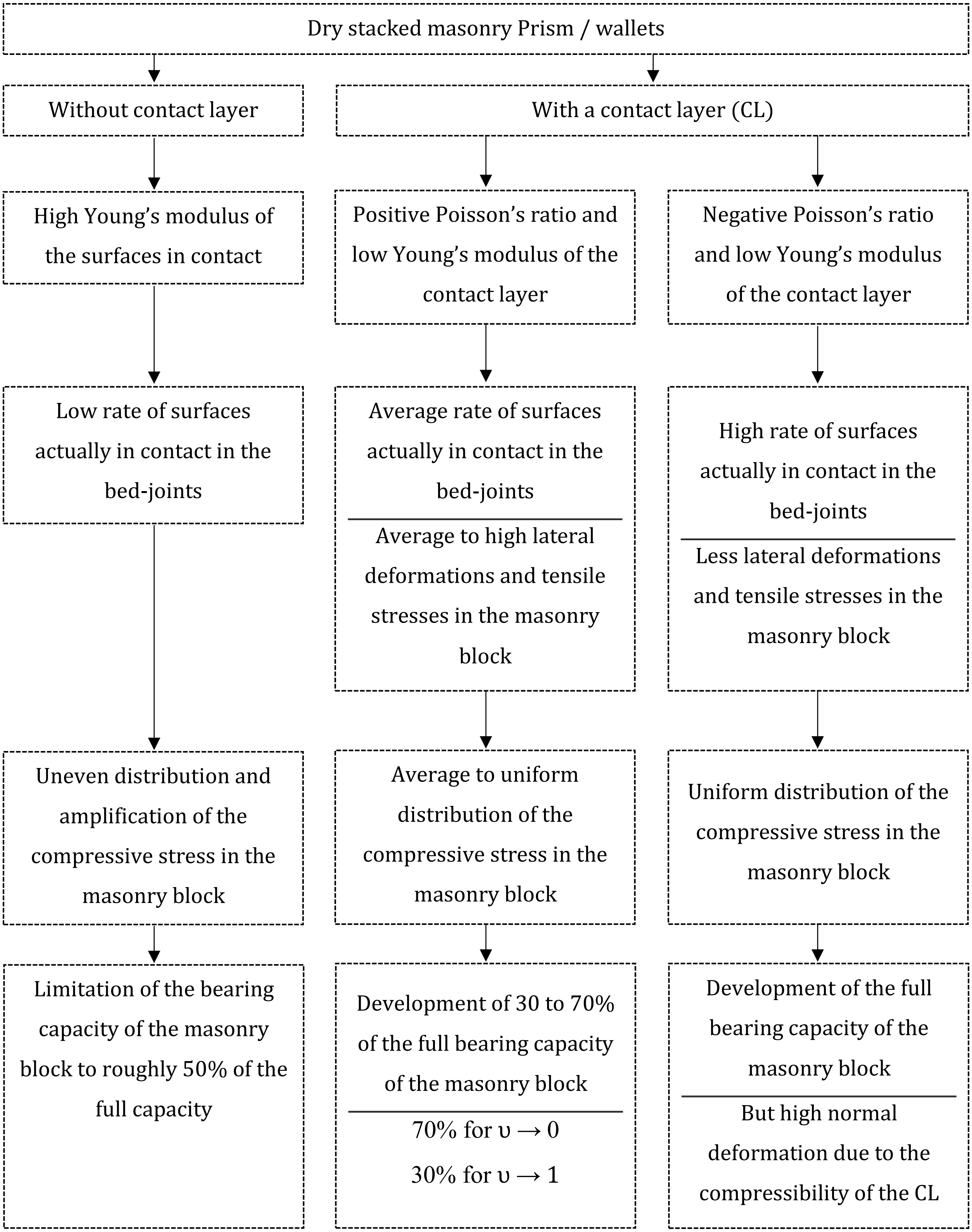

Figure 127. General overview of the response of a normal and an improved DSM$_b$